NASA Developments in Solid State Power Amplifiers

Regis F. Leonard
NASA Lewis Research Center

Over the last ten years, NASA has undertaken an extensive program aimed at development of solid state power amplifiers for space applications. Historically, the program may be divided into three phases. The first efforts were carried out in support of the Advanced Communications Technology Satellite (ACTS) program, which is developing an experimental version of a Ka-band commercial communications system. These first amplifiers attempted to use hybrid technology. The second phase was still targeted at ACTS frequencies, but concentrated on monolithic implementations, while the current third phase is a monolithic effort, but focusses on frequencies appropriate for other NASA programs and stresses amplifier efficiency.

I. 20 GHZ HYBRID AMPLIFIERS

As required by the ACTS program, the first solid state amplifiers developed by NASA Lewis were at 20 GHz. Two of the units (designed and built by TRW and Texas Instruments) utilized GaAs MESFET technology, while a third was based on GaAs IMPATT devices. All were based on discrete devices and external power combining to achieve the required power levels. The results of these three efforts are shown in Table 1.

TABLE 1.
PERFORMANCE OF HYBRID 20 GHZ AMPLIFIERS

	TI GaAs FET	TRW GaAs FET	TRW IMPATT
BANDWIDTH (GHZ)	2.5	1.5	0.220
GAIN (dB)	30	39.	29.0
POWER OUTPUT (W)	9.0	8.2	15.5
EFFICIENCY (%)	<8.	<8.	10.

As a result of these three efforts, all of which ended about 1984, and all of which were aimed at the production of a single port amplifier which would be appropriate as a tube replacement, NASA concluded that solid state amplifiers were not yet at a level where a 20 GHz single port amplifier at this power level was feasible for space applications. This decision was based primarily on the efficiency achieved at that time. Efforts since then have concentrated on the development of improved devices (efficiencies better than 30%) and their incorporation into monolithic low power (< 1 watts) amplifiers.

II. 20 GHZ MONOLITHIC MESFET POWER AMPLIFIERS

This work has been carried out under contract and has been aimed at several potential applications. The first round of

developments was again centered out at 20 GHz. The target application again was an ACTS-like commercial satellite, requiring multiple, steerable beams. The development of appropriate monolithic power amplifiers (and receivers and phase shifters) would permit such a system to be implemented using phased array antennas rather than the extensive network of ferrite phase shifters and power dividers used by ACTS. This phase of the NASA program, carried out between approximately 1983 and 1986, produced two 20 GHz monolithic amplifiers, each designed and built by Texas Instruments, and each based again on GaAs MESFET technology. The first of these, a variable power module, was a four stage amplifier which utilized dual gate FETs to achieve power variations while maintaining efficiency. A summary of its performance compared to design goals is shown in Table 2.

TABLE 2
TEXAS INSTRUMENTS 20 GHZ VARIABLE POWER AMPLIFIER

	DESIGN GOAL	PERFORMANCE
BANDWIDTH (GHZ)	2.5	2.5
MAX POWER OUTPUT (W)	0.5	0.25
EFFICIENCY AT MAX OUTPUT (%)	15	---
GAIN (dB)	20	20
4TH STAGE GATE WIDTH (MM)	----	1.2

The second 20 GHz chip was focussed entirely on the production of the maximum possible 20 GHZ power in a monolithic chip. Once more the contractor was Texas Instruments. This effort resulted in a three stage amplifier using single gate FETs. The performance of this chip is summarized in Table 3.

TABLE 3.
TEXAS INSTRUMENTS 20 GHZ HIGH POWER AMPLIFIER

	DESIGN GOAL	PERFORMANCE
BANDWIDTH	2.5	2.5
MAX POWER OUTPUT (W)	2.5	>2.0
EFFICIENCY AT MAX POWER (%)	20	16
GAIN (dB)	15	18
LAST STAGE GATE WIDTH (MM)	----	3.6

It is clear, however, that both of these units, although they constituted a benchmark achievement at this frequency, suffered from the same problem as the earlier hybrid implementations of solid state technology. Their efficiencies make their use marginal for space applications, except in very limited numbers, such as would be required if they were used as a driver for a higher efficiency final stage. An attempt to use multiple chips with any kind of combining would lead to prohibitively large prime power requirements.

III. HIGH EFFICIENCY MONOLITHIC POWER AMPLIFIERS

At the present time NASA Lewis is sponsoring the development of four monolithic power amplifier chips. One of these at 15 GHz is a candidate for use in the proximity communications system of the space station. Two at 32 GHz are for possible use in the space (transmitter) portion of the deep space communications network. The fourth at 60 GHz is intended for application to intersatellite communications, such as might be required by Advanced TDRSS or lunar/Mars exploration.

The space station proximity communications system is intended to provide communications within a radius of several 10's of kilometers of the space station. Users would include free flying experimental platforms, the orbital maneuvering vehicle (OMV), and astronauts in EVA. The original planning for this system utilized frequencies in Ku-band. It is not clear at this time whether that assignment will be maintained, inasmuch as there exist possible interferences with commercial, fixed satellite services. Nevertheless, several chips have been developed at 13-15 GHz to accommodate this application. The most challenging of these was a variable power amplifier intended primarily for use by astronauts during EVA. The system design requires approximately 1 watt of output power. Power variability is necessary because of the wide variation in range experienced by the astronaut. Of course, high efficiency is also a prime consideration. The development of the chip was undertaken by Texas Instruments in January 1987. Their design is a four stage monolithic circuit using dual gate GaAs MESFET technology. The chip is shown in Figure 1.

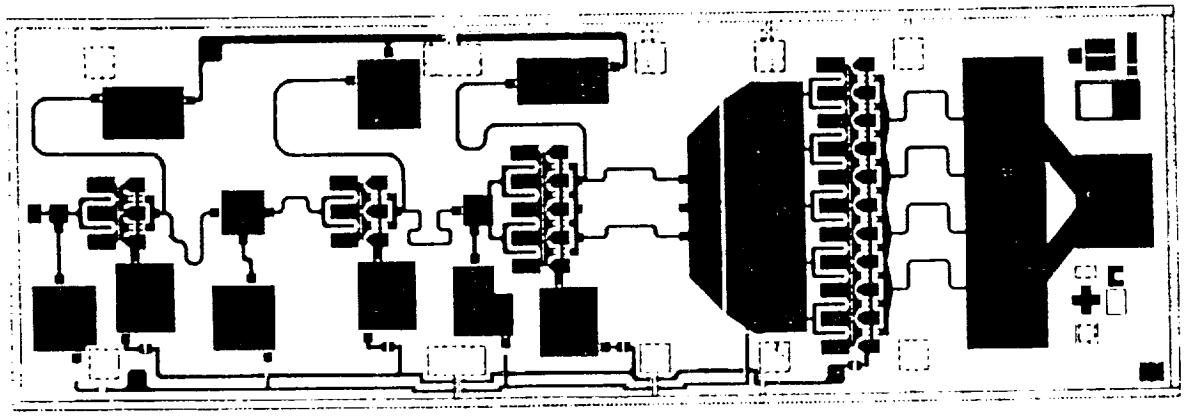

FIGURE 1. 15 GHZ MONOLITHIC VARIABLE POWER AMPLIFIER

The performance of the amplifier, compared to the design goals, is shown in Table 4.

TABLE 4.
15 GHZ HIGH EFFICIENCY VARIABLE POWER AMPLIFIER

	DESIGN GOAL	PERFORMANCE
BANDWIDTH (GHZ)	2.0	20
GAIN (dB)	15.0	29.6
MAX POWER OUTPUT (W)	1.0	.92
EFFICIENCY AT MAX POWER (%)	35	30.
FINAL STAGE GATE WIDTH (MM)	---	1.5

Both the power output and the efficiency achieved by this program essentially meet the system requirements formulated originally by the space station designers. The only problem at the present time is that the chip operates at a center frequency of 17 rather than 14 GHz.

In another application the NASA deep space communications network is considering a conversion to Ka-band. The primary motivation for such a change is the significant increase in antenna gain (for a fixed aperture size) and the corresponding decrease in power requirements (for a fixed data rate). Increased antenna gain, however, implies smaller beams and therefore more stringent pointing requirements. Such a situation, of course, is ideal for implementation of an electronically steerable phased array, which does not disturb other critically-pointed spacecraft instruments in the way a mechanically steered antenna would. To support breadboard evaluations of such a system, 32 GHz power amplifier modules are under development. The contractors executing these efforts are Texas Instruments and Hughes Aircraft. The TI work has been under way since May, 1985, and is near completion, while the Hughes effort was initiated in June 1988.

TI proposed and originally designed amplifiers using GaAs MESFET technology, but was directed, after approximately 18 months work, to concentrate on heterojunction devices. Specifically, they have investigated AlGaAs/GaAs HEMT structures and pseudomorphic InGaAs/GaAs structures. At this point it is clear that the pseudomorphic technology outperforms both the AlGaAs HEMT and the GaAs MESFET technology by a significant margin at 32 GHz. The specific pseudomorphic structure which TI has adopted is shown in Figure 2.

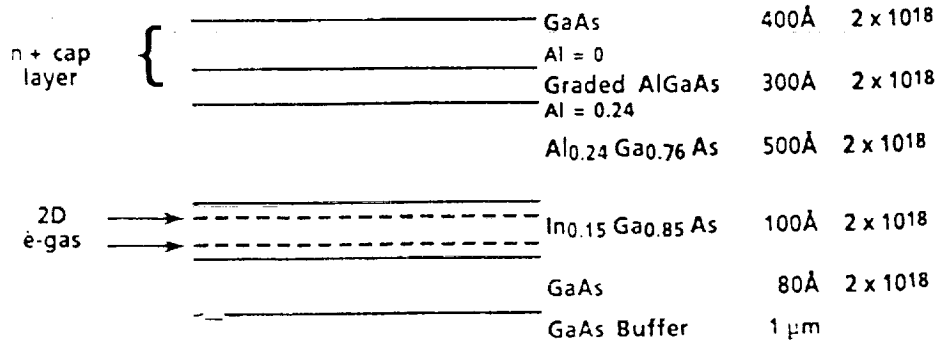

FIGURE 2. Texas Instruments' Pseudomorphic Power Amplifier Structure

The performance parameters for two of the pseudomorphic chips developed under this program are shown in Table 5.

TABLE 5.
TEXAS INSTRUMENTS 32 GHZ MONOLITHIC POWER AMPLIFIER PERFORMANCE

	3-STAGE AMP	1-STAGE AMP
BANDWIDTH (GHZ)	2.0	2.0
GAIN (dB)	23	4.6
GATE LENGTH (uM)	0.25	0.25
FINAL STAGE GATE WIDTH (MM)	.25	.25
POWER OUTPUT (mW)	190	460
EFFICIENCY (%)	30	24

The layouts of the two chips are shown in Figures 3 and 4.

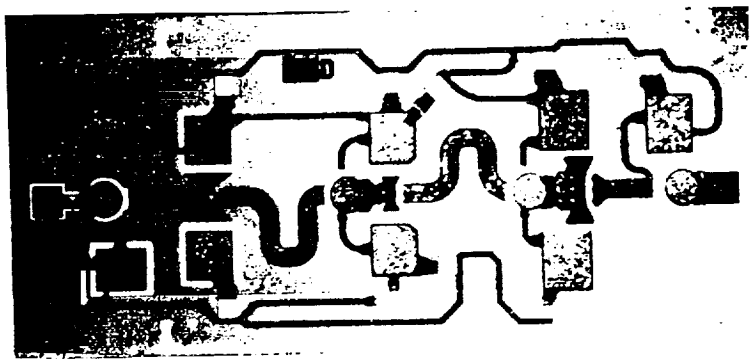

FIGURE 3. TI's 3-STAGE MONOLITHIC 32 GHZ AMPLIFIER

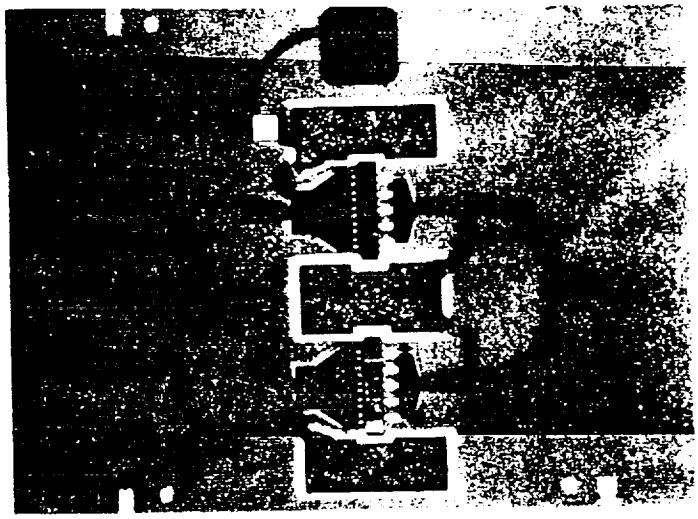

FIGURE 4. TI's ONE-STAGE MONOLITHIC 32 GHZ POWER AMPLIFIER

In a parallel 32 GHz effort Hughes Aircraft Corporation's Microwave Products Division and Malibu Research Laboratories are collaborating on the development of a 32 GHz variable power amplifier. The design goals for this chip are shown in Table 6.

TABLE 6.
DESIGN GOALS FOR HUGHES 32 GHZ VARIABLE POWER AMPLIFIER

BANDWIDTH (GHz)	2.0
MAX POWER OUTPUT (mW)	150
EFFICIENCY AT MAX POWER(%)	40
GAIN AT 1 DB COMP. (dB)	15.0

The Hughes contract, like most such developments at this time is to be carried out in several phases. These will consist of (1) the optimization of a single gate device design, (2) the development of a single stage amplifier, (3) the development of a dual gate device, (4) the design, fabrication, and test of a three-stage, single gate amplifier, and finally, (5) a three stage dual gate amplifier. In the 16 months that the Hughes team has been under contract, they have carried out the first two phases. The epitaxy which they have selected for the basic device is similar to that utilized by TI, except that Hughes has elected not to dope the active layer. It does,however, utilize a single active InGaAs layer with donors on each side. The layout and performance parameters for the basic 32 GHZ device are shown in Figure 5.

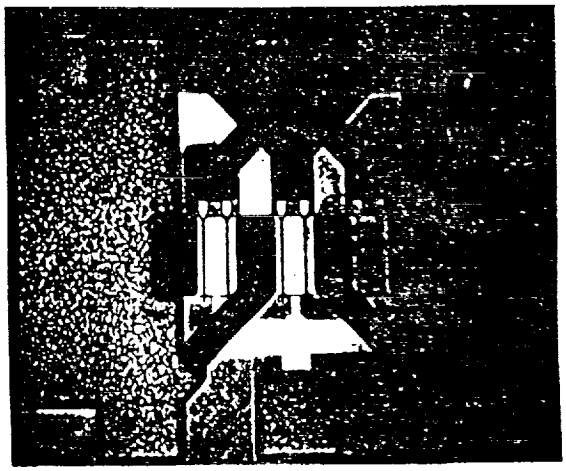

FREQUENCY	32.0
GAIN*	4(5) dB
POWER OUTPUT*	222(123)mW
EFFICIENCY*	23(41)%
GATE WIDTH	300 uM
GATE LENGTH	0.2 uM

*tuned for max power(eff)

Figure 5. Layout and Performance of Hughes 32 GHz Power MODFET

This device has been incorporated into a single stage amplifier, whose performance is shown in Table 7. This amplifier is intended as the third stage of the final monolithic module.

TABLE 7.
Performance of Hughes 32 GHz Single Stage Amplifier

GAIN (dB)	5.5
POWER OUTPUT (mW)	125
EFFICIENCY (%)	21

These results represent the first iteration of this chip, and significant improvement is expected before the program ends.

In addition, under the same contract, Hughes is developing a 60 GHz monolithic power amplifier. The justification for this program is eventual application in intersatellite links. Although NASA's plans for the Advanced Tracking and Data Relay Satellite (ATDRS) do not presently call for 60 GHz crosslinks, it seems likely that if such technology were available it would eventually find application in that area. The performance goals for the program, are shown below in Table 8.

TABLE 8. Performance Goals for Hughes' Pseudomorphic 60 GHz Power Amplifier

BANDWIDTH (GHz)	2.0
MAX POWER OUTPUT (W)	0.1
GAIN (dB)	15
EFFICIENCY (%)	30.

At 60 GHz Hughes is using the same basic pseudomorphic device structure as at 32 GHz, although the gate lengths have been shortened somewhat (0.1 to 0.15 uM). The layout and the performance achieved for a single stage amplifier are shown in Figure 6. As in the 32 GHz module, the amplifier shown is intended as the third (high power) stage of the completed monolithic amplifier.

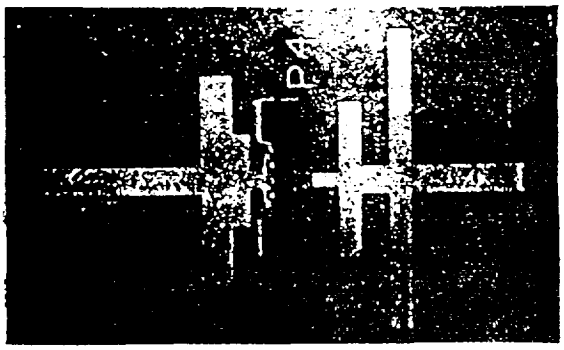

POWER OUT	112 mW
GAIN	6 dB
EFFICIENCY	26%

FIGURE 6. Hughes Single Stage Monolithic 60 GHz Amplifier

IV. FUTURE ACTIVITIES

The 32 GHz power amplifier modules developed by Texas Instruments and described here are scheduled to be incorporated into a breadboard transmitter array antenna which will also utilize phase shifters developed under NASA Lewis sponsorship. This work is being carried out at NASA's Jet Propulsion Laboratory, where a two dimensional array is expected to be completed late in calendar year 1990.

The Hughes work at both 32 Ghz and 60 Ghz is probably at least a year away from being used even in a breadboard system. Although the contract is scheduled for completion in early 1991, it has

yet to address what has been one of the major difficulties in the fabrication of a multistage power amplifier - inadequate large signal device models. It has been a common experience for a designer to develop excellent individual stage amplifiers, which meet all the requirements of the overall power and gain budget, only to find that the multistage module performance falls far short of the program requirements. Consequently, it appears optimistic to expect that Hughes will complete their development by 1991. 1992 would appear to be more realistic. At that time, it is anticipated that a 60 GHz breadboard array will be built, either at JPL or at NASA Lewis. As with the Ka-band array, it will utilize monolithic phase shifters which are being developed in parallel at Hughes.

NASA Technical Memorandum 101960

Performance of Five 30 GHz Satellite Receivers

Robert J. Kerczewski, George E. Ponchak,
and Robert R. Romanofsky
Lewis Research Center
Cleveland, Ohio

Prepared for the
1989 IEEE MTT-S International Microwave Symposium
Long Beach, California, June 13–15, 1989

NASA

PERFORMANCE OF FIVE 30 GHz SATELLITE RECEIVERS

Robert J. Kerczewski, George E. Ponchak, and Robert R. Romanofsky

National Aeronautics and Space Administration
Lewis Research Center
Cleveland, Ohio 44135

Technology development contracts funded by NASA have resulted in five 30 GHz satellite receivers of various design. This paper presents and discusses the results of tests performed at NASA Lewis Research Center to determine the operating characteristics of the receivers and their ability to perform in a digital satellite link.

Introduction

For the past 10 years, NASA has been developing technology intended to enhance the performance of future satellite communication systems. This work has focused on systems operating at 30 GHz uplink and 20 GHz downlink frequencies. A major part of this technology thrust is the development of 30 GHz low noise satellite receivers. As a result of technology development contracts, five receivers of various design have been delivered. These receiver models have undergone extensive testing at NASA Lewis Research Center to determine their operating characteristics and their performance in a satellite communication system transmitting high rate digital data. In the following sections, the design of the receivers will be described, and the results of performance measurements will be presented and discussed.

30 GHz Low Noise Satellite Receiver Designs

The delivery of completed hardware from the five development contracts spanned the time period of 1982 through 1987. Two parallel contracts, under the management of NASA Lewis, were completed in late 1982 by LNR Communications, Inc. and ITT Defense Communications Division. Figure 1 shows the basic functional design of these receivers.[1] Both LNR and ITT used an image-enhanced diode mixer for the receiver front end, followed by a FET IF amplifier. The designs varied in method of local oscillator (LO) generation and operating frequency. The resulting hardware consisted of a complete receiver unit, requiring only dc bias and an LO reference.

NASA Goddard Space Flight Center initiated a contract with Hughes Aircraft Company, Microwave Product Division, which resulted in the delivery of completed receiver models in the fall of 1984. One receiver was sent to NASA Lewis for evaluation under the Lewis satellite communication system component test program. As shown in Fig. 2, the Hughes design consists of a hybrid combination of GaAs FET microwave integrated circuits (MIC's) developed by Hughes for this project.[2] The receiver front end is a 30 GHz GaAs FET low noise amplifier (LNA) MIC, which is followed by an MIC mixer and an IF amplifier. The LO is an internally generated 22 GHz FET dielectric resonator oscillator. The complete receiver package requires only a dc bias.

These three receivers are generally intended for use in 30/20 GHz satellite communication systems with single-feed satellite receive antenna systems. Such an antenna system may consist of a single feed horn or a feed-horn cluster which would permit a beam-hopping system. This system would consist of an array where different groups of feed horns are switched on to provide receive coverage scanning geographically isolated areas. In all these cases, the received signal is collected and combined to provide an input signal to a single receiver.

For electronically scanned antenna systems, a multi-element phased array antenna is used. This system consists of an array of antenna elements, each connected to an individual receiver which includes controllable phase shifters and variable gain amplifiers. Control of these elements allows the antenna beam to be spatially scanned. Each receiver processes only a portion of the signal incident on the antenna. The receiver outputs are then combined into single received signal. For this type of system, a monolithic microwave integrated circuit (MMIC) receiver is required. Therefore, a development program was initiated by NASA Lewis in 1982. Contracts were awarded to Hughes Aircraft Co., Microwave Products Division[5] and Honeywell Sensors and Signal Processing Lab[6] for the development of a 30 GHz monolithic receiver. The receivers consist of an LNA, mixer, gain control amplifier (GCA), and phase shifter. Although both contractors were to meet the same program goals, Hughes and Honeywell used different design approaches. Honeywell performed all amplification and phase shifting at 30 GHz, while Hughes did the phase shifting at the LO frequency and the GCA at the IF. Extra filtering and amplification were added by NASA Lewis to create a complete satellite

receiver in order to allow testing. The block diagrams of the Honeywell and Hughes MMIC receivers are shown in Fig. 3 and 4, respectively.

Test Results

To determine their performance in a high data rate digital satellite transmission system, the receivers were tested in the automated measurement system shown in Fig. 5. The system simulates an end-to-end satellite communications link, operating at a data rate of 220 Mbps. The modulation type is serial minimum shift keying (SMSK). Discrete amounts of noise are added at the system output to allow measurement of the BER as a function of Eb/No.[4] An example of the results of such a measurement is shown in Fig. 6 for the five receivers tested at an input power level of -30 dBm.

A summary of the test results obtained is given in Table I. The RF test data is presented in detail in Refs. 1 to 3, 5 and 6. The BER data given represents the degradation of the measured curve, in dB, compared to the theoretical curve, at a BER of 10^{-6}. For a typical system, the receiver with the highest gain and lowest noise figure should give the lowest BER. At the lower power levels, the BER performance is directly related to the noise figure of the receiver. A BER of 10^{-6} could not be obtained for the Honeywell receiver below a -50 dBm input and for the Hughes MMIC receiver below -30 dBm input because of their high noise figure. The Hughes MMIC receiver performed poorly because the LNA operated optimally at 32-34 GHz; at 30 GHz, the noise figure was very high and no gain was obtained. The Honeywell MMIC receiver used a two-stage LNA. Honeywell's final design will use a six-stage LNA, which will provide a significant gain increase and noise figure reduction. In NASA's tests, the MMIC receivers, consisting of two or more interconnected MMIC fixtures, suffered significantly from interstage mismatch problems.

At higher power levels, the noise figure was not a factor in BER performance except for the Hughes MMIC receiver. The most important factor above -50 dBm was the frequency response of the combined receiver and test system. Due to the various output operating frequencies of the receivers, it was not always possible to test them at their optimum design frequency and the band center of the test system simultaneously. Therefore, the variation of BER results between the receivers at the higher power levels does not necessarily indicate significant performance differences. We consider any BER degradation less than 3.0 dB to indicate acceptable receiver performance.

Conclusion

In general, digital satellite communication systems are required to provide a maximum BER of 10^{-6}. The Hughes MMIC receiver is the only one which did not meet this criteria at the power levels tested. The other receivers met this criteria with a maximum Eb/No degradation of 2.6 dB for an input power of -30 dBm. System performance degradation is observed when the receiver input power is reduced to the noise figure limit of the receiver. Thus, the receiver noise figure is a limiting factor in system performance. The three hybrid receivers performed well for input powers as low as -50 dBm.

The MMIC receivers performed poorly relative to the hybrid receivers. Since an MMIC scanning antenna system would combine the outputs of many MMIC receivers, the system Eb/No obtained would be higher than for each individual receiver. Therefore, adequate system performance may still be obtained with these receivers. In addition, further improvements in MMIC design and optimization are likely to improve performance.

References

1. Conroy, M.J., and Kerczewski, R.J., "Testing of 30 GHz Low Noise Receivers," Eleventh Communications Satellite Systems Conference, AIAA, 1986, pp. 326-340(NASA TM-87171).

2. Watkins, E.T., and Schellenberg, S.M., "Hybrid Microwave Integrated Circuit Ka-Band Low Noise Receiver," (NASA Contract NAS5-26731) Hughes Aircraft Co., Microwave Products Division, Torrance, CA, 1984.

3. Ponchak, G.E., and Romanoffsky, R.R., "Monolithic Microwave Integrated Circuit Technology for Advanced Space Communication," NASA TM-100829, 1988.

4. Kerczewski, R.J., Daugherty, E.S., and Kramarchuk, I., "Automated Measurement of the Bit-Error Rate as a Function of Signal-to-Noise Ratio for Microwave Communications Systems," NASA TM-89898, 1987.

5. Bauhahn, P., Geddes, J., Sokolov, V., and Contolatis, T., "30 GHz Monolithic Receive Module," NASA CR-180849, 1988.

6. Liu, C.S., Asher, P.G., Wang, S.K., and Chang, C.D., "30 GHz Monolithic Receive Module," (NASA Contract NAS5-26731) Hughes Aircraft Co., Microwave Products Division, Torrance, CA, 1987.

TABLE I. - SUMMARY OF TEST RESULTS FOR FIVE 30 GHz SATELLITE RECEIVERS

Parameter	Receiver				
	LNR Communications 1982	ITT Defense Communications 1982	HAC Microwave Products Divison 1984	Honeywell Sensors and Signal Process Lab 1987	HAC Microwave Products Division
Input band, GHz	27.5 to 30.0	27.5 to 30.0	27.5 to 30.0	27.5 to 30.0	27.5 to 30.0
Output band, GHz	3.7 to 6.2	2.3 to 4.8	5.5 to 8.0	4.5 to 7.0	3.0 to 5.5
LO frequency, GHz	23.8	25.2	22.0	23.0	24.5
Gain (maximum), dB	22	19	41	13	-5.2
Gain variation over 2.5 GHz, dB	3.8	4.8	5.2	5.2	5.0
Noise figure (minimum), dB	5.8	6.8	3.7	14.0	>20
Input VSWR (Max. over 2.5 GHz)	2.3:1	3.4:1	[a]1.3:1	3.6:1	>10:1
Output VSWR (Max. over 2.5 GHz)	1.7:1	1.4:1	2.3:1	8.5:1	3.8:1
1 dB Compression point midband (input), dBm	-7	-8	-27	-3	-2
BER degradation, -30 dBm In, HPA saturated, dB	1.1	2.0	2.6	0.9	6.8
BER degradation, -40 dBm In, HPA saturated, dB	1.0	2.1	1.5	2.5	----------
BER degradation, -50 dBm In, HPA saturated, dB	1.2	2.5	2.5	18.4	----------
BER degradation, -60 dBm In, HPA saturated, dB	3.8	6.6	2.5	----------	----------
Dynamic range at -10 dBm input, dB	N/A	N/A	N/A	>13	>18
Insertion phase envelope as a function of gain, deg	N/A	N/A	N/A	±10	±15
Gain envelope as a function of phase state, dB	N/A	N/A	N/A	±2	±2
Phase shift/ phase shift increment, deg	N/A	N/A	N/A	360/ 11.25	180/ Continuous
Design topology	Hybrid	Hybrid	Hybrid - MIC	Multiple-chip MMIC	Multiple-chip MMIC

[a]Hughes measurement

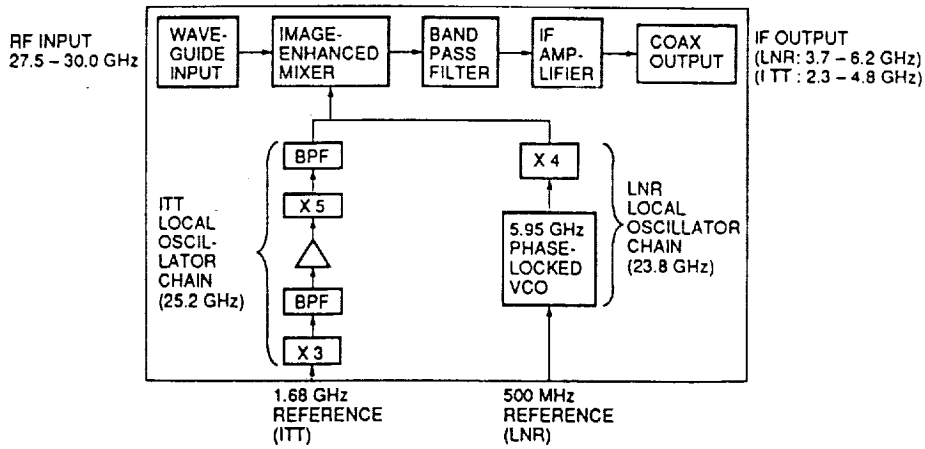

Figure 1. - Functional block diagram for the LNR Communications, Inc., and ITT Defense Communications 30 GHz low noise receivers.

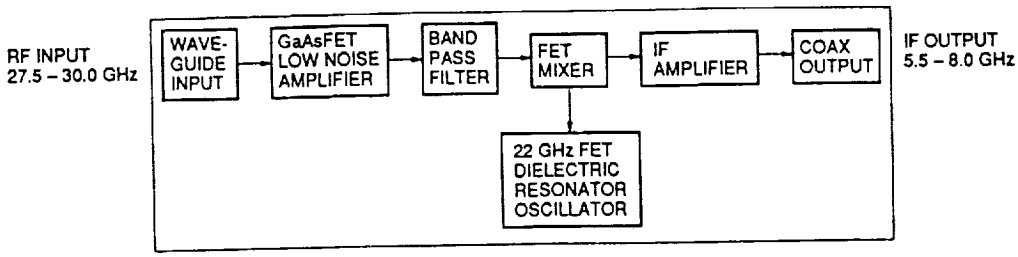

Figure 2. - Functional block diagram for the Hughes Hybrid – MIC 30 GHz low noise receiver.

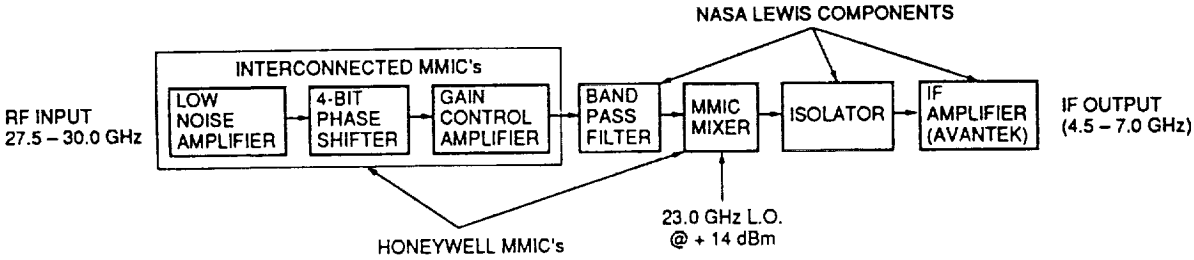

Figure 3. - Honeywell MMIC receiver test configuration.

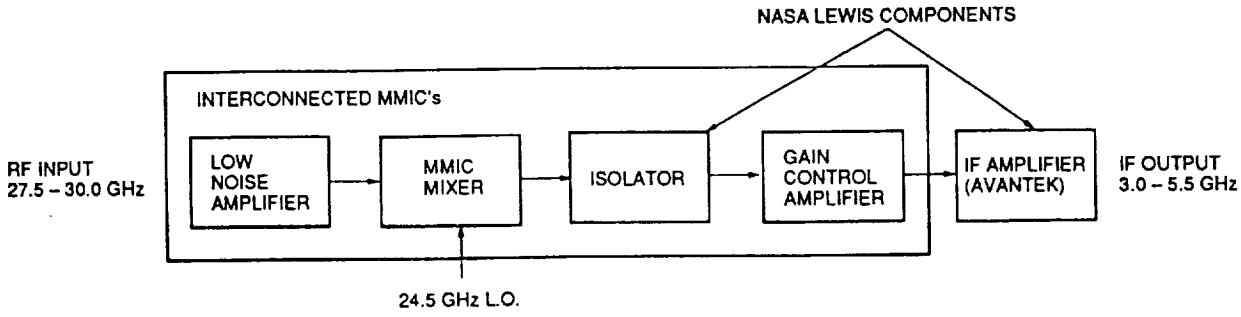

Figure 4. - Hughes MMIC receiver test configuration.

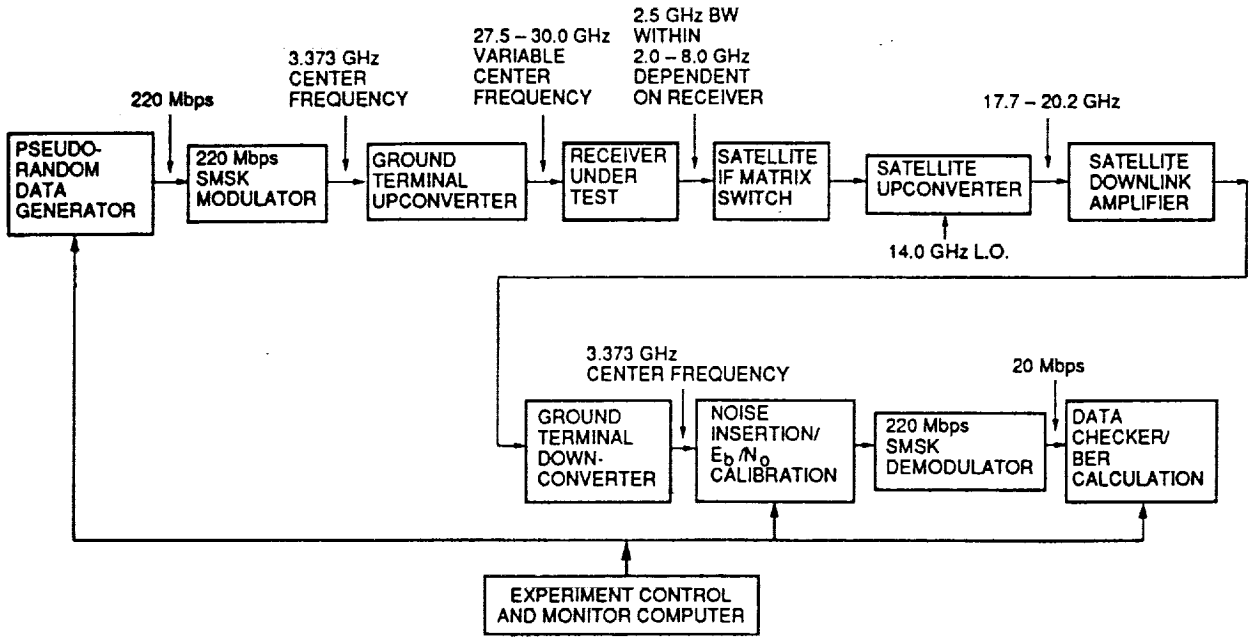

Figure 5. - Block diagram of the receiver BER measurement system.

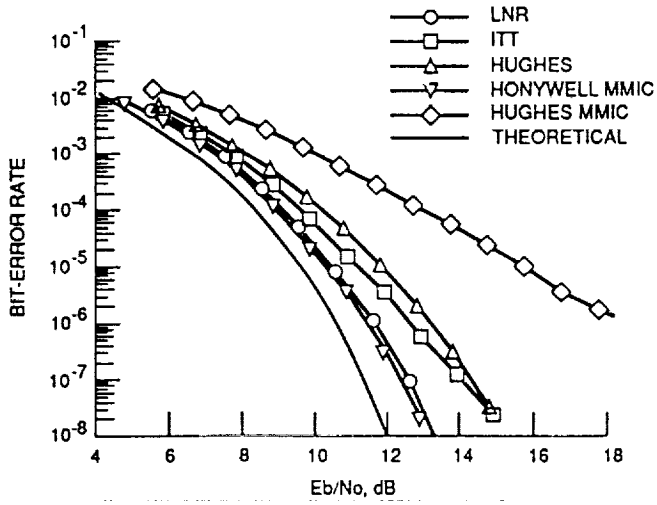

Figure 6. - Measured BER curves, for the LNR, ITT Hughes Hybrid-MIC, Honeywell MMIC, and Hughes MMIC receivers. Input power to the receivers is -30 dBm, and the satellite high power amplifier is in saturation.

NASA Technical Memorandum 102550

Optical Control of an 8-Element Ka-Band Phased Array Using a High-Speed Optoelectronic Interconnect

M.A. Richard and P.C. Claspy
Case Western Reserve University
Cleveland, Ohio

K.B. Bhasin
Lewis Research Center
Cleveland, Ohio

and

M. Bendett
Honeywell, Inc.
Bloomington, Minnesota

Prepared for the
1990 AP-S International Symposium
sponsored by the Institute of Electrical and Electronic Engineering
Dallas, Texas, May 7-11, 1990

NASA

OPTICAL CONTROL OF AN 8-ELEMENT Ka-BAND PHASED ARRAY ANTENNA USING A HIGH-SPEED OPTOELECTRONIC INTERCONNECT

M. A. Richard and *P. C. Claspy, Department of Electrical Engineering,
Case Western Reserve University, Cleveland, OH,
K. B. Bhasin, National Aeronautics and Space Administration,
Lewis Research Center, Cleveland, OH,
and M. Bendett, Honeywell, Inc.,
Sensors and Signals Technology Center, Bloomington, MN

ABSTRACT

Optical distribution of control signals in electronically steered phased array antennas is being considered. This paper describes a demonstration experiment in which a high speed hybrid GaAs optoelectronic integrated circuit (OEIC) was used to control an eight element phased array antenna. The OEIC, which accepts a serial optical control signal as input and converts it to 16 demultiplexed parallel outputs, was used to control the monolithic GaAs phase shifters of a Ka-band patch panel array antenna. Antenna pattern switching speeds of 2.25 μs, limited by interface circuitry, were observed.

E-5365

1. INTRODUCTION

Because of advantages such as low weight and high beam steering speeds offered by phased array antennas, future NASA missions such as Mars Rover and Mission Planet Earth call for the use of such antennas for purposes of communication and radiometry.[1] While the development of steerable microwave frequency phased arrays has been stymied in the past by the lack of small phase shifters and power amplifiers, recent advances in GaAs monolithic microwave integrated circuit (MMIC) technology have resulted in the development of high quality integrated power amplifiers and phase shifters.[2] With these advances, large arrays, on the order of 100 to 1000 elements, are becoming feasible.

The use of such a large number of elements at millimeter wave frequencies presents unique challenges in the distribution of RF and control signals to each element because of the small element spacings involved. As a way to surmount this problem, various fiber optic-based solutions have been proposed and investigated. Optical fibers hold much promise for use in large phased arrays because of their light weight, low attenuation, mechanical flexibility, large bandwidth, and immunity to cross talk and EMI. As the operational frequencies of arrays increase, the amount of available space for interconnection of elements decreases, so multiplexing of control signals onto a single fiber would clearly be advantageous. This would allow beam control data to be brought from a data source and be distributed locally to the phase shifters and amplifiers while simultaneously achieving a reduction in weight and space consumed.[3] When this is done, the input data rate becomes high even though the rate to an individual control line may be low. In this paper we describe the use of a single optical fiber to distribute control data to the phase shifters of an eight-element array.

---

*NASA Resident Research Associate at Lewis Research Center.

2. EXPERIMENTAL ARRANGEMENT

A system consisting of a phased array antenna, an optoelectronic integrated circuit (OEIC) controller, and optical source and fiber, and the necessary electronics, shown schematically in Fig. 1, was set up to demonstrate optical control of a phased array antenna. The OEIC, which has been described in a previous publication,[4] is a hybrid device that requires a serial optical bit stream input, as well as electrical clock and synchronization inputs, and produces 16 parallel, demultiplexed, electrical outputs and a data valid (clock divided by 16) output. It is capable of operation at speeds up to approximately 300 Mb/sec.

The antenna, shown in Fig. 2, was developed by Honeywell[5] for another program, and is a narrow band, eight element system that is tuned to 28.2 GHz. It has an eight-way corporate feed network that divides the input power equally among eight phase shifters that, in turn, feed the eight radiating elements, each of which consists of 10 patches spaced by 1.94 cm. Each phase shifter is a 4-bit device that has 16 possible delay settings in 22.5° increments from 0° to 337.5°.[6,7] The 64 control lines are brought out to two ribbon connectors on opposite sides of the antenna. A phase look-up table was available to permit compensation for path length differences within the feed network in establishing an antenna beam direction. As a result of process tolerances the pinchoff voltages of the FET's in the antenna phase shifters ranged from -5 V to -6 V, and a voltage control circuit to accommodate this was obtained from Honeywell.

Since the OEIC and the antenna phase shifters were not designed to be directly interfaced, voltage level shifting was required between the two systems. The OEIC was therefore used to control an electronic switch which, in turn controlled the voltages applied to the phase shifters. Rather than controlling all 32 bits of the array (8 shifters × 4 bits/shifter), eight bits were strategically selected so that by changing only these bits the antenna pattern could be switched between normal to the plane of the antenna and 20° from the normal to the plane. For the optical control experiment an oscillator/amplifier combination was used to feed a 28.2 GHz signal, at +21 dBm, to a 25 dB horn that served as a transmitter radiator. An HP 8018 data source was programmed to output a sequence of data so that the demultiplexed outputs of the OEIC, that controlled the previously selected eight antenna phase shifter bits, would alternate between high and low levels at 200 KHz. The array was centered on and perpendicular to the horn axis, with a separation of 3 m.

3. EXPERIMENTAL RESULTS

Toggling the phase shifters between the two states caused the array pattern to alternately point directly toward the transmitter, then 20° from it, with the result that the output signal from the antenna alternated from a maximum to nearly zero, as shown in Fig. 3. In the figure the top trace is one OEIC output data line and the lower trace is the amplified detector output. (In the lower trace the response speed was limited by the time constant of the detector that was used to record the antenna output.) In this experiment the clock frequency was 50 MHz, the average optical power to the OEIC was 200 μW and the beam switching rate was 3.2 μs. By rearranging the data pattern the switching rate could be reduced to 2.25 μs, but in all cases the maximum switching speed was limited by the interface circuitry.

4. CONCLUSIONS

In this paper we have reported the results of an experiment involving the optical control of a 28.2 GHz phased array antenna. In this work an eight element antenna was controlled by the demultiplexed output of a single optically fed controller, demonstrating the feasibility of applying such devices to the antenna control problem. The speed of switching was limited by the interface circuitry to 2.25 μs.

The authors wish to acknowledge the assistance and support of Doug Carlson, Mark Vickberg, and Vladimir Sokolov of Honeywell's Sensors and Signals Technology Center.

1. K. B. Bhasin and R. R. Kunath, "Optically interconnected phased arrays," SPIE Advances in kSemiconductors and Superconductors: Physics and Device Applications Conference, Newport, CA, March 1988. Also published as NASA Technical Memorandum 100855, 1988.
2. Microwave Integrated Circuits, J. Frey and K. B. Bhasin, eds. (Artech House, 1985).
3. K. B. Bhasin, et. al., "Optical techniques to feed and control GaAs MMIC modules for phased array antenna applications," 11th Communications Satellite Systems Conference, pp. 506-513, AIAA, New York, 1986. Also published as NASA Technical Memorandum 87218, 1986.
4. P. C. Claspy, M. Richard, K. B. Bhasin, M. Bendett, G. Gustavson, and W. Walters, "A high-speed GaAs MESFET Optical Controller," IEEE Photonics Tech. Lett., vol. 1, pp. 389-391, 1989.
5. V. Sokolov and M. Komen, "Electronically Steerable Patch Panel Array Antenna," Honeywell Final Report, Report No. AFATL-TR-87-19, Air Force Armament Laboratory, Eglin Air Force Base, FL, April 1987.
6. V. Sokolov, P. Bauhahn, J. Geddes, A. Contolatis, and C. Chao, "A Ka-Band GaAs Monolithic Phase Shifter," IEEE Trans. Electron Devices, vol. ED-30, pp. 1855-1861, 1983.
7. P. Bauhahn, C. Butter, V. Sokolov, and A. Contolatis, "30 GHz Multi-bit Monolithic Phase Shifter," IEEE Microwave Theory Tech 1985 Symposium Proc. pp. 4-7, May 1985.

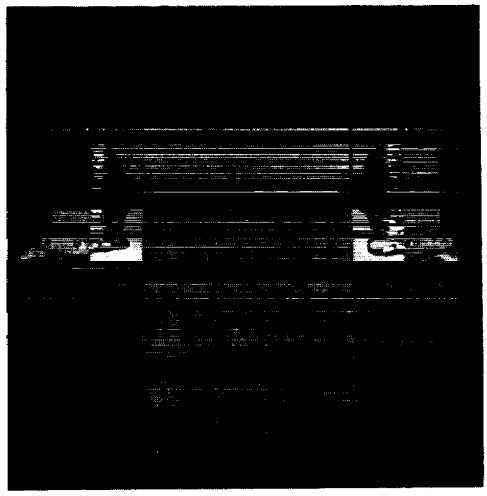

Fig. 1. The 8-element Ka-band phased array antenna.

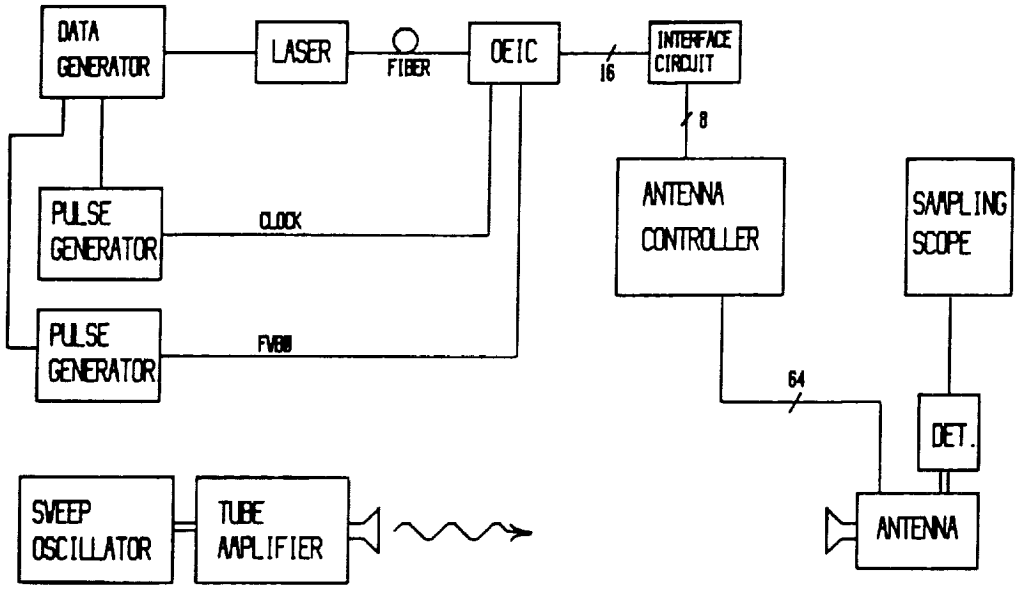

Fig. 2. Experimental arrangement.

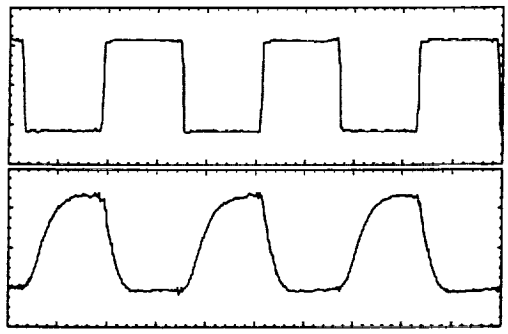

Fig. 3. Antenna switching results. Top trace: Single data line of antenna control signal. Vertical scale: 60μV/div.; Bottom trace: Detector output. Vertical scale: 4 mV/div. Horizontal scale for both traces: 2 μs/div.

NASA Technical Memorandum 103110

Performance of a 300 Mbps 1:16 Serial/Parallel Optoelectronic Receiver Module

M.A. Richard and P.C. Claspy
Case Western Reserve University
Cleveland, Ohio

K.B. Bhasin
Lewis Research Center
Cleveland, Ohio

and

M.B. Bendett
Honeywell, Inc.
Bloomington, Minnesota

Prepared for the
Technical Symposium on Optical Engineering and Photonics
in Aerospace Sensing
sponsored by the Society of Photo-Optical Instrumentation Engineers
Orlando, Florida, April 16–20, 1990

NASA

Performance of a 300 Mbps 1:16 serial/parallel optoelectronic receiver module

M.A. Richard, P.C. Claspy

Case Western Reserve University, Department of Electrical Engineering
Cleveland, OH 44106

K.B. Bhasin

NASA Lewis Research Center
21000 Brookpark Rd., Cleveland, OH 44135

M.P. Bendett

Honeywell, Inc.
Bloomington, MN

E-5434

ABSTRACT

Optical interconnects are being considered for the high speed distribution of multiplexed control signals in GaAs MMIC-based phased array antennas. This paper describes the performance of a hybrid GaAs optoelectronic integrated circuit (OEIC), along with a description of its design and fabrication. The OEIC converts a 16-bit serial optical input to a 16 parallel line electrical output using an on-board 1:16 demultiplexer and operates at data rates as high as 305 Mbps. The performance characteristics as well as potential applications of the device are presented.

INTRODUCTION

The advantages of large directly radiating phased array antennas for rapid beam scanning are well known, but conventional hardware is heavy and bulky, and architectures for implementing these arrays have resulted in cumbersome, topologically complex, and high loss internal distribution systems. GaAs monolithic microwave integrated circuits (MMIC's), which have undergone extensive development and which could be used as array output modules, represent a major step toward improved and light weight arrays[1]. Yet, the interconnection of these devices into a beam formation network (BFN), is still a rather formidable problem. Conventional methods carrier and control signal distribution to the radiating elements suffer from cross talk and electromagnetic interference between elements. To alleviate these problems, several optics-based signal distribution methods have been proposed as solutions. Among the propose methods are those which use fiber optics to interconnect the BFN's[2-5], and those which use optical processing within the BFN's.[6-9]

The work described here is addressed toward the meeting of needs of fiber optic interconnected BFN's. The GaAs MMIC's in a phased array antenna are relatively complex. They include a variable phase shifter and a variable power amplifier which permit the creation of the aperture phase and amplitude distribution that is appropriate to the desired radiated beam configuration. Some proposed architectures also include a local oscillator and a mixer at each antenna element.[10,11] In fiber optic interconnected systems, optical fibers would be used to carry the control signals to the variable phase shifters and amplifiers as well as the signal to be transmitted

and the local oscillator phase locking signal. All control signals for the array including phase shifter and amplifier control signals could be multiplexed onto one optical channel as seen in Fig. 1. Although the actual rate at which a single phase shifter or power amplifier requires data may be low, the large number of elements involved necessitates a high overall data transfer rate, and thus a wide bandwidth channel will be required. Some demonstrations of the use of optical interconnects in phased array applications, using discrete components, have been reported[12], and Crow et. al., have reported a demultiplexing OEIC[13]. In this paper we report on the design and fabrication of a hybrid, high speed GaAs MESFET integrated circuit optical receiver/demultiplexer.

The constructed device is a hybrid optoelectronic integrated circuit (OEIC). Two GaAs circuits, an optical receiver and a demultiplexer, are packaged together in a 34-pin flatpack with a fiber pigtail attached for optical input. The inputs to the OEIC are a 16 bit optical serial data stream at 830 nm, an electrical high-speed clock, and a synchronization signal (FWBO). The outputs are 16 parallel TTL-level electrical outputs and an input clock divided by 16.

DESIGN AND FABRICATION

A PIN photodiode was chosen in place of the conventional MSM photodetector because of its superior noise performance, its speed capability, and its enhanced photosensitivity. It also has the advantage over the MSM or NPN structures commonly used for monolithic integration in that it can be operated in the photovoltaic mode if necessary since it is an asymmetric device. It was implemented using an interdigitated structure (2 μm finger width, 5 μm finger spacing) with an overall size of 40 μm x 60 μm. To achieve high speed and sensitivity a multi-stage differential amplifier is used to boost the signal from the detector up to logic levels. This amplifier consists of a transimpedance input stage followed by two additional capacitively coupled stages, each with a gain of approximately 10 dB. A constant output level is achieved by using a digital amplifier output section. The output from the receiver chip is fed into the 1:16 demultiplexer, that employs direct coupled FET logic (DCFL) circuitry. Although this does not necessarily provide the optimum speed and power dissipation characteristics, it permits circuit construction using established design rules which have been proven during previous development programs. In order to keep the electrical power consumption as low as possible and to reduce the number of high speed circuits, the demultiplexer design incorporated a high speed front end followed by lower speed stages. The outputs of the demultiplexer chip were designed to drive a TTL load and therefore are the major power consumers in the OEIC.

Optical input to the circuit is achieved through the use of a pigtailed optical multimode fiber with a 50 μm core. The fiber is mounted flush on top of the optical receiver wafer. By polishing the end of the fiber at a 58 degree angle, total internal reflection occurs and the light is forced to exit through the side of the fiber. This scheme allows the use of a planar photodiode without the need to bring the fiber in perpendicular to the device. In addition, some focusing of the light is provided by the fiber's curved surface.

All of the circuits were designed using Honeywell GaAs E/D MESFET design and layout rules, and the entire OEIC is amenable to monolithic integration on a single chip. The design was implemented using Honeywell's GaAs Self-Aligned Gate MESFET

process, which is based on selective ion implantation into 3-inch GaAs substrates. Efforts were made initially to fabricate the integrated optical detectors using the standard E/D MESFET implants. In the final fabrication, however, the process was modified to add deep n+ and p+ implants for the PIN detector to permit more efficient collection of carriers that are photogenerated below the wafer surface. The basic process uses 1 μm gate length FET's with V_T's of -0.6 V for Dmode and +0.3 V for Emode devices. Photolithography is accomplished using a projection aligner with die-by-die alignment. (A cross-sectional view of a wafer at various points in the fabrication process is shown in Fig. 2) In this process, Be and Si are implanted through a thin Si_3N_4 implant cap to form the p-buried layer as well as the enhancement and depletion channels, as shown in Fig. 2a. After channel activation the anneal cap is stripped and the refractory metal gate is sputter-deposited and patterned using reactive ion etching. This gate metal then serves as the self-aligned implant mask for the n+ source and drain implants of the FET's, with photoresist masking outside the device areas. (Fig. 2b) Finally, the PIN detector is photolithographically defined and the deep n+ and p+ implants are made, then annealed with a Si_3N_4 cap, using a rapid optical annealer. Ohmic contacts are formed by evaporation using a AuGe-based metal and then lifted off and sintered (Fig. 2c), and interconnect metallization consists of two-level metals defined by a dielectric-assisted liftoff (DAL) technique. This DAL process, together with filled VIA's for interlevel interconnects, permits a complete planarity of the chip topology, which is important in obtaining a high yield for LSI/VLSI fabrication. Both interconnect levels have sheet resistances less than 0.07 ohms per square, which provides for low IR drops and small RC time constants in complex high-speed circuits.

OPERATION

For testing and characterization the completed circuits were packaged in a 34 lead flatpack with a fiber pigtail. These flatpacks were then mounted in a test fixture for an initial performance test. The test fixture is a circuit board with a card edge connecter for the power supply inputs, and coaxial connections for the RF inputs and demultiplexer outputs. A compression clamp connects the flatpack leads to the circuit board tracings. An HP 8080 serial word generator was used to directly modulate an Ortel laser through an HP bias tee, which in turn fed into the optical controller. The word generator was programmed to cycle a 64 bit word output in an NRZ format, and by viewing the demultiplexer outputs on an HP sampling oscilloscope the operation of the device was confirmed. Because of the 1:16 demultiplexer, each output of the controller cycled a 4 bit word. The maximum clock frequency of the controller, limited by the demultiplexer, was found to be 305 MHz. Due to the oscilloscope's 50 Ω inputs, the waveforms were limited to an amplitude of less than 800 mV. Fig. 3 shows three of the 16 output channels along with the data valid line as viewed with a sampling oscilloscope. In this plot the clock frequency was 240 MHz, and the input data was a repeated 64 bit word.

The controller requires less than 200 μW of optical input power. Although tests at Honeywell have demonstrated that powers as low as 1 μW are sufficient, equipment limitations precluded operation of the device at such low optical powers. The electrical power consumption of the controller was found to be always less than 370 mW, and was measured to be as low as 120 mW in some cases. Because most of the power is consumed by the TTL drivers, the terminations of the output leads affected the power consumption greatly.

Initial tests of the device showed that the outputs had uncertainties. A clean output with a definite bit pattern could only be obtained by adjusting the clock frequency to certain values. In addition, the bit pattern sent to a specific output did not necessarily appear on that output. The latter problem was immediately identified as a timing problem in the synchronization (FWBO) signal; the FWBO pulses were not arriving at the proper moment so that the demultiplexer would know which bit was the first. Because the data was input through the laser, fiber and detector/amplifier while the FWBO was input directly into the demultiplexer, the FWBO arrived before the corresponding data. Likewise, the output uncertainty problem was found to be caused largely by the timing of the high speed clock input, which was out of phase with the optically input data because of propagation path length differences. These problems were overcome by using a pulse generator with a variable delay control to regenerate both the clock and FWBO signals shifted in time.

APPLICATIONS

The optical controller described in this paper was developed primarily for use as a phased array antenna controller. As such, the use of the device has been demonstrated in the control of monolithic Ka-Band phase shifter,[14] and in the control of a 30 GHz 8-element phased array antenna.[15] However, many other applications are conceivable as shown in Fig. 4. The built in demultiplexer makes this OEIC suitable for many high data rate transfer applications including neural networks, signal processing interconnections, and integrated modulator/detector arrays.

CONCLUSION

We have described a hybrid MESFET optical controller capable of data rates as high as 300 Mbps. The device uses less than 370 mW of electrical power and requires less than 200 μW of optical power. Because of the on-board demultiplexer, the OEIC has many potential applications beyond its intended phased array antenna application. A fully monolithic version of this device has been fabricated and will be tested in the near future. This device shows that optical and digital technologies are monolithically integratable, and any additional circuitry such as coding or clock recovery that can be fabricated using E/D MESFET design can easily be added to address a specific application.

REFERENCES

1. K.B. Bhasin and D.J. Connolly, "Advances in Monolithic Microwave Integrated Circuit Technology for Space Communications Systems," IEEE Trans. Microwave Theory Tech., vol. MTT-34, pp. 994-1001, 1986.

2. A.M. Levine, "Fiber Optics for Radar and Data Systems," SPIE Proceedings, vol. 150, pp. 992-998, 1978.

3. J. Austin and J.R. Forrest, "Design Concepts for Active Phased-Array Modules," IEE Proceedings F, vol. 127, pp. 290-300, 1980.

4. K.B. Bhasin, G. Anzic, R.R. Kunath, and D.J. Connolly, "Optical Techniques to Feed and Control GaAs MMIC Modules for Phased Array Antenna Applications," 11th Annual AIAA Communications Satellite Systems Conference, AIAA, New York, pp. 506-514, 1986.

5. R.R. Kunath and K.B. Bhasin, "Optically Controlled Phased Array Antenna Concepts Using Monolithic Microwave Integrated Circuits," 1986 International IEEE AP-S Symposium Digest vol. 1, pp. 353-355.

6. G.A. Koepf, "Optical Processor for Phased-Array Antenna Beam Formation," Proc. SPIE, vol. 477, pp. 75-81, 1984.

7. P.G. Sheehan and J.R. Forrest, "The Use of Optical Techniques for Beamforming in Phased Arrays," Proc. SPIE, vol. 477, p. 82-89, 1984.

8. R.A. Soref, "Voltage-Controlled Optical/RF Phase Shifter," J. Lightwave Tech., vol. LT-3, pp. 992-998, 1985.

9. L.P. Anderson, F. Boldissar, and D.C.D. Chang, "Antenna Beamforming using Optical Processing," Proc. SPIE, vol. 886, pp. 228-232, 1988.

10. P.R. Herczfeld, A.S. Daryoush, A. Rosen, A.K. Sharma, and V.M. Contarino, "Indirect Subharmonic Optical Injection Locking of a Millimeter-Wave IMPATT Oscillator," IEEE Trans. Microwave Theory Tech., vol. MTT-34, pp. 1371-1376, 1986.

11. I.D. Blanchflower and A.J. Seeds, "Optical Control of Frequency and Phase of GaAs MESFET Oscillator," Electron. Lett., vol. 25, pp. 359-360, 1989.

12. A. Paolella and P.R. Herczfeld, "Optical Gain Control of a GaAs MMIC Distributed Amplifier," Microwave Optical Tech. Lett., vol. 1, pp. 13-16, 1988.

13. J.D. Crow, C.J. Anderson, S. Bermon, A. Callegari, J.F. Ewen, J.D. Feder, J.H. Greiner, E.P. Harris, P.D. Hoh, H.J.Hovel, J.H. Magerlein, T.E. Mckoy, A.T.S. Pomerene, D.L. Rogers, G.J. Scott, M. Thomas, G.W. Mulvey, B.K. Ko, T. Ohashi, M. Scontras, and D. Widiger, "A GaAs MESFET IC for optical multiprocessor networks," IEEE Trans. Electron Devices, vol. 36, pp. 263-268, 1989.

14. K.B. Bhasin, P.C. Claspy, M.A. Richard, R.R. Romanofsky, M. Bendett, G.Gustafson, W. Walters, "Control of a GaAs Monolithic Ka-Band Phase Shifter Using a High-Speed Optical Interconnect," To be published in IEEE Trans. Microwave Theory Tech., May, 1990.

15. M.A. Richard, P.C. Claspy, K.B. Bhasin, and M. Bendett, "Optical Control of an 8-Element Ka-Band Phased Array Antenna Using a High-Speed Optoelectronic Interconnect," To be published in IEEE AP-S Proceedings, 1990.

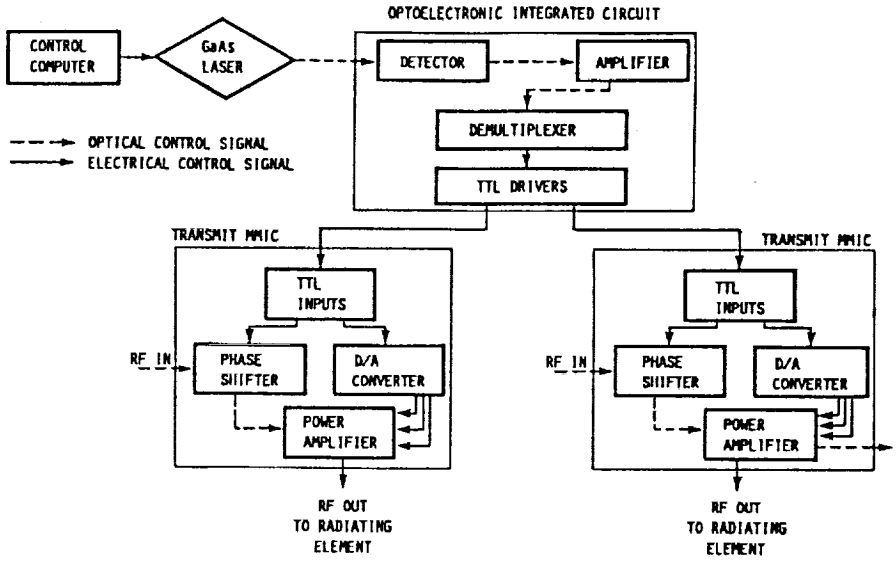

Fig. 1. A possible signal multiplexing scheme.

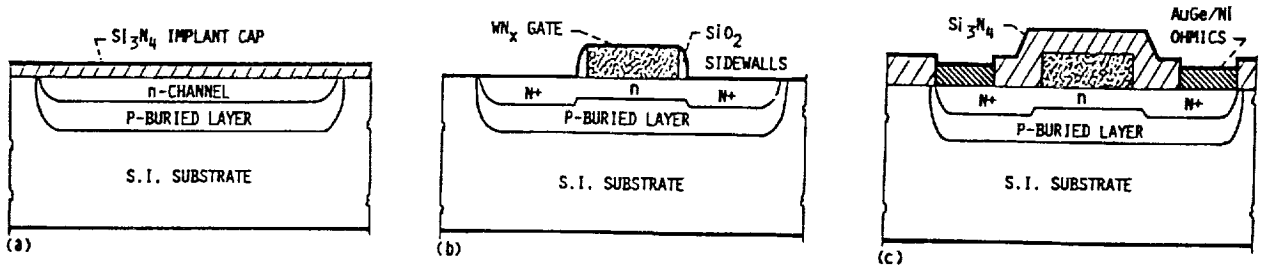

Fig. 2. Fabrication steps: (a) n, n^-, p implantation through Si_3N_4 cap, (b) WN metallization, N^+ implant self-aligned using SiO_2 side-wall spacers, (c) ohmic contact metallization.

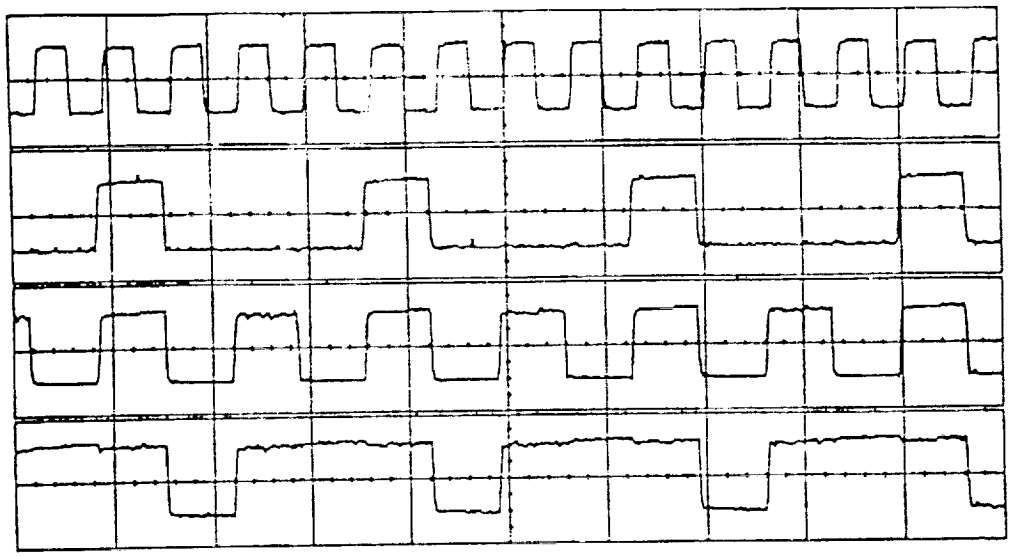

Fig. 3. Outputs of the OEIC. The top trace is the output clock divided by 16 while the lower three traces are data outputs. The input data is a 64 bit repeating word at a clock rate of 240 MHz. The ordinate for each trace is 200 mv/div. while the timebase is 100 ns/div.

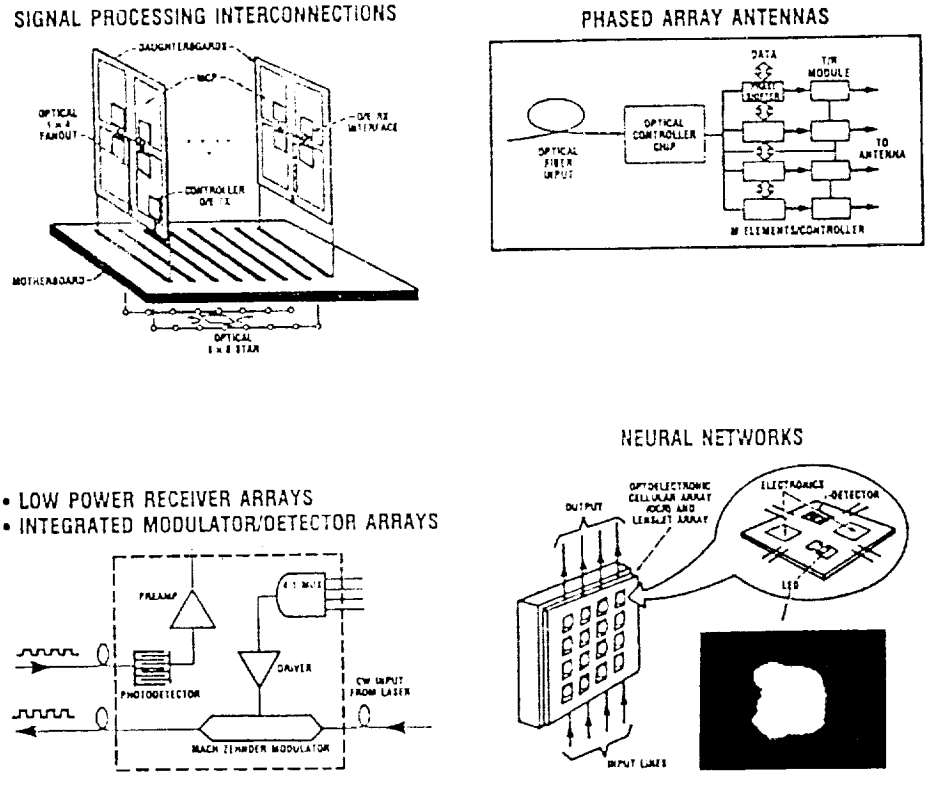

Fig. 4. Potential applications of OEIC include signal processing interconnections, phased array antennas, detector arrays, and neural networks.

NASA Technical Memorandum 101485

Microwave Characteristics of GaAs MMIC Integratable Optical Detectors

Paul C. Claspy
Lewis Research Center
Cleveland, Ohio

Scott M. Hill
Case Western Reserve University
Cleveland, Ohio

and

Kul B. Bhasin
Lewis Research Center
Cleveland, Ohio

Prepared for the
1989 IEEE MTT-S International Microwave Symposium
Long Beach, California, June 13–15, 1989

NASA

MICROWAVE CHARACTERISTICS OF GaAs MMIC INTEGRATABLE OPTICAL DETECTORS

Paul C. Claspy*
NASA Lewis Research Center
Cleveland, Ohio 44135

Scott M. Hill
Case Western Reserve University
Cleveland, Ohio 44106

and

Kul B. Bhasin
NASA Lewis Research Center
Cleveland, Ohio 44135

Summary

Interdigitated photoconductive detectors have been fabricated on microwave device structures, making them easily integratable with MMIC's. Detector responsivity as high as 2.5 A/W and an external quantum efficiency of 3.81 were measured. Response speed was nearly independent of electrode geometry, and all detectors had usable response at frequencies to 6 GHz. A small signal model of the detector, based on microwave measurements is also developed.

Introduction

Over the past few years technology advances have occurred which have increased the possibility that in the near future phased array antennas composed of monolithic microwave integrated circuits (MMIC's) will become a practical reality.[1] To take maximum advantage of the potential size reduction that this advance represents it will be essential to effect a similar size reduction in the chip-to-chip high frequency interconnects that the system will require. Various authors have suggested that fiber optic links, which are small and lightweight, may be a viable alternative to coaxial cables and waveguides for this application.[2] If these links are to be practical, however, high frequency optical transmitters and receivers must be available, and it would be particularly desirable that optical components be process- and material-compatible with GaAs heterostructure MMIC's so that they can be integrated onto the same chip.

In this paper we report the results of a study of the optical and electrical characteristics of interdigitated photoconductive detectors of various geometries that were fabricated on a HEMT-type heterostructure material. The operating wavelength was chosen to be 820 nm.

*P.C. Claspy is a National Research Council - NASA Senior Research Associate. Permanent address: Department of Electrical Engineering and Applied Physics, Case Western Reserve University, Cleveland, Ohio 44106.

Detector Fabrication

The detectors were fabricated on the MBE-grown GaAlAs/GaAs heterostructure material shown schematically in Fig. 1. A typical detector is shown in Fig. 2. Interdigitated electrode geometries, with finger spacings ranging from 1 to 4 μm, were used because they increase the effective active area of the detector while keeping the transit distance small. Since the GaAlAs window that remains after fabrication is essentially transparent to the incident 820 nm radiation, almost all of the photon absorption, and therefore the electron-hole pair generation, occurs within the undoped GaAs layer. For testing, the detectors were mounted directly on the Teflon insulation of a specially prepared length of semi-rigid coaxial cable, with short wire-bonded leads to the center conductor and the shield.

Optical Response Measurements

Frequency domain response measurements were made over the range 0.01 to 10 GHz using the system shown schematically in Fig. 3, and normalized responses of detectors of three different geometries are shown in Fig. 4. The detectors exhibit nearly identical response dispersion, with a 3 dB cutoff frequency at approximately 185 MHz. The gain decays at about 12 dB/decade in the decade between 100 MHz and 1 GHz, with a small plateau at 510 MHz, then falls off at 20 dB/decade after a larger plateau at 1 GHz. The shape of the response suggests that device characteristics are limited by trapping effects.[3]

Detector responsivities at 500 MHz, R(500 MHz), were measured using an Ortel SL620 diode laser, and lie in the range 0.13 to 0.31 A/W. On the basis of measurements at 500 MHz, the low frequency responsivity of the 1 by 1 μm detector was calculated to be 2.5 A/W. The (internal) quantum efficiency of this detector is 5.44, and the external quantum efficiency is 3.81, all of which are comparable to results reported for GaAs detectors.

Microwave Impedance Measurements and Model

DC and AC impedance characteristics of the detectors were studied under various levels of illumination. DC I-V curves for our detectors were taken using white light illumination, and a typical result is given in Fig. 5. The DC resistance of the detectors is low and constant for small bias, smoothly increases as the bias is increased, becoming very large at high bias as a result of carrier velocity saturation. The decrease of resistance with increasing optical power is also shown in Fig. 5.

The reflection coefficient, S_{11}, was measured over the frequency range 0.5 to 5.5 GHz at various bias levels and incident white light intensities using an HP-4910 Network Analyzer. Some results of these measurements are shown in Figs. 6 to 8. Figure 6 shows that S_{11} decreases with detector feature size, Fig. 7 shows that it increases with bias voltage, at moderate illumination, and Fig. 8 shows that it decreases with increasing illumination, at moderate bias.

A small-signal, high frequency model, consisting of a parallel RC combination with an inductance in series with each node of the RC network, as shown in Fig. 9(a), was developed from the measured S_{11} results. The model, which is similar to that developed by Wojtczuk and Ballantyne[4] leads to a complex impedance given by

$$Z = \frac{R(V,\Phi) + j\omega\{(L_1 + L_2) - CR^2(\omega,\Phi)\}}{1 + \omega CR^2(V,\Phi)} \qquad (1)$$

where the resistance, $R(V,\Phi)$, is a function of both the DC bias and the illumination.

The light intensity primarily affects R, which at low bias drops from well over 100 Ω at ambient to only a few tens of ohms at high intensity. Therefore, at low bias and high light level the low resistance effectively short-circuits the device capacitance, reducing the impedance to

$$Z = R + j\omega(L_1 + L_2), \qquad (2)$$

as shown in Fig. 9(b). The AC resistance was observed to increase significantly with bias, so that at high bias the complex impedance eventually simplifies to

$$Z = \frac{R}{\omega CR^2} - \frac{j}{\omega C}, \qquad (3)$$

as shown in Fig. 9(c). This change from inductive to capacitive behavior suggests the possibility of a zero reactance operating point by the elimination of any RC or R/L time constants if the detector is time constant limited. The impedance of the zero reactance point is determined by setting the imaginary part of Eq. (1) equal to zero. Then, if $(\omega CR^2) << 1$, the impedance reduces to

$$Z = \sqrt{(L_1 + L_2)/C}, \qquad (4)$$

which for our devices is about 250 Ω at somewhat less than 3 V bias.

Summary and Conclusion

The high frequency characteristics of interdigitated photoconductive detectors fabricated on a HEMT structure have been presented. The fabrication process was completely compatible with that used to fabricate MODFET's making these detectors easily integrable for MMIC usage. It should be noted that while the detectors did not exhibit an extremely high bandwidth, they did possess usable response well into the GHz range, and the change from inductive to capacitive reactance with bias suggests the possibility of a zero reactance operating point. In conclusion, then, the combination of fabrication compatibility and performance characteristics makes these devices interesting for interconnection applications.

References

1. J. Frey, and K.B. Bhasin, eds., Microwave Integrated Circuits, 2nd Ed. Dedham, MA: Artech House, 1985.

2. K.B. Bhasin, G. Anzic, R.R. Kunath, and D.J. Connolly, "Optical Techniques to Feed and Control GaAs MMIC Modules for Phased Array Antenna Applications," in AIAA 11th Annual Communications Satellite Systems Conference, New York: AIAA, pp. 506-514, 1986 (NASA TM-87218).

3. G.J. Papaionannou, and J.R. Forrest, "On the Photoresponse of GaAs MESFET's: Backgating and Deep Traps Effect," IEEE Trans. Electron Devices, vol. ED-33, no. 3, pp. 373-378, Mar. 1986.

4. S.J. Wojtczuk, and J.M. Ballantyne, "Impedance Properties and Broad-Band Operation of GaAs Photoconductive Detectors," J. Lightwave Tech., vol. LT-5, no. 3, pp. 320-324, Mar. 1987.

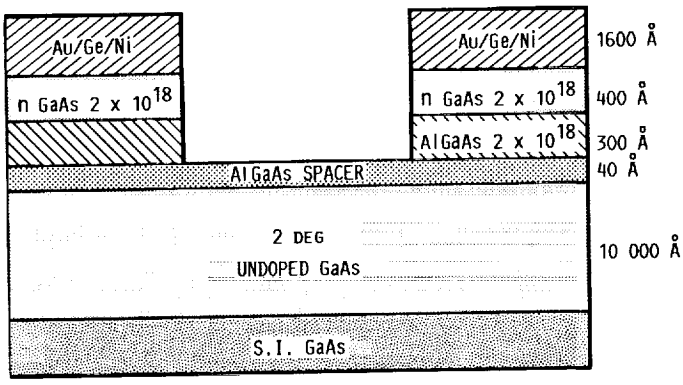

Fig. 1. Schematic cross section of photodetector material.

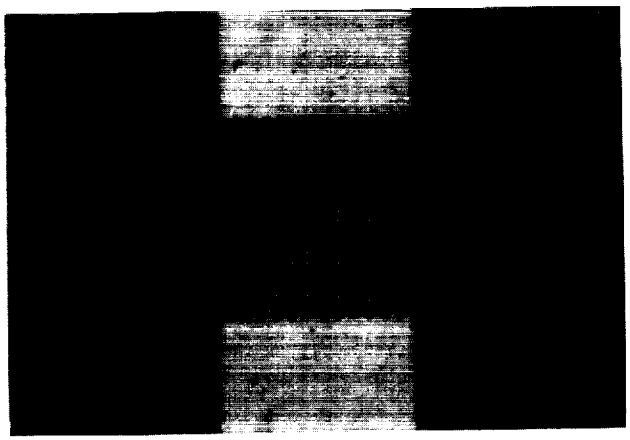

Fig. 2. 1 μm x 1 μm detector.

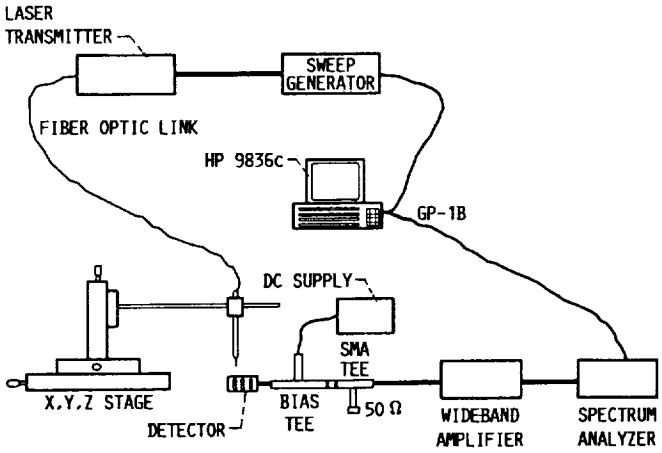

Fig. 3. Frequency domain measurement system.

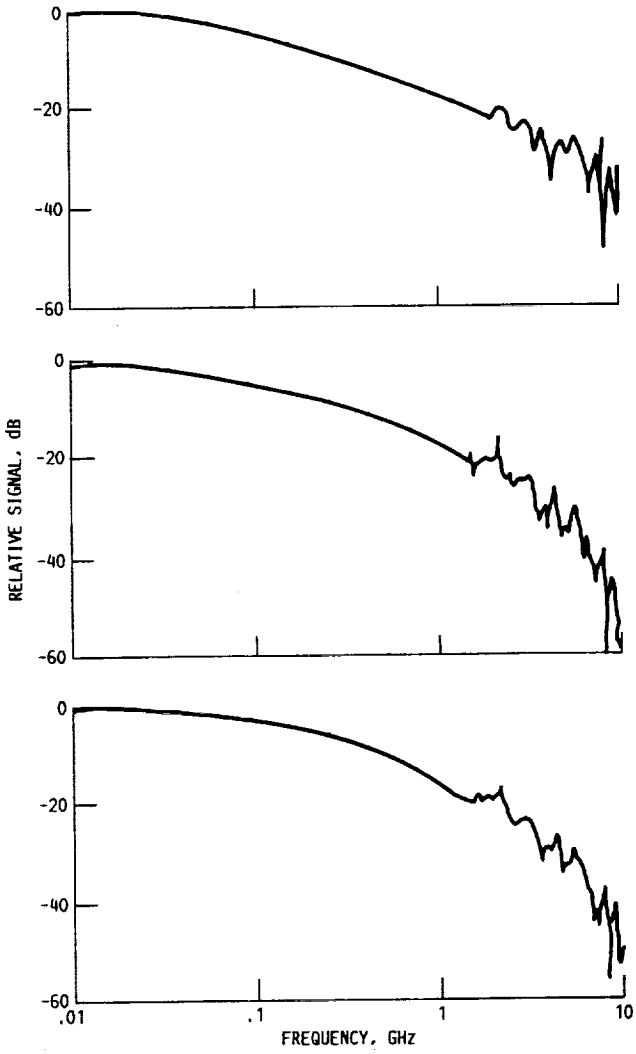

Fig. 4. Normalized frequency response of typical detectors.
(a) 1 μ x 1 μm; (b) 2 μm x 2 μm;
(c) 2 μm x 2 μm.

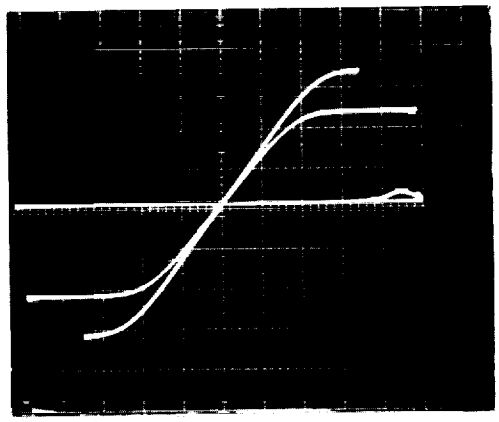

Fig. 5. I-V characteristic curve for 1 μm x 1 μm detector.

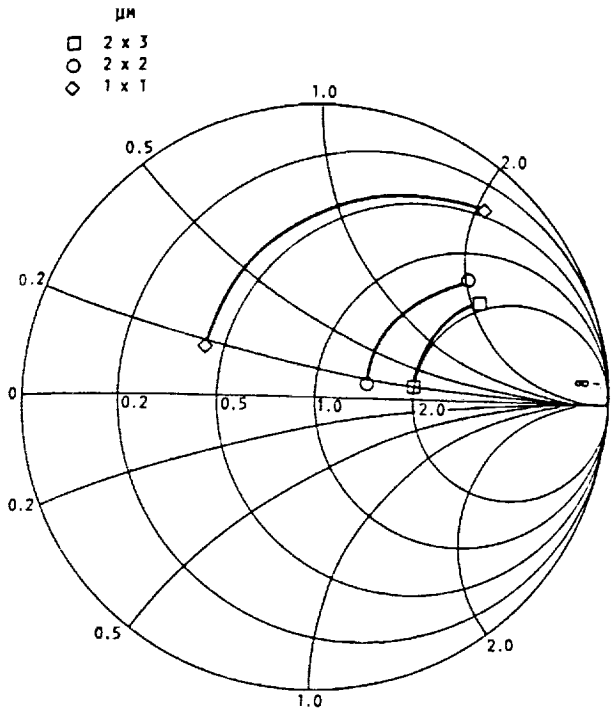

Fig. 6. Effect of electrode geometry on S_{11}.

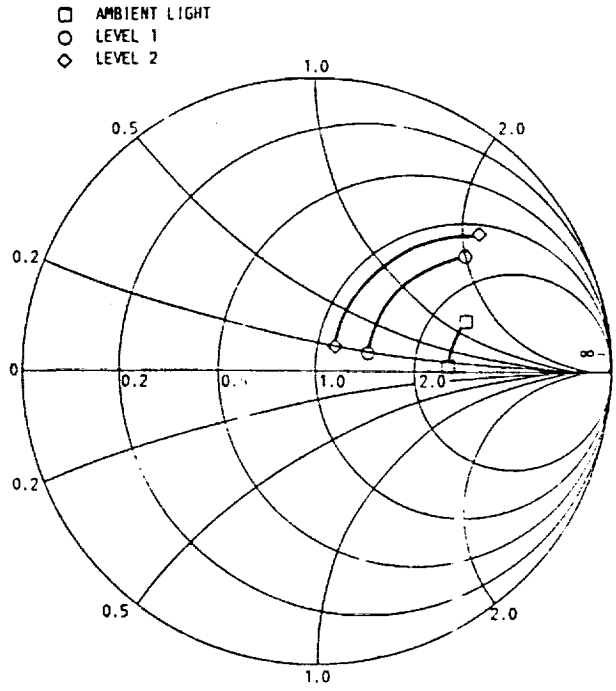

Fig. 8. Effect of illumination on S_{11} for 2 μm x 2 μm detector.

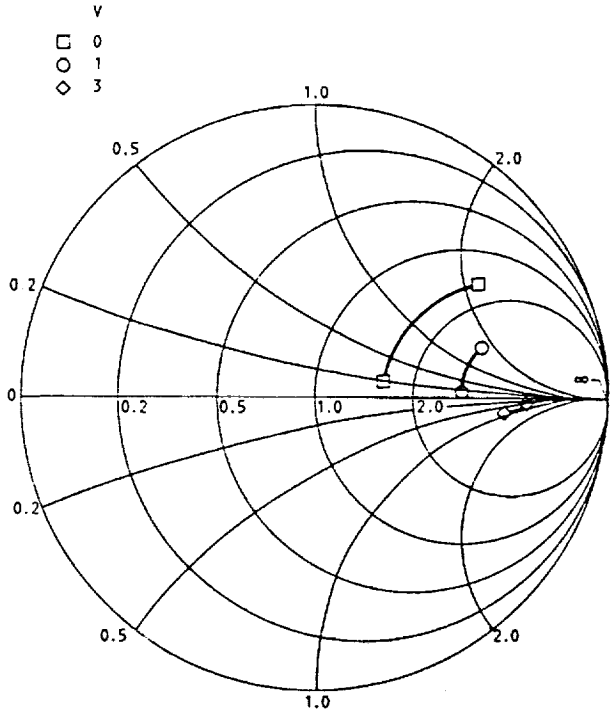

Fig. 7. Effect of bias voltage on S_{11} for 2 μm x 3 μm detector.

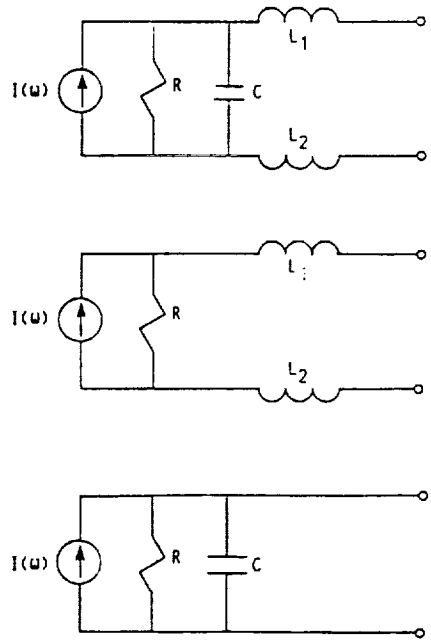

Fig. 9 Detector equivalent circuit models. (a) General equivalent circuit; (b) Low bias equivalent circuit; (c) High bias equivalent circuit.

A High-Speed GaAs MESFET Optical Controller

P. C. CLASPY, SENIOR MEMBER, IEEE, M. RICHARD, K. B. BHASIN, SENIOR MEMBER, IEEE, M. BENDETT, MEMBER, IEEE, G. GUSTAFSON, AND W. WALTERS

Abstract— **Optical interconnects are being considered for control signal distribution in phased array antennas. This paper describes a packaged hybrid GaAs optical controller with a 1:16 demultiplexed output that is suitable for this application. The controller, which was fabricated using enhancement/depletion mode MESFET technology, operates at demultiplexer-limited input data rates up to 305 Mbits/s and requires less than 200 μW optical input power.**

INTRODUCTION

PHASED array antennas are being considered for microwave and millimeter wave communication systems that will be used on future satellites and space vehicles [1]. The requirement for control of the phase and amplitude of signals at each of the several hundred monolithic microwave integrated circuits (MMIC's) that would constitute such an array necessitates the transfer of a large amount of control data to phase shifters and amplifiers in a short period of time when the beam direction is to be changed. One possible method of transmitting these data, with a concurrent reduction in weight and power consumption over more conventional methods, is to multiplex the control signals onto optical carriers, transmit the resulting signals to optical receiver-demultiplexers on the antenna, and distribute the demultiplexed control signals locally [2]. The requirements imposed upon optical links for this application are different from those imposed by telecommunications applications because of the short distances involved and the burst nature of the data. Furthermore, this type of link places an emphasis on reducing power, weight, and size over considerations such as dispersion and attenuation. Therefore, integration of the complete receiver/demultiplexer can provide a significant enhancement of the system.

Over the past several years, various authors have reported optoelectronic integrated circuits ranging from a diode-preamplifier combination [3] to detector-amplifier circuits [4] to an optical receiver with clock recovery [5]. In this letter, we report on the design, fabrication, and characteristics of a packaged hybrid integrated circuit optical controller consisting of two integrated submodules. As shown schematically in Fig. 1, the integrated submodules of our controller

Manuscript received July 11, 1989; revised August 30, 1989.

P. C. Claspy is a National Research Council Senior Research Associate at the National Aeronautics and Space Administration, Lewis Research Center, Cleveland, OH, on leave from Case Western Reserve University, Cleveland, OH.

M. Richard is with Case Western Reserve University, Cleveland, OH.

K. B. Bhasin is with the National Aeronautics and Space Administration, Lewis Research Center, Cleveland, OH.

M. Bendett, G. Gustafson, and W. Walters are with Sensors and Signal Processing Laboratory, Honeywell, Inc., Bloomington, MN.

IEEE Log Number .

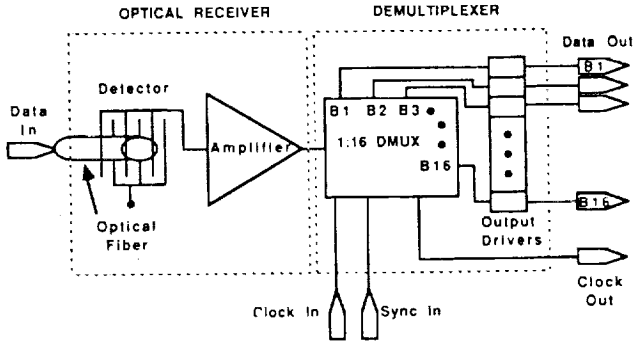

Fig. 1. Block diagram of the controller.

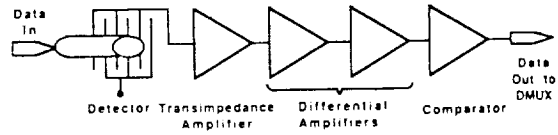

Fig. 2. Block diagram of the optical receiver section of the controller.

are an optical receiver, consisting of a photodetector and a three-stage amplifier with a comparator-based output, and a demultiplexer with output line drivers. The required input signals to the controller are an 830 nm optical serial data stream to the detector and electrical clock and synchronization signals to the demultiplexer. The output is 16 parallel TTL-compatible data streams and a clock at 1/16 of the input clock rate.

FABRICATION

Since the intended application of the controller is in satellite-based systems, low power consumption was a primary design criterion. To ensure this low power consumption as well as for process simplicity and reproducibility we chose to employ enhancement/depletion mode (E/D-mode) GaAs MESFET technology for both the receiver and the demultiplexer. This common technology will also permit future monolithic integration of the controller. The fabrication was based upon a refractory metal self-aligned gate process which is similar to a submicron process that was previously reported [6]. The only modifications to that process were that a 1 μm gate length was used here and that deep n+ and p+ implant steps were added so that the p-i-n photodiodes could be fabricated.

CIRCUIT DESIGN

The receiver section, shown schematically in Fig. 2, consists of an interdigitated p-i-n photodiode, a three-stage amplifier, and an output comparator. The optical input is laterally coupled through the cladding of a multimode fiber (50 μm

1041-1135/89/1100-0389$01.00

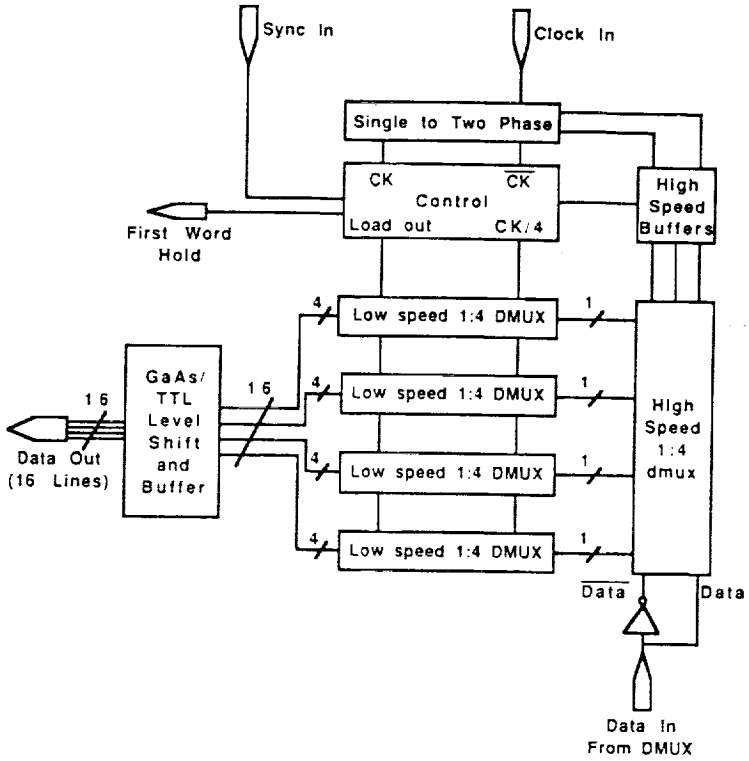

Fig. 3. Block diagram of the demultiplexer-output driver section of the controller

core) to the photodiode. The fiber is mounted with its axis parallel to the wafer surface and the fiber end is polished at a 58° angle to ensure total internal reflection. The light exits through the curved side of the fiber, which provides some focusing onto the detector [7]. The three-stage amplifier consists of a transimpedance input amplifier followed by a two-stage high-gain differential amplifier to increase sensitivity while allowing high speed. Capacitive coupling is used between amplifier stages to reduce sensitivity to dc offsets resulting from mismatch between the complementary amplifier stages. Each stage of the amplifier produces a gain of 8–11 dB, and the power consumption of the amplifier is less than 100 mW.

The demultiplexer was designed using direct-coupled FET logic (DCFL) in a multistage circuit which operates at input data rates greater than 200 Mbits/s. Fig. 3 is a block diagram of the circuit, which has a high-speed front end followed by lower speed stages. This design reduces power consumption and limits the number of circuits that must be tightly coupled to the high-speed clock. It was used largely because it is based upon existing circuitry, although it does not necessarily provide optimum power and speed characteristics. The output drivers were designed for TTL levels and as a result they are the most power-consuming portion of the chip. The power dissipation in this stage is dependent upon the output logic states and upon the specific voltage level required of the TTL load driver.

Operation

The packaged controllers were tested in a fixture that permits separate observation of any of the 16 data output channels. To characterize the controller, the data output (NRZ format) from a word generator was used to directly modulate the output of a laser diode, which in turn provided data input to the receiver section. Concurrently, the clock and first word bit zero (FWB0) from the word generator were input as electrical signals directly to the demultiplexer section of the controller, as shown schematically in Fig. 1.

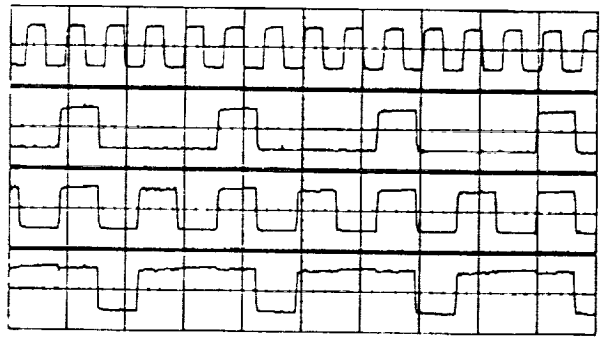

Fig. 4. Example of controller outputs. Top trace is the output clock and the remaining traces are three output data channels. The input data was a 64 bit word stream at a clock rate of 240 MHz. The ordinate for each trace is 200 mV/div and the abscissa is 100 ns/div.

The demultiplexed outputs of the controller were observed with a sampling oscilloscope, and an example of three of these, along with the output clock, is shown in Fig. 4. In this example, the input clock was 240 MHz and the input data was a repeated 64 bit word. By adjusting the dc operating point of the laser and the level of the ac drive power to it, the minimum average optical power required by the controller

was found to be less than 200 μW. The maximum clock rate of the tested controller, which is limited by the demultiplexer, was measured to be 305 MHz.

Conclusion

In this paper, we have described the design and operating characteristics of a packaged hybrid low-power GaAs MESFET demultiplexing optical controller that is suitable for use in controlling a phased array antenna. The two submodules of the controller were fabricated using identical technologies, making monolithic integration possible. The controller operates at input clock speeds greater than 300 MHz, and it requires less than 200 μW of optical power as the input signal and less than 370 mW of electrical power.

References

[1] K. B. Bhasin and D. J. Connolly, "Advances in monolithic microwave integrated circuit technology for space communications systems," *IEEE Trans. Microwave Theory Tech.*, vol. MTT-34, pp. 994-1001, 1986.

[2] K. B. Bhasin, G. Anzic, R. R. Kunath, and D. J. Connolly, "Optical techniques to feed and control GaAs MMIC modules for phased array antenna applications," in *Proc. 11th Annu. AIAA Commun. Satellite Syst. Conf.*, AIAA, New York, 1986, pp. 506-514.

[3] R. M. Kolbas, J. Abrokwah, J. K. Carney, D. H. Bradshaw, B. R. Elmer, and J. R. Biard, "Planar monolithic integration of a photodiode and a GaAs preamplifier," *Appl. Phys. Lett.*, vol. 43, pp. 821-823, 1983.

[4] M. Ito, T. Kumai, H. Hamaguchi, M. Makiuchi, K. Nakai, O. Wada, and T. Sakurai, "High-speed monolithically integrated GaAs photoreceiver using a metal-semiconductor-metal photodiode," *Appl. Phys. Lett.*, vol. 47, pp. 1129-1131, 1985.

[5] J. D. Crow, C. J. Anderson, S. Bermon, A. Callegari, J. F. Ewen, J. D. Feder, J. H. Greiner, E. P. Harris, P. D. Hoh, H. J. Hovel, J. H. Magerlein, T. E. Mckoy, A. T. S. Pomerene, D. L. Rogers, G. J. Scott, M. Thomas, G. W. Mulvey, B. K. Ko, T. Ohashi, M. Scontras, and D. Widiger, "A GaAs MESFET IC for optical multiprocessor networks," *IEEE Trans. Electron Devices*, vol. 36, pp. 263-268, 1989.

[6] K. L. Tan, H. K. Chung, G. L. Grung, and S. M. Shin, "A submicron self-aligned gate GaAs MESFET technology for low power subnanosecond static RAM fabrication," in *Tech. Dig., 1987 GaAs IC Symp.*, IEEE, 1987, pp. 121-124.

[7] P. R. Haugen, S. Rychnovsky, A. Husain, and L. D. Hutcheson, "Optical interconnects for high speed computing," *Opt. Eng.*, vol. 25, pp. 1076-1085, 1986.

Control of a GaAs Monolithic *Ka*-Band Phase Shifter Using a High-Speed Optical Interconnect

K. B. BHASIN, SENIOR MEMBER, IEEE, P. C. CLASPY, SENIOR MEMBER, IEEE, M. A. RICHARD, R. R. ROMANOFSKY, MEMBER, IEEE, M. BENDETT, MEMBER, IEEE, G. GUSTAFSON, AND W. WALTERS

Abstract—The use of a high-speed optical interconnect in the control of a *Ka*-band GaAs monolithic phase shifter is described. A 16 b serial control signal was used to modulate the output of a laser transmitter, and the transmitted optical signal was detected and demultiplexed into 16 parallel electrical outputs using a high-speed hybrid GaAs optoelectronic integrated circuit (OEIC). Four of the parallel output lines were interfaced to the 4 b phase shifter, and high-speed, optically controlled switching of the phase shifter was observed at clock frequencies to 30 MHz using an interferometric technique.

I. Introduction

GaAs monolithic microwave integrated circuits (MMIC's), which could be used as array output modules, represent a major step toward improved, lightweight directly radiating phased array antennas for space communications applications [1]. The interconnection of these MMIC modules into a beam forming network (BFN), however, still represents a rather formidable topological problem that requires innovative solutions. In an effort to overcome these problems a variety of optics-based BFN's have been proposed [2]–[4].

The GaAs MMIC's in a phased array antenna are relatively complex. They include a variable phase shifter and a variable power amplifier which permit the creation of the aperture phase and amplitude distribution that is appropriate to the desired radiated beam configuration. Some proposed architectures also include a local oscillator and a mixer at each antenna element [5], [6]. In fiber-optic-interconnected systems, optical fibers would be used to carry the control signals to the variable phase shifters and amplifiers as well as the signal to be transmitted and the local oscillator phase locking signal. Our research is addressed toward the meeting of needs for distribution of digital control signals within a phased array antenna. Because of the inherent wide bandwidth and low loss of optical fibers, all control signals for the variable phase shifter and amplifier on a MMIC module, or for several modules, could be multiplexed onto one optical channel, as shown schematically in Fig. 1, if appropriate optical receiver/demultiplexers were available. Even though the required data input rate to an individual phase shifter or amplifier control line may be modest, the overall multiplexed data rate from the controller will be high, and a wide bandwidth channel will be required. Some proof-of-concept demonstrations of the use of optical interconnects in the context of a phased array, using discrete components, have been reported [7]. In this paper we present the results of the application of a high-speed GaAs MESFET integrated circuit optical receiver/demultiplexer to the optics-based control of a monolithic *Ka*-band phase shifter.

II. The Optoelectronic Integrated Circuit

The optoelectronic integrated circuit (OEIC) that was used in the control of a MMIC phase shifter has been described in a previous publication [8]. It consists of two integrated submodules that were packaged together in a 34 lead flat pack, with a fiber pigtail for optical input, as shown in Fig. 2. The input chip is the receiver section, consisting of an interdigitated p-i-n photodetector and a three-stage amplifier, and the output chip includes a demultiplexer and output drivers [14]. The inputs to the OEIC are a 16 b serial optical data stream and an electrical bit clock and synchronization signal. The outputs are 16 parallel TTL level data streams and the input clock divided by 16. As reported in our previous paper, the demultiplexer-limited maximum clock frequency of the controller is 305 MHz. The minimum frequency is determined by the capacitive coupling between the amplifier stages, so the minimum data rate is dependent upon the pattern of the data being sent.

III. Optical Control of a *Ka*-Band Phase Shifter

To demonstrate the potential use of the OEIC in a phased array context, the demultiplexed outputs of the optical controller

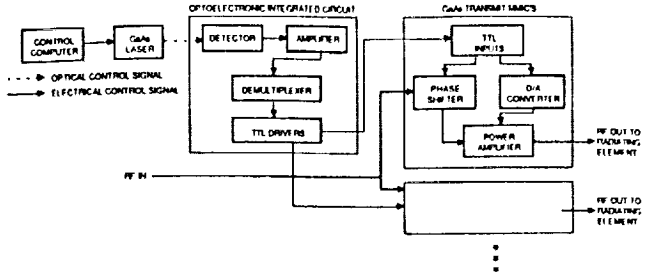

Fig. 1. Schematic diagram of an optically interconnected phased array.

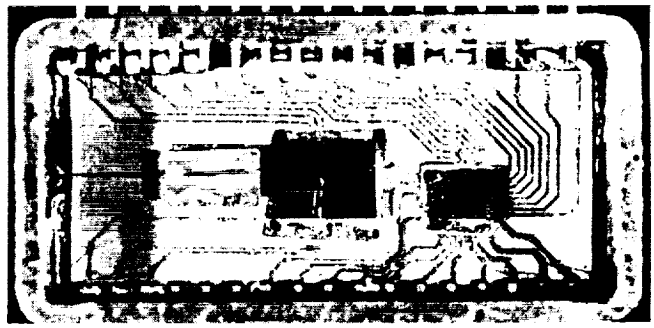

Fig. 2. The packaged optoelectronic integrated circuit.

Manuscript received October 26, 1989; revised November 23, 1989.

K. B. Bhasin and R. R. Romanofsky are with the Lewis Research Center, National Aeronautics and Space Administration, Cleveland, OH 44135.

P. C. Claspy and M. A. Richard are with the Department of Electrical Engineering, Case Western Reserve University, Cleveland, OH 44106.

M. Bendett, G. Gustafson, and W. Walters are with the Sensors and Signal Processing Laboratory, Honeywell, Inc., Bloomington, MN 55420.

IEEE Log Number 9034519.

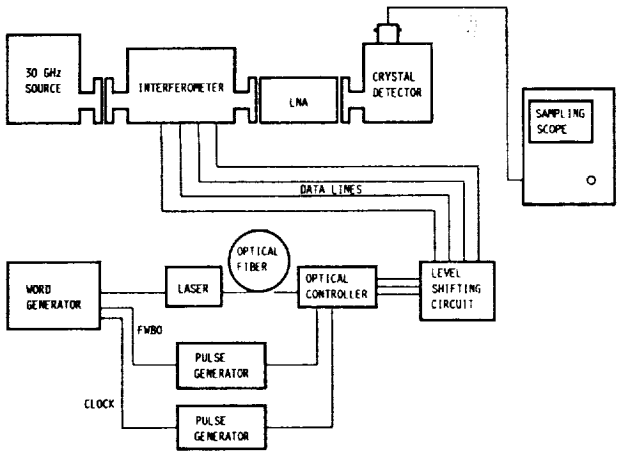

Fig. 3. Block diagram of the microwave interferometer.

were interfaced to the inputs of a 30 GHz 4 b monolithic phase shifter that was produced by Honeywell under a separate contract with NASA, and that has been described in previous publications [9]. The 4 b required by the phase shifter control three switched lines, each of which requires a bit and its complement, and one loaded line. Since the phase shifter and the optical controller were developed under separate programs and therefore were not designed with the interfacing of the two in mind, a voltage level shifting interface circuit was required. The interface circuit consisted of inverting gates to generate the complements and CMOS analog multiplexers to shift the optical controller's TTL outputs to the phase shifter's required 0 V and -6 V inputs, and was the speed-limiting element for this demonstration.

An interferometric technique was devised to allow real-time measurement of fast changes in the effect of the phase shifter on the phase of a *Ka*-band signal. As shown schematically in Fig. 3, the phase shifter was inserted in one leg of an interferometer. A 30 GHz microwave signal of -8 dBm was applied to the input of a 10 dB power splitter. The higher power output from the splitter was fed through the phase shifter input into the output port of a 3 dB power splitter that was used as a power combiner, while the lower power output was input directly into the second port of the power combiner. To compensate for the 9 dB insertion loss of the phase shifter, a 30 GHz low-noise amplifier [10] was connected to the output of the test setup. A crystal detector attached to the output of the combiner indicated the level of output power. To set the initial condition of the system, the propagation time through the phase shifting leg of the interferometer was adjusted, by changing the bit settings on the phase shifter, until the detector indicated maximum power output, corresponding to constructive interference between the two recombined signals. Beginning with this configuration, switching the 180° bit of the phase shifter caused the power output to fall to zero, indicating complete destructive interference, while switching the 45° and 90° bits caused intermediate levels of destructive interference.

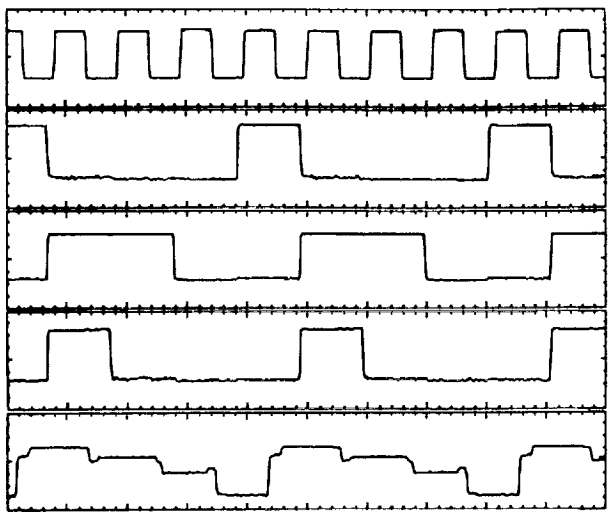

Fig. 4. Controller and interferometer outputs when three phase shifter bits are controlled at a high-speed clock frequency of 30 MHz. The top trace is the clock divided by 16, the center three traces are the OEIC output data, and the lower trace is the interferometer output. The ordinate scale is 200 mV/div for the top four traces and 1 mV/div for the lower trace. The abcissa scale for all traces is 500 ns/div.

Three demultiplexed outputs from the OEIC were used, along with their complements, to control the 180°, 90°, and 45° switched lines of the phase shifter. Since the data input to the controller are through the laser, fiber, and detector, while the clock and synch (FWB0) are input directly to the demultiplexer as electrical signals, problems with timing can cause uncertainties in the output waveforms. To eliminate this problem, a delayable triggered pulse generator was used to adjust the delay of the two electrical signals and synchronize them with the optical input. For this experiment the average input optical power was 250 μW and the high-speed (input) clock was kept at 30 MHz in order to stay within the limitations of the level-shifting circuitry. Different input data patterns were used to control each phase shifter input bit so that combinations of delay lines could be inserted into the path and their effects observed. An example of the success in combining the OEIC with the phase shifter to control the phase of a 30 GHz signal is given in Fig. 4, where one set of input data patterns, along with the resulting interferometer outputs and the output clock, is shown. It should be noted that there are constant delays between the clock and data and between the data and the interferometer response. The former are the result of different propagation times for data and clock in the OEIC, while the latter are the result of delays in the CMOS level-shifting circuit, as are the irregularities in the interferometer signal.

IV. Conclusions

In this paper we have described the first experiment in which a *Ka*-band monolithic phase shifter is controlled through a high-speed fiber-optic interconnect. The interface between the serially encoded optical control signal and the electrically controlled phase shifter uses a new optoelectronic integrated circuit that converts the serial optical input into 16 parallel optical outputs. Switching of the 4 b phase shifter at instrumentation-limited input clock frequencies to 130 MHz was observed in real time using a novel interferometric technique. The optical control of a phase shifter in this manner represents a significant step toward the development of an optically controlled phased array antenna.

REFERENCES

[1] K. B. Bhasin and D. J. Connolly, "Advances in monolithic microwave integrated circuit technology for space communications systems," *IEEE Trans. Microwave Theory Tech.*, vol. MTT-34, pp. 994–1001, 1986.

[2] A. M. Levine, "Fiber optics for radar and data systems," *SPIE Proc.*, vol. 150, pp. 992–998, 1978.

[3] J. Austin and J. R. Forrest, "Design concepts for active phased-array modules," *Proc. Inst. Elec. Eng.*, pt. F, vol. 127, pp. 290–300, 1980.

[4] K. B. Bhasin, G. Anzic, R. R. Kunath, and D. J. Connolly, "Optical techniques to feed and control GaAs MMIC modules for phased array antenna applications," in *Proc. 11th Ann. AIAA Commun. Satellite Syst. Conf.* (New York), 1986, pp. 506–514.

[5] P. R. Herczfeld, A. S. Daryoush, A. Rosen, A. K. Sharma, and V. M. Contarino, "Indirect subharmonic optical injection locking of a millimeter-wave IMPATT oscillator," *IEEE Trans. Microwave Theory Tech.*, vol. MTT-34, pp. 1371–1376, 1986.

[6] I. D. Blanchflower and A. J. Seeds, "Optical control of frequency and phase of GaAs MESFET oscillator," *Electron. Lett.*, vol. 25, pp. 359–360, 1989.

[7] A. Paolella and P. R. Herczfeld, "Optical gain control of a GaAs MMIC distributed amplifier," *Microwave Opt. Technol. Lett.*, vol. 1, pp. 13–16, 1988.

[8] P. C. Claspy *et al.*, "A high speed GaAs MESFET optical controller," *IEEE Photon. Technol. Lett.*, vol. 1, pp. 389–391, 1989.

[9] V. Sokolov, J. J. Geddes, A. Contolatis, P. E. Bauhahn, and C. Chao, "A *Ka*-band GaAs monolithic phase shifter," *IEEE Trans. Microwave Theory Tech.*, vol. MTT-31, no. 12, pp. 1077–1088, 1983.

[10] V. Sokolov, J. Geddes, and P. Bauhahn, "GaAs monolithic receivers for 30/20 GHz satellite communications," presented at IEEE Eascon 86, Washington, DC, Sept. 1986.

II. COPLANAR WAVEGUIDE DEVELOPMENT

COAX-TO-CHANNELISED COPLANAR WAVEGUIDE IN-PHASE N-WAY, RADIAL POWER DIVIDER

Indexing terms: Waveguides, Transmission lines

A novel nonplanar, wideband power divider which makes use of a coax-to-CCPW transition is demonstrated. The transition utilises a coaxial transformer whose outer conductor is slotted along the length for RF power division and also for exciting the CCPWs in equal amplitude and phase at the radial junction. The measured (8–16GHz) excess insertion loss at the output ports is 0·5dB for a four-way divider. The amplitude and phase balance are within 0·5dB and 5°, respectively. The power divider should find applications in the feed network of phased arrays.

Introduction: Channelised coplanar waveguides (CCPW)[1] are a new variant of the conventional coplanar waveguide (CPW).[2] The CCPW has all the advantages of conventional CPW and also has lower radiation loss. In the conventional CPW, the loss of power by radiation to free space occurs from the printed circuit and the substrate. By embedding the substrate in a channel, the radiation loss from the substrate is suppressed. A practical CPW circuit such as a power divider also has several bend and step type discontinuities which can excite higher order CPW modes and surface wave modes. These modes can propagate if the cross-sectional geometry is favourable and may reduce the isolation between adjacent circuits besides giving rise to insertion loss spikes. The metal channel of the CCPW also acts as an effective barrier against interference through the substrate.

We demonstrate a novel power divider which uses a nonplanar coax-to-CCPW transition. The new design has advantages over the conventional planar, in-line Wilkinson type,[3] power divider. It eliminates the need for right angle bends which require dielectric overlays for phase velocity correction.[4] It eliminates the unreliable and nonreproducible bondwires which are used to tie the two ground planes to the same potential. It is also capable of simultaneously exciting multiple odd or even number CCPWs in equal amplitude and phase.

Radial junction: A coax-to-CCPW in-phase, four-way radial power divider is shown in Fig. 1. The junction is formed by the intersection of four CCPW lines. Power is coupled to this junction from a coaxial cable whose outer conductor is slotted along the z direction to form four coupled transmission lines. The centre pin of the coaxial line meets the intersecting CCPW centre conductors and the four coupled outer conductors meet the CCPW ground planes. The electric current at the open end of the coax is divided into the four CCPW lines illustrated in Fig. 2. This arrangement has the advantage of holding the ground planes at the same potential and exciting the four CCPW lines in equal amplitude and phase without the need for bond wires. Each of the four CCPW lines, Fig. 3, has an impedance of 135Ω at the junction. The net impedance seen by the coaxial line is approximately 34Ω. A quarter wave coaxial dielectric transformer ($\varepsilon_r = 4$) was used at the junction to match the 50Ω coaxial line to the 34Ω CCPW junction impedance. The characteristic impedance of the quarter wave coaxial dielectric transformer section as determined from Reference 5 is approximately 40Ω. The characteristic impedance ($Z_0 = V^2/P$) of the CCPW line at the output ports was set to 70Ω to provide a good match to the 50Ω coaxial connector.[4]

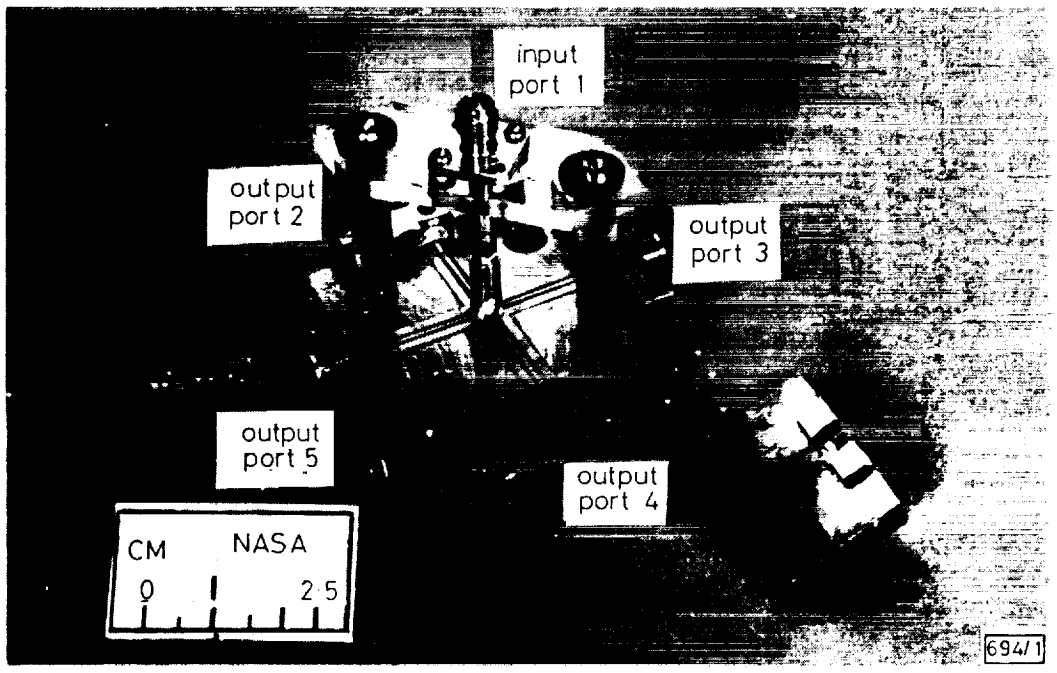

Fig. 1 *Coax to CCPW in-phase, four-way, radial power divider*

Each of the three pairs of slits in the ground plane of the CCPW (Fig. 3) acts as a tuning stub to improve the CCPW to coaxial connector impedance match over the measured frequency range.

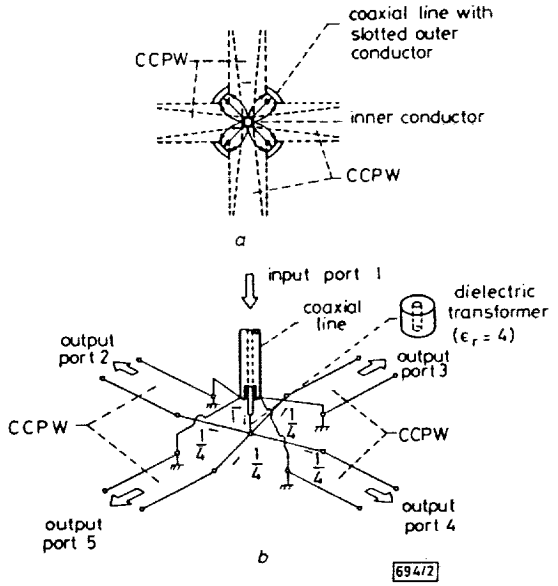

Fig. 2 *Radial power divider characteristics*
a Electric field distribution at end of slotted coaxial line
b Equivalent circuit of junction

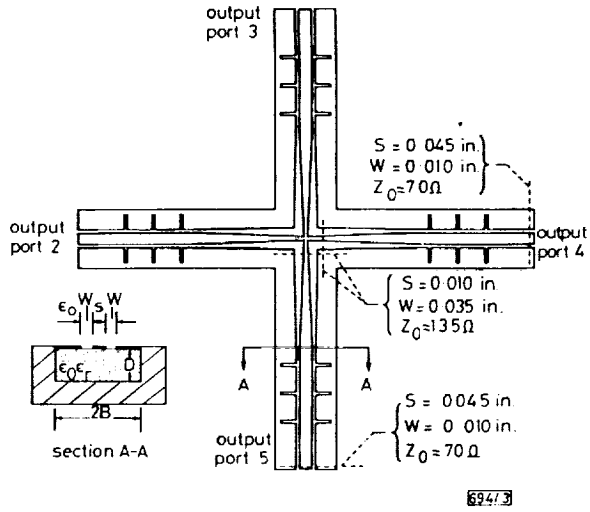

Fig. 3 *Coax to CCPW in-phase, four-way, radial power divider details*

Experimental results: The measured amplitude of the power coupled to one of the output ports over an octave bandwidth (8–16 GHz) is shown in Fig. 4 and is typical of the junction. The −6·5 dB measured amplitude at the output ports is in good agreement with the −6·0 dB expected for a 1 : 4 ideal lossless junction. The additional loss of 0·5 dB includes the CCPW to coaxial transformer and two coaxial connector losses. Also superimposed on Fig. 4 is the return loss of the input port which is greater than 10 dB. The amplitude and phase balance of this circuit are within 0·5 dB and 5°, respectively. These values are a function of the mechanical structure itself since all the ports are identical. The isolation between the ports is approximately 10 dB.

Conclusion: The design, implementation and characterisation of a *N*-way, in-phase, radial power divider which employs a novel coax-to-CCPW transition has been demonstrated. This is the first successful implementation of a copolanar waveguide power divider. The low loss and wide bandwidth characteristics of the divider would facilitate the implementation of

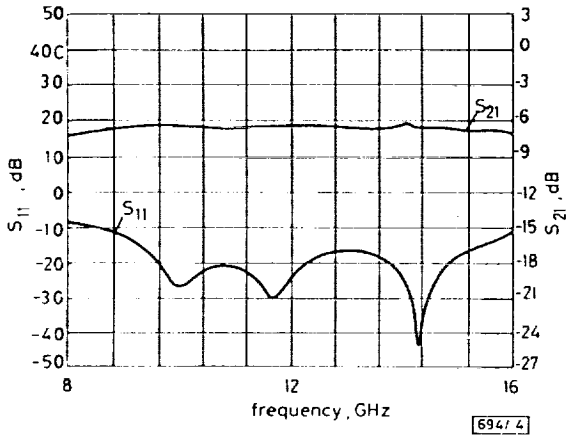

Fig. 4 *Measured coupled power and return loss*

a CCPW feed network in a phased array antenna system. The divider is observed to possess excellent amplitude and phase balance.

R. N. SIMONS
G. E. PONCHAK
NASA Lewis Research Center, 21000 Brookpark Road
Cleveland, OH 44135, USA

1st February 1990

References

1 SIMONS, R. N., PONCHAK, G. E., MARTZAKLIS, K. S., and ROMANOFSKY, R. R.: 'Channelized coplanar waveguide: Discontinuities, junction and propagation characteristics'. Digest IEEE MTT-S Int. Microwave Symposium, 1989, Vol. III, pp. 915–918
2 WEN, C. P.: 'Coplanar waveguide: A surface strip transmission line suitable for nonreciprocal gyromagnetic device applications', *IEEE Trans.*, 1969, **MTT-17**, pp. 1087–1090
3 EDWARDS, T. C.: 'Foundations for microstrip circuit design' (John Wiley, New York, 1981), p. 244
4 SIMONS, R. N., and PONCHAK, G. E.: 'Modeling of some coplanar waveguide discontinuities', *IEEE Trans.*, 1988, **MTT-36**, pp. 1796–1803
5 DUNCAN, J. W., and MINERVA, V. P.: '100 : 1 bandwidth balum transformer', *Proc. IRE*, 1960, **48**, pp. 156–164

NASA Technical Memorandum 102477

A New Rectangular Waveguide to Coplanar Waveguide Transition

George E. Ponchak
Lewis Research Center
Cleveland, Ohio

and

Rainee N. Simons
Case Western Reserve University
Cleveland, Ohio

Prepared for the
1990 IEEE MTT-S International
Microwave Symposium
Dallas, Texas, May 8-10, 1990

NASA

A NEW RECTANGULAR WAVEGUIDE TO COPLANAR WAVEGUIDE TRANSITION

George E. Ponchak
NASA Lewis Research Center
Cleveland, Ohio 44135

Rainee N. Simons*
Case Western Reserve University
Cleveland, Ohio 44106

ABSTRACT

A new rectangular waveguide to coplanar waveguide transition is described. The transition uses a ridge in one of the broad walls of the waveguide and a nonradiating slot in the opposite wall to split and rotate the electromagnetic fields of the rectangular waveguide TE10 mode into the CPW fields.

INTRODUCTION

Coplanar waveguide (CPW) is an attractive transmission line for microwave integrated circuits since the ground planes are on the same side of the substrate as the conducting strip (1). This permits the integration of both series as well as shunt circuit elements without the need for back side processing and via holes. A second important advantage of CPW which has recently emerged is in the design of microwave probes for on-wafer characterization of field effect transistors and for fast, inexpensive evaluation of microwave integrated circuits (2).

In order to fully utilize these advantages, transitions between CPW and other microwave transmission media are required. A coaxial connector to CPW transition in which the center pin and the ground connection of the coaxial connector make contact with the CPW center strip and ground planes respectively has been demonstrated at 18 GHz (3). By reducing the diameter of the coaxial connector, the upper frequency of these transitions has been extended to 50 GHz. Further reduction of the coaxial connector dimensions to increase the frequency of operation may be limited by the fragility of the connectors. Also, millimeter wave sources use rectangular waveguide at the output ports. Therefore, there is a need to develop rectangular waveguide to CPW transitions for applications at V-Band (50 to 75 GHz) and W-Band (75 to 110 GHz).

A waveguide to CPW transition has been reported by Bellantoni, et al. (4). The transition uses a finline taper to concentrate the electric fields and a wire bond to split the electric currents between the two ground planes. The difficulty with the design is positioning the wire bond such that the two slots are excited in equal magnitude and phase. A further difficulty with finline transitions is the occurrence of resonances created by the transition (4,5). This paper presents the design and characteristics of a new rectangular waveguide to CPW transition which uses a ridge in one of the broad walls of the waveguide and a nonradiating slot in the opposite wall. This arrangement transforms the rectangular waveguide TE10 mode into the CPW mode with equal magnitude and phase excitation of the slots. The transition is capable of providing full waveguide bandwidth.

TRANSITION DESIGN

Figure 1 is a schematic of the transition. The printed circuit board shown in Fig. 1(a) forms the bottom wall of the rectangular waveguide. On this printed circuit board, a nonradiating slot is etched which gradually tapers to a width equal to $S + 2W$, where S and W are the width of the CPW center strip and slot, respectively. The cosine tapered ridge shown in Fig. 1(b) protrudes from the top wall of the waveguide and extends down to the printed circuit board metalization at the end of the taper. The ridge width is matched to the width of the center strip conductor, S, of the CPW. The electric field distribution at cross sectional planes along the transition is illustrated in Fig. 2. One can easily visualize that the ridge and the nonradiating slot gradually split the electromagnetic fields of the TE10 waveguide mode and rotate them through 90° to match the fields of the CPW.

TEST RESULTS FOR K BAND TRANSITION

A transition has been designed for K band. The printed circuit portion of the transition has been fabricated on a 0.125 in. thick 5880 RT/Duroid substrate with single sided copper cladding. The ridged waveguide portion of the transition is copper. The cosine taper is 1.5 in. long or approximately 1.5 λ_g at the center frequency. The S and W of the CPW are 0.032 and 0.008 in. respectively yielding a 75 Ω transmission line. For testing, the two transitions were connected back to back through a 0.8 in. length of CPW transmission line. The characteristics for this transition are shown in Fig. 3. The return loss is greater than 11 dB

*NASA Resident Research Associate at Lewis Research Center (work funded by NASA Grant NAG3-816).

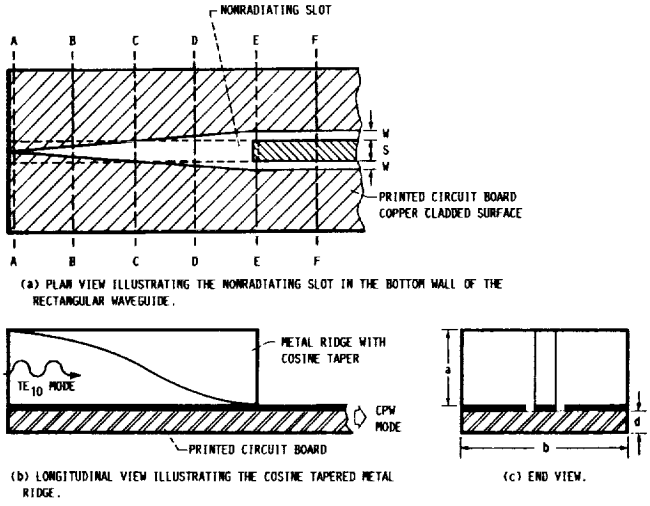

(a) PLAN VIEW ILLUSTRATING THE NONRADIATING SLOT IN THE BOTTOM WALL OF THE RECTANGULAR WAVEGUIDE.

(b) LONGITUDINAL VIEW ILLUSTRATING THE COSINE TAPERED METAL RIDGE.

(c) END VIEW.

FIGURE 1. - SCHEMATIC OF THE TRANSITION.

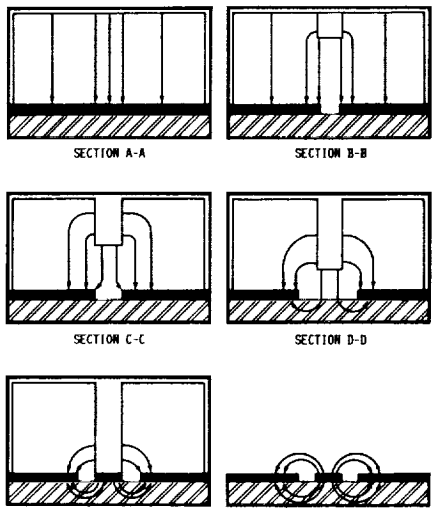

FIGURE 2. - ELECTRIC FIELD DISTRIBUTION AT VARIOUS CROSS-SECTIONS ALONG THE TRANSITION.

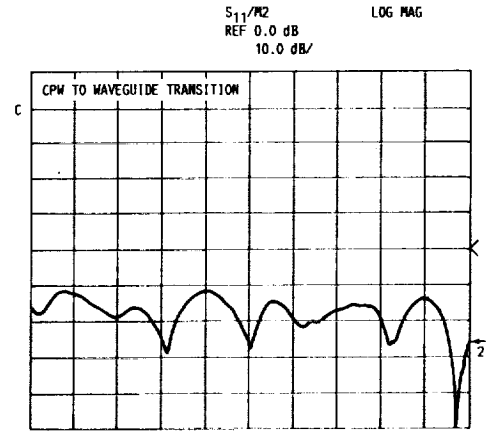

(a) INPUT RETURN LOSS AS MEASURED AT THE WAVEGUIDE PORT.

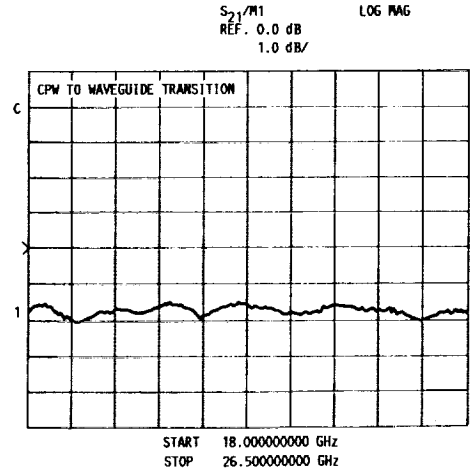

(b) MEASURED INSERTION LOSS OF TWO TRANSITIONS CONNECTED BACK TO BACK.

FIGURE 3.

across the band. The average insertion loss for the back-to-back transitions is 1.75 dB with 0.25 dB ripple.

CONCLUSIONS

A new rectangular waveguide to CPW transition has been developed with full waveguide bandwidth. This transition should permit the use of CPW based circuits in the millimeter wave frequency range and the development of microwave probes above 50 GHz for fast and inexpensive testing of the millimeter wave circuits.

REFERENCES

(1) C.P. Wen, "Coplanar Waveguide: A Surface Strip Transmission Line Suitable for Nonreciprocal Gyromagnetic Device Applications," IEEE Trans. Microwave Theory Tech., vol. MTT-17, no. 12, pp. 1087-1090, 1969.

(2) K.E. Jones, E.W. Strid, and K.R. Gleason, "mm-Wave Wafer Probes Span 0 to 50 GHz," Microwave J., vol. 30, no. 4, pp. 177-183, 1987.

(3) M. Houdart and C. Aury, "Various Excitation of Coplanar Waveguide," in IEEE MTT-S International Microwave Symposium Digest, 1979, pp. 116-118.

(4) J.V. Bellantoni, R.C. Compton, and H.M. Levy, "A New W-Band Coplanar Waveguide Text Fixture," in IEEE MTT-S International Microwave Symposium Digest, 1989, pp. 1203-1204.

(5) G. Begemann, "An X-Band Balanced Fin-Line Mixer," IEEE Trans. Microwave Theory Tech., vol. MTT-26, no. 12, pp. 1007-1011, 1978.

NASA Technical Memorandum 102289

Channelized Coplanar Waveguide Pin-Diode Switches

G.E. Ponchak
Lewis Research Center
Cleveland, Ohio

and

R.N. Simons
Case Western Reserve University
Cleveland, Ohio

November 1989

NASA

CHANNELIZED COPLANAR WAVEGUIDE PIN-DIODE SWITCHES

G.E. Ponchak
National Aeronautics and Space Administration
Lewis Research Center
Cleveland, Ohio 44135

and

R.N. Simons*
Case Western Reserve University
Cleveland, Ohio 44106

SUMMARY

Three different types of p-i-n diode, reflective CPW switches are presented. The first two switches are the series and the shunt mounted diode switches. Each has achieved greater than 15 dB of isolation over a broad bandwidth. The third switch is a narrow band, high isolation switched filter which has achieved 19 dB of isolation. Equivalent circuits and measured performance for each switch is presented.

INTRODUCTION

Coplanar waveguide, CPW, on a dielectric substrate consists of a center strip conductor with semi-infinite ground planes on either side (ref. 1). Channelized coplanar waveguide, CCPW, consists of CPW transmission line placed in a metal enclosure (ref. 2). Because the ground planes and the center conductor are on the same side of the substrate, shunt as well as series mounting of circuit components can be done without the need for wraparounds or via-holes. The improvements in circuit yield and the reduction in inductance for ground paths over microstrip based circuits should permit microwave integrated circuits, MIC's, to be fabricated at higher frequencies and less expensively. However, the extent of applications of CPW circuits is limited due to the unavailability of circuit elements and models which can be incorporated into CAD programs.

Microwave switches are a basic circuit element for phase shifters and radiometers. A CPW switchable attenuating medium propagation, SAMP, switch has been demonstrated by Fleming et al. (ref. 3). This device is useful for GaAs MMIC circuits but it is not easily incorporated into MIC's on passive substrates such as alumina or duroid. P-i-n diodes are good microwave switches since the impedance of the diode can be changed from a very high value to nearly zero in a short time (refs. 4 and 5).

This paper presents for the first time CPW p-i-n diode, reflective switches. Three basic switches are presented. The first is a shunt mounted diode switch. This switch is similar to fin line shunt mounted diode switches (ref. 4). The second switch is a series mounted diode across a gap in the center strip conductor. The last switch is a novel design which converts a CPW interdigital coupler with bandpass filter characteristics into a spurline, bandstop filter.

---

*NASA Resident Research Associate at Lewis Research Center.

The three switches have been fabricated on CCPW transmission lines. All of the circuits have been fabricated on RT/Duroid 5880 substrates with Metelics Corporation beam lead diodes, MBP-1030-B11. Figure 1 is the equivalent circuit

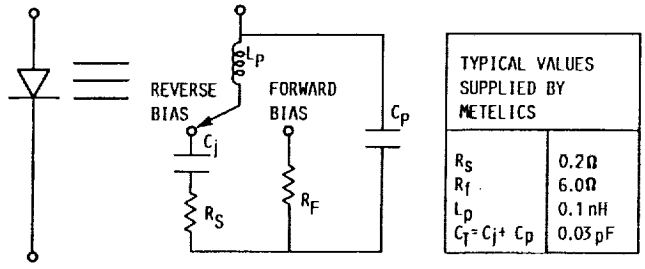

FIGURE 1. - P-I-N DIODE EQUIVALENT CIRCUIT AND TYPICAL CIRCUIT ELEMENT VALUES.

of the diode with the circuit element values supplied by Metelics. Although no tuning to resonate off the diode parasitics was done, the CPW slots were made equal to the length of the packaged diode to minimize the package inductance, Lp. Testing of the switches has been done on an HP 8510 automatic network analyzer with bias tees to supply the dc bias to the diodes. The test fixture is comprised of a 2 in. length of CCPW with a 0.045 in. center strip and 0.010 in. slot. Connection to 3.5 mm coax cables is made through a pair of coaxial connectors. Tuning notches in the ground plane have been used to improve the coax-to-CCPW characteristics over selected frequency bands. The test fixture has a total insertion loss of 0.5 dB and a return loss greater than 15 dB for the frequencies reported in this paper.

P-I-N DIODE SHUNT SWITCH

In a shunt mounted configuration, a pair of diodes are placed in parallel across the slots of the CCPW transmission line (fig. 2). When the diodes are

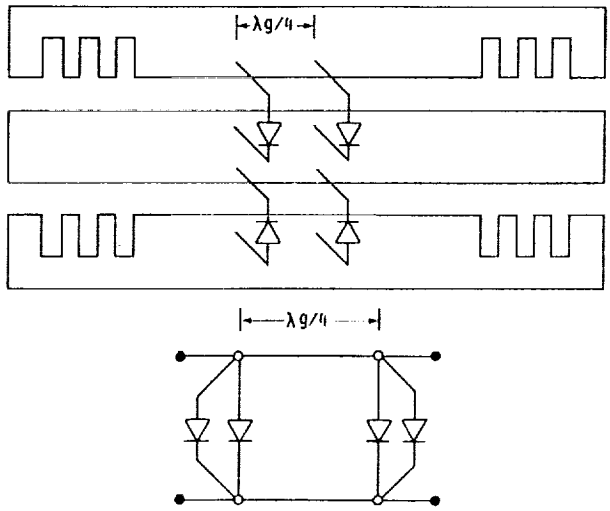

FIGURE 2. - SCHEMATIC AND EQUIVALENT CIRCUIT OF CPW P-I-N DIODE SHUNT SWITCH.

forward biased, each slot is loaded by the forward bias impedance of the diode; at 10 GHz, the impedance across the slot is approximated by $Rf + j\omega Lp \approx 8.7\ \Omega$ << Zo. The shunt impedance for CPW, with two parallel slots, is therefore 4.35 Ω. This low impedance loading the slot reflects the propagating wave. When the diode is reverse biased, each slot is loaded by an impedance approximated by $1/(j\omega Ct) \approx 530\ \Omega >> Zo$. This is an equivalent shunt impedance of 265 Ω for CPW. This load results in a small attenuation. Using expressions by Watson (ref. 6) modified for two parallel shunt elements, an isolation of 16 dB and an insertion loss of 0.04 dB is predicted.

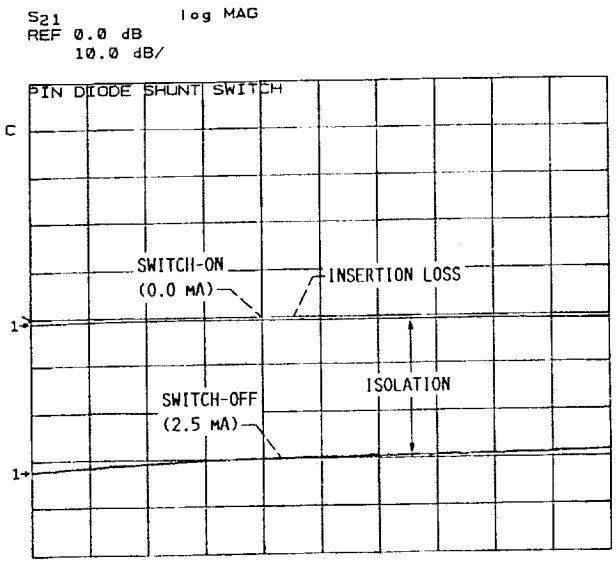

(a) MEASURED INSERTION LOSS AND ISOLATION.

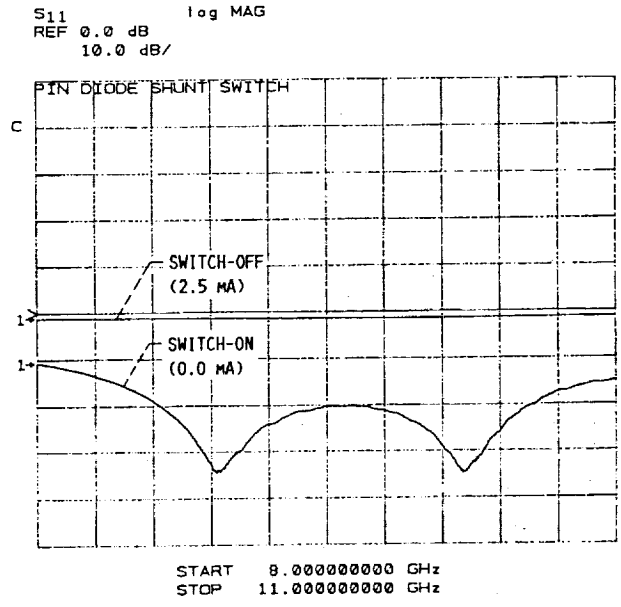

(b) MEASURED RETURN LOSS.

FIGURE 3. - CPW P-I-N DIODE SHUNT SWITCH WITH TWO PAIRS OF DIODES.

An insertion loss less than 1 dB and an isolation of 15 dB has been measured over the frequency band of 8 to 11 GHz. The return loss was less than 10 dB across the band. By incorporating more than one pair of diodes across the slots with a $\lambda g/4$ separation, higher isolation can be achieved. Typically, two pairs of diodes have resulted in an isolation of 30 dB over the 8 to 11 GHz frequency band with little increase in insertion loss, this is shown in figure 3(a). Figure 3(b) shows the return loss which is less than 10 dB across the band.

P-I-N DIODE SERIES SWITCH

In the series mounted diode configuration, a diode is mounted across an 0.008 in. gap in the center strip conductor of the CCPW line (fig. 4). The

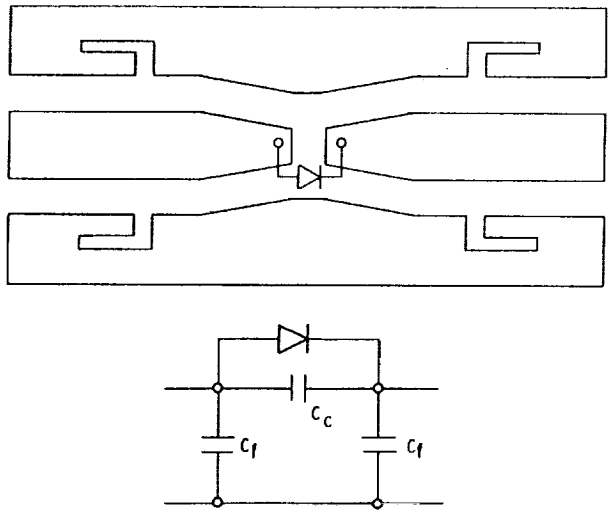

FIGURE 4. - SCHEMATIC AND EQUIVLENT CIRCUIT OF CPW P-I-N DIODE SERIES SWITCH.

center strip has been tapered to the width of the beam lead diode to provide a better match to the width of the diode package. The gap appears as an equivalent capacitive π network (ref. 7). When the diode is forward biased, the coupling capacitance is shorted by the low diode impedance and the wave is transmitted. Reverse biasing the diode results in an impedance across the gap which can be approximated by $1/[j\omega(Ct + Cc)] >> Zo$ at 10 GHz. Therefore, the propagating signal is reflected as if from an open circuit. A measured insertion loss of 1 dB and an isolation of 15 dB has been obtained from 0.045 to 8 GHz (fig. 5(a)). The return loss over this band is less than 10 dB (fig. 5(b)). The gap impedance is not large enough at higher frequencies to provide good isolation. The gap can be lengthened to decrease Cc but the increase in inductance from the longer diode leads will ultimately limit the gap separation. Resonating out these reactances is required for higher frequency operation (ref. 6).

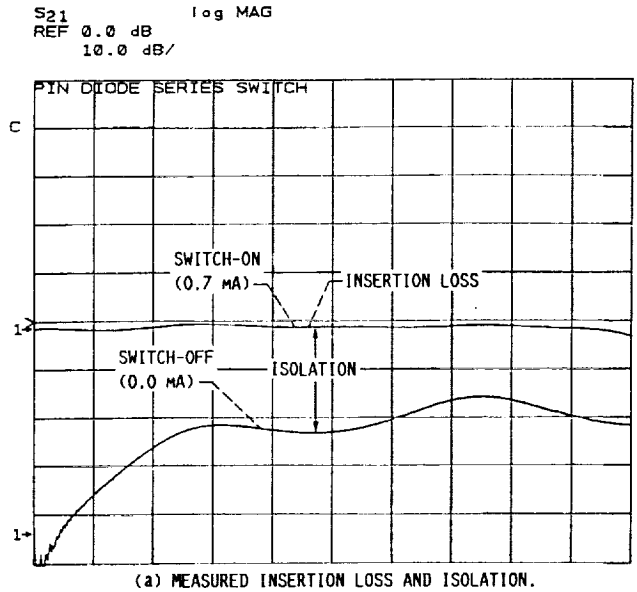

(a) MEASURED INSERTION LOSS AND ISOLATION.

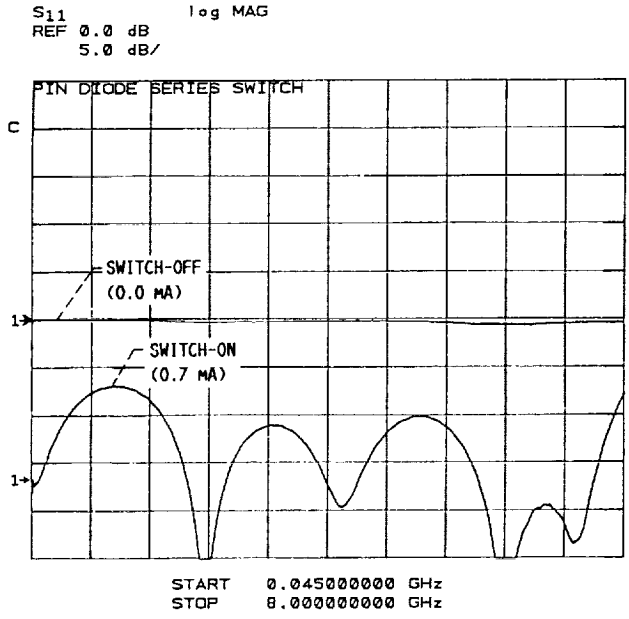

(b) MEASURED RETURN LOSS.

FIGURE 5. - CPW P-I-N DIODE SERIES SWITCH.

P-I-N DIODE SPDT SWITCH

To realize a SPDT switch, a CCPW Tee-junction with gaps in the center strip conductor at the junction was formed (fig. 6). Diodes were mounted across the gaps in parallel. As shown in figure 7, the measured insertion loss is 1 dB and the isolation is greater than 15 dB over the octave bandwidth of 2.25 to 5.5 GHz. The return loss was less than 10 dB.

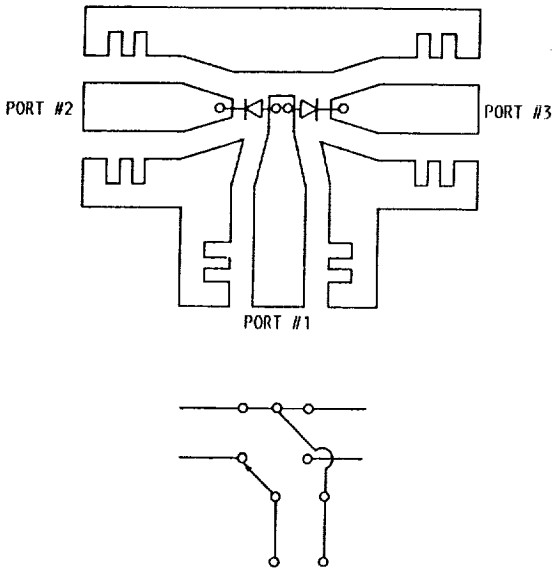

FIGURE 6. - SCHEMATIC AND EQUIVALENT CIRCUIT OF SERIES MOUNTED P-I-N DIODE CPW SPDT SWITCH.

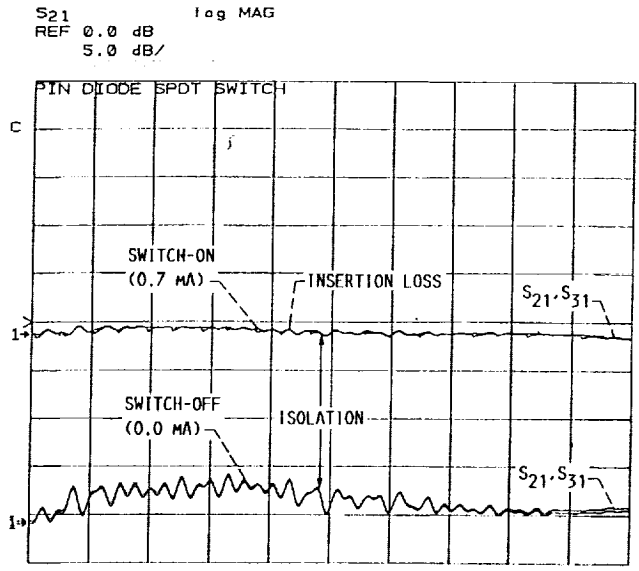

FIGURE 7. - MEASURED INSERTION LOSS AND ISOLATION OF SERIES MOUNTED PIN DIODE CPW SPDT SWITCH.

P-I-N DIODE SWITCHED-SERIES-STUB SWITCH

A diode is mounted across the open end of a $\lambda g/4$ stub which is in series with the center strip conductor of the CCPW as shown in figure 8. When the diode is unbiased, the stub is terminated in an effective open circuit and therefore appears as a series short circuit. Hence, the wave propagates with negligible attenuation. This is the on-state of the switch. When the diode is forward biased, the stub is terminated in an effective short circuit which

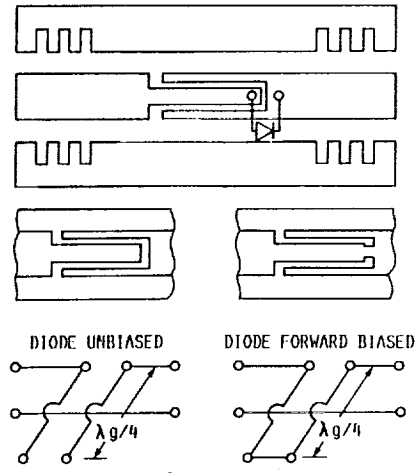

FIGURE 8. - SCHEMATIC AND EQUIVALENT CIRCUIT OF CPW P-I-N DIODE SWITCHED-SERIES-STUB SWITCH.

therefore appears as a series open circuit. The wave is therefore reflected; this is the off-state of the switch. The diode reactances result in an effective lengthening of the stub and can easily be compensated for. A measured insertion loss of 1.0 dB and an isolation of 19 dB has been obtained at 9 GHz (fig. 9(a)). Figure 9(b) shows the return loss.

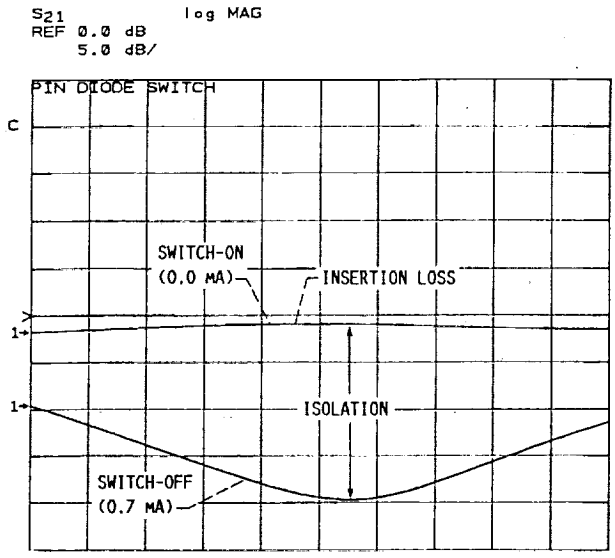

(a) MEASURED INSERTION LOSS AND ISOLATION.

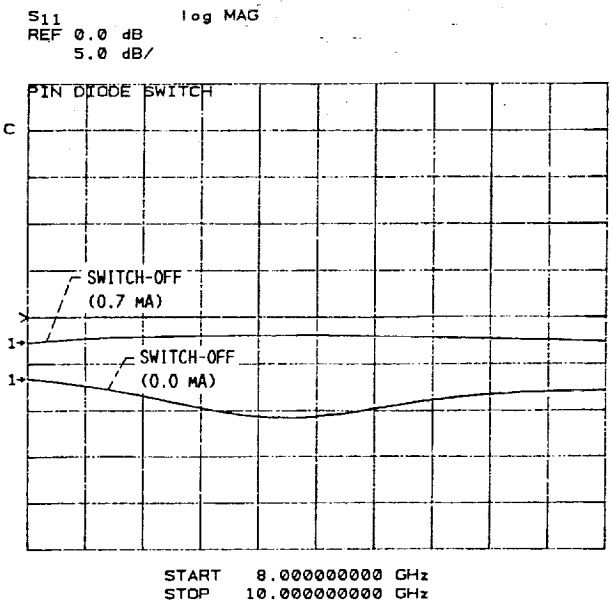

(b) MEASURED RETURN LOSS.

FIGURE 9. - CPW P-I-N DIODE SWITCHED-SERIES-STUB SWITCH.

CONCLUSIONS

P-I-N diode reflective switches are easily realizable on CCPW transmission line and therefore CPW transmission line. Each of the three type of switches presented are practical for specific applications. The performance of the

switches could be improved through typical tuning of the diode reactances once the necessary CPW circuit models become available.

REFERENCES

1. Wen, C.P., "Coplanar Waveguide, A Surface Strip Transmission Line Suitable for Nonreciprocal Gyromagnetic Device Applications," 1969, IEEE Trans. Microwave Theory Tech., vol. MTT-17, pp. 1087-1090.

2. Simons, R.N., Ponchak, G.E., Martzaklis, K.S., and Romanofsky, R.R., "Channelized Coplanar Waveguide: Discontinuities, Junctions, and Propagation Characteristics,: 1989, IEEE MTT-S International Microwave Symposium Digest, IEEE, Piscataway, NJ, pp. 915-918.

3. Fleming, P.L., Smith, T., Carlson, H.E., and Cox, W.A., "GaAs SAMP Device for Ku-Band Switching," 1979, IEEE Trans. Microwave Theory Tech., vol. MTT-27, pp. 1032-1035.

4. Bhat, B., and Koul, S.K., Analysis, Design and Applications of Fin Lines, Artech House, Norwood, MA, 1987.

5. White, J.F., Microwave Semiconductor Engineering, Van Nostrand Reinhold Co., New York, 1982.

6. Watson, H.A., Microwave Semiconductor Devices and Their Circuit Applications, McGraw-Hill Book Company, New York, 1969.

7. Simons, R.N., and Ponchak, G.E., "Modeling of Some Coplanar Waveguide Discontinuities," IEEE Trans. 1988, Microwave Theory Tech., vol. MTT-36, pp. 1796-1803.

NASA Technical Memorandum 102494

Experimental Investigations on Channelized Coplanar Waveguide

Rainee N. Simons
Case Western Reserve University
Cleveland, Ohio

George E. Ponchak
Lewis Research Center
Cleveland, Ohio

Konstantinas S. Martzaklis
University of Akron
Akron, Ohio

and

Robert R. Romanofsky
Lewis Research Center
Cleveland, Ohio

April 1990

NASA

EXPERIMENTAL INVESTIGATIONS ON CHANNELIZED COPLANAR WAVEGUIDE

Rainee N. Simons*
Case Western Reserve University
Cleveland, Ohio 44106

George E. Ponchak
National Aeronautics and Space Administration
Lewis Research Center
Cleveland, Ohio 44135

Konstantinos S. Martzaklis†
University of Akron
Akron, Ohio

Robert R. Romanofsky
National Aeronautics and Space Administration
Lewis Research Center
Cleveland, Ohio 44135

SUMMARY

This paper presents a new variant of coplanar waveguide (CPW) which has been termed channelized coplanar waveguide (CCPW). Measured propagation characteristics for CCPW such as $\varepsilon(\text{eff})$ and unloaded Q as a function of geometrical parameters and frequency are presented. The measured and modeled $\varepsilon(\text{eff})$ are also compared. Equivalent circuit model element values are presented for a CCPW open circuit and a CCPW right angle bend. A CCPW matched T-junction, matched 1:3 junction, and a novel coax-to-CCPW in-phase, N-way, radial power divider are also demonstrated.

E-5285

INTRODUCTION

Coplanar waveguide, CPW, on a dielectric substrate consists of a center strip conductor with semi-infinite ground planes on either side (ref. 1). A variant of CPW is grounded coplanar waveguide, GCPW, which has an additional ground plane on the opposite side of the substrate to facilitate heat removal and packaging (ref. 2). These transmission lines have several advantages which make them ideally suited for microwave integrated circuits. The disadvantage of CPW and GCPW is that the structure can support spurious modes besides the CPW mode since the transverse dimensions may be several wavelengths.

This paper presents a new variant of CPW. The new structure has side walls which, together with the ground plane, constitute a channel and hence is

---

*NASA Resident Research Associate at Lewis Research Center (work funded by NASA Grant NAG3-816).
†Student Co-op at NASA Lewis Research Center.

appropriately termed as channelized coplanar waveguide, CCPW. A shielding structure may also be used to further confine the electromagnetic fields. This structure is shown in figure 1. The enclosure of the CPW transmission line eliminates radiation loss and spurious surface modes created at discontinuities. Also, because the basic transmission line structure is CPW, CCPW maintains the inherent advantages over microstrip for easy shunt as well as series mounting of active and passive components.

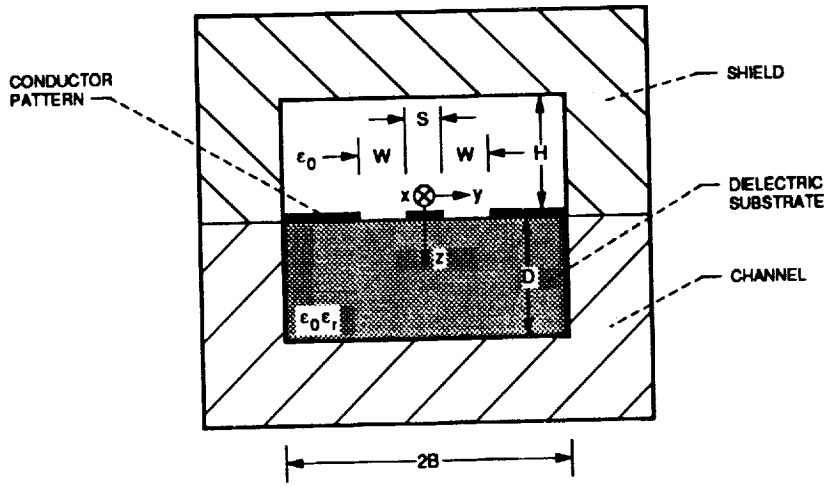

Figure 1. - Schematic of channelized coplanar waveguide (CCPW).

To maintain a single CPW mode of propagation, CCPW must be designed to suppress the dielectric filled rectangular waveguide mode, the microstrip mode, and the rectangular coax mode. The channel width, 2B, is chosen such that the rectangular waveguide mode is cutoff. The microstrip and rectangular coax modes are suppressed by the proper selection of the slot width, W, the center strip width, S, and the substrate thickness, D. The ratios W/D and S/D must be sufficiently small to suppress the microstrip mode. The ratio (S + 2W)/2B must be small to suppress the rectangular coax mode.

This paper presents lumped element circuit models for several CCPW discontinuities, together with their element values as a function of frequency. The discontinuities characterized are an open circuit and a right angle bend. The measured frequency dependence of the effective dielectric constant, ε(eff), and the unloaded quality factor, Q, are also presented for CCPW lines fabricated on $\varepsilon(r) = 2.2\pm0.02$ RT/Duroid 5880, $\varepsilon(r) = 6.0\pm0.15$ RT/Duroid 6006, and $\varepsilon(r) = 10.2\pm0.25$ 3M Epsilam-10 substrates. This is followed by the design and characterization of a CCPW matched T-junction and a matched 1:3 junction. Lastly, the performance of a novel Coax-to-CCPW in-phase, N-way, radial power divider circuit is presented.

METHOD OF MEASUREMENTS

A resonator technique similar to that described by Richings (ref. 3) and Stephenson and Easter (ref. 4) was used. The $\lambda/4$ end coupled stubs could not be etched off as in the case of microstrip since this would alter the CCPW open end parameters. Hence, a four resonator set had to be fabricated for each frequency to determine the end effects.

This will contribute some errors to the results because the resonator lengths and gaps will not be identical for the two $\lambda/2$ and λ resonators. In addition, S and W varied slightly for each resonator set since the resonators were not processed in parallel. The circuit dimensions were measured to ±0.0002 in. The coupling gaps were varied to maintain a coupling coefficient, β, less than 1. For most of the resonator sets, $\beta \leq 0.3$. This is a sufficient condition to minimize the loading of the resonator for transmission lines with $Q \geq 100$ as are reported in this paper. The Q was determined through a technique given in reference 5.

EFFECTIVE DIELECTRIC CONSTANT

The ε(eff) was measured over the frequency range of 3 to 18 GHz for several unshielded CCPW lines and the results are shown in figure 2. The CCPW lines have been modeled using reference 6 and the ε(eff) is plotted for each CCPW line. ε(eff) of GCPW calculated from the closed form expression of Ghione

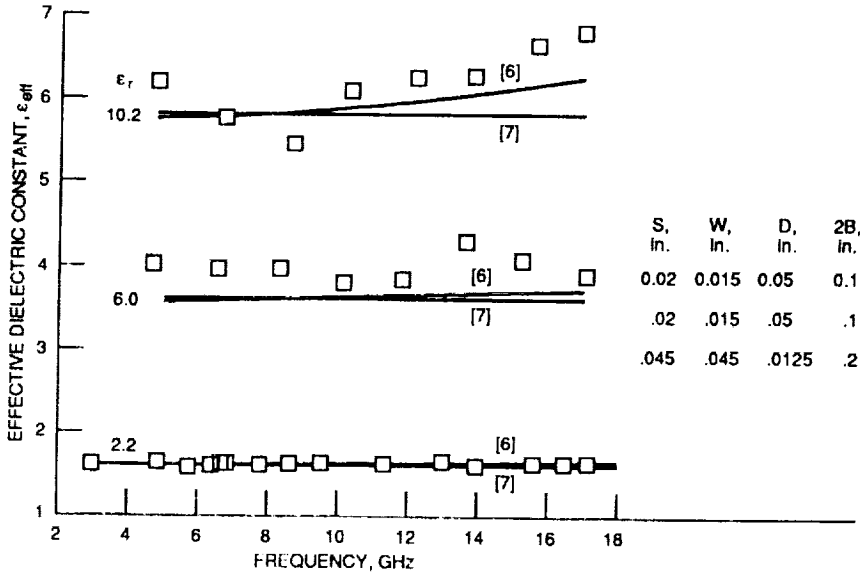

Figure 2. - Measured effective dielectric constant for unshielded CCPW as a function of frequency.

and Naldi (ref. 7) is also plotted for comparison. For the low dielectric substrate, either reference 6 or 7 could be used to predict ε(eff). For the higher dielectric substrates, both methods predicted lower ε(eff) than what was measured.

Effect of Substrate Thickness

ε(eff) was measured as a function of frequency for unshielded CCPW lines fabricated on substrates with D in the range of 0.062 to 0.250 in. The CCPW parameters S, W, 2B, and ε(r) were held fixed at 0.045 in., 0.010 in., 0.200 in., and 2.2, respectively. No variation in ε(eff) was observed for the thicker substrates, $W/D \leq 1/12.5$. ε(eff) of the thinner substrate, $W/D \approx 1/6$, was 0.7 percent higher than the other measured cases. This agrees with the calculated ε(eff) (ref. 6) and results in reference 2. The increase in ε(eff) is due to a microstrip mode.

To verify this, an RF probe was used to sample the electric fields under the center of the strip at the plane of the bottom conductor, the probe placement is shown in figure 3. Since odd mode CPW propagation has zero electric fields at this point, any fields measured by the probe must be due to a microstrip mode. The sampled field was measured for the thickest substrate and this value was used as a calibrated zero. No microstrip mode was measured as D was decreased until W/D ≈ 1/6, when an increase in the sampled field amplitude of ≈3 dB was measured.

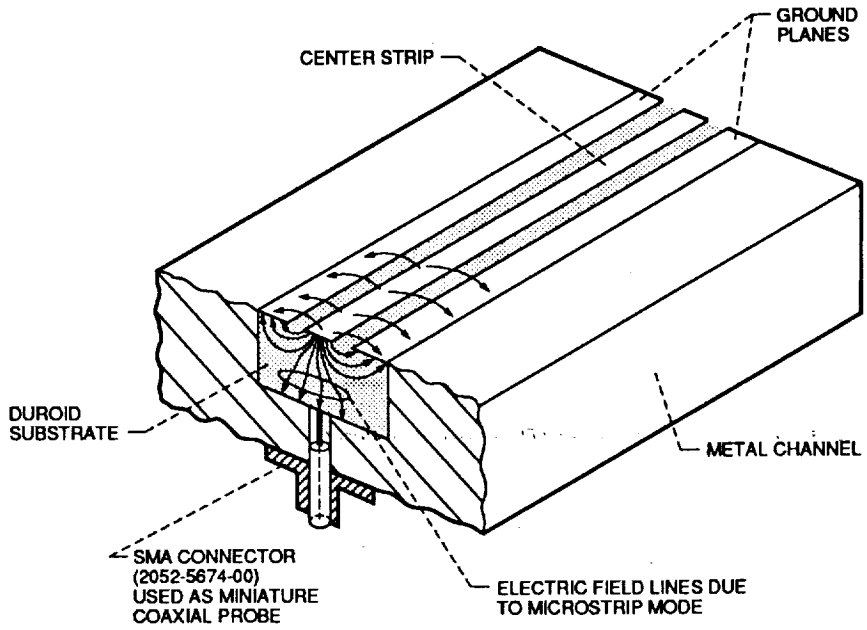

Figure 3. - Probe placement to sample the electric fields due to the microstrip mode.

Effect of Cover Height

ε(eff) was measured for shielded CCPW lines with cover heights of H = D, 2D, and 4D. Resonators were tested with ε(r), D, S, and W equal to 2.2, 0.125 in., 0.045 in., and 0.010 in., respectively. Resonators were also fabricated on D = 0.050 in., ε(r) = 6 and 10.2 substrates. In all the cases, the change in ε(eff) from the unshielded case was negligible.

LOSS MEASUREMENTS

Effect of S and Shielding

Figure 4 shows the measured Q for resonators of length λ as a function of S for a fixed frequency. The Q of the unshielded resonators decreases with increasing S while the Q of the shielded resonators increases with increasing S. Therefore, radiation loss increases as S increases.

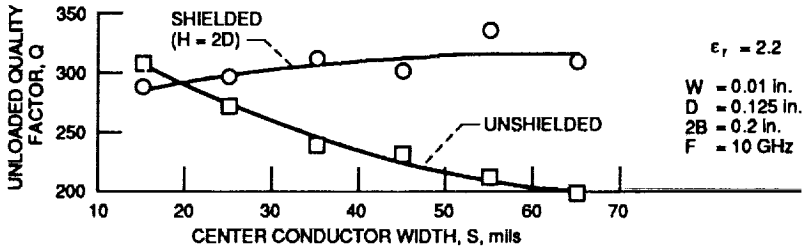

Figure 4. - Measured unloaded quality factor, Q, for CCPW as a function of the center conductor width, with and without a shielding enclosure.

Effect of Frequency and Shielding

Figure 5 shows the measured Q over the frequency range of 3 to 18 GHz for λ resonators both with and without shielding. The reduction in Q with increasing frequency for the unshielded case is due to the increase in radiation loss. With shielding, the Q is observed to increase with frequency or the attenuation per unit wavelength decreases. A change in the cover height from H = 2D to H = D showed no measurable difference in Q.

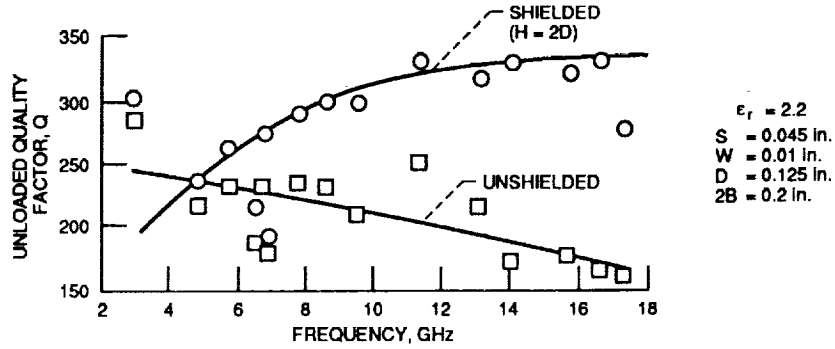

Figure 5. - Measured unloaded quality factor, Q, for CCPW as a function of frequency, with and without a shielding enclosure.

Effect of D and $\varepsilon(r)$

The effect of varying D in the range of 0.062 to 0.250 in. on Q was measured. No measurable variation in Q over the frequency range of 8 to 18 GHz was observed. CCPW resonators on the higher $\varepsilon(r)$ substrates had lower Q's. This is expected since the higher dielectric substrates concentrate more of the fields in the lossy substrate.

CHANNELIZED CPW OPEN CIRCUIT

When a CPW line is terminated in an open circuit, there is an excess fringing of the electromagnetic fields which gives rise to a capacitance, Cf (ref. 8). This capacitance is equivalent to a short length of a transmission line, Lo, terminated in a perfect open circuit as illustrated in figure 6. The open end line extension for the unshielded CCPW de-embedded from the resonator data is shown as a function of frequency in figure 7. Although strict dimensional standards were used to select resonators, a large spread in Lo was present. The exact cause of this spread, particularly at the lower frequencies, is unexplained. There was no variation in Lo for resonators with a

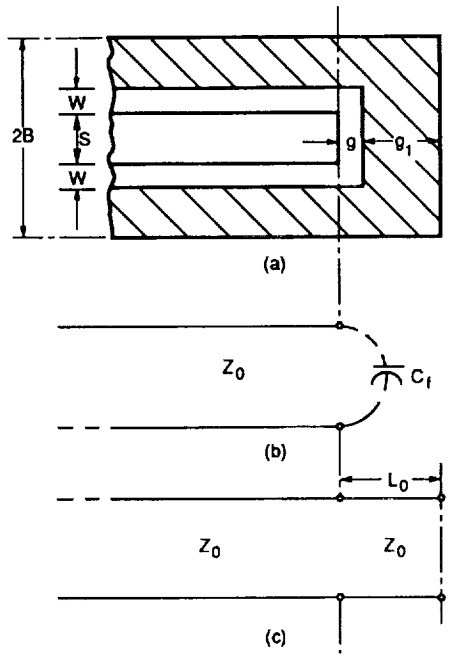

(a) Schematic of a CCPW open circuit.
(b) Equivalent end fringing capacitance, C_f.
(c) Equivalent CCPW end-effect length, L_0.
Figure 6. - CCPW open circuit.

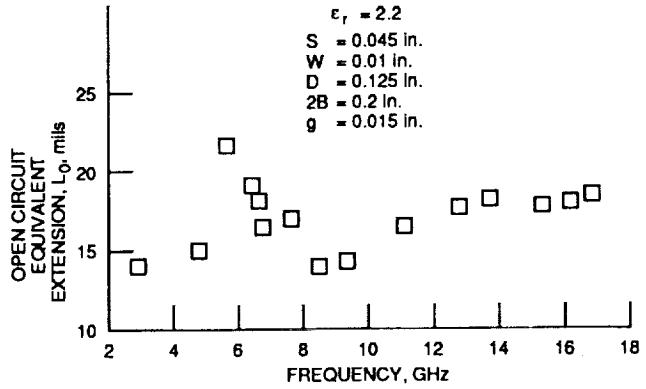

Figure 7. - Experimentally determined open circuit equivalent end-effect length as a function of frequency.

cover height of H $\geq$ 2D since its presence has negligible effect on the fringing fields. Also, Lo was found to be independent of the distance between the open circuit and the end of the substrate, g1.

CHANNELIZED CPW RIGHT ANGLE BEND

A CCPW right angle bend and its equivalent circuit are shown in figure 8. The capacitance, C, is created by the accumulation of excess charge at the corners in the two slots and the resulting excess electric fields to the ground plane. The current flow interruption creates the excess inductance which can be equated to a length of transmission line, L. Radiation from the corner is represented by the shunt conductance, Gr.

To experimentally determine the capacitance, C, a voltage antinode has to be placed at the discontinuity. This is realized by placing a right angle bend at the center of an open circuit terminated resonator of length λ. To

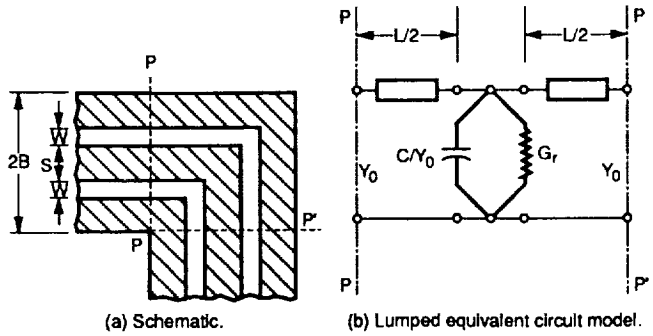

(a) Schematic. (b) Lumped equivalent circuit model.

Figure 8. - CCPW right angle bend.

determine the inductance, a voltage node has to be placed at the discontinuity. This is realized by placing a right angle bend in the center of a $\lambda/2$ resonator. The C and L are determined from the measured resonant frequencies using the following two equations (ref. 4):

$$L_n = \frac{nv}{2f_n \sqrt{(\varepsilon(eff))}} - (l_n + Lo + Lg) \tag{1}$$

$$C/Yo = \frac{1}{\pi f_2} \tan\left[\frac{\pi f_2 \sqrt{\varepsilon(eff)}\, L_2}{v}\right] \tag{2}$$

where

$f_n \equiv$ resonant frequency of the $n\lambda/2$ resonator

$Lg \equiv$ gap equivalent extension

$L_n \equiv$ Extension due to the parasitic reactance, either resulting from a voltage antinode for an $n = 2$ resonator or a voltage node for an $n = 1$ resonator

$Lo \equiv$ open circuit equivalent extension

$l_n \equiv$ physical length of the $n\lambda/2$ resonator

$n \equiv$ order of resonance

$v \equiv 3 \times 10^8$ m/sec

The radiation conductance, Gr, was calculated by deriving a lumped element equivalent circuit model for the shielded and unshielded resonators incorporating a right angle bend (ref. 5). The difference in the resonator circuit conductance is then attributed to an equivalent radiation conductance. The model is valid near the resonant frequency. Table I presents the normalized capacitance C/Yo, L, and the normalized radiation conductance Gr/Yo as a function of the frequency. The radiation conductance is very small at low frequencies, however, it increases rapidly with frequency.

TABLE I. - CCPW RIGHT ANGLE BEND DISCONTINUITY

[S = 0.045 in., W = 0.010 in., $\varepsilon(r) = 2.2$, 2B = 0.200 in.]

Frequency, GHz	L, mil	C/Yo, pF·Ω	Gr/Yo
2.97	22.622	4.219	0.0003635
4.92	26.241	4.353	.0014154
9.74	30.972	3.192	.010823
13.49	27.867	2.950	.011765
17.84	31.794	3.848	---------

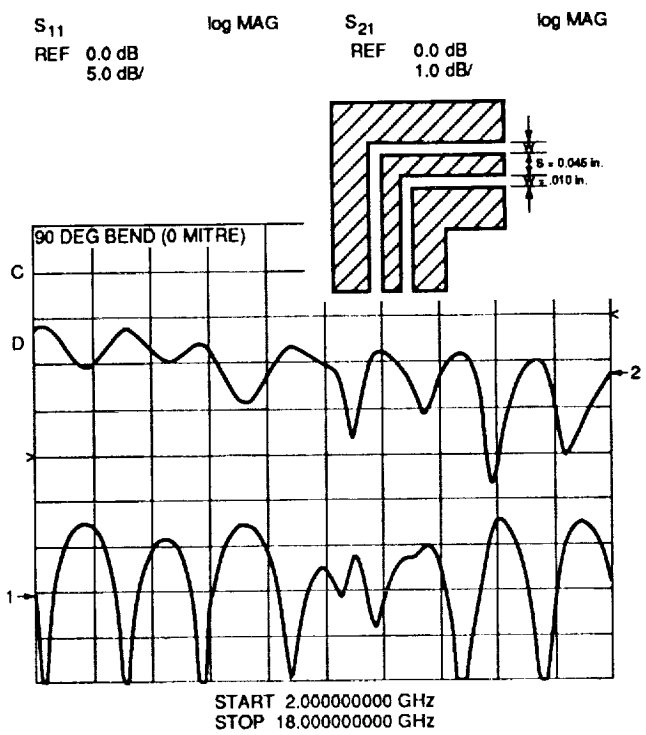

(a) Uncompensated right angle bend.

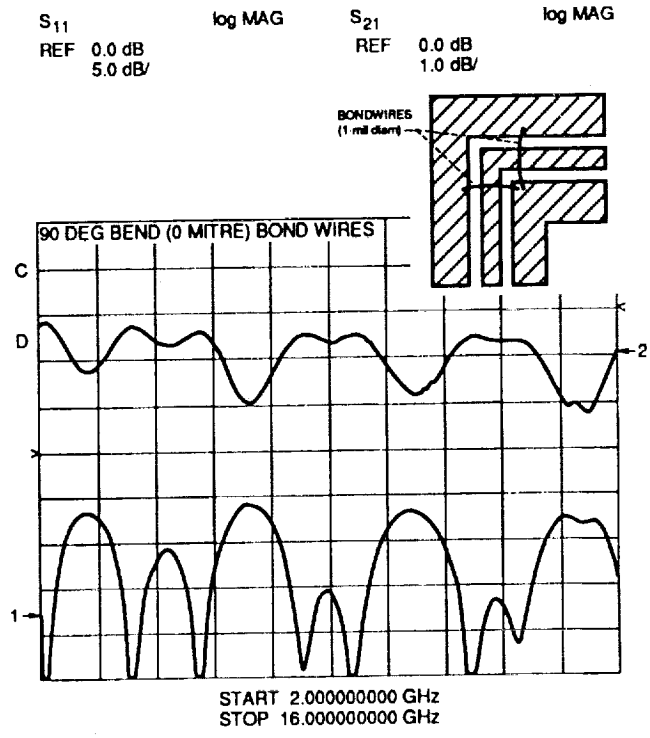

(b) Right angle bend with bond wires.

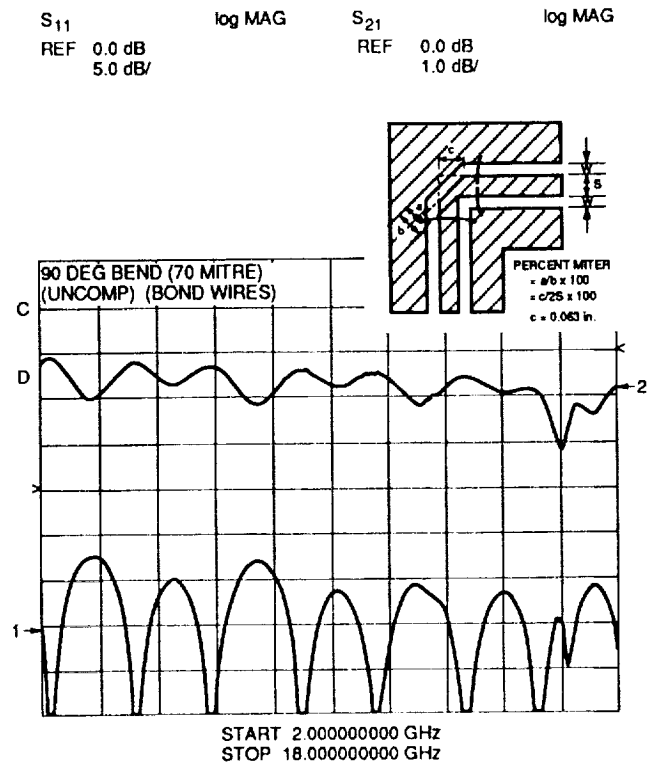

(c) Right angle bend with bond wires and 70 percent miter.

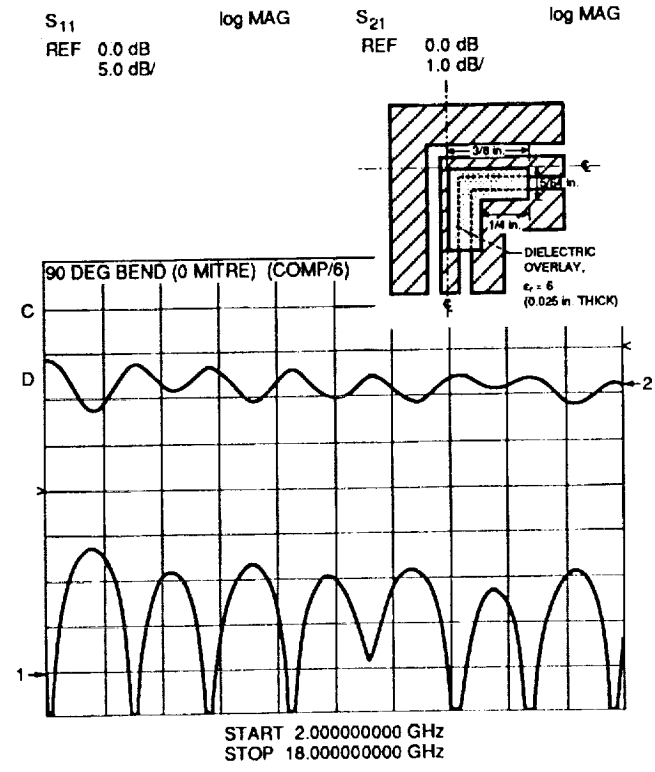

(d) Right angle bend with dielectric overlay.

Figure 9. - Measured RF characteristics for CCPW right angle bends with configurations inset.

The path length differences between the two slots at the CCPW right angle bend degrade the RF characteristics. Therefore, compensating techniques such as miters (ref. 9) and dielectric overlays (ref. 8) were investigated. Figure 9 illustrates a CCPW right angle bend and three possible compensating techniques and shows the measured insertion and return loss for each of the bends. The use of bond wires (fig. 9(b)), to hold the ground planes to the same potential at the element reference planes reduced the resonances in the insertion loss characteristics. To further reduce the path length difference, miters as large as 70 percent were tried. The miter and bond wires eliminated most of the resonances (fig. 9(c)). Finally, a dielectric overlay was placed on the inner slot (fig. 9(d)). The overlay slows the signal travelling along the inner slot so the signal emerging from each of the slots after the right angle bend is in phase. As shown in figure 9(d), the insertion loss and the return loss were less than 1.0 dB and greater than 10 dB, respectively, over a 2 to 18 GHz band. This agrees with the characteristics of a straight thru circuit.

CHANNELIZED CPW MATCHED T-JUNCTION

A pen-plot of a CCPW matched T-junction is shown in figure 10. At the T-junction, the characteristic impedance of the two side arms, Z1, are in parallel and the net impedance the input arm sees is Z1/2. Therefore, for impedance matching, the characteristic impedance, Z0, of the feed arm was set equal to Z1/2. To accomplish this, the output arms were tapered to an impedance of ≈135 Ω and the input arm was tapered to ≈67 Ω. At the coax-to-CCPW transitions, the CCPW impedance was ≈70 Ω to provide a good match to the 50 Ω coaxial line (ref. 8). When a shielding cover of height H = D was used, an insertion loss and return loss of 0.5 dB and 10 dB, respectively, were measured up to 12.5 GHz. A pair of bond wires were added to hold the ground planes at the junction at the same potential (refs. 10 and 11). This increased the bandwidth to 16.5 GHz. The measured insertion loss and return loss of the T-junction with bond wires are presented in figure 11. When the bond wires were used, the measured insertion loss and return loss was independent of the use of a cover.

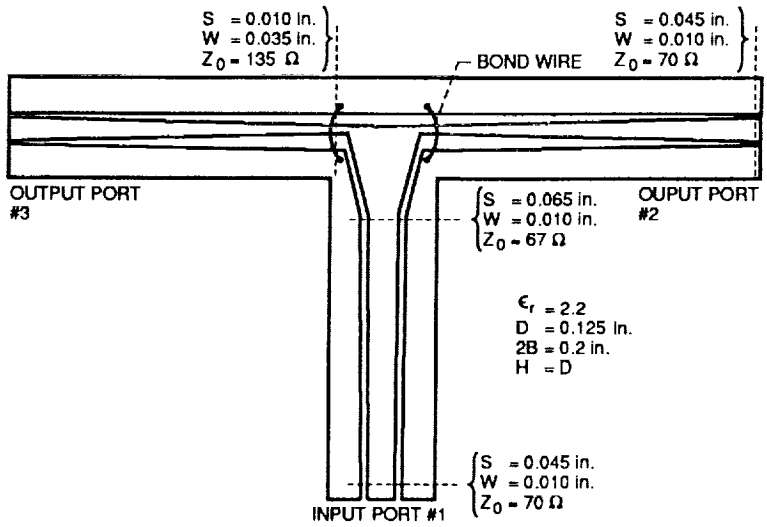

Figure 10. - Pen-plot of a CCPW matched T-junction.

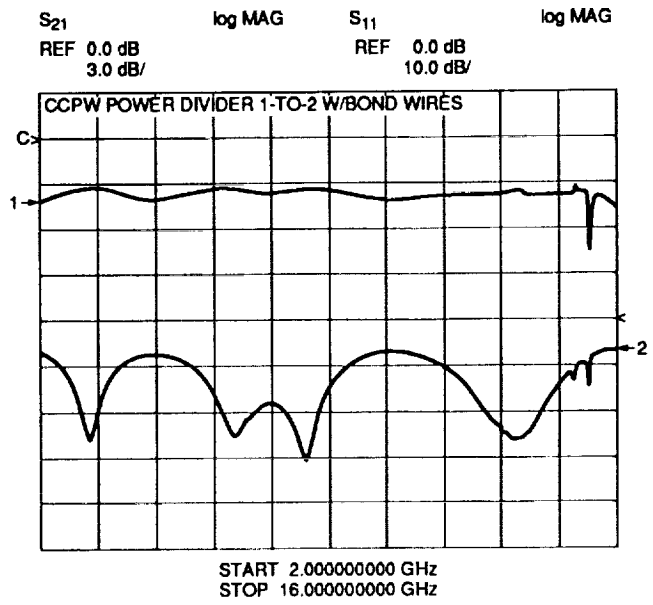

Figure 11. - Measured amplitude of the power coupled to one of the output ports and the return loss of the input port for a CCPW matched T-junction.

CHANNELIZED CPW MATCHED 1:3 JUNCTION

A pen-plot of a CCPW matched 1:3 junction is shown in figure 12. The output arms have been tapered to ≈135 Ω at the junction. The input arm was tapered to 45 Ω for impedance matching. When a shielding enclosure of height H = D was used, a return loss greater than 10 dB and low insertion loss was measured through 12.5 GHz. However, a maximum phase imbalance between ports 2 and 3 of ≈70° exists at 12.5 GHz.

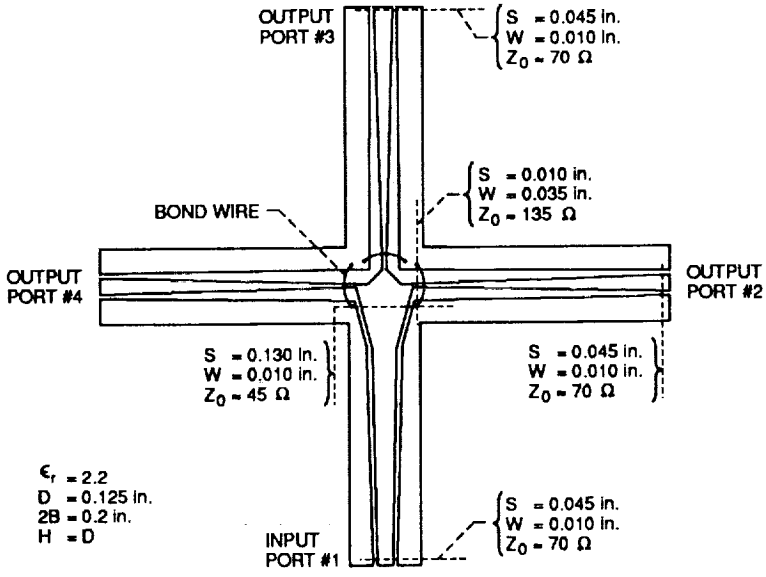

Figure 12. - Pen-plot of CCPW matched 1-to-3 junction.

The use of three bond wires as shown in figure 12 increased the bandwidth to 16.0 GHz. In addition, the bond wires reduced the phase imbalance between ports 2 and 3 by 20° at 12.5 GHz. The measured insertion loss and return loss of the three-way junction with bond wires are presented in figure 13. The average measured amplitude of -5 dB at the output ports agrees well with the expected -4.8 dB. There was negligible amplitude and phase imbalance between ports 2 and 4. A maximum of 1 dB of amplitude imbalance was measured between ports 2 and 3. The phase imbalance between ports 2 and 3 increased linearly from ≈0° at 2 GHz to 70° at 16 GHz. The use of a shielding enclosure with the bond wires did not result in any further improvement in the characteristics.

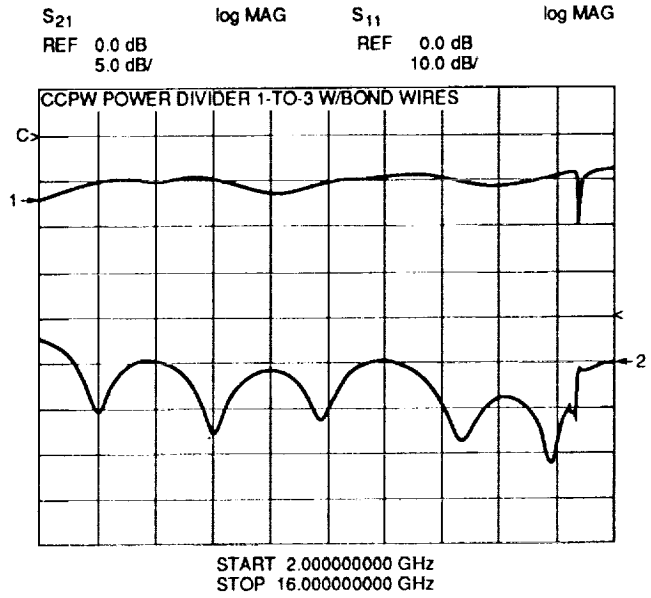

Figure 13. - Measured amplitude of the power coupled to one of the output ports and the return loss of the coaxial input port for a CCPW matched 1-to-3 junction.

COAX-to-CHANNELIZED CPW IN-PHASE N-WAY RADIAL POWER DIVIDER

A coax-to-CCPW in-phase, four-way radial power divider is shown in figure 14. The junction is formed by the intersection of four CCPW lines. Power is coupled to this junction from a coaxial cable whose outer conductor is slotted along the z direction to form four coupled transmission lines. The center pin of the coaxial line meets the intersecting CCPW center conductors while the four coupled outer conductors meet the CCPW ground planes. Therefore, the electric current at the open end of the coax is divided into the four CCPW lines as illustrated in figure 15. This arrangement has the advantage of holding the ground planes at the same potential and exciting the four CCPW lines in equal amplitude and phase without the need for bond wires. Each of the four CCPW lines, figure 16, has an impedance of 135 Ω at the junction. Therefore, the net impedance seen by the coaxial line is ≈34 Ω. A quarter wave coaxial dielectric transformer ($\varepsilon(r) = 4$) was used at the junction to match the 50 Ω coaxial line to the 34 Ω CCPW junction impedance. Each of the three pairs of slits in the ground plane of the CCPW acts as a stub and helps improve the CCPW to coaxial connector impedance match over the measured frequency range.

ORIGINAL PAGE
BLACK AND WHITE PHOTOGRAPH

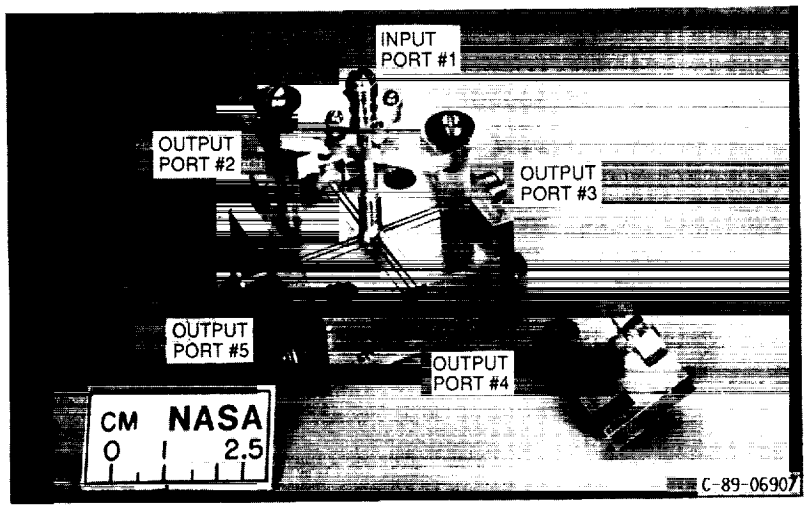

Figure 14. - Coax-to-CCPW in-phase, four-way, radial power divider.

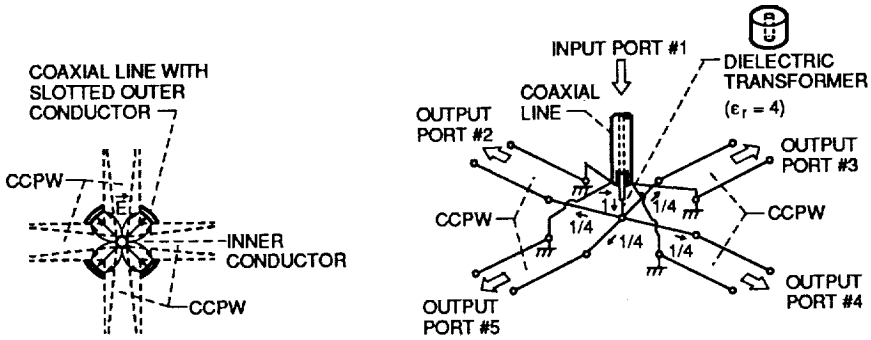

(a) Electric field (E) distribution at the end of the slotted coaxial line.

(b) Equivalent circuit of the junction showing the input RF current (I) being divided into the four ports.

Figure 15. - Coax-to-CCPW junction.

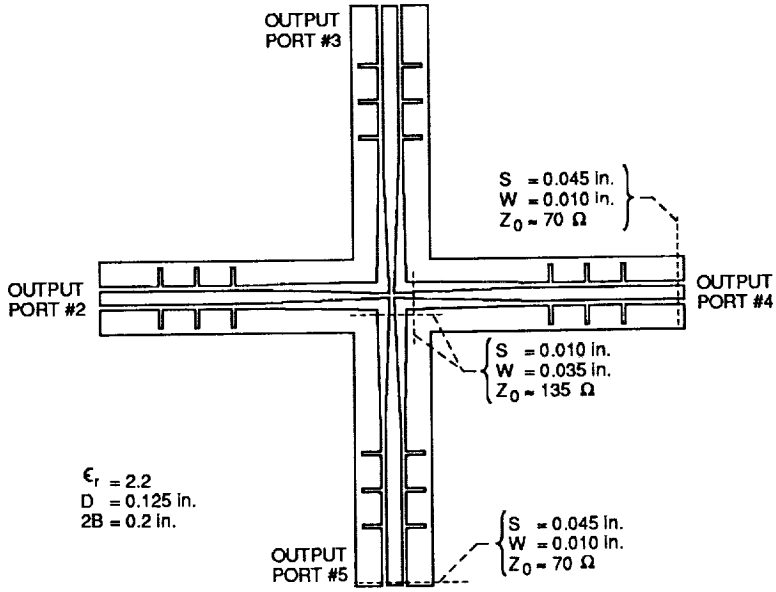

Figure 16. - Pen-plot of the coax-to-CCPW in-phase, four-way, radial power divider.

The measured amplitude of the power coupled to one of the output ports over an octave bandwidth is shown in figure 17 and is typical of the junction. The -6.5 dB measured amplitude at the output ports is in good agreement with the -6.0 dB expected for a 1:4 junction. The additional loss includes the CCPW to coaxial transformer and connector losses. Also superimposed on figure 18 is the return loss of the input port. Figure 18 is a measurement of the amplitude and phase balance for the four output ports; the amplitude and phase balance are within 0.5 dB and 5°, respectively. These values are a function of the mechanical structure itself since all of the ports are identical. The isolation between the ports is ≈10 dB.

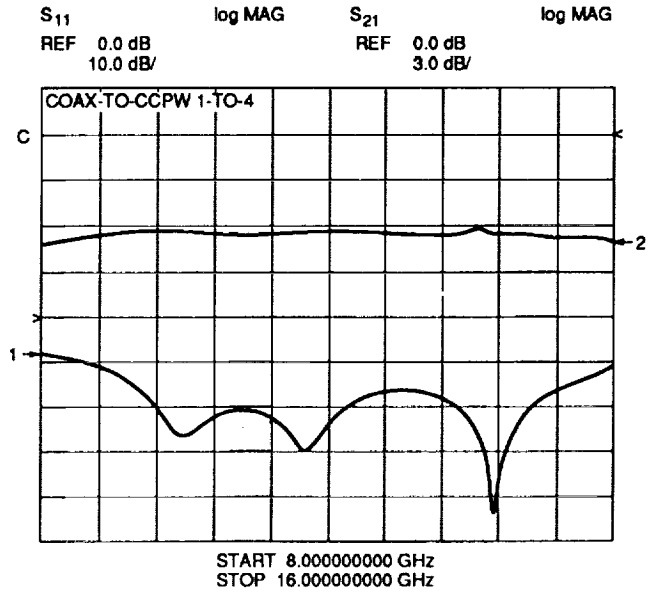

Figure 17. - Measured amplitude of the power coupled to one of the output ports and the return loss of the coaxial input port for a four-way radial power divider.

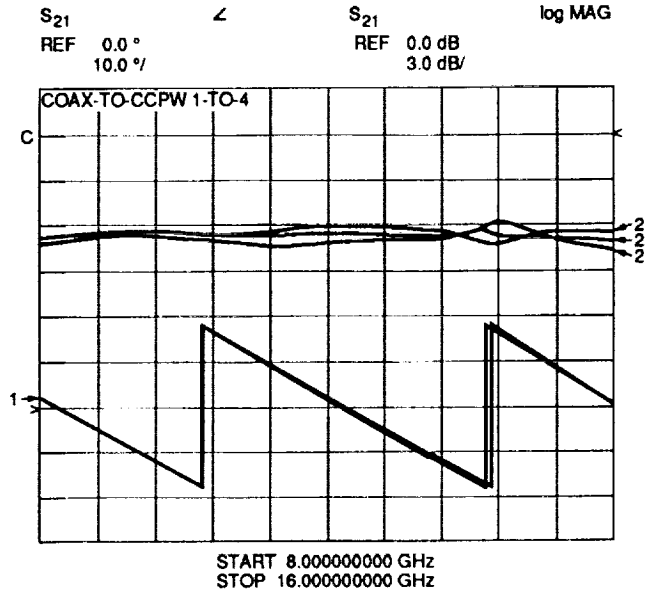

Figure 18. - Measured amplitude and phase balance for a coax-to-CCPW four-way power divider.

A coax-to-CCPW two-way radial power divider with the same basic structure as that described above was fabricated. The outer conductor of the coaxial line was slotted to form two coupled transmission lines. A dielectric transformer was not used with this structure. The measured amplitude at the output ports and the return loss at the coax input port are presented in figure 19. The amplitude imbalance for this circuit is less than 0.5 dB and the phase imbalance is less than 5°. Again, these values are dependent on the mechanical realization of the power divider.

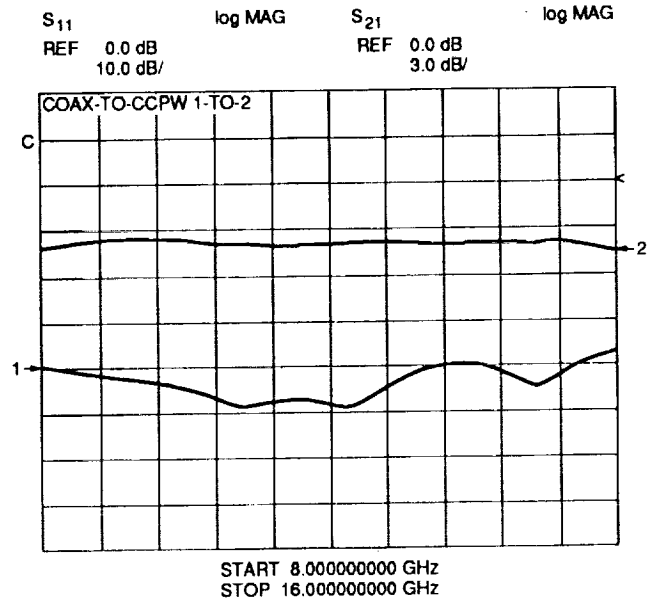

Figure 19. - Measured amplitude of the power coupled to one of the output ports and the return loss of the coaxial input port for a two-way radial power divider.

CONCLUSIONS

A new variant of CPW which has been termed CCPW has been demonstrated. The propagation characteristics of this structure show it to be useful for wide bandwidth, low loss microwave circuits where the favorable size advantage of CCPW over rectangular waveguide may be needed. Equivalent circuit model element values are presented for a CCPW open circuit and a CCPW right angle bend. A matched CCPW T-junction, a matched 1:3 junction, and a novel coax-to-CCPW in-phase, N-way, radial power divider are also demonstrated. These exhibit low loss and wide bandwidth and hence should facilitate the implementation of CCPW in microwave signal distribution networks such as in a phased array antenna system.

REFERENCES

1. Wen, C.P.: Coplanar Waveguide: A Surface Strip Transmission Line Suitable for Nonreciprocal Gyromagnetic Device Applications. IEEE Trans. Microwave Theory Tech., vol. MTT-17, no. 12, Dec. 1969, pp. 1087-1090.

2. Shih, Y.C.; and Itoh, T.: Analysis of Conductor-Backed Coplanar Waveguide. Electron. Lett., vol. 18, no. 12, June 10, 1982, pp. 538-540.

3. Richings, J.G.: An Accurate Experimental Method for Determining the Important Properties of Microstrip Transmission Lines. Marconi Rev., vol. 37, no. 195, 1974, pp. 209-216.

4. Stephenson, I.M.; and Easter, B.: Resonant Techniques for Establishing the Equivalent Circuits of Small Discontinuities in Microstrip. Electron. Lett., vol. 7, no. 19, Sept. 23, 1971, pp. 582-584.

5. Romanofsky, R.R.: Analytical and Experimental Procedures for Determining Propagation Characteristics of mm-Wave GaAs Microstrip Lines. NASA TP-2899, 1989.

6. Simons, R.N.: Suspended Coupled Slotline Using Double Layer Dielectric. IEEE Trans. Microwave Theory Tech., vol. MTT-29, no. 2, Feb. 1981, pp. 162-165.

7. Ghione, G.; and Naldi, C.: Parameters of Coplanar Waveguides with Lower Ground Plane. Electron. Lett., vol. 19, no. 18, Sept. 1, 1983, pp. 734-735.

8. Simons, R.N.; and Ponchak, G.E.: Modeling of Some Coplanar Waveguide Discontinuities. IEEE Trans. Microwave Theory Tech., vol. MTT 36, no. 12, Dec. 1988, pp. 1796-1803.

9. Douville, R.J.P.; and James, D.S.: Experimental Study of Symmetric Microstrip Bends and Their Compensation. IEEE Trans. Microwave Theory Tech., vol. MTT-26, no. 3, Mar. 1978, pp. 175-182.

10. Houdart, M.: Coplanar Lines: Application to Broadband Microwave Integrated Circuits. 6th European Microwave Conference, Microwave Exhibitions and Publishers Ltd., Sevenoaks, England, 1976, pp. 49-53.

11. Stegens, R.E.: Coplanar Waveguide FET Amplifiers for Satellite Communications Systems. Comsat Tech. Rev., vol. 9, no. 1, Spring 1979, pp. 255-267.

NASA Technical Memorandum 102522

Coplanar Waveguide Fed Phased Array Antenna

R.N. Simons
Sverdrup Technology, Inc.
NASA Lewis Research Center Group
Cleveland, Ohio

G.E. Ponchak and R.Q. Lee
National Aeronautics and Space Administration
Lewis Research Center
Cleveland, Ohio

N.S. Fernandez
University of Puerto Rico
Rio Piedras, Puerto Rico

Prepared for the
1990 IEEE AP-S International Symposium
and URSI Radio Science Meeting
Dallas, Texas, May 7–11, 1990

COPLANAR WAVEGUIDE FED PHASED ARRAY ANTENNA

R.N. Simons
Sverdrup Technology, Inc.
NASA Lewis Research Center Group
Cleveland, Ohio 44135

G.E. Ponchak and R.Q. Lee
National Aeronautics and Space Administration
Lewis Research Center
Cleveland, Ohio 44135

N.S. Fernandez*
University of Puerto Rico
Rio Piedras, Puerto Rico 00931

SUMMARY

A K-band four element linear phased array has been designed and tested. Coplanar waveguide (CPW) is used for the microwave distribution system. A CPW to twin strip transition is used to interface with the printed dipole antennas. MMIC phased shifters are used for phase control.

E-5327

INTRODUCTION

Coplanar waveguide (CPW) is a transmission line which consists of a center strip and a semi-infinite ground plane on either side of it (ref. 1). CPW is useful for integrating MMIC's together to form a microwave distribution network since the ground planes are readily accessible on the top side of the substrate. Grounded CPW (GCPW) is a variant of CPW which incorporates an additional ground plane on the back side of the substrate (ref. 2). This additional ground plane can serve as a heat sink and provide mechanical strength. In addition, this ground plane serves as a shield between stacked antennas boards to improve isolation.

Several CPW fed antennas have been reported in the literature. A GCPW fed coplanar stripline antenna constructed by widening the center strip of the GCPW to form a rectangular patch has been reported (ref. 3). This antenna produces a linearly-polarized pattern normal to the plane of the substrate. Coplanar waveguide fed slot antennas which are the complement to printed dipole antennas have also been reported (ref. 4). This antenna also radiates in a direction normal to the plane of the substrate. Although end-fire antennas are required for many large phased arrays, no CPW fed end-fire antennas have been reported yet in the literature.

*Summer Student Intern at Lewis Research Center.

In this paper we demonstrate a K-Band four element, printed dipole linear array which uses GCPW for the feed network and the integration of the MMIC phase shifters. This array radiates in the end fire direction and is suitable for large two-dimensional arrays.

CIRCUIT DESCRIPTION

The microwave distribution network and antennas is shown in figure 1. The microwave distribution network is fed by a single coaxial transmission line. The microwave signal is then split equally onto four GCPW transmission lines by three GCPW T-junctions. Wire bonds were used to tie the ground planes of the GCPW at the bends and T-junctions. The insertion loss for the one-to-four power divider is shown in figure 2. The MMIC phase shifters are DC isolated from the rest of the network by a pair of GCPW couplers. The couplers have been optimized to have a passband at the antenna operating frequency. The GCPW was tapered to provide a better match to the line width of the microstrip lines on the MMIC. The insertion loss for the two couplers with a GaAs 50 microstrip through connection in place of the phase shifters was 2.0 dB. The transition from the unbalanced GCPW to the balanced coplanar strip transmission line was made through a coplanar balun (ref. 5). The circuit was fabricated on 0.0625 in. thick CuFlon material.

The phase shifters shown in figure 3(a) were developed by Hughes Aircraft Corporation under contract to NASA (ref. 6). The phase shifters are reflection type and utilize a Lange coupler and two reverse biased varactor diodes to provide continuous 180° phase shift. The phase shifters were characterized individually before integration with the antenna network. By applying bias voltages from 0 to 4 V, 170° of phase shift was obtained as shown in figure 3(b) with an average insertion loss of 6.15 dB. Amplitude control can be added by the addition of MMIC amplifiers, variable attenuators, or switches.

ARRAY PERFORMANCE CHARACTERISTICS

The measured radiation pattern for a single GCPW fed printed dipole antenna is shown in figure 4(a). As expected, the pattern is broad due to the low gain of the antenna. The measured radiation pattern for the four element linear array is shown in figure 4(b). The pattern was measured with identical GaAs 50 Ω microstrip through lines in place of the phase shifters. The E-plane and H-plane patterns have 3-dB beam widths of 15° and 40°, respectively. The E-plane pattern has a shift in the main lobe which is probably due to path length differences in the feed network. The radiation pattern of the array with the MMIC phase shifters is in the process of being made.

CONCLUSIONS

A K-Band four element linear array of printed dipole antennas which demonstrates the advantages of CPW for MMIC integration and microwave signal distribution has been fabricated and tested. The radiation characteristics for the antenna is excellent.

REFERENCES

1. C.P. Wen, "Coplanar Waveguide: A Surface Strip Transmission Line Suitable for Nonreciprocal Gyromagnetic Device Applications," IEEE Trans. Microwave Theory Tech., vol. MTT-17, no. 12, pp. 1087-1090, 1969.

2. Y.C. Shih and T. Itoh, "Analysis of Conductor-Backed Coplanar Waveguide," Electron Lett., vol. 18, no. 12, pp. 538-540, 1982.

3. J.W. Greiser, "Coplanar Stripline Antenna," Microwave J., vol. 19, no. 10, pp. 47-49, 1976.

4. A. Nesic, "Slotted Antenna Array Excited by a Coplanar Waveguide," Electron. Lett., vol. 18, no. 6, pp. 275-276, 1982.

5. R.E. DeBrecht, "Coplanar Balun Circuits For GaAs FET High-Power Push-Pull Amplifiers," IEEE G-MTT International Microwave Symposium Digest, New York: IEEE, pp. 309-311, 1973.

6. L.C.T. Liu, et al., "A 30-GHz Monolithic Receiver," IEEE Trans. Microwave Theory Tech., vol. MTT-34, no. 12, pp. 1548-1552, 1986.

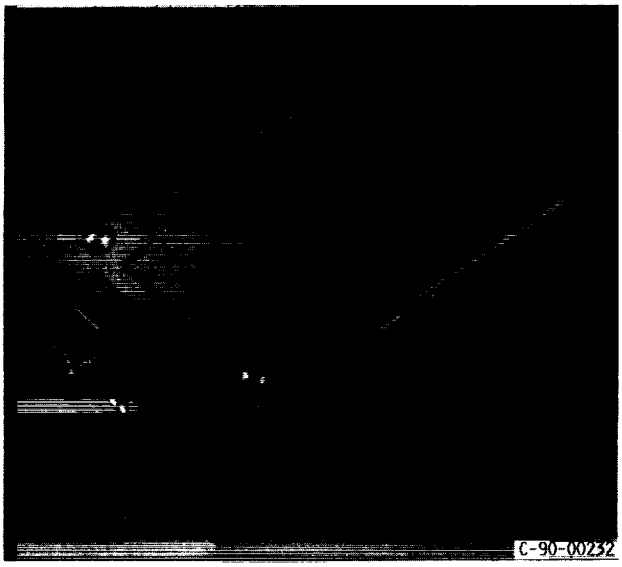

FIGURE 1. - GCPW FED FOUR ELEMENT PRINTED DIPOLE PHASED ARRAY.

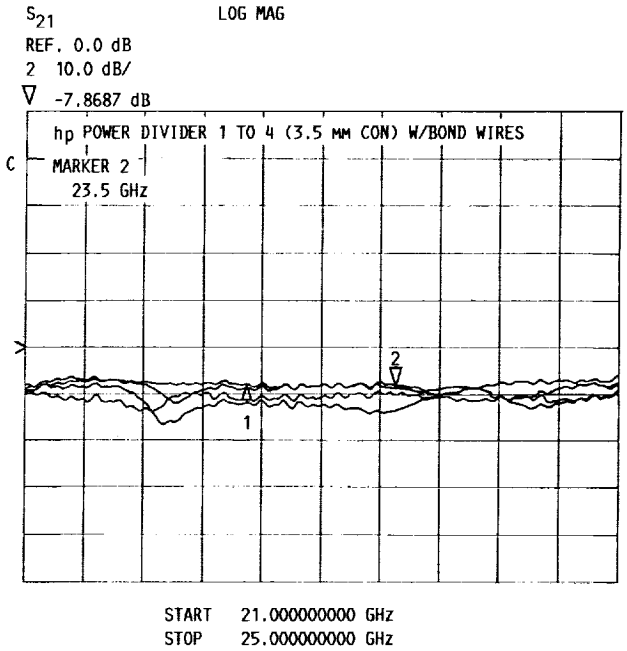

FIGURE 2. - GCPW ONE-TO-FOUR POWER DIVIDER AMPLITUDE CHARACTERISTICS.

(a) PHASE SHIFTER CONFIGURATION.

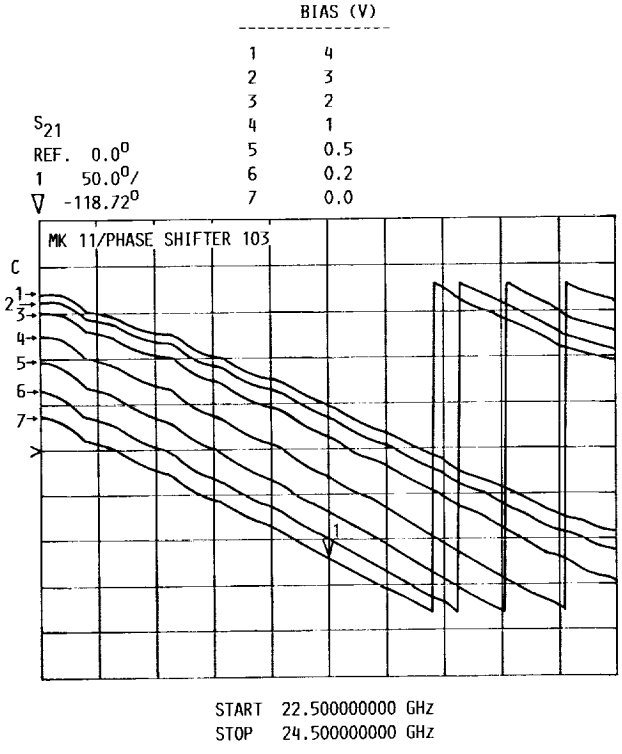

(b) MEASURED PHASE SHIFT AS A FUNCTION OF THE FREQUENCY FOR DIFFERENT VOLTAGES.

FIGURE 3. - GaAs MMIC PHASE SHIFTER.

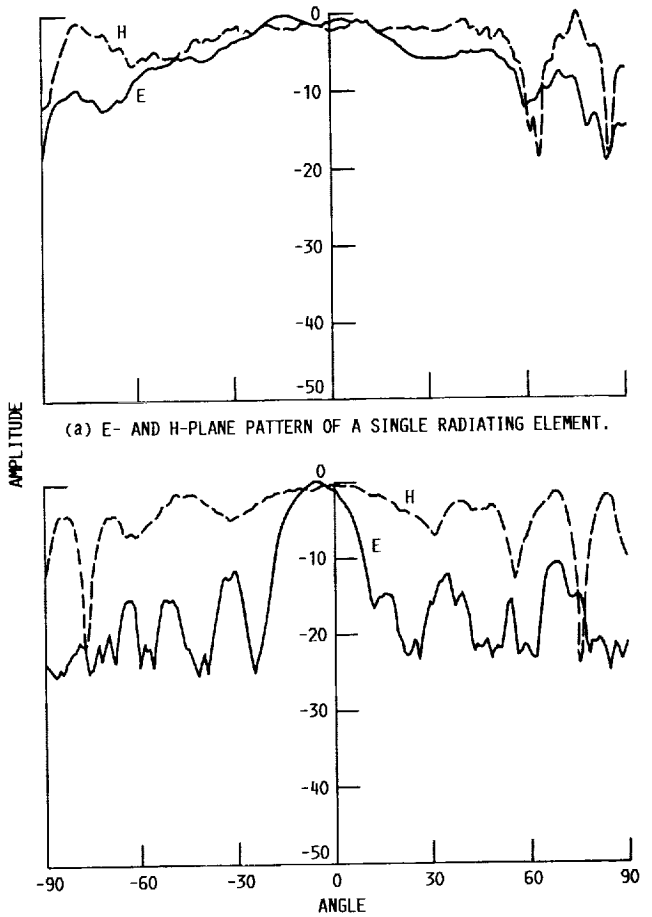

(a) E- AND H-PLANE PATTERN OF A SINGLE RADIATING ELEMENT.

(b) E- AND H-PLANE PATTERN OF THE FOUR ELEMENT ARRAY AT 21.3 GHz.

FIGURE 4. - MEASURED RADIATION PATTERN.

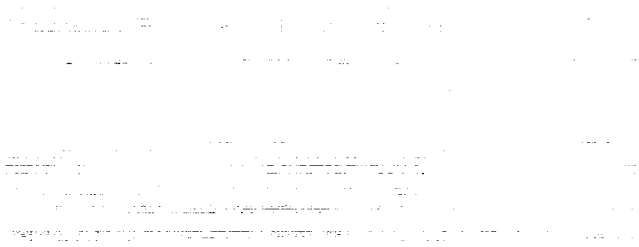

III. SUPERCONDUCTING FILMS

Microwave Conductivity of Laser Ablated $YBa_2Cu_3O_{7-\delta}$ Superconducting Films and Its Relation to Microstrip Transmission Line Performance

K.B. Bhasin, J.D. Warner
National Aeronautics and Space Administration
Lewis Research Center
Cleveland, Ohio

C.M. Chorey
Sverdrup Technology, Inc.
Lewis Research Center Group
Brook Park, Ohio

B.T. Ebihara, R.R. Romanofsky, and V.O. Heinen
National Aeronautics and Space Administration
Lewis Research Center
Cleveland, Ohio

F.A. Miranda and W.L. Gordon
Case Western Reserve University
Cleveland, Ohio

Preprint for the Advances in Material Science and Applications of High Temperature Superconductors sponsored by NASA Goddard Space Flight Center Washington, D.C., April 2-6, 1990

NASA

MICROWAVE CONDUCTIVITY OF LASER ABLATED $YBa_2Cu_3O_{7-\delta}$ SUPERCONDUCTING FILMS AND ITS RELATION TO MICROSTRIP TRANSMISSION LINE PERFORMANCE

K.B. Bhasin,* J.D. Warner,* C.M. Chorey,† B.T. Ebihara,* R.R. Romanofsky,* V.O. Heinen,* F.A. Miranda‡, and W.L. Gordon‡

*NASA Lewis Research Center
Cleveland, Ohio 44135

†Sverdrup Technology, Inc., Lewis Research Center Group
Brook Park, Ohio 44142

‡Department of Physics, Case Western Reserve University
Cleveland, Ohio 44106

ABSTRACT

We report on the values of the microwave conductivity in the normal (σ_N) and superconducting ($\sigma^*=\sigma_1-j\sigma_2$) states of two laser ablated $YBa_2Cu_3O_{7-\delta}$ thin films at 35 GHz, in the temperature range from 20 to 300 K. The films (0.7 and 0.4 μm) were deposited on $LaAlO_3$ by laser ablation. The conductivity was obtained from the microwave power transmitted through the films and assuming a two-fluid model. Values of $\sigma_N \sim 2.3 \times 10^5$ S/m at room temperature for both films, and of $\sigma_1 \sim 6.3 \times 10^5$ and 4.6×10^5 S/m at temperatures around 80 K were obtained for the 0.7 and 0.4 μm films respectively. For σ_2 values of 4.9×10^6 and 5.4×10^6 S/m were obtained for the 0.7 and 0.4 μm films at 80 K. The expected conductor losses and Q-factor of a superconducting ring resonator were calculated using these conductivity values. The theoretical values were then compared with the experimental results obtained for a resonator fabricated from one of these films.

The discovery of high transition temperature (T_c) superconductors has raised the possibility of a new class of microwave and millimeter wave devices operating at temperatures considerably higher than liquid helium temperatures. Therefore, materials properties such as microwave conductivity (σ), critical current density (J_c), microwave surface resistance (R_s), transport anisotropies, thermal expansion, and others have to be well characterized and understood. To date, measurements of R_s at microwave and millimeter wave frequencies and of J_c of $YBa_2Cu_3O_{7-\delta}$ superconducting oxides have been very abundant.[1-3] Nevertheless, reports on the microwave conductivity of these new oxides have been rare.[4,5] The need for more data on the microwave conductivity of these oxides arises from the fact that knowledge of this parameter provides a way to calculate other relevant properties such as the normal skin depth (δ_n) and the magnetic penetration depth in the superconducting state (λ_s). From the practical application point of view, it provides valuable aid for the design of microwave devices and circuits, based on superconducting microstrip lines.[6,7]

In this paper we report on the microwave conductivity of laser ablated $YBa_2Cu_3O_{7-\delta}$ superconducting thin films at 35 GHz in the temperature range from 20 to 300 K. The values of the conductivities were obtained from the microwave power transmitted through the film, assuming a two-fluid model. The expected conductor losses and Q-factor of a superconducting ring resonator were calculated using

these conductivity values. The theoretical values were then compared with the experimental results obtained for a resonator fabricated from one of these films.

The pulsed laser ablation technique is similar to that reported by other researchers.[8,9] The deposition was performed at a substrate temperature of 750° C at an ambient oxygen pressure of 170 mtorr. The laser wavelength was 248 nm, the pulse length and rate were 20 to 30 ns and 4 pps* respectively. During this process the distance between the target and the sample was kept at 7.5 cm and the laser fluence on the target was maintained at 2.0 J/cm^2 per pulse. The laser beam was continually scanned 1 cm across the target using an external lens on a translator. When the deposition was finished, the oxygen pressure was raised to 1 atm and the temperature was lowered to 450° C at a rate of 2° C/min. The temperature was held at 450° C for two hrs before it was lowered to 250° C at the same rate already mentioned. Finally, the heater power was turned off and the sample was allowed to cool to 40° C or less before it was removed from the chamber. This deposition process is explained in more detail in reference 10.

Two $YBa_2Cu_3O_{7-\delta}$ superconducting thin films, deposited by laser ablation on $LaAlO_3$, have been considered in this study. The films' thicknesses were 0.7 and 0.4 μm respectively. $LaAlO_3$ is a convenient substrate because of its perovskite crystal structure and its lattice constant of a=3.792 Å which match very well with the lattice constant of the $YBa_2Cu_3O_{7-\delta}$ superconducting oxide. Also, its low dielectric constant (~22) makes it suitable for microwave device applications. The films were analyzed by X-ray diffraction, dc resistance versus temperature measurements and scanning electron microscopy (SEM). Transitions temperatures (T_c, R=0) of 89.7 and 86.0 K were measured for the 0.7 and 0.4 μm thin films respectively. The dc resistance versus temperature curves are shown in fig.1. The X-ray diffraction pattern revealed that both films are single phased with a strong c-axis orientation. Both films exhibit a very smooth surface as observed from scanning electron micrographs. A grain size of ~¼ μm was observed for both films.

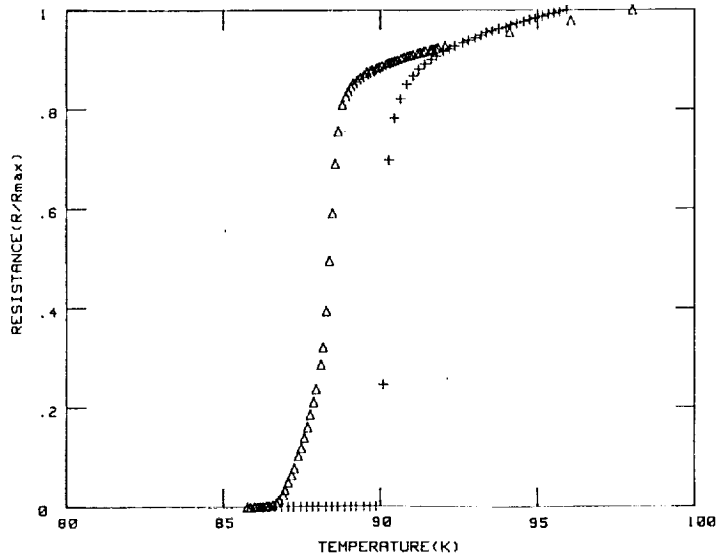

FIGURE 1. dc resistance versus temperature of 0.7 μm (+) and 0.4 μm (Δ) laser ablated $YBa_2Cu_3O_{7-\delta}$ thin films on $LaAlO_3$.

*Pulses per second.

The power transmission measurements were performed using an HP-8510 network analyzer connected to a helium gas closed cycle refrigerator by Ka-band (26.5 to 40.0 GHz) waveguides. All the measurements were taken under vacuum ($<10^{-3}$ torr) in a custom designed vacuum chamber. Inside the vacuum chamber the sample was clamped between two waveguide flanges mounted on top of the cold finger of the refrigerator. The waveguides were made of stainless steel to minimize heat conduction from the external waveguide arrangement and their inner surfaces were gold-plated to reduce microwave energy losses. Vacuum was maintained at the waveguide feedthroughs by means of 'O' rings and mica sealing windows. The temperature of the sample was monitored using silicon diode sensors mounted on the waveguide flanges supporting the sample. All the measurements were taken during sample cooling.

The measured temperature dependence of the transmitted power through the sample for both films under consideration is shown in fig.2 . Note that for the 0.7 μm film, both the onset temperature for the transition from the normal to the superconducting state (~91 K) and the transition temperature T_c (89.7 K), are clearly observed in this measurement. For the thinner film a sharp drop in transmitted power is observed below the onset temperature, with an attenuation of approximately 20 dB at temperatures around 80 K. The most relevant feature of the power versus temperature curve for this film is the sudden increase in transmitted power at temperatures below 80 K. This feature is an indication of the formation of a leakage source (micro-crack or pinhole) which broadens as the temperature decreases allowing more power to leak through the film. At temperatures below 50 K the amount of power leaking through the film reaches a constant value suggesting no significant variation of the leakage sources as a function of temperature in this temperature region.

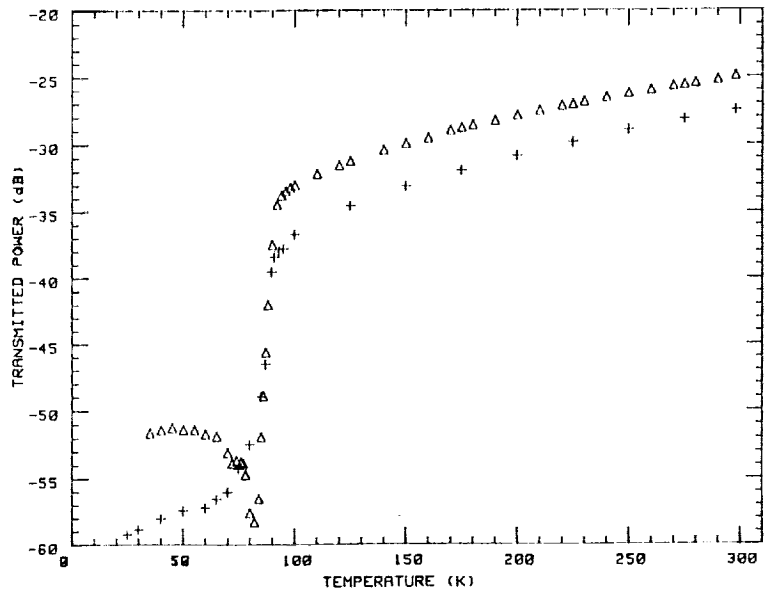

FIGURE 2. Transmitted power versus temperature of 0.7 μm (+) and a 0.4 μm (Δ) laser ablated $YBa_2Cu_3O_{7-\delta}$ thin films on $LaAlO_3$ at 35 GHz.

The normal state microwave conductivity, σ_N, was obtained from the power transmitted through the sample in the normal state, P_N, according to the expression[5]

$$\sigma_N=(-RP_N + [(RP_N)^2-4GP_N(HP_N-8n^2)]^{\frac{1}{2}})/2GP_NdZ_c \quad (1)$$

where

$$G=(n^2+1)+(n^2-1)\cos(2k\ell) \quad (1.a)$$
$$R=2(3n^2+1)+2(n^2-1)\cos(2k\ell) \quad (1.b)$$
$$H=n^4+6n^2+1-(n^2-1)^2\cos(2k\ell) \quad (1.c)$$

with Z_c the characteristic impedance of the waveguide, d the film thickness, ℓ and n the substrate thickness and the index of refraction respectively, and k the wave number. At temperatures below the beginning of the transition, the microwave conductivity takes the form $\sigma^*=\sigma_1-j\sigma_2$, where σ_1 is the conductivity due to the remaining normal electrons and σ_2 is the conductivity due to the superconducting electron pairs. We have calculated σ_1 by using $\sigma_1=\sigma_N(T/T_c)^4$, as defined under the two-fluid model approximation. Values of σ_2 were obtained using the relation[5]

$$\sigma_2/\sigma_c= -\beta/(2\sigma_cdZ_c) + \{[(\beta/2)^2-\gamma]/(\sigma_cdZ_c)^2 -\alpha\sigma_1/\sigma^2dZ_c -(\sigma_1/\sigma_c)^2 +\ldots \ldots (P_c/P_s)[1+\alpha/\sigma_cdZ_c + \gamma/(\sigma_cdZ_c)^2\}^{\frac{1}{2}} \quad (2)$$

with P_s the power transmitted through the film for $T<T_c$, σ_c and P_c are the conductivity and transmitted power respectively at $T=T_c$, $\alpha=R/G$, $\gamma=H/G$ and $\beta=[-2n(n^2-1)\sin(2k\ell)]/G$.

Figure 3 shows the temperature dependence of σ_r ($\sigma_r=\sigma_N$ for $T>T_c$ and $\sigma_r=\sigma_1$ for $T<T_c$) for the samples under study. The conductivities (~2.3 X 10^5 S/m) at room temperature are in close agreement for the two films considered. These values also compare favorably with reported values for the dc conductivity in this type of film.[11] Hence, using the value of σ_N we found a typical resistivity, ρ, of about 435 $\mu\Omega$-cm at room temperature and of 133 and 160 $\mu\Omega$-cm at temperatures around 100 K, for the 0.7 and 0.4 μm films respectively. These resistivity values are on average a factor of 1.5 greater than the values for ρ (ρ~290 $\mu\Omega$-cm at 300 K and ρ~95 $\mu\Omega$-cm at 100 K) obtained from surface resistance (R_s) measurements in strongly c-axis oriented $YBa_2Cu_3O_{7-\delta}$ thin films on $SrTiO_3$ as reported by Klein, et al.[12] The normal conductivity of both films exhibit a metallic behavior with decreasing temperature, reaching values of ~7.7 X 10^5 S/m for the thicker film and of ~6.3 X 10^5 S/m for the thinner one, at the onset temperature. Below T_c, the values of σ_1 were obtained using the value of the conductivity at the onset temperature in the expression $\sigma_1=\sigma_N(T/T_c)^4$. Values for σ_1 of ~6.3 X 10^5 and 4.6 X 10^5 S/m were obtained at 85 K for the 0.7 μm and 0.4 μm films respectively. At temperatures around 50 K and below the values for σ_1 for the 0.7 μm film has decreased by one order of magnitude. Because the 0.4 μm film exhibited leakage of microwave power below 80 K, no data are shown below this temperature.

Figure 4 shows the imaginary part of σ^* for both films. For the 0.7 μm film, values for σ_2 of ~4.9 X 10^6 and 7.0 X 10^6 S/m were obtained at temperatures around 80 and 50 K respectively. These values are greater than those obtained for $YBa_2Cu_3O_{7-\delta}$ laser ablated films deposited on MgO and ZrO_2.[5] Due to the leakage sources formed in the 0.4 μm film, we were unable to obtain values of σ_2 at

temperatures below 80 K. A value of 3.5 X 10^6 S/m was obtained just below the onset temperature (~92 K) and of 5.4 X 10^6 S/m at 85 K. Note that the increase of σ_2 with decreasing temperature corresponds to an increase in electron pairs which implies a reduction of the normal carrier density.

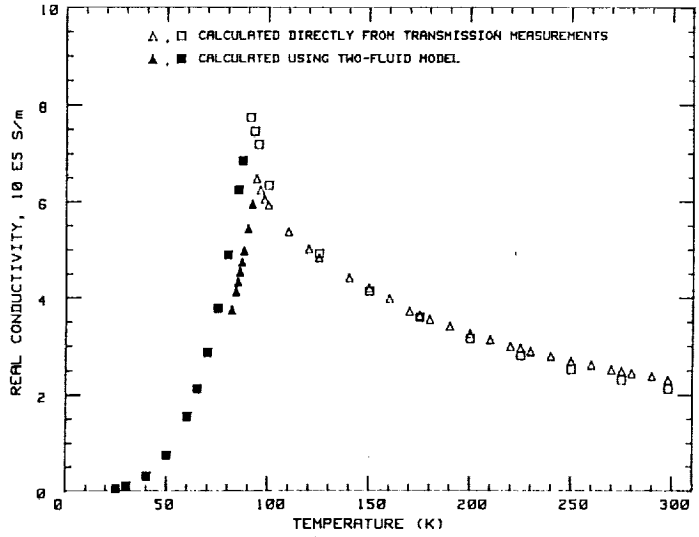

FIGURE 3. Real part of the conductivity, σ_r, versus temperature for 0.7 μm (□) and 0.4 μm (Δ) laser ablated $YBa_2Cu_3O_{7-\delta}$ thin films on $LaAlO_3$ at 35 GHz; $\sigma_r=\sigma_N$ for $T>T_c$ and $\sigma_r=\sigma_1$ for $T<T_c$. Open symbols represent values of the conductivity calculated directly from power transmission measurements and filled symbols represent values of the conductivity calculated using the two-fluid model.

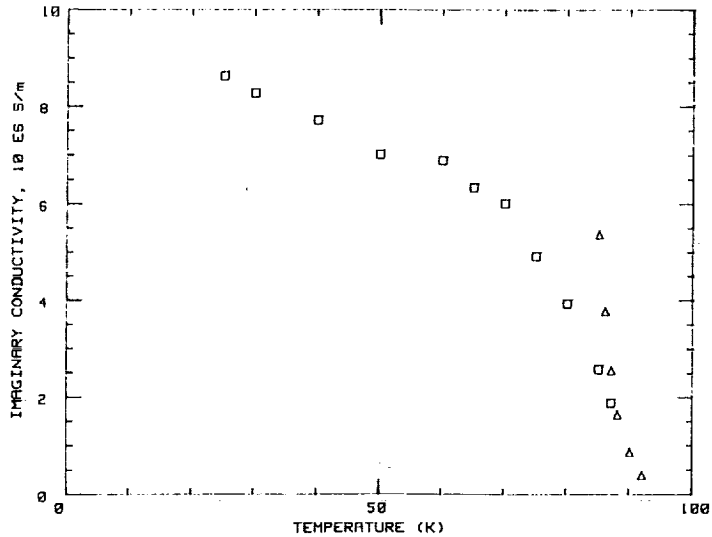

FIGURE 4. Imaginary part of the conductivity, σ_2, versus temperature for 0.7 μm (□) and 0.4 μm (Δ) laser ablated $YBa_2Cu_3O_{7-\delta}$ thin films on LaAlO3 at 35 GHz.

The values of σ_1 and σ_2 have been used to estimate values for the magnetic penetration depth λ and the surface resistance R_s.[13] Values of λ_o=0.67 μm and R_s~9mΩ at 77 K were obtained. These values are in close agreement with those obtained by other researchers.[12]

The conductivity values have been used to calculate the Q-factor of a ring resonator, which has a superconducting strip and a normal conducting ground plane. This resonator is shown in figure 5 and consists of a microstrip ring with a circumference that is three wavelengths in length at the design frequency of 35 GHz. Straight lengths of superconducting strip provide input to the ring with coupling achieved by small capacitive gaps. The substrate is 10 milli-inch thick lanthanum aluminate; and the characteristic impedance of the line is 45 ohms.

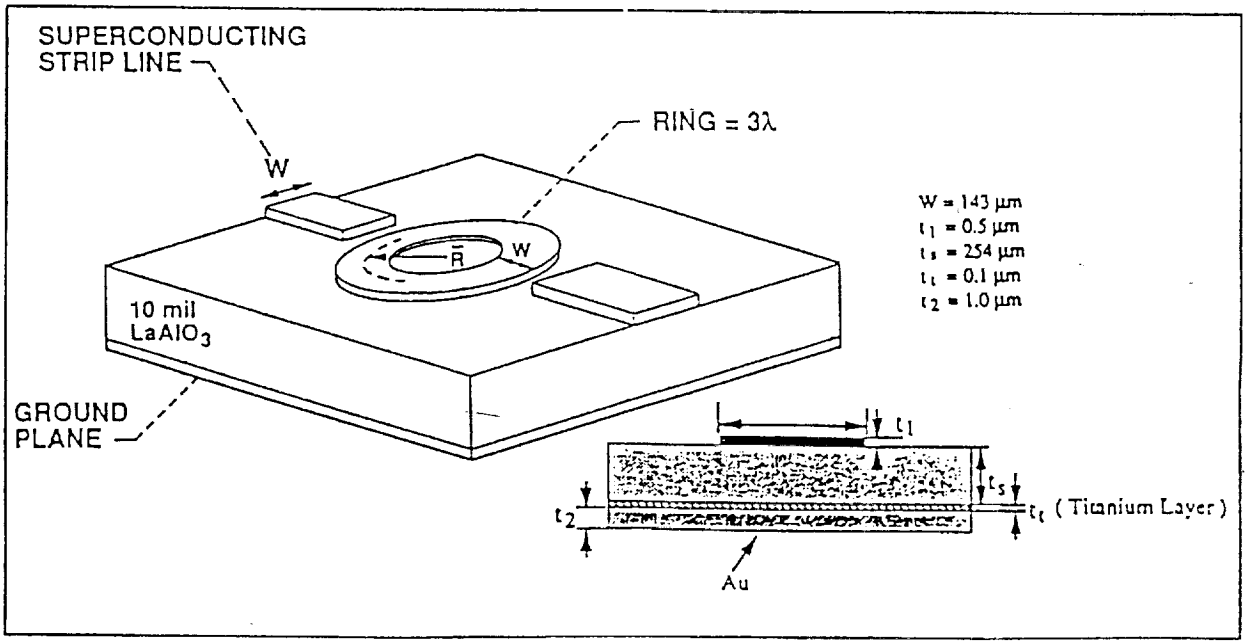

FIGURE 5. 35 GHz ring resonator microstrip transmission line circuit.

The "Q" of the ring is determined by two major loss mechanisms, 1) dielectric loss in the substrate and 2) resistive losses in the conductors. Radiation loss is assumed to be negligible in this case since the resonator, when being measured experimentally, is shielded by a section of waveguide below cutoff which acts to suppress radiation by the circuit. Dielectric losses can be calculated using:

$$\alpha_d = 3.15\ (q^*\epsilon/\epsilon_{eff})\ (\tan\delta/\lambda g)\quad \text{Nepers/m} \qquad (3)$$

where α_d[14] is the attenuation constant due to dielectric loss, 'q' is a geometrical 'filling factor', ϵ and ϵ_{eff} are the static and effective dielectric constants, $\tan\delta$ is the dielectric loss tangent and λ_g is the transmission line wavelength. In these calculations we have used a value of 5.8×10^{-4} for $\tan\delta$[15] but it should be noted that authoritative values for the loss tangent have not been established.

The conductor losses were calculated by the Phenomenological Loss Equivalence Method (PEM), an analytical solution for loss in microstrip lines that accounts for thin conductors. The attenuation due to the loss in the conductors is given by :

$$\alpha_c = Z_{ri}/(2*Z_c) \quad \text{Nepers/m} \tag{4}$$

where Z_{ri} is the real part of the internal impedance of the strip and ground plane and Z_c is the characteristic impedance of the line. The internal impedance (Z_i) is obtained through the PEM where:

$$Z_{ix} = Z_{sx} * G_x * \coth(Z_{sx} * \sigma_x * G_x * A) \tag{5}$$

G_x is a geometrical factor, A the cross sectional area of the strip, Z_{sx} is the surface impedance and σ_x the conductivity of the conductor material of the strip or ground plane (x denotes different values for strip and ground plane). The σ values are obtained from the transmission data and the surface impedance is calculated from them. The "Q" of the ring is calculated as:

$$\frac{1}{Q} = \frac{2(\alpha c + \alpha d)}{\beta} \tag{6}$$

where β is the propagation constant of the line.

Using values of the conductivity obtained form the .7μm film and the tanδ as noted above, the "Q" values were calculated and compared to results obtained from a resonator made from a film fabricated under similar conditions (figure 6). Also shown are the measured "Q" values for a resonator with a normal metal (gold) strip and ground plane. While the superconducting strip performs better than the normal metal, the measured "Q" values do not follow those predicted by the calculations using the transmission conductivity values.

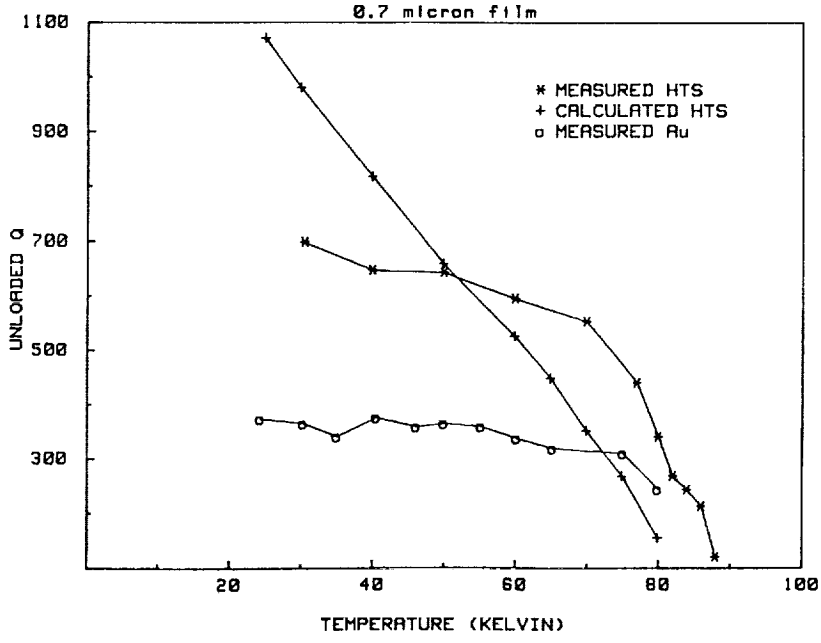

FIGURE 6. Measured and calculated values of unloaded Q for superconducting and normal resonators.

In summary, we have obtained the microwave conductivity at 35 GHz of laser ablated $YBa_2Cu_3O_{7-\delta}$ thin films in the temperature range from 20 to 300 K. The conductivity values at room temperature are in close agreement with dc values reported for the same type of material. Comparing the values for σ_1 and σ_2 for both films with those previously reported for laser ablated $YBa_2Cu_3O_{7-\delta}$ thin films on MgO and ZrO_2 suggest that $LaAlO_3$ is a superior substrate for microwave applications. From these conductivity values, values for the zero-temperature magnetic penetration depth λ_o and the surface resistance R_s, fundamental in the design of microwave devices and circuits, have been obtained. We have used the conductivity values to obtain conductor losses and Q-factors of a microwave transmission line. However, predicted and experimentally observed values are not in good agreement. Further work is needed in developing an accurate correlation between measured conductivity values and microstrip performance.

ACKNOWLEDGEMENT

We would like to gratefully acknowledge Mr. K. S. Kong and Prof. T. Itoh of the University of Texas at Austin for their calculation of the Q values of the ring resonator.

REFERENCES

1. J. P. Carini, A. M. Awasthi, W. Beyermann, G. Gruner, T. Hylton, K. Char, M. R. Beasley and A. Kapitulnik, "Millimeter-wave surface resistance measurements in highly oriented $YBa_2Cu_3O_{7-\delta}$ thin films", Phys. Rev. B. 37 (16), 9726-9729 (1988).

2. N. Klein, G. Muller, H. Piel, B. Roas, L. Shultz, U. Klein and M. Peiniger, "Millimeter wave surface resistance of epitaxially grown $YBa_2Cu_3O_{7-x}$ thin films", Appl. Phys. Lett. 54 (8), 757-759 (1989).

3. H. Kupfer, C. Keller, K. Salama and V. Selvamanickam, "Inductive current measurements in an oriented grained $YBa_2Cu_3O_x$ superconductor", Appl. Phys. Lett. 55 (18), 1903-1905 (1989).

4. P. H. Kobrin, W. Ho, W. F. Hall, P. J. Hood and A. B. Harker, Presented at the M^2S-HTSC Conference, Stanford Ca., July 24-28, 1989. To be published in Physica C.

5. F. A. Miranda, W. L. Gordon, K. B. Bhasin, V. O. Heinen, J. D. Warner and G. J. Valco, NASA TM-102345 (1989) and to be published in "Superconductivity and Applications", Plenum Press Publishing Corporation (1990).

6. F. Huret, D. Kinowski, P. Pribetich and P. Kennis, "Spectral domain analysis of a microstrip thin superconducting line laid on GaAs substrate", Microwave and Optical Tech. Lett. 2 (6), 205-208 (1989).

7. K. B. Bhasin, C. M. Chorey, J. D. Warner, R. R. Romanofsky, V. O. Heinen, K. S. Kong, H. Y. Lee and T. Itoh, NASA TM-102526 (1990).

8. A. Inam, M. S. Hedge, X. D. Wu, T. Venkatesan, P. England, P. F. Miceli, E. W. Chase, C. C. Chang, J. M. Tarascon and J. B. Watchman, "As-deposited high

T_c and J_c superconducting thin films made at low temperatures", Appl. Phys. Lett. 53 (10), 908-910 (1988).

9. B. Roas, L. Schultz, and G. Endres, "Epitaxial growth of $YBa_2Cu_3O_{7-x}$ thin films by a laser evaporation process", Appl. Phys. Lett. 53 (16), 1557-1559 (1988).

10. J. D. Warner, J. E. Meola and K. A. Jenkins, NASA TM-102350 (1989).

11. R. T. Collins, Z. Schlesinger, R. H. Koch, R. B. Laibowitz, T. S. Poaskett, P. Freitas, W. J. Gallacher, R. L. Sandstrom and T. R. Dinger, "Comparative study of superconducting energy gaps in oriented films and polycrystalline bulk samples of Y-Ba-Cu-O", Phys. Rev. Lett. 59 (6), 704-707 (1987).

12. N. Klein, G. Muller, S. Orbach, H. Piel, H. Chaloupka, B. Roas, L. Schultz, U. Klein and M. Peiniger, "Millimeter wave surface resistance and London penetration depth of epitaxially grown $YBa_2Cu_3O_{7-x}$ thin films", Physica C 162-164, 1549-1550 (1989).

13. F. A. Miranda, W. L. Gordon, K. B. Bhasin, J. D. Warner and V. O. Heinen, "Microwave Conductivity of Laser Ablated $YBa_2Cu_3O_{7-\delta}$ Superconducting Thin Film on $LaAlO_3$ Substrate", submitted to Appl. Phys. Lett.

14. R. A. Pucal, D. J. Masse, C. P. Hartwig, "Losses in Microstrip", IEEE Trans. Microwave Theory and Tech., vol. MTT-16, no. 6, 342-350 (1968).

15. R.W. Simon, C. E. Platt, A. E. Lee, G. S. Lee, K. P. Daly, M. S. Wire, J. A. Luine and M. Urbanik, "Low -loss substrate for epitaxial growth of high-temperature superconductor thin films", Appl. Phys. Lett., vol. 53 (26) 2667-2679 (1988).

16. H. Y. Lee and T. Itoh, "Phenomenological Loss Equivalence Method for Planar Quasi-TEM Transmission Line with a Thin Normal Conductor or Superconductor," IEEE Trans. Microwave Theory and Tech., Vol. MTT-37, no. 12, 1904-1909 (1989).

NASA Technical Memorandum 102345

Millimeter Wave Transmission Studies of $YBa_2Cu_3O_{7-\delta}$ Thin Films in the 26.5 to 40.0 GHz Frequency Range

F.A. Miranda and W.L. Gordon
Case Western Reserve University
Cleveland, Ohio

K.B. Bhasin, V.O. Heinen,
and J.D. Warner
Lewis Research Center
Cleveland, Ohio

and

G.J. Valco
The Ohio State University
Columbus, Ohio

Corrected Copy

Prepared for the
Third Annual Conference on Superconductivity and Applications
sponsored by The New York State Institute on Superconductivity
Buffalo, New York, September 19–21, 1989

NASA

MILLIMETER WAVE TRANSMISSION STUDIES OF $YBa_2Cu_3O_{7-\delta}$ THIN FILMS IN THE 26.5 TO 40.0 GHz FREQUENCY RANGE.

F.A. Miranda and W.L. Gordon
Department of Physics, Case Western Reserve University,
Cleveland, Ohio 44106

K.B. Bhasin, V.O. Heinen and J.D. Warner
National Aeronautics and Space Administration,
Lewis Research Center, Cleveland, Ohio 44135

G.J. Valco
Department of Electrical Engineering,
The Ohio State University,
Columbus, Ohio 43210

E-5053

ABSTRACT

Millimeter wave transmission measurements through $YBa_2Cu_3O_{7-\delta}$ thin films on MgO, ZrO_2 and $LaAlO_3$ substrates, are reported. The films (0.2 to 1.0 μm) were deposited by sequential evaporation and laser ablation techniques. Transition temperatures T_c, ranging from 89.7 K for the laser ablated film on $LaAlO_3$ to approximately 72 K for the sequentially evaporated film on MgO, were obtained. The values of the real and imaginary parts of the complex conductivity, σ_1 and σ_2, are obtained from the power transmitted through the film, assuming a two fluid model. The magnetic penetration depth is evaluated from the values of σ_2. These results will be discussed together with the frequency dependence of the normalized power transmission, P/P_c, below and above T_c.

INTRODUCTION

Millimeter wave measurements of the new high T_c superconductors are of fundamental importance due to the potential applicability of these oxides in the fabrication of devices operational in these frequency ranges.[1] Through these measurements, information on the nature of superconductivity in these new superconductors can be obtained from the temperature dependence of parameters such as the surface resistance,[2-6] and the complex conductivity.[7-9] Another important question is the applicability of millimeter wave measurements for the characterization of superconducting thin films. While dc resistance versus temperature measurements give no further information once the zero resistance state is achieved, millimeter wave transmission and absorption measurements provide a sensitive, contactless technique, which yield important information about the microstructure of superconducting films[10]

and their behavior at temperatures below the critical temperature (T_c). Millimeter and microwave absorption studies in low and high T_c superconductors have been performed using resonant cavities.[10-16] Usually, those studies applying millimeter or microwave transmission analysis, have reported results at just one particular frequency.[8,9]

In this work we have measured the power transmitted through $YBa_2Cu_3O_{7-\delta}$ thin films at frequencies within the frequency range from 26.5 to 40.0 GHz and at temperatures from 20 to 300 K. From these measurements and assuming a two fluid model, we have obtained values of the normal and complex conductivities above and below T_c respectively. The zero temperature magnetic penetration depth has been obtained using the value of the imaginary part of the complex conductivity, σ_2.

ANALYSIS

We have applied the two fluid model due to its simplicity and because in the past it has given good results for the microwave properties of metallic type II superconductors in cases for $\hbar\omega << E_{gap}$.[17] Since the energy gap for $YBa_2Cu_3O_{7-\delta}$ superconductors corresponds to frequencies in the terahertz range, we expect the model to be applicable in the frequency range studied. In this phenomenological model, the complex conductivity is defined as

$$\sigma = \sigma_1 - i\sigma_2 \tag{1}$$

with

$$\sigma_1 = \sigma_c t^4 \qquad \text{and} \qquad \sigma_2 = \sigma_c(1 - t^4)/\omega\tau \ . \tag{2}$$

Here, σ_c is the normal conductivity at $T = T_c$, $\omega = 2\pi f$ is the angular frequency, t is the reduced temperature T/T_c, and τ is the mean carrier scattering time. Thus, to determine either σ_1 or σ_2 we need to know the transition temperature T_c and the value of σ_c. Furthermore, the value of τ must be known beforehand if σ_2 is to be obtained from Eq. (2).

In this study, the value of T_c was determined from the standard four-point probe versus temperature measurements. To determine the normal and complex conductivities, we used the method applied by Glover and Tinkham.[18] In this method, the transmission of a normally incident plane wave through a film of thickness d(<< wavelength or skin depth) deposited on a substrate of thickness ℓ and index of refraction n, is measured. Following the notation of Glover and Tinkham[18] the power transmission is given by

$$\mathbf{T} = \frac{8n^2}{A + B\cos 2k\ell + C\sin 2k\ell} \tag{3}$$

where

$$A = n^4 + 6n^2 + 1 + 2(3n^2 + 1)g + (n^2 + 1)(b^2 + g^2)$$

$$B = 2(n^2 - 1)g - (n^2 - 1)^2 + (n^2 - 1)(b^2 + g^2)$$

$$C = 2(n^2 - 1)nb$$

$$k = n\omega/c$$

and

$$y = g - ib = YZc = (G - iB)Z_c = (\sigma_1 - i\sigma_2)dZ_c$$

is the dimensionless complex admittance per square of the film in units of the characteristic admittance, Z_c^{-1}, of the wave guide ($Z_c = Z_o/\sqrt{1 - (f_c/f)^2}$, $Z_o = 377\ \Omega$, mks; $Z_o = 4\pi/c$, cgs; f_c = cutoff frequency of the TE mode wave guide and f is the operational frequency).

In the normal state, Eq. (3) becomes

$$\mathbf{T}_N = \frac{8n^2}{\sigma_N^2 d^2 Z_c^2 Q + \sigma_N dZ_c R + P} \tag{4}$$

where

σ_N = normal conductivity

$Q = (n^2 + 1) + (n^2 - 1)\cos 2k\ell$

$R = 2(3n^2 + 1) + 2(n^2 - 1)\cos 2k\ell$

$P = n^4 + 6n^2 + 1 - (n^2 - 1)^2 \cos 2k\ell.$

The normal state conductivity of the film can be expressed conveniently in terms of the power transmission as

$$\sigma_N = \frac{-R\mathbf{T}_N \pm \sqrt{R^2\mathbf{T}_N^2 - 4Q\mathbf{T}_N(P\mathbf{T}_N - 8n^2)}}{2Q\mathbf{T}_N dZ_c} \tag{5}$$

where only the expression with the + sign has physical relevance. It is convenient to use the ratio $\mathbf{T}_S/\mathbf{T}_N$ in the analysis of the superconducting state, where $\mathbf{T}_S$ refers to the transmission in the superconducting state given by Eq. (3). Thus,

$$\frac{\mathbf{T}_S}{\mathbf{T}_N} = \frac{\sigma_N^2 d^2 Z_c^2 Q + \sigma_N dZ_c R + P}{A + B\cos 2k\ell + C\sin 2k\ell} \tag{6}$$

Solving (6) for the imaginary part, σ_2, of the conductivity, and using the value of σ_N at $T = T_c$ we have

$$\sigma_2/\sigma_c = -\beta/2\,\frac{1}{\sigma_c dZ_c} + \left\{\frac{1}{(\sigma_c dZ_c)^2}\left[(\beta/2)^2 - \gamma\right] - \frac{\alpha\sigma_1}{\sigma_c^2 dZ_c} - \left(\frac{\sigma_1}{\sigma_c}\right)^2 + (\mathbf{T}_c/\mathbf{T}_S)\left[1 + \frac{\alpha}{\sigma_c dZ_c} + \frac{\gamma}{(\sigma_c dZ_c)^2}\right]\right\}^{1/2} \tag{7}$$

where σ_c and $\mathbf{T}_c$ are the conductivity and the transmissivity at $T = T_c$, and

$$\alpha = \frac{1}{D}\,[6n^2 + 2 + 2(n^2 - 1)\cos 2k\ell]$$

$$\beta = \frac{1}{D}\,[-2n(n^2 - 1)\sin 2k\ell]$$

$$\gamma = \frac{1}{D}\,[n^4 + 6n^2 + 1 - (n^2 - 1)\cos 2k\ell]$$

$$D = n^2 + 1 + (n^2 - 1)\cos 2k\ell \ .$$

Thus, from the relation for σ_1 in Eq. (2), and Eq. (7), the real and imaginary parts of the complex conductivity can be determined.

The magnetic penetration depth, λ, can be obtained from the London expression

$$\lambda = \left(\frac{1}{\mu_o \omega \sigma_2}\right)^{1/2} \tag{8}$$

which can be written in terms of the superfluid density N_S, as

$$\lambda = \left(\frac{m}{\mu_o N_S e^2}\right)^{1/2} \tag{9}$$

where m is the effective mass of the charge carriers. From the two fluid model

$$\frac{N_S}{N} = 1 - t^4 \tag{10}$$

where $N = N_n + N_S$ is the total number of carriers per unit volume, we have

$$\lambda = \left[\frac{m}{\mu_o N e^2}\right]^{1/2} (1 - t^4)^{-1/2} = \lambda_o\,(1 - t^4)^{-1/2} \tag{11}$$

From this expression the zero-temperature penetration depth, λ_o, can be obtained. Because Eq. (9) applies to homogeneous superconductors, the values of λ_o obtained in this method are larger than those that would be obtained for homogeneous films.

Our measurements were made on thin films (0.2 to 1.0 μm thickness) of $YBa_2Cu_3O_{7-\delta}$ on $LaAlO_3$, MgO and ZrO_2 substrates. The substrates were generally between 0.025 and 0.100 cm thick. The deposition techniques used for the preparation of the films used in this study are described in Refs. 19 and 20. For the laser ablated films, X-ray diffraction data showed that the films were c-axis oriented on $LaAlO_3$ and partially c-axis oriented for those on MgO and ZrO_2. They had T_c's ranging from 89.7 K for the film on $LaAlO_3$ to 79 and 78 K for those deposited on MgO and ZrO_2 respectively. The film deposited by sequential evaporation on MgO had a T_c of approximately 72 K.

The power transmission measurements were made using a Hewlett-Packard model HP-8510 automatic network analyzer connected to a modified closed cycle refrigerator by Ka-band (26.5 to 40.0 GHz) waveguides. Inside the vacuum chamber of the cryosystem, the sample was clamped

between two waveguide flanges which were in direct contact with the cold head of the refrigerator. The power transmitted through the sample was obtained by measuring the scattering parameters as described in Ref. 21. The temperature gradient of the waveguide flanges between the top and bottom of the sample, was estimated to be 2.5 K or less at 90 K. The system was properly calibrated with short, open, load and through calibration standards before each measurement cycle was started.

RESULTS

Figures 1 and 2 show the temperature dependence of the normalized power transmitted through $YBa_2Cu_3O_{7-\delta}$ thin films deposited by laser ablation on $LaAlO_3$ and MgO respectively. The data are normalized with respect to the transmitted power at the critical temperature T_c. The measurements of the power transmitted through the films were started at room temperature and then carried out during sample cooling. In Fig. 1, it can be observed that the rapid decrease in transmitted power occurs at T_c. This is typical of films with a high degree of homogeneity, where all the regions of the film undergo the superconducting transition simultaneously. This is not the case for the film considered in Fig. 2, for which the transmitted power starts to decrease rapidly at temperatures just below an onset temperature (~90 K) approximately 11 K above its transition temperature of 79 K. This behavior may be associated with the presence of inhomogeneities, resulting in a distribution of transition temperatures. For temperatures below T_c both films are characterized by a smooth decrease of the power transmitted through them.

The behavior shown in Figs. 1 and 2 for the power transmitted through the film-substrate combination, as a function of decreasing temperature, was also observed for the laser ablated film on ZrO_2 and for

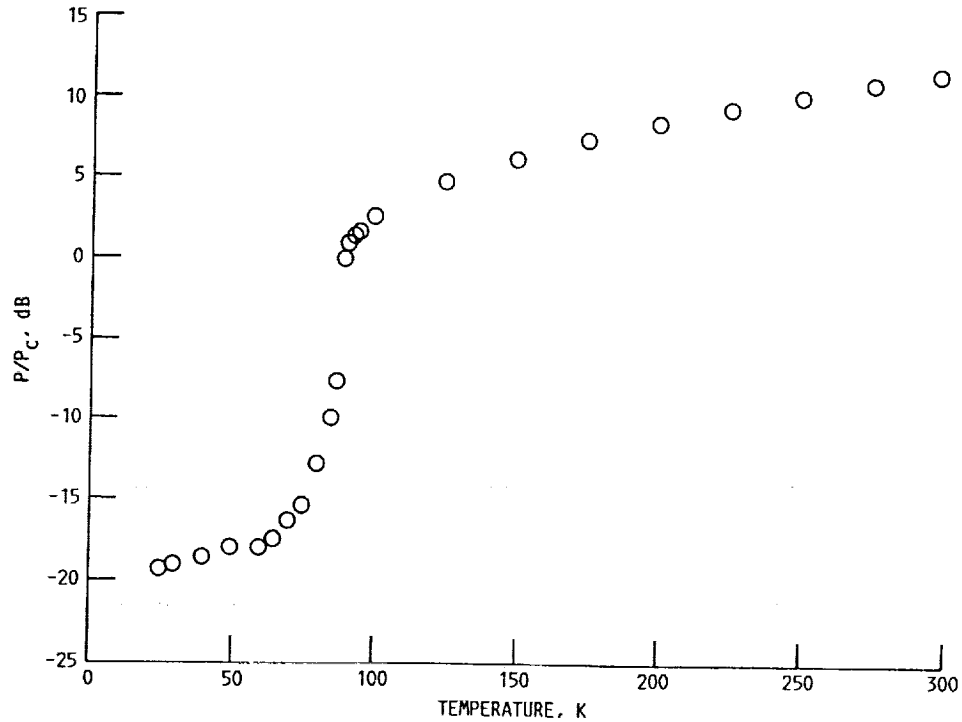

FIGURE 1. - NORMALIZED TRANSMITTED POWER VERSUS TEMPERATURE FOR A LASER ABLATED $YBa_2Cu_3O_{7-\delta}$ THIN FILM (0.7 MICRONS) ON $LaAlO_3$ AT 37.0 GHz.

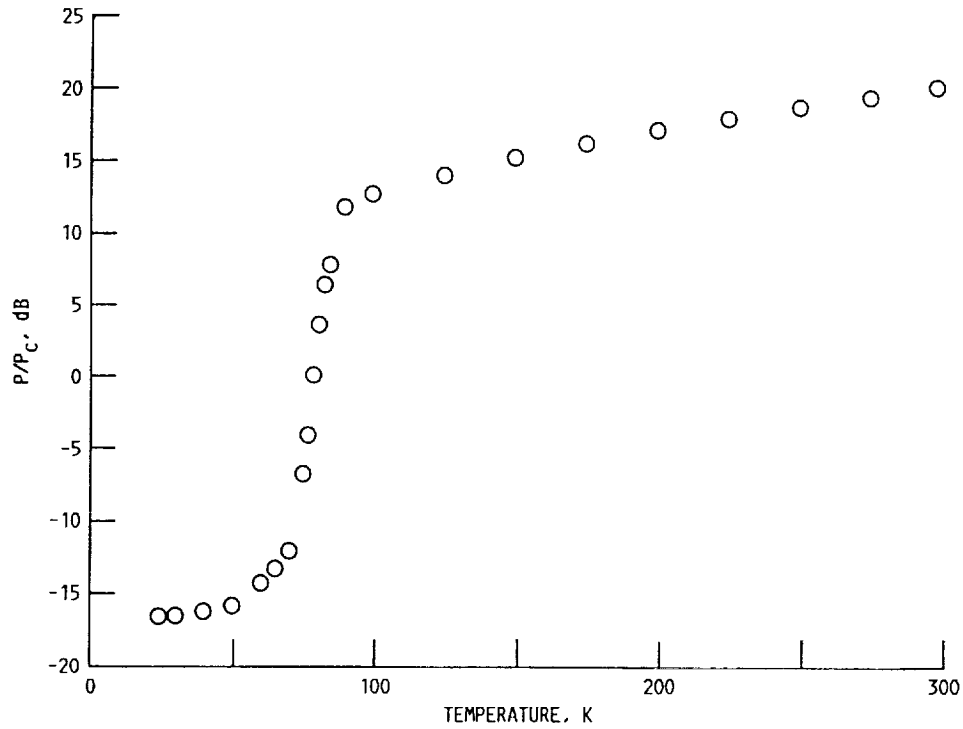

FIGURE 2. - NORMALIZED TRANSMITTED POWER VERSUS TEMPERATURE FOR A LASER ABLATED $YBa_2Cu_3O_{7-\delta}$ THIN FILM (0.2 MICRONS) ON MgO AT 28.5 GHz.

the sequentially evaporated film on MgO. For the latter film the transmission data suggest a lower film quality when compared to the film deposited on MgO by laser ablation. The films on ZrO_2 and sequentially evaporated on MgO also show a wide transition region. This temperature behavior was verified to be frequency independent for the frequencies employed in this study, and our analysis suggest that it is related to the degree of homogeneity and quality of the films.

Figures 3 to 10 and Table I, show the results for the conductivity above and below T_c, and at different frequencies, for the various films considered in this study. Figures 3 and 4 show the real and imaginary parts of the conductivity, σ_r and σ_2 respectively, corresponding to the $YBa_2Cu_3O_{7-\delta}$ film deposited on $LaAlO_3$ by laser ablation. The value for the normal conductivity at room temperature, 2.0×10^5 S/m, compares reasonably well with reported values of the dc conductivity in this type of film.[22,23] The cusp in σ_r at the transition temperature can be observed clearly in Fig. 3 and again indicates the high level of homogeneity and quality of this film. The imaginary part of the conductivity increases as a function of decreasing temperature, as can be seen in Fig. 4. Values of 5.17×10^6 S/m and 6.80×10^6 S/m are obtained at 70 and 40 K respectively. Using Eq. (8) we find $\lambda = 0.81$ μm at 70 K and $\lambda = 0.70$ μm at 40 K. From the value of λ at 40 K we found $\lambda_o = 0.69$ μm.

Figures 5 to 10 show the real and imaginary parts of the complex conductivity for the laser ablated films on MgO and ZrO_2, and for the sequentially evaporated film on MgO. Note that the normal to the superconducting transition region has been clearly identified in Figs. 5, 7 and 9. In the absence of a physical model which can account for the

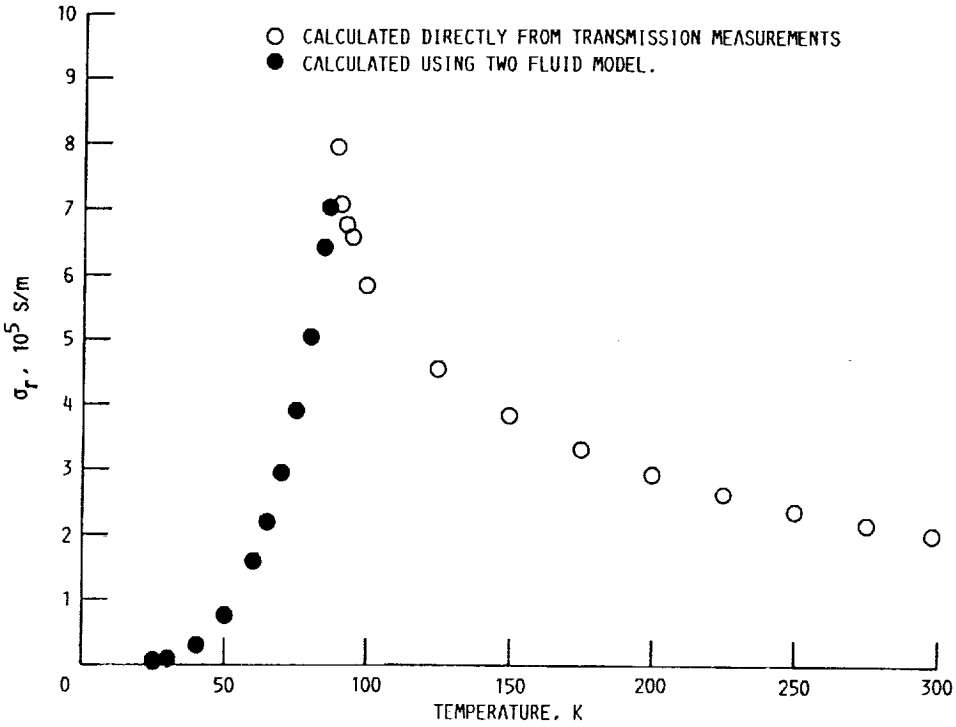

FIGURE 3. - REAL PART OF THE CONDUCTIVITY, σ_r, VERSUS TEMPERATURE FOR A LASER ABLATED $YBa_2Cu_3O_{7-\delta}$ THIN FILM (0.7 MICRONS) ON $LaAlO_3$ AT 37.0 GHz. $\sigma_r = \sigma_N$ FOR $T > T_c$ AND $\sigma_r = \sigma_1$ FOR $T < T_c$.

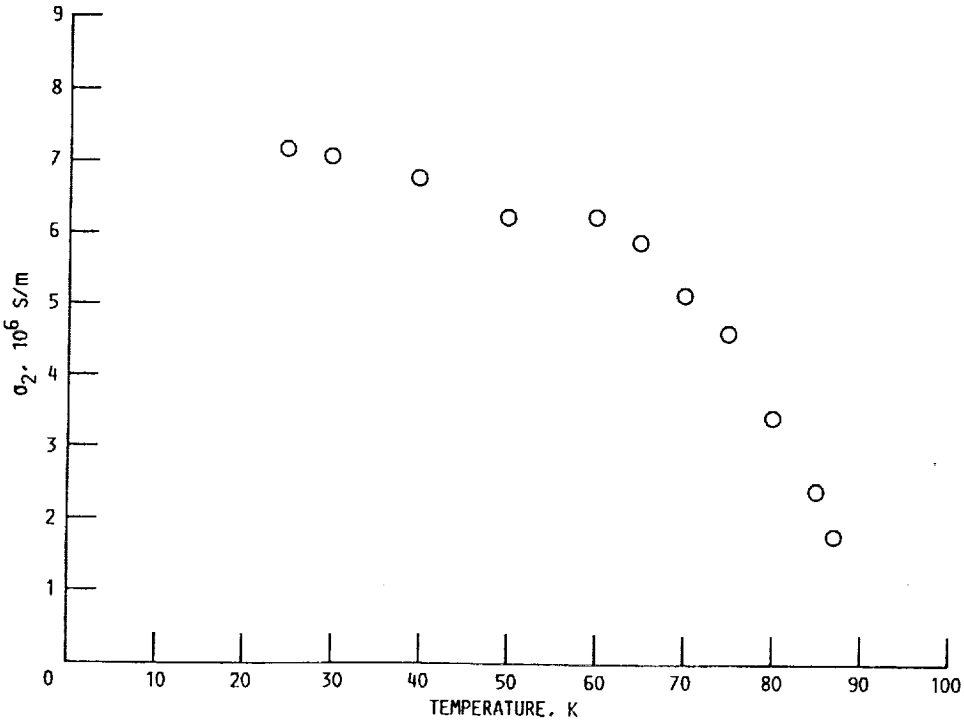

FIGURE 4. - IMAGINARY PART OF THE CONDUCTIVITY, σ_2, VERSUS TEMPERATURE FOR A LASER ABLATED $YBa_2Cu_3O_{7-\delta}$ THIN FILM (0.7 MICRONS) ON $LaAlO_3$ AT 37.0 GHz.

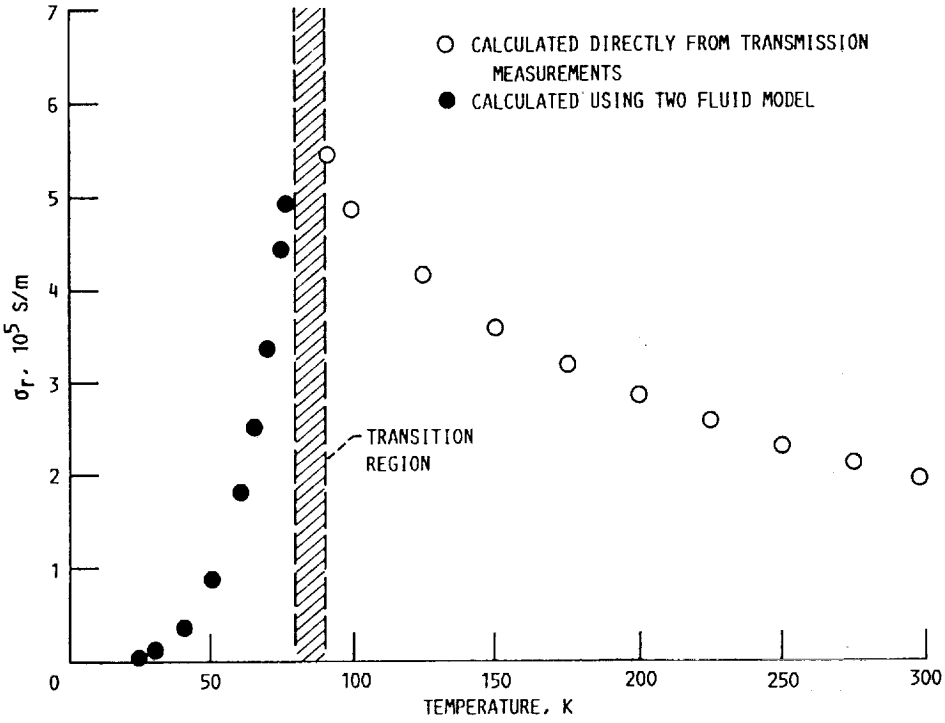

FIGURE 5. - REAL PART OF CONDUCTIVITY, σ_r, VERSUS TEMPERATURE FOR A LASER ABLATED $YBa_2Cu_3O_{7-\delta}$ THIN FILM (0.2 MICRONS) ON MgO AT 28.5 GHz. $\sigma_r = \sigma_N$ FOR $T > T_c$ AND $\sigma_r = \sigma_1$ FOR $T < T_c$.

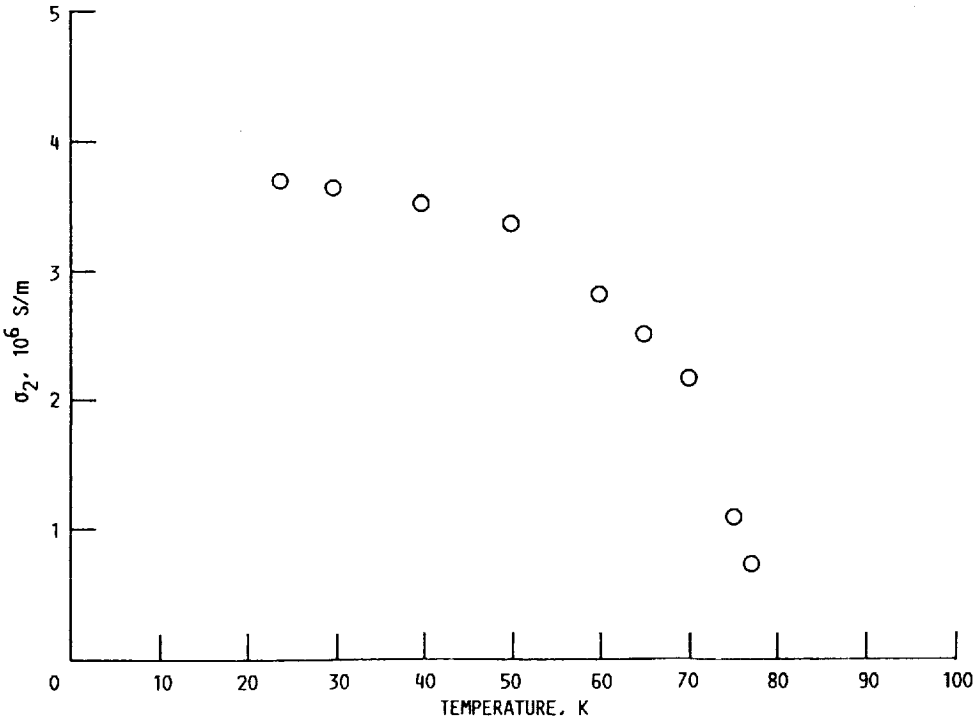

FIGURE 6. - IMAGINARY PART OF THE CONDUCTIVITY, σ_2, VERSUS TEMPERATURE FOR A LASER ABLATED $YBa_2Cu_3O_{7-\delta}$ THIN FILM (0.2 MICRONS) ON MgO AT 28.5 GHz.

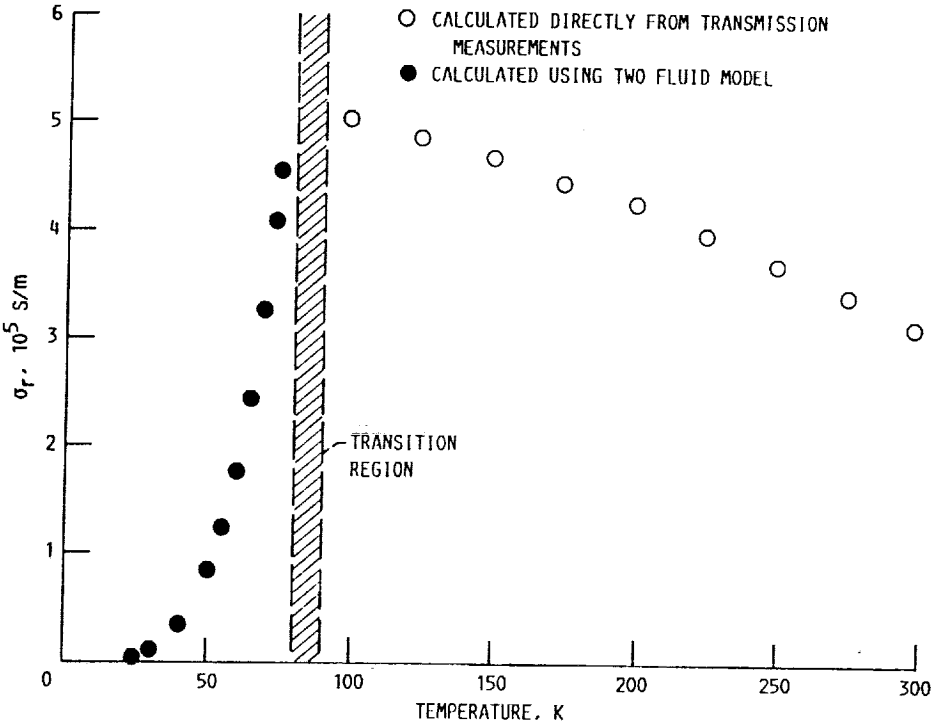

FIGURE 7. - REAL PART OF THE CONDUCTIVITY, σ_r, VERSUS TEMPERATURE FOR A LASER ABLATED $YBa_2Cu_3O_{7-\delta}$ THIN FILM (0.75 MICRONS) ON ZrO_2 AT 37.0 GHz. $\sigma_r = \sigma_N$ FOR $T > T_c$ AND $\sigma_r = \sigma_1$ FOR $T < T_c$.

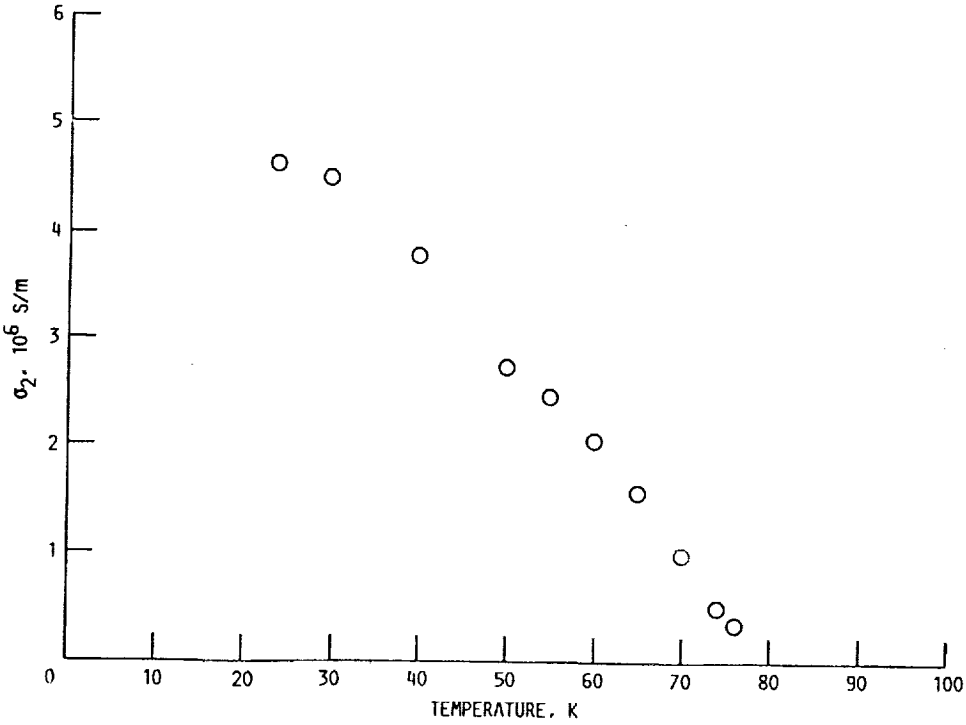

FIGURE 8. - IMAGINARY PART OF THE CONDUCTIVITY, σ_2, VERSUS TEMPERATURE FOR A LASER ABLATED $YBa_2Cu_3O_{7-\delta}$ THIN FILM (0.75 μm) ON ZrO_2 AT 37.0 GHz.

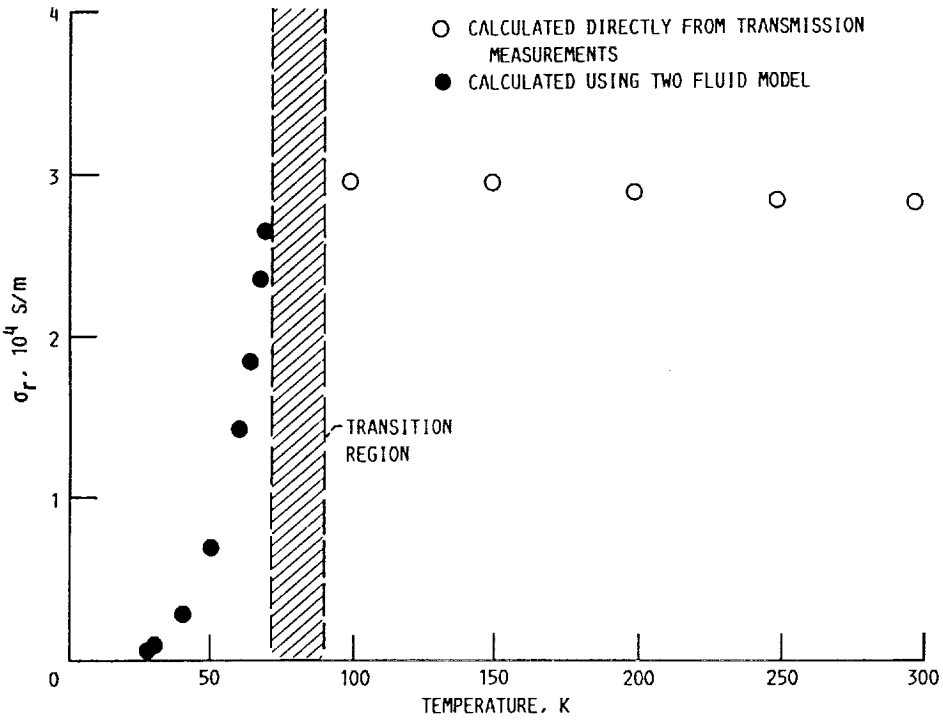

FIGURE 9. - REAL PART OF THE CONDUCTIVITY, σ_r, VERSUS TEMPERATURE FOR A SEQUENTIALLY EVAPORATED $YBa_2Cu_3O_{7-\delta}$ THIN FILM (1.0 MICRON) ON MgO AT 33.0 GHz. $\sigma_r = \sigma_N$ FOR $T > T_c$ AND $\sigma_r = \sigma_1$ FOR $T < T_c$.

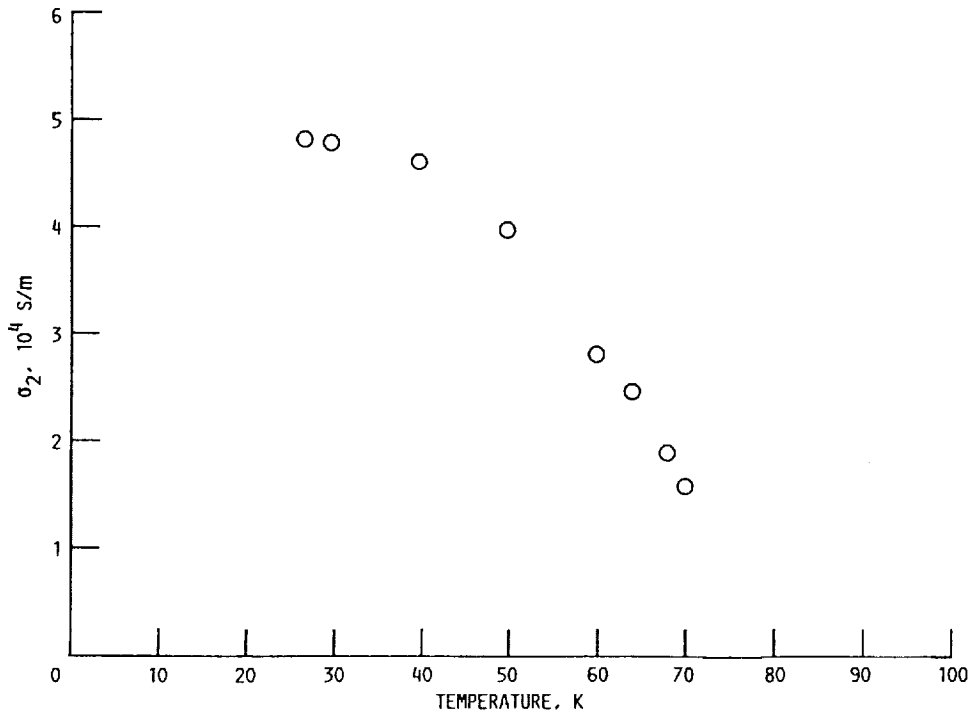

FIGURE 10. - IMAGINARY PART OF THE CONDUCTIVITY, σ_2, VERSUS TEMPERATURE FOR A SEQUENTIALLY EVAPORATED $YBa_2Cu_3O_{7-\delta}$ THIN FILM (1.0 MICRON) ON MgO AT 33.0 GHz.

TABLE I. - MILLIMETER WAVE CONDUCTIVITIES (σ_1,σ_2) AND ZERO TEMPERATURE PENETRATION DEPTH (λ_o) AT 35.0 GHz FOR $YBa_2Cu_3O_{7-\delta}$ THIN FILMS DEPOSITED ON DIFFERENT SUBSTRATES BY LASER ABLATION (LA) AND SEQUENTIAL EVAPORATION (SE)

Parameter	Substrates			
	MgO		$LaAlO_3$	ZrO_2
	SE	LA	LA	LA
σ_1 (70K)	3.0×10^4 S/m	3.9×10^5 S/m	3.3×10^5 S/m	1.7×10^5 S/m
σ_2 (70K)	1.9×10^4 S/m	1.1×10^6 S/m	6.4×10^6 S/m	1.1×10^6 S/m
σ_1 (40K)	3.1×10^3 S/m	4.1×10^4 S/m	3.5×10^4 S/m	1.9×10^4 S/m
σ_2 (40K)	7.1×10^4 S/m	4.0×10^6 S/m	7.7×10^6 S/m	3.6×10^6 S/m
λ_o	6.8 μm	0.91 μm	0.67 μm	0.96 μm

distribution of normal and superconducting material in the transition region, we can not accurately determine the normal conductivity down to the transition temperature T_c. Therefore, we have considered the critical conductivity to be the conductivity at or just above the onset temperature. Since the two fluid model approximation is based upon the assumption that the normal to the superconducting state transition is a sharp one, as for the film on $LaAlO_3$, the values of σ_1 obtained using $\sigma_c = \sigma_{onset}$ in Eq. (2) will be less than those expected for a sharp transition. The magnitude of this difference will depend upon the width ΔT of the transition region and the overall film quality. To estimate the size of the discrepancy between using σ_c at T_{onset} and σ_c at T_c, one can extrapolate σ_r above T_{onset} to T_c. When this is done, the σ_c obtained is 12 percent larger for the laser ablated film on MgO, 3.3 percent for the laser ablated film on ZrO_2 and 1.7 percent larger for the sequentially evaporated film on MgO. In the better films the discrepancy between σ_{onset} and the extrapolated value of σ_r at T_c, is larger due to the larger slope of σ_r for temperatures above the onset temperature as can be seen in Figs. 5, 7, and 9. This discrepancy becomes smaller as T_{onset} nears T_c, as for the film on $LaAlO_3$.

Figures 6, 8 and 10 show the imaginary part of the complex conductivity for the laser ablated films on MgO and ZrO_2, and for the sequentially evaporated film on MgO. Using Eq. (8) we obtain values for λ of 1.1, 0.95, and 9.1 μm, at 40 K, for the laser ablated films on MgO and ZrO_2 and for the sequentially evaporated film on MgO respectively. Additional values for the conductivities and for λ_o at 35.0 GHz are given in Table I. The value for λ_o obtained for the laser ablated film on $LaAlO_3$, compares favorably with that reported by Kobrin, et al.[24] ($\lambda_o \sim 0.48$ μm, at 60.0 GHz) for ion-beam sputtered $YBa_2Cu_3O_{7-\delta}$ films on $LaAlO_3$.

CONCLUSIONS

Millimeter wave power transmission studies have been performed on $YBa_2Cu_3O_{7-\delta}$ thin films at frequencies within the frequency range from 26.5 to 40.0 GHz and at temperatures from 20 to 300 K. The normal, σ_N, and complex, $\sigma_1 - i\sigma_2$, conductivities have been determined for laser ablated films on $LaAlO_3$, MgO and ZrO_2. The conductivities of films on MgO grown by laser ablation and sequential evaporation have been compared. From the results obtained in this study, it is apparent that at least for films deposited on MgO, films deposited by laser ablation appear to have a higher quality than those deposited by the sequential evaporation technique. We have also shown that millimeter wave transmission and conductivity measurements can be used as a test of thin film quality. It was observed that for a film with a narrow transition region, the two fluid model should be more applicable than for those films with a wide transition region. Finally, values for the zero-temperature magnetic penetration depth have been determined from the obtained values of σ_2 .

ACKNOWLEDGMENT

The authors are pleased to acknowledge helpful suggestions by Dr. S. Sridhar and Dr. J. Halbritter. Our thanks to Dr. S. Alterovitz, Dr. M. Stan and Dr. T. Eck for helpful discussions.

REFERENCES

1. Hartwig, W.; and Passow, C.: RF Superconducting Devices -- Theory, Design, Performance, and Applications. Applied Superconductivity, vol. 2, V.L. Newhouse, ed., Academic Press, New York, 1975, pp. 541-639.

2. Martens, J.S.; Beyer, J.B.; and Ginley, D.S.: Microwave Surface Resistance of $YBa_2Cu_3O_{6.9}$ Superconducting Films. Appl. Phys. Lett., vol. 52, no. 21, 23 May 1988, pp. 1822-1824.

3. Carini, J.P., et al.: Millimeter-Wave Surface Resistance Measurements in Highly Oriented $YBa_2Cu_3O_{7-\delta}$ Thin Films. Phys. Rev. B, vol. 37, no. 16, 1 June 1988, pp. 9726-9729.

4. Newman, H.S., et al.: Microwave Surface Resistance of Bulk Tl-Ba-Ca-Cu-O Superconductors. Appl. Phys. Lett., vol. 54, no. 4, 23 Jan. 1989, pp. 389-390.

5. Klein, N., et al.: Millimeter-Wave Surface Resistance of Epitaxially Grown $YBa_2Cu_3O_{6-x}$ Thin Films. Appl. Phys. Lett., vol. 54, no. 8, 20 Feb. 1989, pp. 757-759.

6. Sridhar, S.; Shiffman, C.A.; and Handed, H.: Electrodynamic Response of $Y_1Ba_2Cu_3O_y$ and $La_{1.85}Sr_{0.15}CuO_{u-s}$ in the Superconducting State. Phys. Rev. B, vol. 36, no. 4, 1 Aug. 1987, pp. 2301-2304.

7. Cohen, L., et al.: Surface Impedance Measurements of Superconducting $YBa_2Cu_3O_{6+x}$. J. Phys. F: Met. Phys., vol. 17, 1987, pp. L179-L183.

8. Ho, W., et al.: Millimeter-Wave Complex-Conductivity Measurements of Bi-Ca-Sr-Cu-O Superconducting Thin Films. Phys. Rev. B, vol. 38, no. 10, 1 Oct. 1988, pp. 7029-7032.

9. Nichols, C.S., et al.: Microwave Transmission Through Films of $YBa_2Cu_3O_{7-\delta}$. To be published in Phys. Rev. B.

10. Tyagi, S., et al.: Low-Field AC Susceptibility and Microwave Absorption in YBaCuO and BiCaSrCuO Superconductors. Physica C, vol. 156, 1988, pp. 73-78.

11. Maxwell, E.; Marcus, P.M.; and Slater, J.C.: Surface Impedance of Normal and Superconductors at 24,000 Megacycles per Second. Phys. Rev. vol. 76, no. 9, 1 Nov. 1949, pp. 1332-1347.

12. Pippard, A.B.: The Surface Impedance of Superconductors and Normal Metals at High Frequencies. Proc. R. Soc. A, vol. 203, no. 1072, 7 Sept. 1950, pp. 98-118.

13. Gittleman, J.I.; and Bozowski, S.: Transition of Type-I Superconducting Thin Films in a Perpendicular Magnetic Field: A Microwave Study. Phys. Rev., vol. 161, no. 2, 10 Sept., 1967, pp. 398-403.

14. Durny, R., et al.: Microwave Absorption in the Superconducting and Normal Phases of Y-Ba-Cu-O. Phys. Rev. B, vol. 36, no. 4, 1 Aug. 1987, pp. 2361-2363.

15. Tyagi, S., et al.: Frequency Dependence of Magnetic Hysteresis in the Field-Induced Microwave Absorption in High-T_c Superconductors at $T << Tc$. To be published in Phys. Lett. A.

16. Jackson, E.M., et al.: Study of Microwave Power Absorption in Yttrium-Barium-Copper Based High Temperature Superconductors and Allied Compounds. To be published in Supercond. Sci. Technol.

17. Gittleman, J.I.; and Rosemblum, B.: Microwave Properties of Superconductors. IEEE Proc., vol. 52, no. 10, Oct. 1964, pp. 1138-1147.

18. Glover III, R.E.; and Tinkham, M.: Conductivity of Superconducting Films for Photon Energies Between 0.3 and 40 KTc. Phys. Rev., vol. 108, no. 2, 15 Oct. 1957, pp. 243-256.

19. J.D. Warner, J.E. Meola and K.A. Jenkins: "Study of Deposition of YBa2Cu3O7-x on Cubic Zirconia," NASA TM-102350 (1989).

20. G.J. Valco, N.J. Rohrer, J.D. Warner and K.B. Bhasin: "Sequentially Evaporated Thin Y-Ba-Cu-O Superconducting Films on Microwave Substrates" NASA TM-102068 (1989).

21. Miranda, F.A., et al.: Measurements of Complex Permittivity of Microwave Substrates in the 20 to 300 K Temperature Range From 26.5 to 40.0 GHz. NASA TM-102123, 1989.

22. Gurvitch, M.; and Fiory, A.T.: Resistivity of $La_{1.825}Sr_{0.175}CuO_4$ and $YBa_2Cu_3O_7$ to 1100K: Absence of Saturation and Its Implications. Phys. Rev. Lett., vol. 59, no. 12, 21 Sept. 1987, pp. 1337-1340.

23. Collins, R.T., et al.: Comparative Study of Superconducting Energy Gaps in Oriented Films and Pollycrystalline Bulk Samples of Y-Ba-Cu-O. Phys. Rev. Lett., vol. 59, no. 6, 10 Aug. 1987, pp. 704-707.

24. Kobrin, P.H., et al.: Millimeter-Wave Complex Conductivities of Some TlBaCaCuO and $YBa_2Cu_3O_{7-f}$ Films, Presented at the M^2s-HTSC Conference, Stanford, CA, July 24-28, 1989. To be published in Physica C.

NASA Technical Memorandum 102123

Measurements of Complex Permittivity of Microwave Substrates in the 20 to 300 K Temperature Range From 26.5 to 40.0 GHz

Felix A. Miranda and William L. Gordon
Case Western Reserve University
Cleveland, Ohio

and

Vernon O. Heinen, Ben T. Ebihara,
and Kul B. Bhasin
Lewis Research Center
Cleveland, Ohio

Prepared for the
1989 Cryogenic Engineering Conference
sponsored by the University of California, Los Angeles
Los Angeles, California, July 24–28, 1989

NASA

MEASUREMENTS OF COMPLEX PERMITTIVITY OF MICROWAVE SUBSTRATES IN THE 20 TO 300 K TEMPERATURE RANGE FROM 26.5 TO 40.0 GHz

Felix A. Miranda and William L. Gordon
Case Western Reserve University
Cleveland, Ohio

Vernon O. Heinen, Ben T. Ebihara, and Kul B. Bhasin
National Aeronautics and Space Administration
Lewis Research Center
Cleveland, Ohio

SUMMARY

A knowledge of the dielectric properties of microwave substrates at low temperatures is useful in the design of superconducting microwave circuits. In this paper, we report the results of a study of the complex permittivity of sapphire (Al_2O_3), magnesium oxide (MgO), silicon oxide (SiO_2), lanthanum aluminate ($LaAlO_3$), and zirconium oxide (ZrO_2), in the 20 to 300 K temperature range, at frequencies from 26.5 to 40.0 GHz. The values of the real and imaginary parts of the complex permittivity were obtained from the scattering parameters, which were measured using a HP-8510 automatic network analyzer. For these measurements, the samples were mounted on the cold head of a helium gas closed cycle refrigerator, in a specially designed vacuum chamber. An arrangement of wave guides, with mica windows, was used to connect the cooling system to the network analyzer. A decrease in the value of the real part of the complex permittivity of these substrates, with decreasing temperature, was observed. For MgO and Al_2O_3, the decrease from room temperature to 20 K was of 7 and 15 percent, respectively. For $LaAlO_3$, it decreased by 14 percent, for ZrO_2 by 15 percent, and for SiO_2 by 2 percent, in the above mentioned temperature range.

E-4903-1

INTRODUCTION

The successful application of thin films, made with the new high temperature superconductor oxides, in the development of microwave circuits, rest considerably on the dielectric properties of the different substrates used for film deposition. For microwave applications, it is desirable to have substrates with low dielectric constant and loss tangent, (ref. 1) if good performance from microwave components is expected.

Until now, Y-Ba-Cu-O films deposited on $SrTiO_3$, have shown the highest quality when compared with films deposited on other substrates. Nevertheless, due to its extremely temperature dependent dielectric constant, with a value for 300 at room temperature, around 1000 at 77 K, and over 18000 at helium temperatures, and its considerably high loss tangent, (ref. 2) its microwave applicability is rather limited. Although other materials as MgO, $LaAlO_3$, and ZrO_2 are now being used as substrates, information about their dielectric properties at temperatures below room temperature, and for some of them even at room temperature, is rather scarce.

In this paper, we report on the measurements of the microwave complex permittivity of MgO, Al_2O_3, $LaAlO_3$, ZrO_2, and SiO_2, in the 20 to 300 K temperature range and as a function of frequency. The measurements were taken following a method previously reported by other authors (refs. 3 to 5). This method allows the determination of both parts of the complex permittivity in a rather simple way, and is very convenient for cases in which a fast determination of the dielectric constant of a material is needed. Nevertheless, the method has a high uncertainty in the measurement of the imaginary part of the complex permittivity for materials with very low loss tangent.

ANALYSIS

In order to determine the value of the real and imaginary parts of the complex permittivity for the various substrates under consideration, we have followed the method proposed by Nicolson and Ross, (ref. 3) as modified by Wier, (ref. 4) and following the implementation suggestions of reference 5. In an ideal case, consider a piece of material installed in a rectangular wave guide with characteristic impedance Zo, as shown in figure 1.

After solving the corresponding boundary conditions at $x = 0$ and $x = d$, the scattering parameters, $S_{11}(\omega)$ and $S_{21}(\omega)$, can be related with the reflection, Γ, and transmission, T, coefficients, as follows,

$$S_{11} = \frac{(1 - T^2)\Gamma}{1 - \Gamma^2 T^2}, \qquad S_{21} = \frac{(1 - \Gamma^2)T}{1 - \Gamma^2 T^2} \tag{1}$$

The reflection coefficient, when the length of the material is infinite, is given by

$$\Gamma = \frac{Z - Z_o}{Z + Z_o} = \frac{\sqrt{\frac{\mu r}{\epsilon r}} - 1}{\sqrt{\frac{\mu r}{\epsilon r}} + 1} \tag{2}$$

Also, the transmission coefficient, when the length of the material is finite, is given by,

$$T = \exp(-j\omega \sqrt{\mu\epsilon}\, d) = \exp[(-j\omega/c) \sqrt{\mu_r \epsilon_r}\, d] \tag{3}$$

Thus, the reflection and transmission coefficients can be derived by measuring $S_{11}(\omega)$ and $S_{21}(\omega)$, and in turn they can be used to obtain the value of the permittivity.

The experimental configuration used for the measurements of the reflection, $S_{11}(\omega)$, and transmission, $S_{21}(\omega)$, scattering parameters for the samples under consideration, is shown in figure 2. The measurements were made using an HP-8510 automatic network analyzer, properly connected by an arrangement of Ka-band (26.5 to 40.0 GHz) wave guides, to a cooling system. The cooling system consist of a CTI-Cryogenics closed cycle helium refrigerator, associated with a Lake Shore Cryotronics temperature controller, model DRC 91C, which allows measurements to be taken at the required low temperatures.

The measurements were performed under vacuum (<10^{-3} torr), in an aluminum vacuum chamber specifically designed to fit on the top of the external shield of the refrigerator and to give access to the set up of wave guides connecting the network analyzer with the refrigerator. In order to preserve the vacuum inside the chamber, two mica windows were placed at its ends. The material for the windows was selected due to its very low loss and transparency in this frequency range.

In order to measure the scattering parameters, the sample was held in a sample holder which was suspended between two wave guide flanges, as shown in figure 3. The wave guide flanges were in direct contact with a copper plate, which in turn was attached to the cold head of the refrigerator. The two supporting wave guides inside the vacuum chamber, were specially designed to be used at low temperatures. They are made of stainless steel, a relatively poor thermal conductor. A gold plating of their internal surfaces was performed, in order to reduced the microwave losses. Finally, in an attempt to reduce the errors induced in the measurements, possibly due to linear thermal contractions of the wave guides as the temperature decreases, the system was calibrated at all the temperatures at which measurements were taken. These calibrations were stored, so that they could be recalled to be used in later measurements.

RESULTS

The thickness of the substrates used in this study, varies from 0.285 mm for MgO, to 1.641 mm for SiO_2. The thicknesses for the Al_2O_3, $LaAlO_3$, and ZrO_2 samples are 0.496 mm, 0.432 mm, and 0.494 mm respectively. Figures 4 to 7 and table I show the measurement results for the real part of the complex permittivity of the samples, at room temperature and at 20 K. The value for the dielectric constant of MgO at room temperature agrees well with values quoted by other researchers (refs. 6, 7, 9). For Al_2O_3 and SiO_2, the values of the dielectric constant obtained at room temperature, are also in good agreement with the values quoted by Zahopoulos (ref. 8) and Von Hippel (ref. 7) respectively. Although for ZrO_2 there appear to be no data for comparison in this frequency range, the value for its dielectric constant at room temperature is consistent with the one reported by Gorshunov, et al., (ref. 9) at frequencies within 10^{11} to 10^{12} Hz. In the case of $LaAlO_3$, the value obtained for its dielectric constant at room temperature is not consistent with the value of 15.3 reported by Simon, et al. (ref. 1). Due to this discrepancy, measurements were performed in four different $LaAlO_3$ samples, each one made from different batches, in order to determine if the disagreement was due to intrinsic properties of the sample. The value of the dielectric constant obtained from these measurements was practically the same for all the samples and was consistent with our previously determined value. Nevertheless, since not much information for the value of the dielectric constant of this substrate is available yet, additional experimental verification will be appropriate.

Table I shows the real and imaginary parts of the complex permittivity, at four different temperatures and at 32.9 GHz. A decrease in the value of the real part of the complex permittivity is clearly observed in all the substrates under consideration. For MgO and Al_2O_3, a decrease of 6 and 14 percent down to 70 K, and of 7 and 15 percent down to 20 K respectively, is observed. For $LaAlO_3$ and ZrO_2, the value of the real part of the complex permittivity is lowered by 10 and 13 percent respectively, at temperatures around 70 K, and

goes down 14 percent for $LaAlO_3$ and 15 percent for ZrO_2, at 20 K. For SiO_2, the dielectric constant is lowered by 1 percent at 70 K and by 2 percent for temperatures around 20 K.

From comparison of the data of table I with that of the references mentioned, it can be seen that there is relatively good agreement for the real part of the complex permittivity but wider variation for the imaginary part. For example, a comparison of the value for the loss tangent for MgO at room temperature, 8×10^{-2}, obtained from the data in table I, with the value quoted by Von Hippel, 3×10^{-4}, reveals a difference of two orders of magnitude. Due to this fact, it is very difficult to observe a particular temperature and frequency dependence for this parameter. This is an intrinsic limitation of the technique, when applied in the calculation of the imaginary part of the complex permittivity for materials of low loss tangent, as mentioned in the introduction.

The frequency of 32.9 GHz was selected for construction of table I as being typical of the largest variations with temperature. Finally, for these measurements, the statistical error in the real part of the complex permittivity is ± 0.02, while the variation in the imaginary part is larger.

CONCLUSIONS

The real and imaginary parts of the complex permittivity for MgO, Al_2O_3, $LaAlO_3$, ZrO_2 and SiO_2 have been measured. A decrease in the value of the real part of the complex permittivity, with decreasing temperature, was observed in all the substrates. Nevertheless, no considerable change was observed as a function of frequency. The results obtained in this study show that, at least from the stand point of the dielectric constant, the substrates considered appear to be better suited than $SrTiO_3$, for use with the new high temperature superconductors in microwave applications.

REFERENCES

1. Simon, R.W., et al.: Low-Loss Substrate for Epitaxial Growth of High-Temperature Superconductor Thin Films. Appl. Phys. Lett., vol. 53, Dec. 26, 1988, pp. 2677-2679.

2. Padamsee, H., Green, K., Gruschus, J., Kirchgessner, J., Moffat, D., Rubin, D.L., Sears, J., Shu, Q.S., Buhrman, R., Lathrop, D., Noh, T.W., Russek, S., and Sievers, A.: "Superconductivity and Applications" (To be published).

3. Nicolson, A.M.; and Ross, G.F.: Measurement of the Intrinsic Properties of Materials by Time Domain Techniques. IEEE Trans. Instrum. Meas., vol. 19, no. 4, Nov. 1970, pp. 377-382.

4. Weir, W.B.: Automatic Measurement of Complex Dielectric Constant and Permeability at Microwave Frequencies. Proc. IEEE, vol. 62, no. 1, Jan. 1974, pp. 33-36.

5. Hewlett Packard Product Note No. 8510-3, The Measurement of Both Permittivity and Permeability of Solid Materials. pp. 5954-1535 (1985).

6. Hossain, M.D.: Microwave Dielectric Properties of Ti^{4+}/MgO and Ni^{2+}/MgO. Appl. Phys. A., vol. 36, no. 1, Jan. 1985, pp. 63-65.

7. Von Hippel, A.R.: Dielectric Materials and Applications. The MIT Press, Cambridge, MA, 1954.

8. Zahopoulos, C., Kennedy, W.L.; and Sridhar, S.: Performance of a Fully Superconducting Microwave Cavity Made of the High Tc Superconductor $Y_1Ba_2Cu_3O$. Appl. Phys. Lett., vol. 52, no. 25, June 20, 1988, pp. 2168-2170.

9. Gorshunov, B.P., et al.: Submillimetre Properties of High-Tc Superconductors. Physica C, vol. 153-155, pt. 1, 1988, pp. 667-668.

TABLE I. - COMPLEX PERMITTIVITY OF MICROWAVE SUBSTRATES AT 32.9 GHz

[ϵ'_r = real part of complex permittivity. ϵ''_r = imaginary part of complex permittivity.]

Substrate	MgO		Al_2O_3		$LaAlO_3$		ZrO_2		SiO_2	
Temperature, K	ϵ'_r	ϵ''_r	ϵ'_r	ϵ''_r	ϵ'_r	ϵ''_r	ϵ'_r	ϵ''_r	ϵ'_r	ϵ''_r
300	9.88	0.556	9.51	0.675	21.9	1.70	25.4	1.72	3.82	0.516
150	9.45	.726	8.52	.925	21.6	1.48	23.6	1.75	3.80	.159
70	9.26	.351	8.19	.695	19.7	2.98	22.0	2.50	3.78	.688
20	9.19	.420	8.11	.613	18.8	3.71	21.6	2.23	3.75	.298

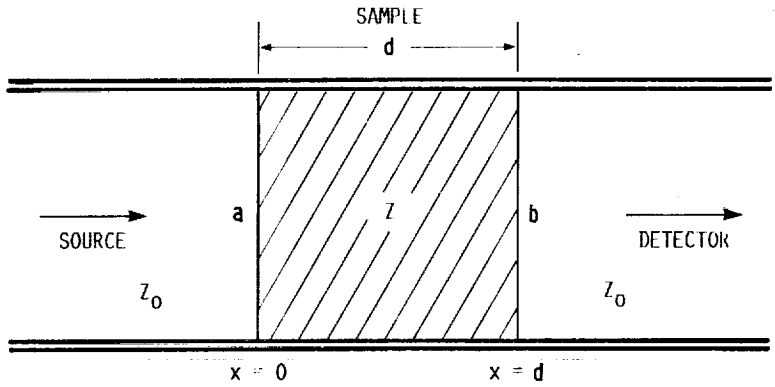

FIGURE 1. - WAVEGUIDE WITH FILLED MATERIAL.

ORIGINAL PAGE
BLACK AND WHITE PHOTOGRAPH

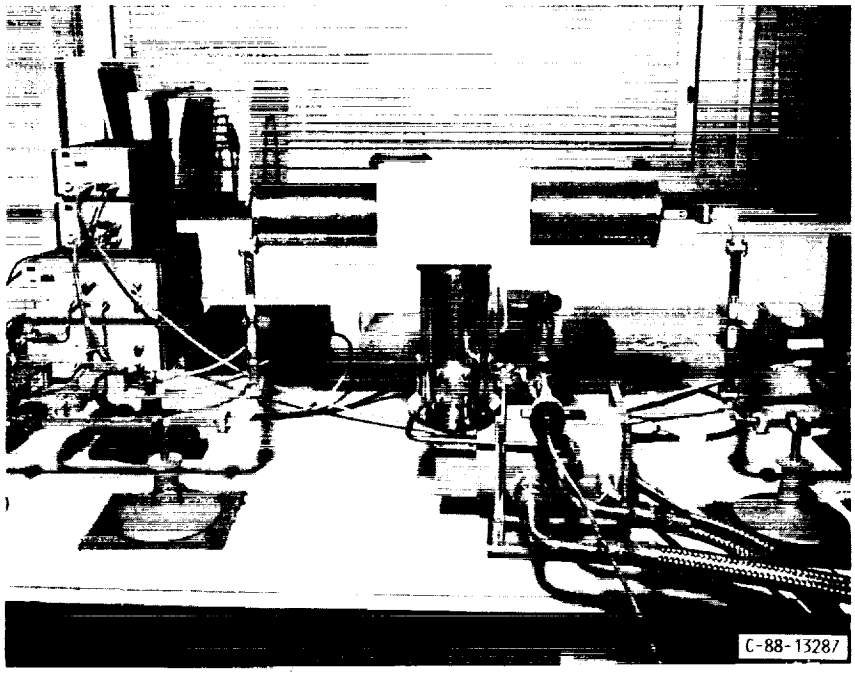

FIGURE 2. - EXPERIMENTAL SETUP.

ORIGINAL PAGE IS
OF POOR QUALITY

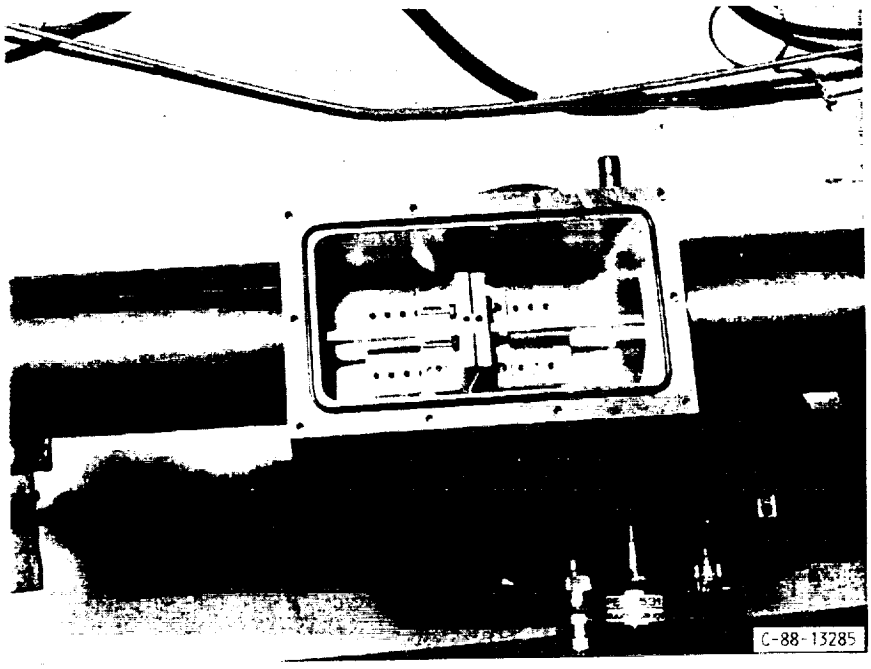

FIGURE 3. - SAMPLE SUSPENSION SETUP.

ORIGINAL PAGE
BLACK AND WHITE PHOTOGRAPH

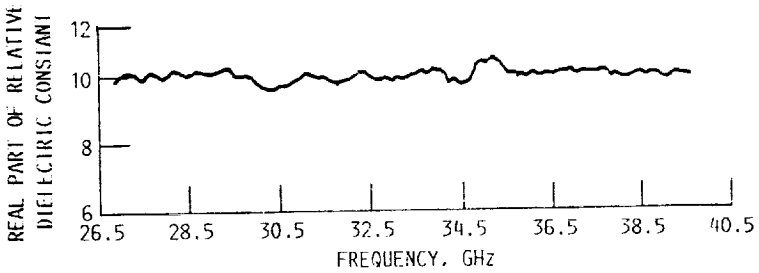

FIGURE 4. - MgO SUBSTRATE AT ROOM TEMPERATURE.

ORIGINAL PAGE IS
OF POOR QUALITY

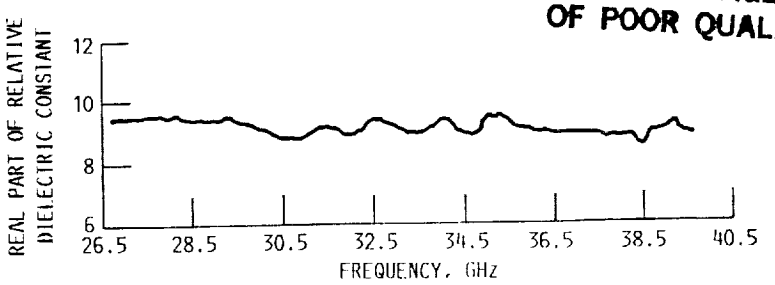

FIGURE 5. - MgO SUBSTRATE AT 20 K.

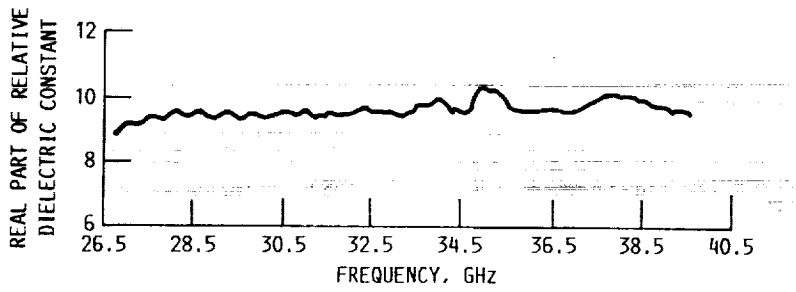

FIGURE 6. - SAPPHIRE SUBSTRATE AT ROOM TEMPERATURE.

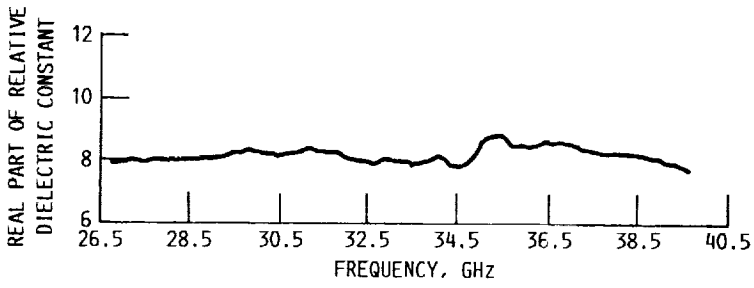

FIGURE 7. - SAPPHIRE SUBSTRATE AT 20 K.

NASA Technical Memorandum 102571

Millimeter Wave Surface Resistance of $RBa_2Cu_3O_{7-\delta}$ (R = Y,Eu,Dy,Sm,Er) Superconductors

F.A. Miranda, W.L. Gordon, and T.G. Eck
Case Western Reserve University
Cleveland, Ohio

K.B. Bhasin, J.D. Warner and K.A. Jenkins
Lewis Research Center
Cleveland, Ohio

Prepared for the
March Meeting of the American Physical Society
Anaheim, California, March 12–16, 1990

NASA

MILLIMETER WAVE SURFACE RESISTANCE OF $RBa_2Cu_3O_{7-\delta}$ (R = Y,Eu,Dy,Sm,Er) SUPERCONDUCTORS

F.A. Miranda, W.L. Gordon, and T.G. Eck
Department of Physics
Case Western Reserve University
Cleveland, Ohio 44106

K.B. Bhasin, J.D. Warner, and K.A. Jenkins
National Aeronautics and Space Administration
Lewis Research Center
Cleveland, Ohio 44135

SUMMARY

We report on the measurements of the millimeter wave surface resistance (R_S) at 58.6 GHz of bulk samples of $RBa_2Cu_3O_{7-\delta}$ (R = Y,Eu,Dy,Sm,Er) and of $YBa_2Cu_3O_{7-\delta}$ superconducting films, in the temperature range from 20 to 300 K. The bulk samples were prepared by cold pressing the powders of $RBa_2Cu_3O_{7-\delta}$ into 1 in. diameter disks which were sintered at 925 °C in one atmosphere of oxygen. The thin films were deposited on $SrTiO_3$ and $LaGaO_3$ substrates by pulsed laser ablation. Each sample was measured by replacing the end wall of a gold-plated TE_{013} circular mode copper cavity with the sample and determining the cavity quality factor Q. From the difference in the Q-factor of the cavity, with and without the sample, the R_S of the sample was determined.

E-5395

INTRODUCTION

Investigation of the properties of the high transition temperature (T_c) superconductors at millimeter wave frequencies is important not only to evaluate their potential for practical microwave applications but also in an attempt to determine the extent to which the standard microscopic theories are able to describe the phenomena of superconductivity in these new materials. From the application point of view, the main interest is to determine how well these materials will perform when implemented to transmission lines and microwave devices in comparison with the most commonly used normal metals (Cu and Au) and lower T_c superconductors currently in use. A parameter which directly provides this information is the surface resistance (R_S). To date, a considerable amount of work has been done on measurements of the R_S both in bulk and thin film high T_c superconductors at different temperatures and frequencies (refs. 1 to 6). Nevertheless, to the best of our knowledge, no measurements of R_S have been reported at frequencies around 60 GHz. In this paper, we report on the measurements of the surface resistance of R-Ba-Cu-O (R = Y,Eu,Dy, Sm,Er) bulk superconductors and $YBa_2Cu_3O_{7-\delta}$ superconducting thin films at 58.6 GHz and at temperatures from 20 to 300 K.

EXPERIMENTAL

The bulk samples were made from cold pressed (20,000 psi) sintered powders made from starting powders of BaO_2 (99.89 percent pure), CuO (99.99 percent pure) and R_2O_3 (R = Y,Eu,Dy,Sm,Er), (99.99 percent pure). The powders were ground together by hand, fired at 925 °C in flowing oxygen (O_2, 99.995 percent pure) for 6 hr, and were cooled to 450 °C at the rate of 2 °C/min. The material was then held at 450 °C for 6 hr before being cooled to room temperature at 2 °C/min. Afterwards, the powders were reground and refired using the same procedure. After the second firing x-ray diffraction showed that the powders were in the superconducting phase. Then the powders were ground and pressed into disks of 1 in. diameter and 1/4-in. thickness and fired at 925 °C.

The pulsed laser ablation technique used for the deposition of the film is similar to that used by other researchers (refs. 7 and 8). The deposition was performed at a substrate temperature of 750 °C at an ambient oxygen pressure of 170 mtorr. The laser wavelength was 248 nm, the pulse length was 20 to 30 ns, and the pulse rate was 4 pps. During deposition, the distance between the target and the sample was kept at 7.5 cm and the laser fluence on the target was maintained at 2.0 J/cm^2 per pulse. During this process, the laser beam was scanned up and down 1 cm over the target using an external lens on a translator. At the end of the deposition process, the oxygen pressure was raised to 1 atm, and the temperature was lowered to 450 °C at a rate of 2 °C/min. The temperature was held at 450 °C for 2 hr before it was lowered to 250 °C at a rate of 2 °C/min. The heater power was turned off and the sample was allowed to cool down to 40 °C or less before it was removed from the chamber. A more detailed description of the deposition technique is given in reference 9.

Surface resistance measurements of both types of samples were made at 58.6 GHz applying the same experimental technique. Using an HP-8510 network analyzer and Ginzton's impedance method (refs. 10 and 11) the Q-factor of the cavity was determined from the reflection coefficient. In each case the end wall of the cylindrical cavity (TE_{013} mode) was replaced by the superconducting sample, and R_s was calculated from the difference in Q values of the bare cavity and the cavity with the sample in place. All the measurements were taken at temperatures from 20 to 300 K, and under a vacuum of less than 10 mtorr.

RESULTS

The dc resistance versus temperature measurements were performed using a standard four probe method. For the bulk samples the transition temperatures (T_c, $R_{dc} = 0$) were distributed between 91.8 K (Eu-Ba-Cu-O) to 79.0 K (Y-Ba-Cu-O and Sm-Ba-Cu-O), as can be seen from dc resistance versus temperature curves shown in figures 1(a) and (b). All the samples had densities from 50 to 60 percent of the ideal, and from SEM micrographs grain sizes of approximately 5 μm were observed. Figure 2 exhibits the measured Q-factor for the cavity as a function of temperature for cases in which its end wall had been replaced by each of the bulk samples under study. It is observed that the Y, Eu, and Dy based samples show a clear increase of the Q-factor at temperatures below T_c, while a rather discrete change is noticed for the Sm-based sample. No change in the rate of increase of Q with decreasing temperature, at temperatures below T_c, is observed for the Er-Ba-Cu-O sample.

Therefore, these observations appear to suggest that although the cold pressing method yields bulk samples with reasonably good T_c values, is does not guarantee obtaining samples with low R_s values. Clear evidence of this is observed in particular in the Er-based sample, and to less extent in the Eu-based sample. The behavior of the Q-factors for the different samples considered is in fair agreement with the concept that the losses in these ceramics appear to be dominated by the weak coupling between grains (ref. 12), especially for grains close to the surface where most of the losses take place.

Figure 3 shows the experimental values of the surface resistance for the Y-, Dy- and Eu based bulk samples. Also plotted is the experimental surface resistance for the gold-plated copper cavity for comparison. It is observed that the R_s for the $YBa_2Cu_3O_{7-\delta}$ sample is smaller than that for the other bulk samples, at temperatures below T_c. The R_s values for the samples at temperatures below T_c are beyond a factor of 2 smaller than the values in the normal state. Nevertheless, none of the samples showed an R_s better than that of the gold-plated cavity even at temperatures below T_c. The fact that the surface resistance obtained for these samples is not comparable with that of gold at any temperature is evidence of the poor quality of the surface of samples prepared by the preparation process considered in this study.

Figure 4 shows the dc resistance versus temperature curves corresponding to $YBa_2Cu_2O_{7-\delta}$ superconducting films deposited on $SrTiO_3$ and $LaGaO_3$ substrates by laser ablation. Zero dc resistance was attained at 90.0 and 88.9 K for the films on $SrTiO_3$ and $LaGaO_3$, respectively. The x-ray diffraction pattern revealed that both films are predominantly c-axis oriented, while SEM micrographs showed that both films are polycrystalline, as can be seen from figure 5. Figure 6 shows the measured Q-factor for the cavity as a function of temperature for cases in which its end wall had been replaced by the $YBa_2Cu_3O_{7-\delta}$ films. A clear increase in the Q-factor is observed for both films at temperatures below T_c, with the rate of increase of the Q-factor with decreasing temperature being higher for the film on $SrTiO_3$ than for the one on $LaGaO_3$ down to 50 K. At temperatures below 50 K we are limited by the resolution of our measurements. Therefore, contrary to what was observed in the bulk material, the value of T_c appears to be directly related with lower microwave losses.

The measured $R_s(T)$ curves for the two films under study are shown in figure 6, in addition to the curve corresponding to the gold-plated copper cavity. The R_s of the films is comparable in the normal state, while the R_s for the film on $SrTiO_3$ was lower than that for the film on $LaGaO_3$ at temperatures just below T_c. Using the normal skin depth formula $R_s = (\omega\mu_o\rho/2)^{1/2}$ a typical resistivity ρ at 300 K of approximately 118 and 158 $\mu\Omega$-cm is obtained for the film $SrTiO_3$ and $LaGaO_3$, respectively. In the superconducting state the films on $SrTiO_3$ and $LaGaO_3$ exhibit a drop of R_s to effective values of 103 and 144 mΩ at 77 K, and 82 and 116 mΩ at 70 K, respectively. The surface resistance at 77 K for the film on $SrTiO_3$ is less than that of the gold-plated cavity, while for the film on $LaGaO_3$ R_s is the same as for the gold-plated cavity. Nevertheless, the value of R_s at 77 K for both films is higher than the theoretical R_s value expected for copper at the same temperature and frequency.

Since we are operating at a fixed frequency, we cannot study the frequency dependence of R_s directly from our measurements. Nevertheless, a comparison

of the R_S values with those reported by other researchers in similar types of films and at different frequencies, may be helpful to formulate a frequency dependence trend for R_S. Thus, using the results obtained by Klein, et al. (ref. 13) for c-axis textured layers samples of $YBa_2Cu_3O_{7-\delta}$, and fitting their data to a quadratic frequency dependence for R_S, gives an R_S value of 102 mΩ at 58.6 GHz and 77 K. This value agrees very well with our experimentally obtained value of 103 mΩ at the same temperature. A similar approach was used for the film on $LaGaO_3$. Using the values for R_S at 22, 86, and 148 GHz and at 70 K reported by Cooke, et al. (ref. 14) for a $YBa_2Cu_3O_{7-\delta}$ superconducting film deposited by magnetron sputtering on $LaGaO_3$, we were able to find by interpolation an R_S value of 106 mΩ at 58.6 GHz. This value is within experimental uncertainty of our measured value of 116 mΩ. These results indicate that our value fit well with the nearly quadratic dependence for R_S ($R_S \alpha \omega^n$, $n = 2.06 \pm 0.14$) reported by Cooke, et al. (ref. 14). Our results, as well as those obtained by the above mentioned researchers, indicates that the quadratic dependence observed for R_S is consistent with the experimental behavior observed in low T_C superconductors and also with the predictions of the BCS theory.

CONCLUSIONS

There appears to be no direct correlation between the surface resistance R_S and the transition temperature T_C in the $RBa_2Cu_3O_{7-\delta}$ bulk superconducting samples obtained by the cold pressing preparation method. Therefore, the dominating factors which control the microwave losses can only be guessed at. Some of the possible factors which could control the losses are: the weak coupling at grain boundaries, the purity of the sample and the possible segregation of composition at the surface. Two main factors can contribute to the presence of weak coupling. The first is the intrinsic mismatch of the lattice and the segregation of impurities to the grain boundaries, while the second could be reactions with the ambient environment (i.e., water vapor and CO_2). This environmental reactions primarily occur at the surface and would not appreciably affect the bulk properties in a short time period. If the losses are due to either the reaction of the surface with the environment or due to porosity, then a different pressing process to make denser pellets should give samples with lower microwave losses.

For the $YBa_2Cu_3O_{7-\delta}$ superconducting films on $SrTiO_3$ and $LaGaO_3$ we found from a correlation of the R_S values obtained for both films with those obtained for similar films measured by other researchers at different frequencies, that these values are consistent with the frequency dependence for R_S observed in classical superconductors, and also with the predictions of the BCS theory.

In summary, we have measured the R_S of bulk $RBa_2Cu_3O_{7-\delta}$ (R = Y,Dy,Eu, Sm,Er) superconducting samples and found that none of them performed as well as gold. Also, for the 1.2 μm thin films of $YBa_2Cu_3O_{7-\delta}$ on $SrTiO_3$ and $LaGaO_3$ we obtained values of R_S significantly lower than gold at temperatures below 70 K, but we are limited by the resolution of our measurement in accurately determining R_S values below 50 K.

REFERENCES

1. Cohen, L., et al.: Surface Impedance Measurements of Superconductivity $YBa_2Cu_3O_{6+x}$. J. Phys. F: Met. Phys., vol. 17, 1987, pp. L179-L183.

2. Sridhar, S.; Shiffman, C.A.; and Hamoleh, H.: Electrodynamic Response of $Y_1Ba_2Cu_3O_y$ and $La_{1.85}Sr_{0.15}CuO_{4-\delta}$ in the Superconducting State. Phys. Rev. B, vol. 36, no. 4, Aug. 1, 1987, pp. 2301-2304.

3. Martens, J.S.; Beyer, J.B.; and Ginley, D.S.: Microwave Surface Resistance of $YBa_2Cu_3O_{6.9}$ Superconduting Films. Appl. Phys. Lett., vol. 52, no. 21, May 23, 1988, pp. 1822-1824.

4. Carini, J.P., et al.: Millimeter-Wave Surface Resistance Measurements in Highly Oriented $YBa_2Cu_3O_{7-\delta}$ Thin Films. Phys. Rev. B, vol. 37, no. 16, June 1, 1988, pp. 9726-9729.

5. Newman, H.S., et al.: Microwave Surface Resistance of Bulk Ti-Ba-Ca-Cu-O Superconductors. Appl. Phys. Lett., vol. 54, no. 4, Jan. 23, 1989, pp. 389-390.

6. Klein, N., et al.: Millimeter Wave Surface Resistance of Epitaxially Grown $YBa_2Cu_3O_{7-x}$ Thin Films. Appl. Phys. Lett., vol. 54, no. 8, Feb. 20, 1989, pp. 757-759.

7. Inam, A., et al.: As-Deposited High T_c and T_c Superconducting Thin Films Made at Low Temperatures. Appl. Phys. Lett., vol. 53, no. 10, Sept. 5, 1988, pp. 908-910.

8. Roas, B.; Schultz, L.; and Endres, G.: Epitaxial Growth of $YBa_2Cu_3O_{7-x}$ Thin Films by a Laser Evaporation Process. Appl. Phys. Lett., vol. 53, no. 16, Oct. 17, 1988, pp. 1557-1559.

9. Warner, J.D.; Meola, J.E.; and Jenkins, K.A.: Study of Deposition of $YBa_2Cu_3O_{7-x}$ on Cubic Zirconia. NASA TM-102350, 1989.

10. Ginzton, E.L.: Microwave Measurements. McGraw-Hill, 1957, p. 406.

11. Romanosky, R.R.: Analytical and Experimental Procedures for Determining Propagation Characteristics of Millimeter-Wave Gallium Arsenide Microstrip Lines. NASA TP-2899, 1989.

12. Hylton, T.L., et al.: Weakly Coupled Grain Model of High-Frequency Losses in High T_c Superconducting Thin Films. Appl. Phys. Lett., vol. 53, no. 14, Oct. 3, 1988, pp. 1343-1345.

13. Klein, N., et al.: Millimeter Wave Surface Resistance and London Penetration Depth of Epitaxially Grown $YBa_2Cu_3O_{7-x}$. Physica C, vol. 162, Dec. 1989, pp. 1549-1550.

14. Cooke, D.W., et al.: Surface Resistance of $YBa_2Cu_3O_7$ Films Deposited on $LaGaO_3$ Substrates. Physica C, vol. 162, Dec. 1989, pp. 1537-1538.

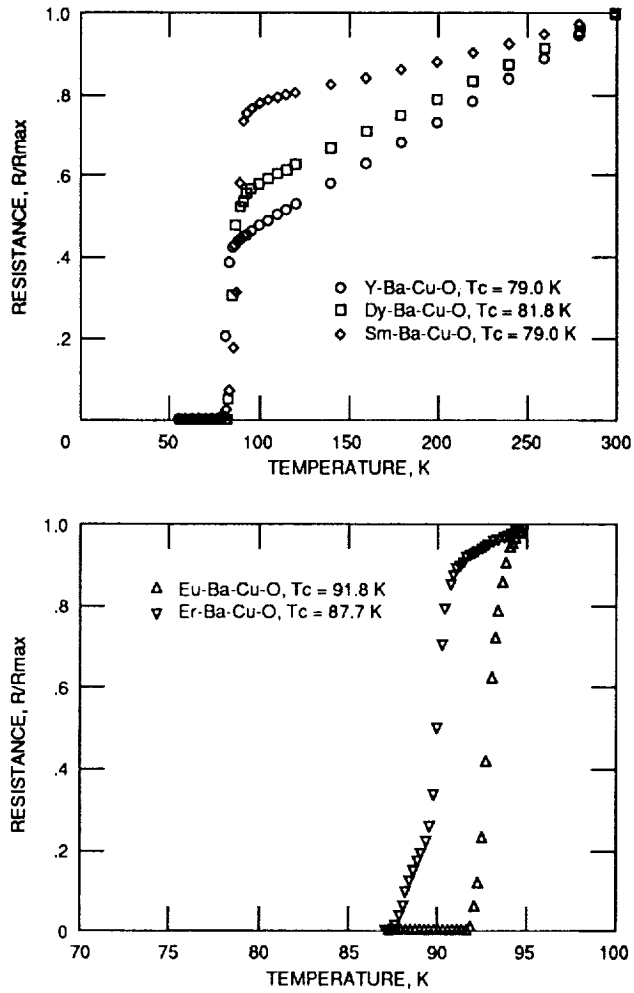

Figure 1. - dc resistance versus temperature measurements of bulk superconducting samples.

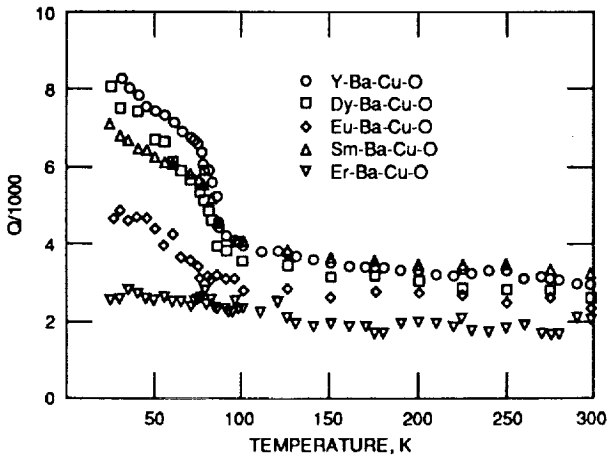

Figure 2. - Measured Q of the cavity, with one end wall replaced by the bulk sample, as a function of temperature.

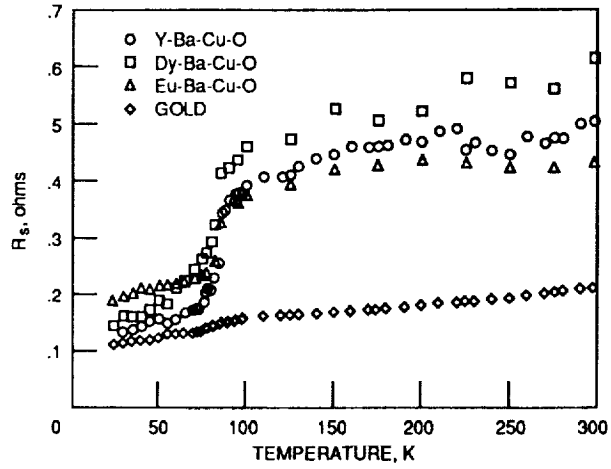

Figure 3. - Surface resistance R_s as a function of temperature and at 58.6 GHz, for bulk superconducting samples.

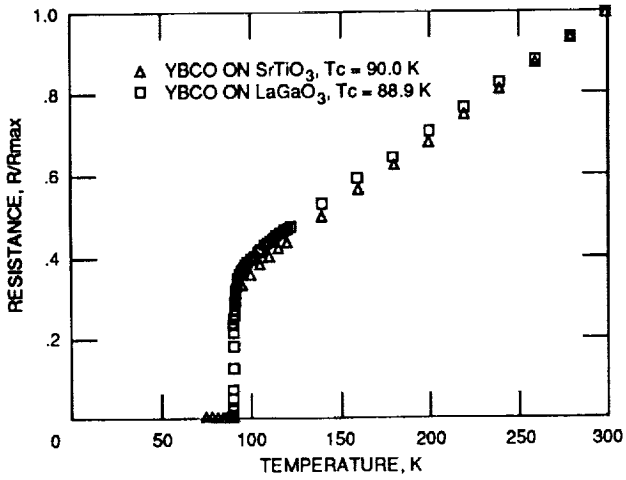

Figure 4. - dc resistance versus temperature measurements of laser ablated $YBa_2Cu_3O_{7-\delta}$ superconducting films on $SrTiO_3$ and $LaGaO_3$ substrates.

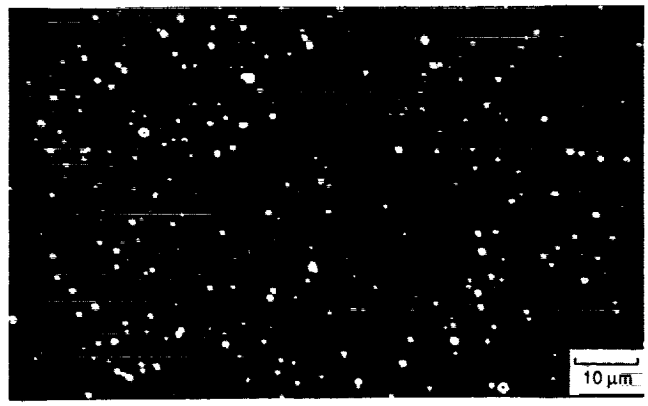

(a)

(b)

Figure 5. - Scanning electron micrographs of laser ablated $YBa_2Cu_3O_{7-\delta}$ superconducting films on $SrTiO_3$ (a) and $LaGaO_3$ (b) substrates.

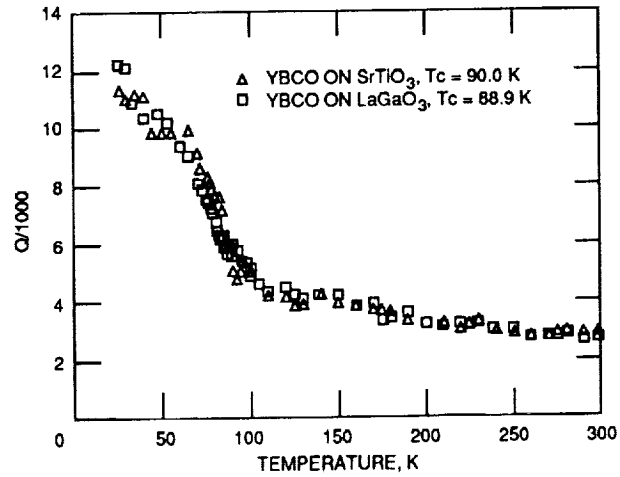

Figure 6. - Measured Q of the cavity, with one end wall replaced by the thin film, as a function of temperature.

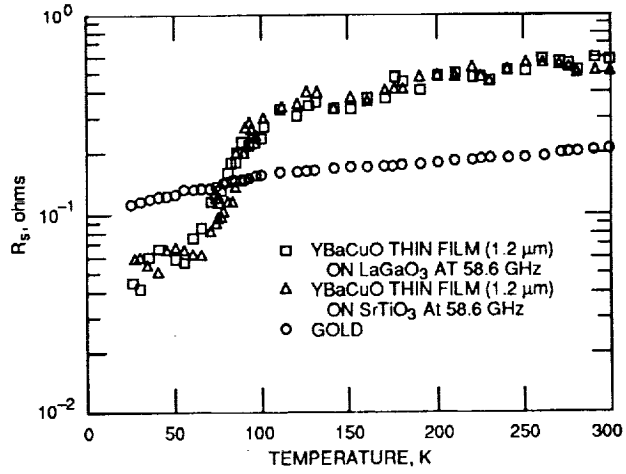

Figure 7. - Surface resistance (R_s) at 58.6 GHz versus temperature for 1.2 μm films of $YBa_2Cu_3O_{7-\delta}$ deposited by laser ablation onto $SrTiO_3$ and $LaGaO_3$ substrates, and for gold-plated cavity.

NASA Technical Memorandum 102346

Growth and Patterning of Laser Ablated Superconducting $YBa_2Cu_3O_7$ Films on $LaAlO_3$ Substrates

J.D. Warner, K.B. Bhasin, N.C. Varaljay, and D.Y. Bohman
National Aeronautics and Space Administration
Lewis Research Center
Cleveland, Ohio

and

C.M. Chorey
Sverdrup Technology, Inc.
NASA Lewis Research Center Group
Cleveland, Ohio

ERRATA

NASA Technical Memorandum 102436

GROWTH AND PATTERNING OF LASER ABLATED SUPERCONDUCTING $YBa_2Cu_3O_7$ FILMS ON $LaAlO_3$ SUBSTRATES

J.D. Warner, K.B. Bhasin, N.C. Varaljay, D.Y. Bohman, and C.M. Chorey
February 1990

Cover and page 8: The NASA report number 102346 should be replaced by 102436.

Prepared for the
36th National Symposium and Topical Conference
sponsored by the American Vacuum Society
Boston, Massachusetts, October 23-27, 1989

NASA

GROWTH AND PATTERNING OF LASER ABLATED SUPERCONDUCTING $YBa_2Cu_3O_7$, FILMS ON $LaAlO_3$ SUBSTRATES

J.D. Warner, K.B. Bhasin, N.C. Varaljay, D.Y. Bohman,
NASA Lewis Research Center Cleveland, OH 44135

C.M. Chorey*
Sverdrup Technology, Inc., NASA Lewis Research Center Group,
Cleveland, OH 44135

ABSTRACT

A high quality superconducting film on a substrate with a low dielectric constant is desired for passive microwave circuit applications. In addition, it is essential that the patterning process does not effect the superconducting properties of the thin films to achieve the highest circuit operating temperatures. We have grown $YBa_2Cu_3O_7$ superconducting films on lanthanum aluminate substrates using a laser ablation technique with resulting maximum transition temperature (T_c) of 90 K. The films were grown on $LaAlO_3$ which was at 775 °C and in 170 mtorr of oxygen and slowly cooled to room temperature in 1 atm of oxygen. These films were then processed using photolithography and a negative photoresist with an etch solution of bromine and ethanol. Results are presented on the effect of the processing on T_c of the film.

I. INTRODUCTION

Laser-ablated, high-temperature superconducting (HTS) $YBa_2Cu_3O_7$ films have been made on many substrates including $SrTiO_3$, MgO, $LaGaO_3$, and ZrO_2.[1-7] These substrates were used because they either had very small interaction with the HTS films during growth or annealing or because the substrates with HTS films had potential electronic applications. In this paper, we report on the growth and patterning of thin $YBa_2Cu_3O_7$ films on $LaAlO_3$ for microwave applications. $LaAlO_3$ was chosen as a substrate because of its relatively low dielectric constant of 22[8] and because of it moderate loss tangent of $8x10^{-5}$ at 10 GHz[9].

Lines varying in width from 10 to 20 μm were patterned using photolithography and wet etching techniques. To determine if the etching or lithography process had influenced the transition temperature of the films. A ring resonator circuit operating at 35 GHz was also fabricated, since the resonator allows the determination of loss and dispersive properties of microstrip transmission line. From the measurement of the quality factor "Q" of a resonator circuit one can determine the microwave losses of the HTS films as compared with those of gold on the same substrates.

*Work done under NASA contract #NAS3-25266; Regis Leonard, monitor.

II. Film Growth

The laser ablation technique used to grow the films on substrates of $LaAlO_3$ is similar to the techniques reported in the literature.[1-7] The details of the geometry of the laser ablation is shown in Fig. 1. The substrates (15 by 15 by 0.25 mm) with orientation (001) were mounted onto a stainless steel plate with a diameter of 63 mm. The plate was heated from the backside using a resistive heater made from Kanthal A-1 wire (made by Kanthal, Inc.). The temperature was measured with a type K thermocouple which was welded to the plate. The thermocouple was 2 mm away from the sample. The sample chamber was evacuated to $3x10^{-7}$ torr, or lower, using a liquid nitrogen cold trapped diffusion pump before the sample was warmed up to 500 °C. A continuous flow of oxygen (120 sccm) was then introduced into the chamber, and the sample heated to 775 °C. During deposition the chamber pressure was 170 mtorr; the laser wavelength was 248 nm; the energy density was 1.5 (J/cm^2)/pulse; the pulse rate was 4 pps; and the distance between the target and the sample was 8 cm. The laser beam was rastered up and down 1 cm over the target using an external lens on a translator. The angle between the laser beam and the normal to the target was 45°. The target used was a sintered 25-mm-diameter pellet of $YBa_2Cu_3O_{7-x}$. After deposition the oxygen pressure was raised to 1 atm, and the temperature was lowered to 450 °C at a rate of 2 °C/min. The temperature was held at 450° C for 2 hr before it was lowered to 250 °C at a rate of 2 °C/min. The heater power was then turned off, and the sample was allowed to cool to 40 °C or less before it was removed the chamber.

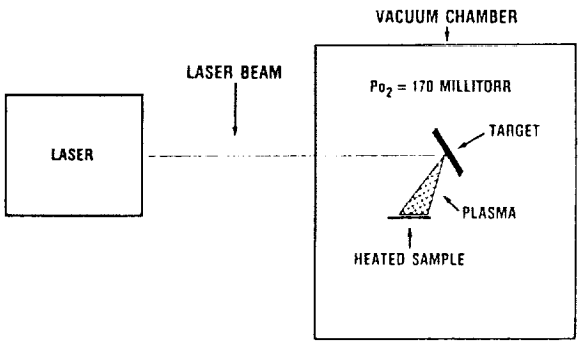

Figure 1. - Schematic of the laser ablation experiment.

The thickness of the HTS films on $LaAlO_3$ was estimated by measuring the thickness of a film grown on quartz plate that was shadow masked. The quartz plate had been placed 1 mm below the bottom of the $LaAlO_3$ on the substrate holder such that the sweep of the plasma plumb was along the line connecting the centers of the quartz and the $LaAlO_3$.

The best film had a T_c of 89.8 K immediately after deposition as determined by a standard four point resistance measurement. Its resistance versus temperature behavior is shown in Fig.2. From the intercept of the extrapolated resistance at 0 K and from the resistance above T_c, one can see that the film is c-axis aligned. This is confirmed by only having the (001) peaks in the x-ray diffraction data (Fig. 3). The surface morphology of the HTS on $LaAlO_3$ is shown in Fig. 4. The surface is very smooth with some small structure. We do not observe large numbers of HTS particulates due to the laser ablation process.

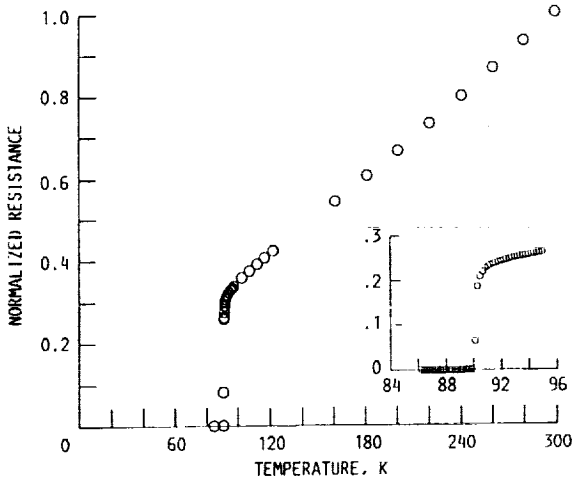

Figure 2. - Normalized resistance of laser ablated $YBa_2Cu_3O_x$ film on $LaAlO_3$.

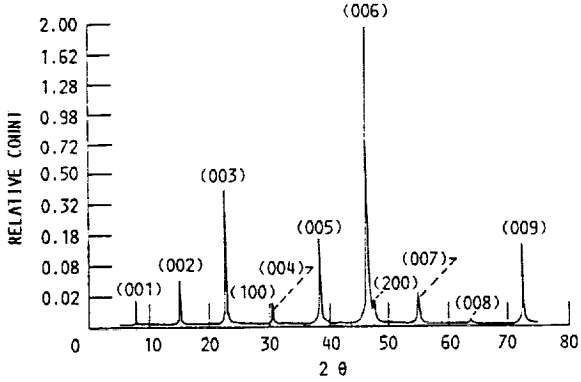

Figure 3. - X-ray diffraction pattern of laser ablated $YBa_2Cu_3O_x$ film on $LaAlO_3$.

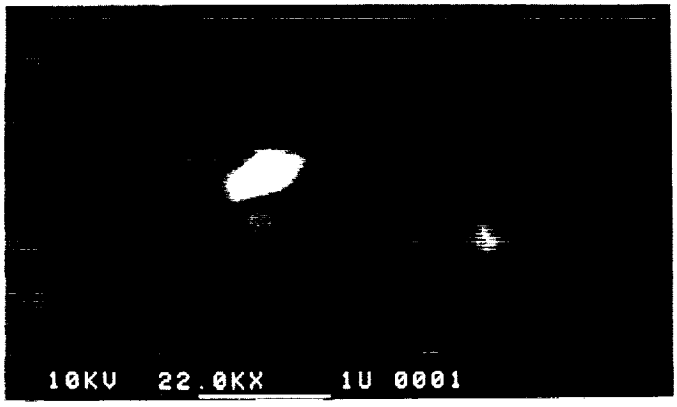

Figure 4. - Scanning electron micrograph of laser ablated $YBa_2Cu_3O_x$ Film on $LaAlO_3$.

PATTERNING

Films on $LaAlO_3$ and $SrTiO_3$ were patterned using photolithography and wet etching. The negative photoresist (752), its developer (802), and the associated rinse (n-butyl acetate) used were obtained from KTI. The photoresist strippers used were Losalin IV (from E.C. Merke), acetone, toluene, and ethanol. Each step of the process was checked to see if it had an effect on the T_c of the HTS films. The results of the different processing steps on T_c are shown in table I. The full process of patterning the HTS films was to spin on the negative photoresist to a thickness of 2 μm, followed by a soft bake at 90° C for 1 hr, and then to expose the photoresist. After developing the photoresist, the film was etched for 500 s in 1 percent molar of bromine in ethanol. After etching, the films were rinsed in ethanol and the photoresist was removed with the Losalin IV photoresist stripper which was at 70 °C. We did not observed any drop in the T_c of the HTS films.

Table I Effect of Photolithography Process on T_c of $YBa_2Cu_3O_x$ Films

Exposure to negative photoresist	None
Soft baking of photoresistat 90 °C for 1 hr)	None
Exposure to photoresist developer and rinse	None
Exposure to different stripping solvents after patterning[a]:	
Boiling ascetone (58 °C) for 10 min	None
Boiling ethanol (78 °C) for 10 min	None
Boiling toluene (111 °C) for 10 min	None
Losalin IV (760 °C) for 5 min	None

[a]Only boiling ethanol and Losalin IV sucessfully removed exposed phoresist.

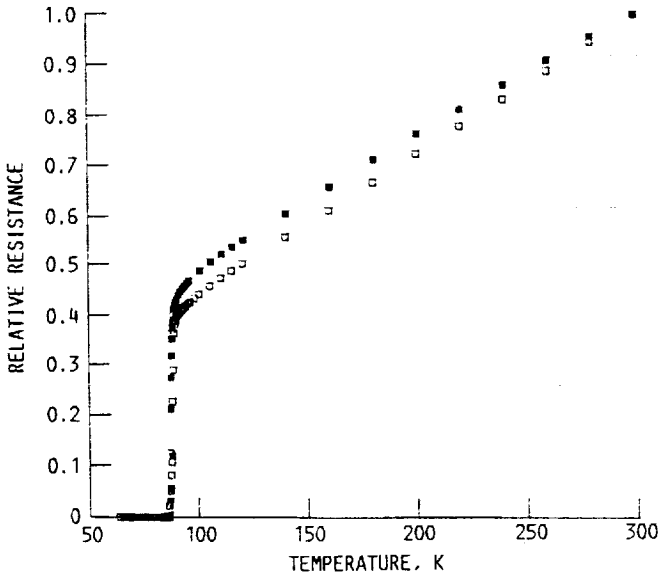

Figure 5. - Normalized resistance of a laser ablated $YBa_2Cu_3O_x$ film on $SrTiO_3$. The film □ is before processing while the film ■ is after exposure to negative photoresist.

The films used to determine the effect of the various fabrication steps had transition temperatures between 77 and 85 K. Fig. 5 shows the effect of exposing the film directly to the photoresist stripper Losalin IV at 70° C. No change in T_c occurred, but the slope of the resistance versus temperature curve did change. Fig. 6 shows the T_c of the film on $LaAlO_3$ before patterning and after it was patterned into a ring resonator, that had operated at 33 GHz, and after it had

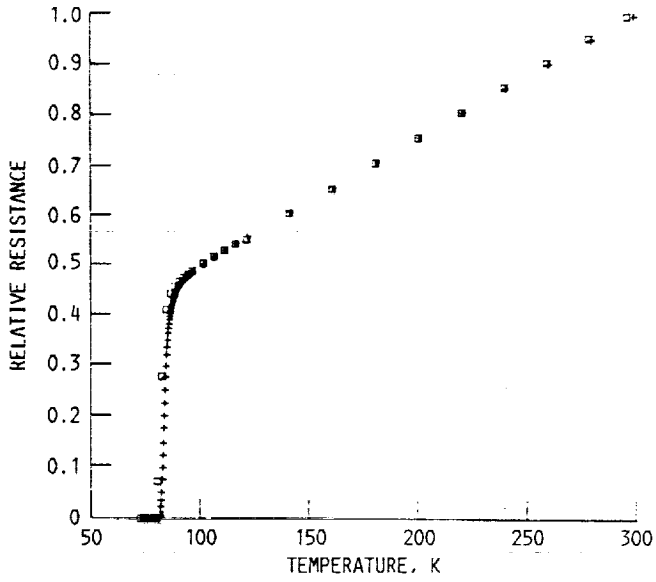

Figure 6. - Comparison of normalized resistance of a laser ablated $YBa_2Cu_3O_x$ film on $LaAlO_3$ before processing □ and after being fabricated into a 35-GHz ring resonator +.

silver contacts evaporated onto it and annealed at 500° C for 1 hr. There is no apparent difference in the T_c or the resistance versus temperature behavior between the film before and after processing.

To test the laser ablation technique's ability to produce uniform film thickness and the variation of T_c across the film, Hall bars with silver contacts were fabricated (Fig. 7). The width of the bar is 10 μm. The film thickness is not very uniform over the 5- by 10-mm area. The time needed to etch the film until the substrate was exposed varied by a factor of 2 from one edge to the other edge of the substrate. However, the T_c did not vary from region to region (table II).

Figure 7. - Finished Hall bar of $YBa_2Cu_3O_x$ film on $SrTiO_3$ substrate.

Table II Variation of on $SrTiO_3$ as Measured With Patterned Hall Bars

Before patterning	70.8 K
10- μm lines after patterning	71.0, 71.5, 72.5 K
20- μm lines after patterning	75.3, 75.5, 76.5 K

Conclusions

Laser-ablated, high-temperature superconducting films on $LaAlO_3$ and $SrTiO_3$ have been grown. The best films had a T_c of 90 K and have their c-axis aligned to the substrate. There is no variation of T_c across the films, but there is a variation of film thickness. These films have been patterned with negative photoresist and a bromine/ethanol etch. There is no detectable degradation of T_c by any step of the fabrication process even though the films were heated to 122° C in toulene.

This fabrication process should be able to be used to make most of the passive and one layer structures without any degradation of the transition temperature.

REFERNCES

1. J.D. Warner, J.E. Meola, and K.A. Jenkins, NASA TM-102350, 1989.

2. D. Dijkkamp, T. Venkatesan, X.D. Wu, S.A. Shaheen, N. Jisrawi, Y.H. Min-Lee, and W.L. Mclean, M. Croft, Appl. Phys. Lett. **51**, 619 (1987).

3. X.D. Wu, D. Dijkkamp, S.B. Ogale, A. Inam, E.W. Chase, P.F. Miceli, C.C. Chang, J.M. Tarascon, and T. Venkatesan, Appl. Phys. Lett. **51**, 861 (1987).

4. J. Narayan, N. Biunno, R. Singh, O.W. Holland, and O. Auciello, Appl. Phys. Lett. **51**, 1845 (1987).

5. L. Lynds, B.R. Weinberger, G.G. Peterson, and H.A. Kransinski, Appl. Phys. Lett. **52**, 320 (1988).

6. T. Venkatesan, C.C. Chang, D. Dijkkamp, S.B. Ogale, E.W. Chase, L.A. Farrow, D.M. Hwang, P.F. Miceli, S.A. Shwarz, J.M. Tarascon, X. D. Wu, and A. Inam, J. Appl. Phys. **63**, 4591 (1988).

7. A.M. Desantolo, M.L. Mandich, S. Sunshine, B.A. Davidson, R.M. Fleming, P. Marsh, and T.Y. Kometani, Appl. Phys. Lett. **52**, 1995 (1988)

8. F.A. Miranda, W.L. Gordon, V.O. Heinen, B.T. Ebihara, and K.B. Bhasin, NASA TM-102123, 1989.

9. R.W. Simon, C.E. Platt, A.E. Lee, G.S. Lee, and K. Daly, Appl. Phys. Lett., **53**, 2677 (1988).

COMPLEX PERMITTIVITY OF LANTHANUM ALUMINATE IN THE 20 TO 300 K TEMPERATURE RANGE FROM 26.5 TO 40.0 GHZ

F. A. Miranda and W. L. Gordon
Case Western Reserve University
Cleveland, Ohio 44106

K. B. Bhasin, B. T. Ebihara, and V. O. Heinen
Lewis Research Center
Cleveland, Ohio 44135

C. M. Chorey
Sverdrup Technology, Inc.
NASA Lewis Research Center Group
Cleveland, Ohio 44135

KEY TERMS

Complex permittivity, superconductors, lanthanum aluminate substrates, microwave measurements

ABSTRACT

Dielectric constants of microwave substrates are required in the design of superconducting microwave circuits at various temperatures. In this paper, we report the results of a study of the complex permittivity of the newly developed lanthanum aluminate ($LaAlO_3$) substrate, in the 20 to 300 K temperature range at frequencies from 26.5 to 40.0 GHz. The value of the complex permittivity was obtained by measuring the sample scattering parameters using a microwave waveguide technique. It is observed that, while the dielectric constant did not change appreciably with frequency, its value decreased by approximately 14 percent from room temperature to 20 K.

INTRODUCTION

The discovery [1] of high transition temperature (T_c) oxide superconductors has opened up a wealth of attractive possibilities, among which, their application in the preparation of thin films to be used in the development of microwave circuits. Therefore, a good knowledge of the dielectric properties of microwave substrates used for film deposition is of paramount importance. Substrates with low dielectric constant and loss tangent [2] are indispensable in order to develop highly reliable microwave components.

At the moment, Y–Ba–Cu–O superconducting thin films deposited in $SrTiO_3$ substrates have shown the best quality when compared with films deposited in other substrates. Unfortunately, its microwave applicability is very limited because of the strong temperature dependence of its dielectric constant —with a value of 300 at room temperature, of 1000 at 77 K, and over 18,000 below 4 K—and its relatively high loss tangent [3].

The recently developed $LaAlO_3$ substrate is actually being used in the fabrication of high T_c superconducting thin films. Nevertheless, the value of its dielectric constant at room temperature and at low temperatures is still not well established. In this paper, we report on the measurements of the microwave complex permittivity of $LaAlO_3$ in the 20 to 300 K temperature range and as a function of frequency.

ANALYSIS

The method for the derivation of the complex permittivity from the sample scattering parameters was first proposed by Nicolson and Ross [4] and modified later for rectangular waveguide applications by Weir [5]. Essentially, for a piece of material properly introduced in a rectangular waveguide with characteristic impedance Z_0 (as shown in Figure 1), the solution of the boundary conditions at $x = 0$ and $x = d$ allows the scattering parameters $S_{11}(\omega)$ and $S_{21}(\omega)$ to be related with the reflection (Γ) and transmission (T) coefficients in the following way:

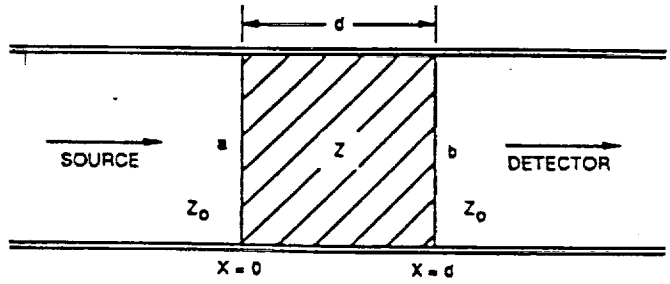

Figure 1 Waveguide with filled material

$$S_{11} = \frac{(1 - T^2)\Gamma}{1 - \Gamma^2 T^2}, \qquad S_{21} = \frac{(1 - \Gamma^2)T}{1 - \Gamma^2 T^2} \tag{1}$$

where

$$\Gamma = \frac{Z - Z_0}{Z + Z_0} = \sqrt{\frac{(\mu_r/\epsilon_r) - 1}{(\mu_r/\epsilon_r) + 1}} \tag{2}$$

and

$$T = \exp(-j\omega\sqrt{\mu\epsilon}\, d) = \exp\left[\left(-j\frac{\omega}{c}\right)\sqrt{\mu_r\epsilon_r}\, d\right] \tag{3}$$

In Equations (2) and (3), Z is the impedance of the sample, d is its thickness, and μ_r and ϵ_r, its relative permeability and permittivity, respectively. Therefore, one can obtain Γ and T from $S_{11}(\omega)$ and $S_{21}(\omega)$, and, in turn, they can be used to determine the permittivity.

The measurements of the reflection, $S_{11}(\omega)$, and transmission, $S_{21}(\omega)$, scattering parameters were performed using an HP-8510 automatic network analyzer, conveniently connected through an arrangement of Ka-band (26.5 to 40.0 GHz) waveguides to a cryogenic system, which allows measurements to be taken at the desired low temperatures. The cryogenic system consists of a closed-cycle helium refrigerator combined with a temperature controller, and an aluminum vacuum chamber, specially designed to fit on top of the external shield of the refrigerator and to give access to the arrangement of waveguides. A vacuum of less than 1.0×10^{-2} torr was maintained throughout the whole measurement procedure. During the actual measurements, the $LaAlO_3$ substrate was suspended perpendicular to the microwave source between two waveguide flanges in such a way that both the transmitted and reflected power can be detected.

Finally, the dielectric constant of $LaAlO_3$ was also measured at room temperature using the well-established parallel-plate capacitor technique, and the value obtained was compared with the one acquired using the scattering parameters method. The capacitor was made with a 10-mil lanthanum aluminate substrate as the filling dielectric, and its plates were made by evaporating gold such that a 1-cm disk was formed on its front surface, with its back surface being completely coated.

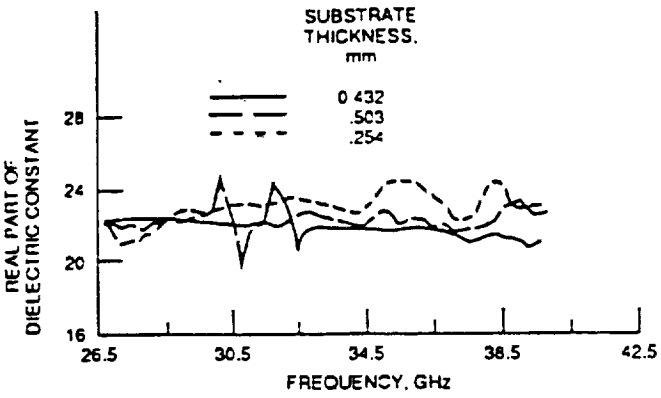

Figure 2 Real part of complex permittivity of $LaAlO_3$ substrates at room temperature

TABLE 1 Complex Permittivity of $LaAlO_3$ at 28.6 GHz

Temperature, K	Real Part of Complex Permittivity, ϵ'	Imaginary Part of Complex Permittivity, ϵ''
300	22.0	1.10
150	20.8	1.10
70	19.7	1.07
20	18.9	0.20

RESULTS

Figure 2 and Table 1 show the results for the room temperature measurements of the dielectric constant for three $LaAlO_3$ substrates. The substrates are 0.254, 0.432, and 0.503 mm thick and were made from different batches of $LaAlO_3$. The value of the dielectric constant is consistent for the three samples, and it has a typical value of approximately 22 ± 1. Hence, neither the difference in thickness nor the fact that the samples come from different batches appears to be an important factor in the determination of the value of the dielectric constant for this substrate. It is also noticed that the frequency dependence for this parameter in the band under consideration is a weak one. We believe that the discontinuities and small variations observed in Figures 2 and 3 are due to systematic errors in the calibration and not to intrinsic properties of the samples.

Although the values of the dielectric constant obtained for the three samples under consideration are in good agreement, they differ considerably from the one reported by Simon et al.

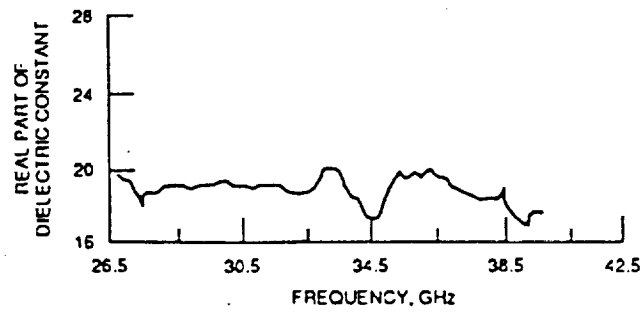

Figure 3 Real part of complex permittivity of $LaAlO_3$ substrate at 20 K

[2]. In view of this discrepancy, we performed measurements on magnesium oxide (MgO), sapphire (Al_2O_3), and silicon oxide (SiO_2), which are substrates with well-known values for the dielectric constant at room temperature. The results of our measurements were consistent with those reported by other researchers [6–8]. Furthermore, we obtained the value of the dielectric constant ϵ of $LaAlO_3$ using a parallel-plate capacitor and the following relations:

$$\epsilon = \frac{\text{measured capacitance}}{\text{ideal vacuum capacitance}} = \frac{C_{\text{measured}}}{C_{\text{ideal vacuum}}} \quad (4)$$

$$C_{\text{ideal vacuum}} = \frac{\epsilon_0 \times \text{area disk}}{\text{plate separation}} = \frac{\epsilon_0 \pi r^2}{d} \quad (5)$$

$$C_{\text{measured}} = \text{measured value} - \text{edge capacitance} \quad (6)$$

and

$$\frac{\text{edge capacitance}}{\text{perimeter}} = -0.229 + 0.105(\epsilon) + 0.214 \log\left(\frac{2\pi r}{d}\right) \quad (7)$$

The value obtained using this approach was $\epsilon \simeq 20 \pm 1$ at 1 MHz. Although this value is a little lower than the one derived using the scattering parameters technique, the two values still are in a better agreement than with the results of [2]. Further, because of the relatively low frequency at which this value was measured, it provides an additional indication of the small variation of the dielectric constant of $LaAlO_3$ as a function of frequency.

Table 1 shows the real and imaginary parts of the complex permittivity at four different temperatures, and at 28.6 GHz, for the sample represented with the small dashed line in Figure 2. Figure 3 shows the real part of the complex permittivity for this same sample at 20 K. A decrease of 14% in the value of the dielectric constant at temperatures around 20 K is observed. Although this change can be considered as a relatively large one, it is almost meaningless when compared with the temperature dependence of the dielectric constant of $SrTiO_3$. Now, from the data in Table 1, it is seen that the value of the imaginary part of the complex permittivity tends to decrease with decreasing temperature. Nevertheless, a comparison of our results at room temperature for MgO, Al_2O_3, and SiO_2 substrates was not in good agreement with previously reported values [6–8]. Because for these substrates the values for the dielectric constant and the loss tangent at room temperature are well established, our confidence in the values for the imaginary part of the permittivity, not only at room temperature but also at low temperature, is rather limited. Therefore, for cases in which an accurate knowledge of this parameter is indispensable and mainly when dealing with low-loss substrates, other techniques must be applied.

CONCLUSIONS

The complex permittivity of the newly developed $LaAlO_3$ substrate has been measured. A decrease in the value of the real part of the complex permittivity with decreasing temperature was observed. No considerable change was noticed in this parameter, neither as a function of frequency nor due to difference in thicknesses and batch of origin. The values obtained for the imaginary part of the complex permittivity, both at room temperature and at low temperature, appear not

to be very accurate, mainly due to limitations of the applied technique when used with very low-loss substrates. The results obtained in this study suggest that, at least from the standpoint of the dielectric constant, the $LaAlO_3$ substrate is better suited than $SrTiO_3$, for use with the new high-temperature superconductors in microwave applications.

REFERENCES

1. J. G. Bednorz and K. A. Muller, "Possible High T_c Superconductivity in the Ba-La-Cu-O System," *Z. Phys. B*, Vol. 64, 1986, pp. 189–193.
2. R. W. Simon, C. E. Platt, A. E. Lee, G. S. Lee, K. P. Daly, M. S. Wire, J. A. Luine, and M. Urbanik, "Low-Loss Substrate for Epitaxial Growth of High-Temperature Superconductor Thin Films," *Appl. Phys. Lett.*, Vol. 53, No. 26, Dec. 26, 1988, pp. 2677–2679.
3. H. Padamsee, K. Green, J. Gruschus, J. Kirchgessner, D. Moffat, D. L. Rubin, J. Sears, Q. S. Shu, R. Buhrman, D. Lathrop, T. W. Noh, S. Russek, and A. Sievers, "Superconductivity and Applications," unpublished.
4. A. M. Nicolson and G. F. Ross, "Measurement of the Intrinsic Properties of Materials by Time Domain Techniques," *IEEE Trans. Instrum. Meas.*, Vol. IM-19, No. 4, Nov. 1970, pp. 377–382.
5. W. B. Weir, "Automatic Measurement of Complex Dielectric Constant and Permeability at Microwave Frequencies," *Proc. IEEE*, Vol. 62, No. 1, Jan. 1974, pp. 33–36.
6. M. D. Hossain, "Microwave Dielectric Properties of Ti^{4+}/MgO and Ni^{2+}/MgO," *Appl. Phys. A*, Vol. 36, No. 1, 1985, pp. 63–65.
7. A. R. Von Hippel, "*Dielectric Materials and Applications*," The MIT Press, Cambridge, MA, 1954.
8. C. Zahopoulos, W. L. Kennedy, and S. Sridhar, "Performance of a Fully Superconducting Microwave Cavity Made of the High T_c Superconductor $Y_1Ba_2Cu_3O_x$," *Appl. Phys. Lett.*, Vol. 52, No. 25, June 20, 1988, pp. 2168–2170.

Received 9-14-89

Microwave and Optical Technology Letters, 3/1, 11–13

CCC 0895-2477/90/$4.00

PERFORMANCE AND MODELING OF SUPERCONDUCTING RING RESONATORS AT MILLIMETER-WAVE FREQUENCIES

K.B. Bhasin, C.M. Chorey*, J.D. Warner, R.R. Romanofsky and V.O. Heinen

NASA Lewis Research Center
21000 Brookpark Road
Cleveland, OH 44135

*Sverdrup Technology/LeRC Group
2001 Aerospace Parkway
Cleveland, OH 44142

K. S. Kong, H. Y. Lee and T. Itoh
Department of Electrical and Computer Engineering
The University of Texas at Austin
Austin, TX 78712

ABSTRACT

Microstrip ring resonators operating at 35 GHz have been fabricated from laser ablated YBCO thin films deposited on lanthanum aluminate substrates. They were measured over a range of temperatures and their performance compared to identical resonators made of evaporated gold. Below 60° Kelvin the superconducting strip performed better than the gold, reaching an unloaded 'Q' ~1.5 times that of gold at 25° K. A shift in the resonant frequency follows the form predicted by the London equations. The Phenomenological Loss Equivalence Method is applied to the ring resonator and the theoretically calculated Q values are compared to the experimental results.

INTRODUCTION

Recent observations of low surface resistance at microwave and millimeter wave frequencies in thin superconducting films [1] suggest their use for low loss/high Q microstrip circuits. Of interest is the surface resistance exhibited by these films across a wide frequency range. To date, measurements of surface resistance in the Ka band and above have been by the cavity technique. This technique fails to model microstrip losses completely because it neglects substrate losses and fails to adequately probe the film-substrate interface. Microstrip resonators patterned from thin films on microwave substrates allow direct measurement of microstrip losses. Several groups have made such measurements at lower microwave frequencies.[2,3,4] In this paper we report on the direct measurement of losses by Ka band microstrip resonators made from laser ablated YBCO films on lanthanum aluminate. Also, we calculate the Q values of the structure using the Phenomenological Loss Equivalence Method and invoking superposition of the internal impedances of the strip and ground plane of the microstrip line. The calculated Q value of the ring resonator with a superconducting strip and a normal conducting ground plane is compared with the experimental results.

GROWTH AND PATTERNING

The superconducting films were deposited by laser ablation of a sintered YBCO pellet onto a heated (700°C) lanthanum aluminate substrate in a 100 mtorr oxygen atmosphere and then slowly cooled to room temperature in 1 atmosphere of oxygen.[5] Films with very smooth surfaces and Tc's of 89.8 have been produced; X-ray analysis has shown that they are c-axis aligned. The microstrip resonators were patterned by standard photolithography using negative photoresist and a 'wet' chemical etchant. This etchant was either a 3% solution of bromine in ethanol or dilute phosphoric acid in water. A metal ground plane was deposited by first evaporating 100 Å of Ti for adhesion followed by 1 micron of gold. In addition to the resonator, each chip also had a test bar for direct Tc testing of the patterned film. Identical resonators were fabricated entirely from gold (both strip and ground plane) using evaporation and lift-off to define the strip.

The resonators were measured using a Hewlett-Packard 8510 Network Analyzer, operating in WR-28 waveguide. The microstrip circuit was mounted in a tapered ridge waveguide to microstrip test fixture which was mounted at the second stage of a two stage, closed cycle helium refrigerator. Circuit temperatures reached approximately 20°K and were monitored by a silicon diode sensor mounted in the test fixture. The entire cold finger and test fixture were enclosed in a custom designed vacuum can. Microwave coupling to the test fixture was through 6 inch sections of WR-28 waveguide made of thin wall stainless steel to minimize heat conduction. Vacuum was maintained at the waveguide feedthroughs by means of 'O' rings and mica sealing windows.

THEORETICAL CALCULATION OF Q

The theoretical Q values were calculated using the Phenomenological Loss Equivalence Method (PEM).[6] This method is applicable to cases where the strip conductor thickness is on the order of a skin depth (for a normal metal) or a penetration depth (for a superconductor). The Incremental Inductance Rule, which is often used to calculate microstrip losses, can only be applied in the case of shallow field penetration, which is not satisfied in this study. Also, PEM has the advantage of simple calculation compared with other numerical techniques such as the Finite Element Method. The technique proceeds on the basis of separately calculating the internal impedances of the strip and the ground plane through use of an equivalent isolated strip, and then adding these impedances to the external impedance of the microstrip structure. First, the ground plane is assumed to be a perfect conductor so that there is no magnetic field penetration into it as shown in figure 1. A geometric factor (G1) for the strip line is then obtained from the magnetic field penetration into it. This G1 factor is used to obtain an equivalent strip; from which the internal impedance of the microstrip line under the assumption of perfect ground plane can be obtained as

$$Z_{i1} = G_1 \bullet Z_{s1} \bullet \coth(Z_{s1} \bullet \sigma_1 \bullet A \bullet G_1)$$

where Z_{s1}, σ_1 and A are the surface impedance, the conductivity of the material and the cross sectional area of the strip, respectively. Next we consider the strip as a perfect conductor as shown in figure 1. Then a geometric factor (G2) is obtained for the field penetration into the ground plane. With the value G2, we obtain the internal impedance of the ground plane based on the assumption of a perfect strip,

$$Z_{i2} = G_2 \bullet Z_{s2} \bullet \coth(Z_{s2} \bullet \sigma_2 \bullet A \bullet G_2)$$

where Z_{s2} and σ_2 are surface impedance and conductivity of the ground, respectively. The internal impedance of the microstrip line is obtained by adding Z_{i1} and Z_{i2}. We add this internal impedance to the external inductance and calculate the propagation constant of the microstrip line by using a transmission line model. It should be emphasized that (1) and (2) are applicable to any field penetration depth.

The conductor losses of the structure in fig. 2 were calculated by applying the method explained above. Then, the Q values of each resonator were calculated by additional consideration of substrate loss; radiation loss was assumed negligible. For the calculation, the value of 5.8x10-4 was used for the loss tangent. Since the current is more concentrated on the strip, the implementation of a superconductor in the strip has more influence on the loss.

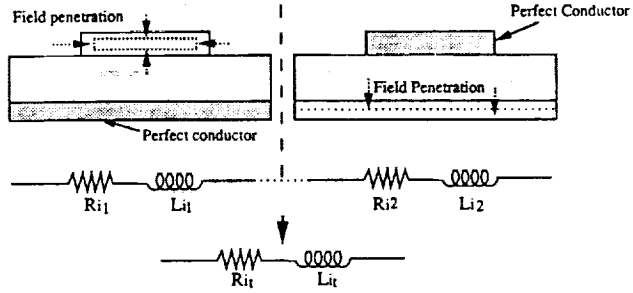

Figure 1. Field penetration in the strip and ground plane; for PEM calculation.

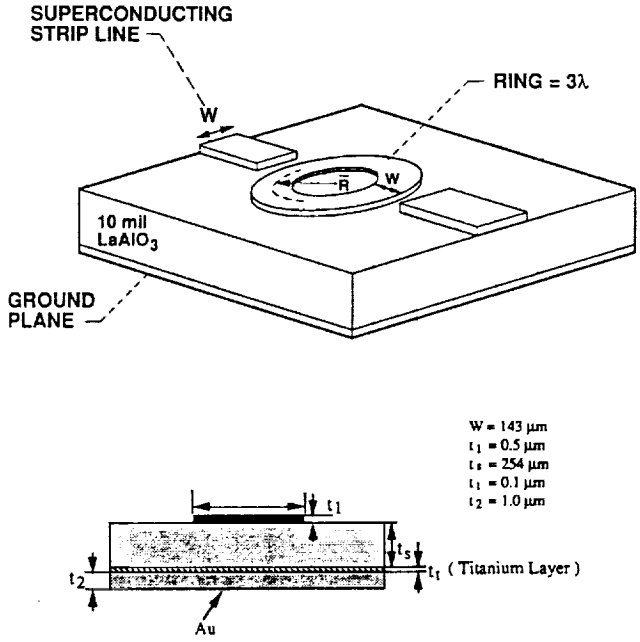

Figure 2. 35GHz Ring Resonator Structure.

The extent of the effect of implementing a superconductor in the microstrip line can be different for different geometries.

RESULTS AND DISCUSSION

In figure 3 are shown plots of S11 for a superconducting resonator at several temperatures. This plot is of the reflected power from the resonator in the test fixture and is thus a measure of the loaded 'Q'. Two features are apparent; 1) the coupling changes with temperature (in this case, starting at near critical coupling just below Tc and going to overcoupled at lower temperatures), and 2) the resonant frequency shifts with temperature. The change in the resonant frequency vs temperature is plotted in figure 4 along with the resonant frequencies of a gold resonator. The variation observed in the gold resonator follows the form expected from thermal contraction in the substrate. But since accurate data on lanthanum aluminate is not readily available, precise comparisons are not possible. The variation seen in the superconducting resonator is a consequence of the dependence of the internal impedance of the strip on the changing normal/superconducting electron densities. The internal inductance of a superconducting strip over a ground plane is given by:[7]

$$L_{int} = \mu_o \cdot \lambda \cdot \coth(t/\lambda)$$

Assuming the Gorter-Casimir temperature dependence of λ:

$$\lambda(T) = \frac{\lambda_o}{[1 - (T/Tc)^4]^{\frac{1}{2}}}$$

the form of the resonant frequency variation based on the changing line inductance matches the experimental observations. However, attempts at numerical fitting to extract λ_o, result in λ_o in excess of 1 micron, indicating that the film quality may not be at its highest.

The best circuit to date has been from a 6500 Å film with a post-processing Tc of 79°K. The unloaded Q of this circuit is plotted against temperature in figure 5 along with the unloaded Q of an identical gold resonator. The Q of the superconducting circuit rises sharply below Tc, exceeding the Q of the gold circuit at ~60°K and reaching a value of 1.5 times that of the gold resonator at 25°K. Comparing the experimental results with the calculated values in the same figure, we see that for the gold resonator, the PEM calculation matches the experimental fairly well. The measured superconducting 'Q', however, is much lower than the calculated values. Several reasons can be given for this. First, the values for the complex conductivity of the superconductor used in the PEM calculation were obtained by microwave reflectance/transmission measurements on separate laser ablated films.[8] It is likely that the quality of those films was higher than the resonator film, in part because these films were unpatterned. In addition, substrate losses in the PEM were calculated on the basis of tanδ=5.8×10E-4 but accurate values for lanthanum aluminate are not available so the actual value may be higher or lower. It seems likely that improvements in the measured Q are possible with increased film quality.

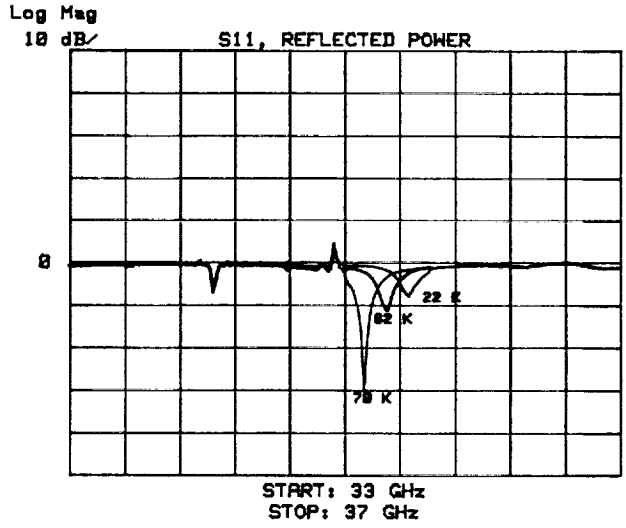

Figure 3. S11 of the superconducting resonator in its test fixture, at three temperatures.

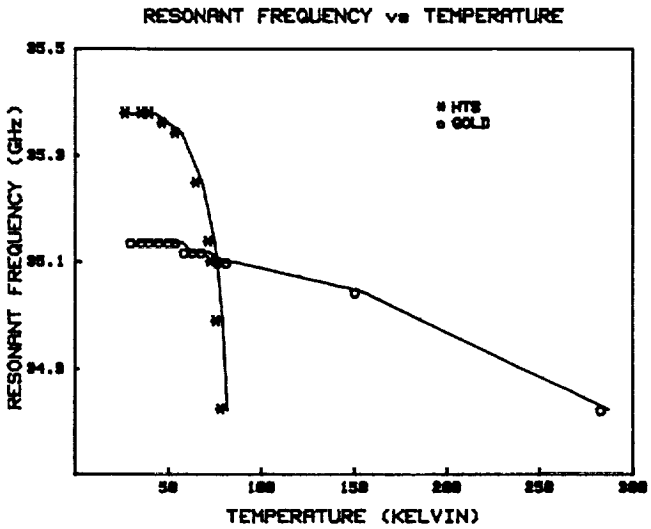

Figure 4. Resonant frequency vs temperature for superconducting and normal strips.

CONCLUSIONS

Ring resonator circuits were fabricated from laser ablated YBCO superconducting films on lanthanum aluminate to determine transmission line losses at millimeter wave frequencies. At 25°K the unloaded Q of the superconducting resonator was 1.5 times the Q of identical resonators made of gold. A shift in the resonant frequency with temperature follows the form predicted by the London equation. Using the PEM we calculated the Q values of the ring resonator with a thin YBCO strip and a gold ground plane. The theoretical results were compared with experimental results of the ring resonator of that structure. The calculated results predict higher values of Q than those actually observed, but improved film quality should increase measured Q values.

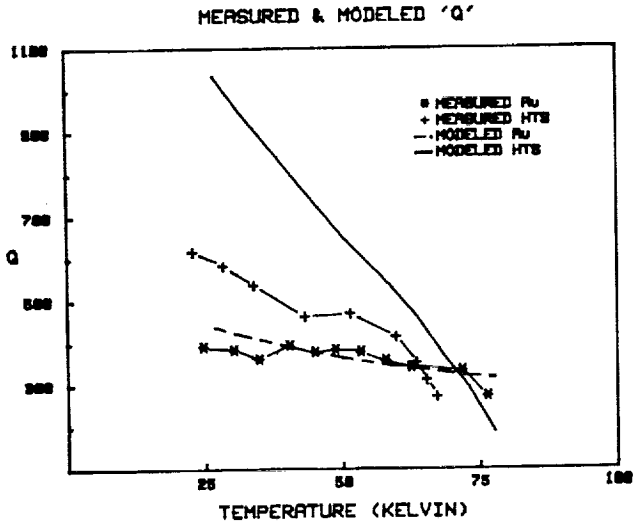

Figure 5. Measured and calculated values of unloaded Q for superconducting and normal resonators.

REFERENCES

1. N. Klein, G. Muller, H. Piel, B. Roas, L. Schultz, U. Klein and M. Peiniger, "Millimeter Wave Surface Resistance of Epitaxially Grown YBCO Thin Films," Appl. Phys. Lett. Vol. 54, pp 757-759.

2. A. A. Valenzuela and P. Russer, "High Q Coplanar Transmission Line Resonators of YBCO on MgO," Appl. Phys. Lett., Vol. 55, pp. 1029-1031, 1989.

3. B. R. McAroy, G. R. Wagner, J. D. Adam, J. Talvacchio and M. Driscoll, "Superconducting Stripline Resonator Performance," IEEE Trans. Magn., Mag. Vol. 25, pp. 1104-1106 (1989).

4. J. H. Takemoto, F. K. Oshita, H. R. Fetterman, P. Kobrin, and E. Sovoro, "Microstrip Ring Resonator Technique for Measuring Microwave Attenuation in High-Tc Superconducting Thin Films," IEEE Trans. Microwave Theory and Tech., Vol. MTT-37, pp. 1650-1652, 1989.

5. J. D. Warner, K. B. Bhasin, N. C. Varaljay, D. Y. Bohman and C. M. Chorey, "Growth and Patterning of Laser Ablated Superconducting YBCO Films on LaAlO3 Substrates," NASA TM-102336.

6. H. Y. Lee, and T. Itoh, "Phenomenological Loss Equivalence Method for Planar Quasi-TEM Transmission Line with a Thin Normal Conductor or Superconductor," IEEE Trans. Microwave Theory and Tech., Vol. MTT-37, no. 12, pp. 1904-1909, 1989.

7. James Swihart, "Field Solution for a Thin-Film Superconducting Strip Transmission Line," Journal Appl. Phys., Vol 32, no. 3, pp. 461-469, 1961.

8. F. A. Miranda, W. L. Gordon, K. B. Bhasin, V. O. Heinen, and J. Valco, "Millimeter Wave Transmission Studies of YBCO Thin Films in the 26.5 to 40 GHz Frequency Range," Proc. Third Annual Conf. on Superconductivity and Applications, to be published by Plenum Press 1990, and NASA TM-102345.

Ka-BAND PROPAGATION CHARACTERISTICS OF MICROSTRIP LINES ON GaAs SUBSTRATES AT CRYOGENIC TEMPERATURES

R. R. Romanofsky, J. C. Martinez, B. J. Viergutz, and K. B. Bhasin
National Aeronautics and Space Administration
Lewis Research Center
Cleveland, Ohio 44135

KEY TERMS

Microstrip line, GaAs substrate, relative permittivity, resonators, low temperature microwave measurements, Q-factor

ABSTRACT

Effective permittivity and loss characteristics of gold microstrip lines on GaAs substrates were obtained by characterizing GaAs linear resonators at cryogenic temperatures (300 to 20 K) from 30–40 GHz. A slight decrease in effective permittivity and a significant reduction in loss were observed with lower temperatures.

INTRODUCTION

Microstrip is a geometrically simple transmission line that has found widespread use in GaAs monolithic microwave integrated circuits (MMIC). Because of the two-wire configuration, it has no lower cutoff frequency. However, upper frequency limitations are imposed due to surface waves and transverse resonance modes that can propagate under certain conditions [1]. The dominant mode of propagation is quasi-TEM (transverse electromagnetic).

Detailed information on propagation characteristics of transmission lines on GaAs at cryogenic temperatures is unavailable. Accurate theoretical analysis is hindered by the inhomogeneous geometry of microstrip, which causes a field discontinuity at the air–dielectric interface. This information is required for the accurate modeling and matching network design of cryogenically cooled GaAs MMICs. Also, such information will prove useful in developing hybrid superconducting/GaAs MMIC circuits. This promising technology will exploit the inherent benefits of superconducting electronics, such as low loss and low noise performance, and simultaneously enhance the active device characteristics due to the cryogenic operating temperature.

DESIGN AND FABRICATION

50-ohm linear open circuit $n\lambda/2$ microstrip resonators were fabricated on 2-in. semiinsulating GaAs wafers along the (100) crystallographic plane in the $[0\bar{1}0]$ direction. The end (fringing) effect was eliminated by using two lines: a short line of length l_1 with a fundamental resonance at f_1 and a long line of length $l_2 = 2l_1$ with a harmonic resonance of $f_2 = f_1$. The resonators were coupled to a feed line via a critical symmetric gap. The gap dimensions ranged from 0.0015–0.00175 in. for the 0.010-in.-thick wafers.

A pattern electroplating technique was established to fabricate the GaAs microstrip resonators. Initially, 200 Å of titanium and 1000 Å of gold were sequentially deposited onto the wafers by evaporation. A layer of positive photoresist was then spin coated onto the wafer and subsequently exposed to UV light through a negative (dark-field) chrome/glass mask. At this point, the desired pattern had been transferred to the substrate. The wafer was then developed, which established windows corresponding to the circuit pattern. The electroplating process entailed submersing the wafer in an aqueous gold–potassium–cyanide solution. A platinum–titanium anode was connected to a constant current source and the wafer (cathode) was grounded. A current density of 3 mA/in.^{2} was maintained to ensure a high quality film. Finally, the thin underlying gold and titanium layers were removed by chemical etch. The wafers were then lapped and polished to 0.010 in. in order to obtain the correct characteristic impedance and surface finish. A titanium–gold ground plane was evaporated onto the wafer reverse. A fully fabricated resonator pair is shown in Figure 1.

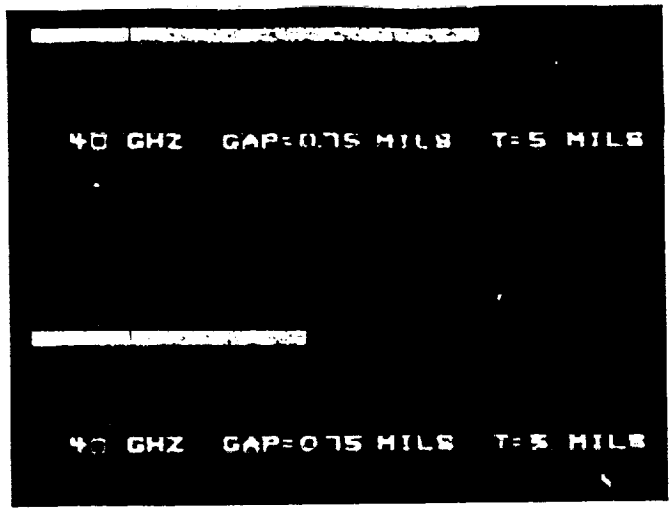

Figure 1 A fully fabricated resonator pair, short line of length l_1 with a fundamental resonance at f_1 and a long line of length $l_2 = 2l_1$, with a harmonic resonance of $f_2 = f_1$. The gap is approximately 0.75 mil

EXPERIMENTAL RESULTS

Swept frequency measurements were performed using an automatic network analyzer system [2] connected to a closed cycle helium refrigerator. A cosine tapered ridge guide test fixture was placed inside the refrigerated chamber and the resonator chip was mounted beneath the ridge using pressure contact (Figure 2). The technique is based on the measurement of reflection coefficients ($S11$) for each microstrip resonator pair. From these data, total loss and effective permittivity can be determined. Raw data yield the loaded quality factor Q_L. Calculation of the unloaded quality factor Q_0 required derivation of the gap coupling coefficient and modeling of the resonator as a transformer coupled RLC tank circuit. Based on the analogous input impedance and accounting for coupling loss, the correct Q_0 was evaluated. Because the devices were enclosed in the waveguide below cutoff, radiation was considered negligible. A complete description of the techniques employed is provided in reference 3.

A number of microstrip resonator pairs were successfully characterized. Figure 3 depicts the measured response of a resonator tested at 300 and 20 K, respectively. Two phenomena were observed upon cooling to cryogenic temperatures. First, there was a consistent shift in the resonant frequency of approximately −2%. The second involved a dramatic change in the loaded quality factor, a consequence of the temperature dependence of loss and a reduction in coupling coefficient. Figure 4 illustrates the temperature dependence of effective permittivity at approximately 31.5 GHz, revealing a trend to diminish slightly upon cooling. Table 1 provides loss data as a function of temperature, demonstrating a 0.15-dB/cm improvement as the material is cooled from 300 to 20 K. It is important to convey that the data for the unshielded resonators contain a large radiation component and should not be interpreted as the loss that would occur along a uniform microstrip line.

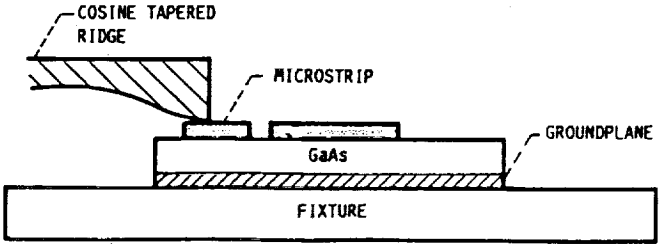

Figure 2 Schematic of cosine tapered ridge guide fixture arrangement

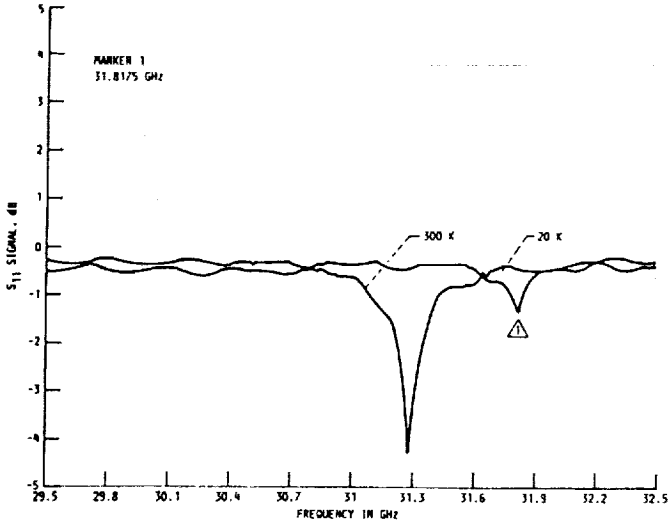

Figure 3 Measure response of a resonator tested at 300 and 20 K

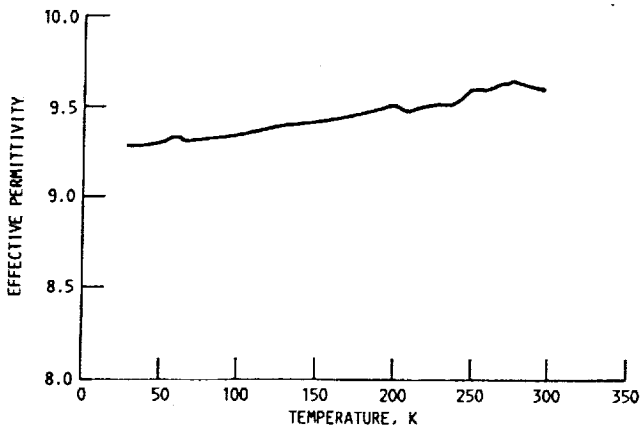

Figure 4 Temperature dependence of effective permittivity of 10-mil-thick GaAs substrate at approximately 31.5 GHz

TABLE 1

Frequency, GHz	Temperature, K	Q_0, Shield	Q_0, Open	Loss, dB/cm
30.2620	300	205	—	0.45
30.5635	300	197	—	0.47
31.6975	300	211	—	0.43
39.0720	300	—	24	4.37
39.1060	300	—	18	5.83
31.0252	77	271	—	0.34
31.9675	77	254	—	0.36
30.8575	20	297	—	0.31

CONCLUSION

Q values from 30–40 GHz were obtained for GaAs microstrip resonators at cryogenic temperatures. It was found that the Q values increased by a factor of approximately 1.25 at 77 K and a factor of 1.5 at 20 K when compared to room temperature data. Also, there is a small but definite decrease in dielectric constant as temperature decreases.

Eventually, as high temperature superconducting technology evolves and merges with GaAs MMIC, such information will be necessary for effective device design. At present, the in situ film processing temperatures exceed the tolerance of GaAs circuitry, due to materials problems ranging from semiconductor diffusion to metal migration.

REFERENCES

1. T. C. Edwards, *Foundations for Microstrip Circuit Design*, Wiley, New York, 1981.
2. J. E. Aitken, "Swept Frequency Microwave Q-Factor Measurement," *Proc. IEE*, Vol. 123, September 1976, pp. 855–862.
3. R. R. Romanofsky, "Analytical and Experimental Procedures for Determining Propagation Characteristics of Millimeter-Wave Gallium Arsenide Microstrip Lines," NASA Report No. TP-2899, 1989.
4. S. Withington, "Cryogenic Performance of Microstrip Substrates," *Electron. Lett.*, Vol. 19, October 13, 1983, pp. 887–888.

Received 1-2-90

Microwave and Optical Technology Letters, 3/4, 117–119

CCC 0895-2477/90/$4.00

TRANSPORT MEASUREMENTS ON GRANULAR Y-BA-CU-O FILMS

M. A. Stan*, S. A. Alterovitz, D. Ignjatovic, and K. B. Bhasin
NASA-Lewis Research Center, 21000 Brookpark Road Cleveland, OH 44135 USA

G. C. Valco and N. J. Rohrer, Department of Electrical Engineering, The Ohio State University Columbus, OH 43210 USA

The critical current in granular YBaCuO films has been measured at temperatures very near the critical temperature, T_c. The critical current is proportional to $(1-T/T_c)^2$ for $T<.9\ T_c$. The current-voltage (I-V) characteristics of the films have also been measured as a function of temperature and indicate that the observed deviation from the $(1-T/T_c)^2$ dependence for $T > .9T_c$ is a natural consequence of the constant field criterion (e.g. .25 μV/mm) used to define the critical current.

1. Introduction

Reports [1,2] have shown that the measured critical current, I_c, near T_c is proportional to $(1-T/T_c)^2$ for $T < .9T_c$ and exhibits a weaker temperature dependence for temperatures nearer to T_c. Our I_c data exhibits qualitatively the same behavior and we will show, with the aid of the (I-V) characteristics, that the variation in the power law near T_c is a result of the measurement criterion. Next we discuss several different criteria for defining the onset of dissipation as it applies to I_c measurements. Finally we show that *i*) the temperature dependence of the I_c can be obtained by fitting the I-V data taken at different temperatures to the simple expression $V=A(I-I_c)^m$, *ii*) the temperature dependence of I_c obtained using this procedure is in good agreement with that of the measured data.

2. Experimental

The superconducting films were prepared by sequential evaporation of Cu,Y, and BaF_2 onto (100) $SrTiO_3$. The films were deposited onto .5 cmx1.0 cm substrates and had a nominal thickness of 1 μm prior to annealing. Details of the film preparation and annealing have been published elsewhere.[3] Scanning-electron-micrographs of the film surface showed irregularly shaped grains .5 μm in size having no epitaxy with the substrate.

A d.c. four probe method was used for all transport measurements. Electrical contact to the films was made by In-soldering to previously deposited 1μm Ag electrodes extending across the short dimension of the films. The critical temperature for the film described below was 62.3K, determined with a measuring current density of $.2A/cm^2$.

3. Results and Discussion

In Fig. 1 the upper four sets of I_c data were obtained using different voltage criteria. The solid lines are guides to the eye. The lowest line in Fig. 1 was obtained from a least-squares fit of the I-V data and will be discussed later in this section. Notice that the upper four curves have a slope of 2 at low temperatures, and show a departure from the straight line behavior at different temperatures depending upon the voltage criterion. The departure from $(1-T/T_c)^2$ as $T \to T_c$ can be understood with the aid of the I-V data in Fig. 2. Here we show a sequence of I-V data obtained at six different

*Also Department of Physics, Kent State University, Kent, Ohio, 44242 USA

0921-4534/89/$03.50

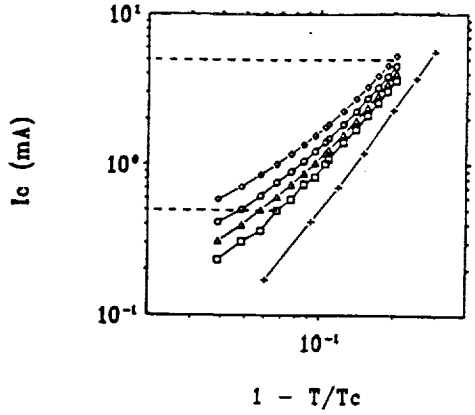

Fig. 1 I_c against $(1-T/T_c)$ obtained using different criteria. From top to bottom 2.5 μV/mm, 1μV/mm, .5μV/mm, .25μV/mm, and data obtained from a least-squares fit of the I-V data to $V=A(I-I_c)^m$.

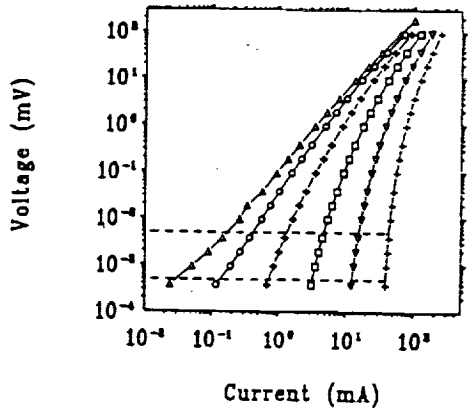

Fig. 2 Voltage against current obtained at a sequence of temperatures. From right to left: 20, 40, 51, 58, 62, and 64K.

temperatures. The upper and lower dashed lines represent the 2.5 μV/mm and .25μV/mm criteria respectively, and a vertical line drawn from the intersection of these lines with the data yields the I_c. At 20K the two criteria result in the same I_c while at 58K they yield numbers differing by a factor of two. The important parameter for evaluating the accuracy of a constant voltage criterion is apparently the logarithmic derivative dlog V/ dLog I. The smaller the logarithmic derivative at the chosen voltage criterion the more one overestimates I_c. Since dLogV/dLogI is rapidly diminishing as $T \to T_c$ it is inevitable that one overestimates I_c which results in the apparent weakening of the temperature dependence near T_c. In principle one would have to define I_c at the same value of the logarithmic derivative (i.e. lower voltages) in order to maintain the same level of accuracy. Since this method is not practical one could use the less stringent resistive criterion whereby a supercurrent is present if $V_c/I_c < R(T_c)$, where V_c is the voltage criterion, and $R(T_c)$ is the smallest detectable resistance in the T_c measurement. In Fig. 1 the top and bottom dashed lines represent the lowest quotable values of I_c for the 2.5 μV/mm and .25μV/mm criteria respectively.

We believe there is yet another way to obtain the temperature dependence of I_c. It has previously been shown that the I-V data can be described by $V=A(I-I_c)^m$ where I_c and m are temperature dependent[4]. By performing a least-squares fit of our data to this relation we obtain I_c and m as a function of temperature. The I_c data obtained in this way are the points on the lowest line in Fig. 1. The exponent is 2.2, in good agreement with the measured data satifying the resistive criterion, and I_c vanishes at 63.8K. In conclusion, we found that I_c is proportional to $(1-T/T_c)^2$ for $T \sim T_c$.

REFERENCES

1) S. B. Ogale, D. Dijkkamp, and T. Venkatesan, Phys. Rev. B36, (1987) 7210

2) J. H. C. de Vries, M. A. M. Gijs, G. M. Stollman, T. S. Baller, and G. N. A. Vern, J. Appl. Phys. 64 (1988) 426.

3) G. J. Valco, N. J. Rohrer, J. D. Warner, and K. B. Bhasin, A.I.P. Proceedings No. 182 (1989) 147.

4) P. England, T. Venkatesan, X. D. Wu, and A. Inam, Phys. Rev. B38 (1988) 7125.

ELECTRICAL TRANSPORT MEASUREMENTS ON POLYCRYSTALLINE SUPERCONDUCTING Y-Ba-Cu-O FILMS

M. A. Stan, S. A. Alterovitz, and D. Ignjatovic

NASA - Lewis Research Center
Cleveland, Ohio

ABSTRACT

The current-voltage, I-V, characteristics of polycrystalline Y-Ba-Cu-O films have been measured as a function of temperature. The I-V characteristics are interpreted using a model based upon an array of weak links with a statistical distribution of critical currents. In addition, we find evidence that the supercurrents flow in nearly independent filaments near T_c. Various criteria are discussed with respect to the definition of the transport critical current, I_c, in these films. A temperature dependence for I_c has also been deduced from the I-V data by appealing to an empirical scaling law. We propose that this temperature dependence, $I_c \propto (1-T/T_c)^{2.2}$, is representative of the weaker links within the critical current distribution.

INTRODUCTION

The T_c measurement is the most commonly used method for the characterization of superconducting materials. However, I_c is a more effective parameter in determining technological usefulness. In particular it is desirable to measure the temperature dependence of I_c in order to illuminate the mechanism limiting I_c, such as depairing in a single crystal sample, or perhaps tunnelling through grain boundaries in a polycrystalline sample. In the presence of a magnetic field, single crystal high temperature superconducting (HTS) samples have been shown to exhibit flux creep[1], while, in polycrystalline samples a variety of effects ranging from weak link limited I_c behavior at low magnetic fields to flux flow limited I_c behavior in high magnetic fields[2] have been

observed. Implicit in any of these I_c measurements is some criterion for the definition of I_c. The selection of a criterion for I_c has been particularly difficult in the HTS materials because, in many instances, the resistive transition is not sharp. Several attempts to standardize the criteria for I_c in the presence of a magnetic field have been proposed[3,4]. However, for thin films in zero magnetic field, a constant field criterion ranging from 0.1 μV/mm to 1 μV/mm is widely used. While this criterion may be satisfactory for epitaxial thin films, where the critical supercurrent density, J_c, is of the order of 10^6 A/cm^2 at 77 K and the transition is sharp, the meaning of an I_c obtained in this way for polycrystalline films is not clear, owing to the broadness of the resistive transition in these films. The lack of a consensus on the temperature dependence of I_c, and in particular, the exponent in the expression $(1-T/T_c)^n$ $(1.5 \leq n \leq 2.0)$, could be symptomatic of the arbitrariness of an I_c obtained from a constant voltage criterion[5,6,7,8]. While the various exponents reported for the temperature dependence of I_c may relate in some way to the microstructure in the films, we believe that one must first understand the mechanism responsible for the transition in order for the measured I_c to have meaning.

To our knowledge, only one attempt has been made to understand the resistive transition in HTS polycrystalline films. This was the work of England et al.[9], where they suggested that the films underwent a phase locking transition similar to that found in compacted polycrystalline Ta samples[10]. Within this model, the phase, θ_i, of the wave function of each of the grains is uncorrelated from grain to grain when $T > T_c$ (T_c being defined at $R = 0$). At T_c, the phase difference, $\theta_i - \theta_j$, between the neighboring grains becomes fixed because the thermal fluctuations ($k_B T_c$) are exceeded by the Josephson coupling energy ($hi_c/2e$). Here i_c is the intergrain critical current. The strongest evidence for this mechanism in polycrystalline HTS films came from the I-V data at T_c, where it was shown that $V(T_c) \propto I^2$. The quadratic dependence of V on I is a prediction of the phase locking model[10].

Recently the resistive transition of sintered Y-Ba-Cu-O wires in a magnetic field has been modeled by Evetts et al.[11] using extensions to the conventional model given for superconducting multifilamentary composites[12]. The extended model, hereafter referred to as the Weak Link Filament Array (WLFA) model, treats the sample as an array of weak links with a normal distribution of I_c's. Essential features of our I-V data are discussed in terms of this model. The implications of this model with respect to defining I_c are then discussed. Finally, by appealing to an empirical scaling law for the I-V data, we can

deduce a temperature dependence for an I_c which is representative of the weakest links in the I_c distribution.

EXPERIMENTAL

Sample Preparation

The films were prepared by sequential evaporation of Cu, Y, and BaF_2 onto (100) $SrTiO_3$. The films had a superstructure period of three, for a total of twelve layers, and a nominal thickness of 1 μm prior to annealing. Details of the deposition parameters and annealing have been published elsewhere[13]. Scanning electron micrographs of the films showed rectangular shaped grains with dimensions of 0.3 μm X 1.0 μm having no epitaxy with the substrate. X-ray diffraction analysis of the films indicated a polycrystalline nature with some a-axis texturing, as well as the presence of $BaCuO_2$ and Y_2O_3 phases. Electrical contact to the films was made by depositing a 1 μm layer of Ag through a shadow mask, resulting in four equally spaced 0.1 cm wide strips traversing the short dimension ($\simeq$ 0.3 cm) of the sample. The contacts were subsequently annealed in dry O_2 at 500° C for approximately two hours resulting in contact resistances of 10 $\mu\Omega$ or less. Wires were then attached to the Ag strips via In-soldering.

Electrical Transport Measurement

Transport measurements in low magnetic fields (0 - 70 Oe) were made in a ^{4}He closed cycle refrigerator with an externally mounted Cu wire Hemholtz coil around the sample chamber. The samples were attached to an OFHC copper holder and housed in an OFHC copper radiation shield. Cooling of the assembly was done by convection through 1 atm (STP) of ^{4}He gas to the refrigerator cold head ($\simeq$ 16 K). The sample temperature was determined by a Si diode which is epoxied into the sample holder, and has a rated accuracy of $\pm$ 0.25 K over the temperature interval of the measurements.

All the transport measurements discussed below were made using the conventional four-probe method. The T_c measurement of the films was made with a typical measuring current density of 0.2 A/cm^2 and a voltage sensitivity of approximately 10 nV. This voltage sensitivity was obtained using a nanovoltmeter in conjunction with signal averaging.

TRANSPORT DATA AND DISCUSSION

Nine samples were measured, but we will present detailed results on one typical film. A common feature of the films is that they have a zero resistance temperature, T_c, in the range 60 K - 70 K. The films exhibit a metallic nature above the onset temperature of 90K but the resistance is not linear in temperature, presumably because of the various grain orientations and presence of other phases.

I-V data, obtained at six different temperatures, is displayed in Fig. 1. The T_c of this film was 62.3 K. The upper and lower horizontal dashed lines in Fig. 1 represent I_c voltage criteria of 2.5 μV/mm and 0.25 μV/mm, respectively. A vertical line drawn from the intersection of one these lines with the I-V data yields a value for I_c. At 20 K the two criteria yield essentially the same I_c while at 58 K they yield numbers differing by a factor of two. Obviously, an important parameter in defining I_c is the logarithmic derivative dLog(V)/dLog(I) commonly referred to as the n value of the resistive transition. The smaller the n value at the chosen voltage criterion the more sensitive I_c is to the voltage criterion. Because the n value is temperature dependent and approaches one at T_c, it is inevitable that this type of criterion will give I_c a weaker temperature dependence the nearer one gets to T_c. This effect is

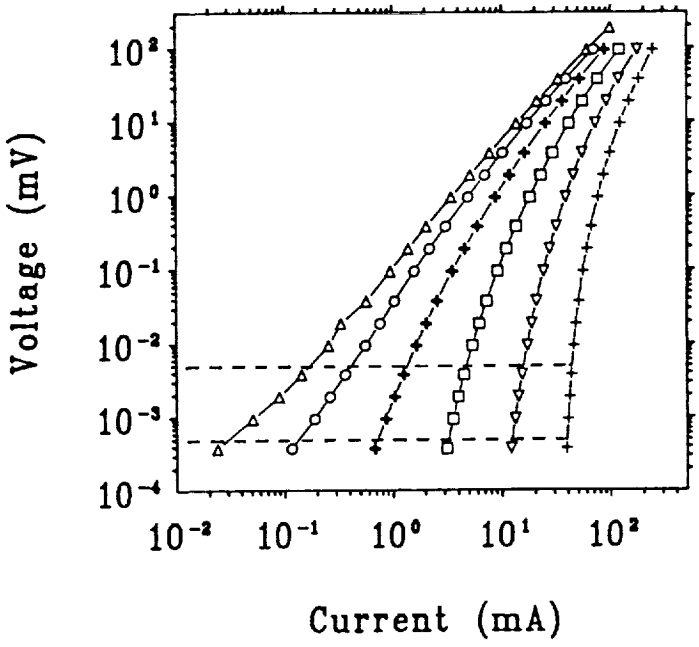

Fig. 1 Voltage against current obtained for a sequence of temperatures. From right to left: 20 K, 40 K, 51 K, 58 K, 62 K, and 64 K.

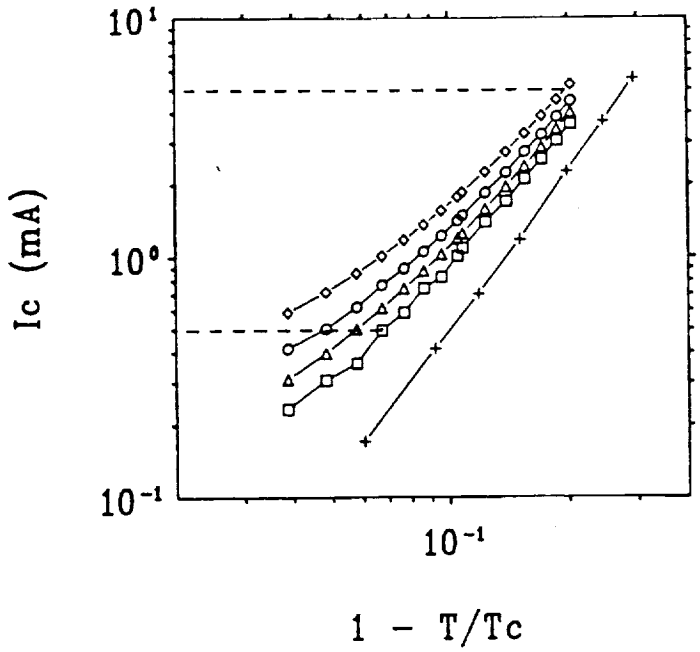

Fig. 2 I_c against $(1-T/T_c)$ obtained using different criteria. From top to bottom: 2.5 μV/mm, 1 μV/mm, 0.5 μV/mm, 0.25 μV/mm, and data from a least-squares fit of the I-V data to $V = A(I-I_c)^n$.

demonstrated in the I_c vs. $1-T/T_c$ characteristic shown in Fig. 2. The upperfour sets of I_c data in Fig. 2 were obtained using different voltage criteria. The solid lines are guides to the eye. The lowest line in Fig. 2 was obtained from a data fitting procedure and will be described later. Notice that the upper four data sets are straight lines at the low temperature end of the graph with a slope of $\simeq 2$. The data show a departure from linear behavior at different temperatures depending upon the voltage criterion. One final note with regard to the constant voltage criterion concerns the lowest meaningful I_c measurement. To be self consistent with the T_c measurement the I_c data must be greater than or equal to V_c/R_c, where R_c is the smallest detectable resistance in the T_c measurement and V_c is the voltage criterion used in the I_c measurement. The upper and lower horizontal dashed lines in Fig. 2 represent the lowest self consistent values of I_c for the I_c voltage criteria of 2.5 μV/mm and 0.25 μV/mm, respectively. Failure to make the T_c and I_c measurements consistent with one another may result in assignment of I_c values to very resistive samples[14]. Regardless of the I_c criterion, one must first understand the nature of the resistive transition before one can attach any physical significance, such as tunneling, to I_c measurements on polycrystalline HTS films.

It has long been recognized that the broad resistive transitions into the flux flow state in type-II superconductors can be explained in terms of the variation in the local I_c along the sample length, where the flux-flow voltage is determined by that fraction of material whose I_c is lower than the applied current[15,16]. The I-V characteristic is then determined by

$$V = \left(\frac{\rho}{A}\right) \int_0^I \int_{i_{cm}}^{i} f(i_c)\, di_c\, di \qquad (1)$$

where $f(i_c)$, ρ, and A are the critical current distribution function, the flux-flow resistivity, and the cross-sectional area, respectively. The lower limit, i_{cm}, on the second integral in Eq. 1 is the smallest i_c in the distribution.

In type-II multifilamentary composites the transition into the flux-flow state is broad as a result of a distribution of localized constrictions along the individual filaments. For such structures the empirical relation $V \alpha I^n$ seems to characterize the resistive transition quite well. Recently a theoretical understanding of this relation was obtained by Plummer and Evetts[12] by assuming the constrictions were normally distributed. The calculations were made using Eq. 1 and were based on either independent filaments or nearest neighbor coupling. There are three important results which apply for either limit: the scaling law $V \alpha I^n$ is a natural consequence of a normal distribution of inhomogeneities; the n value is proportional to $(\langle I_c \rangle/\sigma)^{5/3}$ where $\langle I_c \rangle$ and σ are the mean critical current and the width of the distribution, respectively; and the measured I_c, obtained by a constant voltage criterion, will increasingly underestimate $\langle I_c \rangle$ as the n value decreases.

Recently, Evetts[11] has been successful in qualitatively explaining the resistive transition of sintered Y-Ba-Cu-O wires in a magnetic field using the WLFA model. The WLFA model is an extension of the independent filament model to include long range coupling and the tunnelling nature of the weak links. In the WLFA model, the conductor geometry is essentially a multiply connected weak link network. However, in low density samples near the percolation threshold, there are many junctions in series between parallel interconnections and one has, effectively, an array of independent filaments, in complete analogy to the multifilamentary composite system. If a normal distribution of junction I_c's is assumed, n bears the same significance to $\langle I_c \rangle$ and σ that it does in the multifilamentary composite system.

In the multiply connected limit of the WLFA model it is argued[11] that there is a length scale, Λ, in the direction perpendicular to the direction of applied current, which is used to describe the degree to which junctions within Λ switch to the normal state at the same current. For low values of magnetic field, temperature, and current the network is isotropic and Λ extends across the entire sample. If M represents the number of connected junctions within Λ, then it is argued that the n value is increased by a factor $\sqrt{M}$, as compared to the single filament result, and the effective width of the normal distribution becomes $\sigma/\sqrt{M}$. In the WLFA model Λ falls with increasing current since larger applied currents require larger transverse balancing currents which in turn increase the probability that the transverse junctions will be broken. The reduction in Λ manifests itself as a current dependent reduction of the n value, a result which is qualitatively different from multifilamentary composite systems where n is independent of the current. At this point we caution the reader that when the junctions are multiply connected Eq. 1 no longer applies, and one must resort to numerical techniques[11] in order to obtain an I-V relation.

Referring once again to Fig. 1, we believe that the I-V data qualitatively exhibits the main features of the WLFA model. These features are: the larger the n value, the larger the current required to drive the film normal, and at

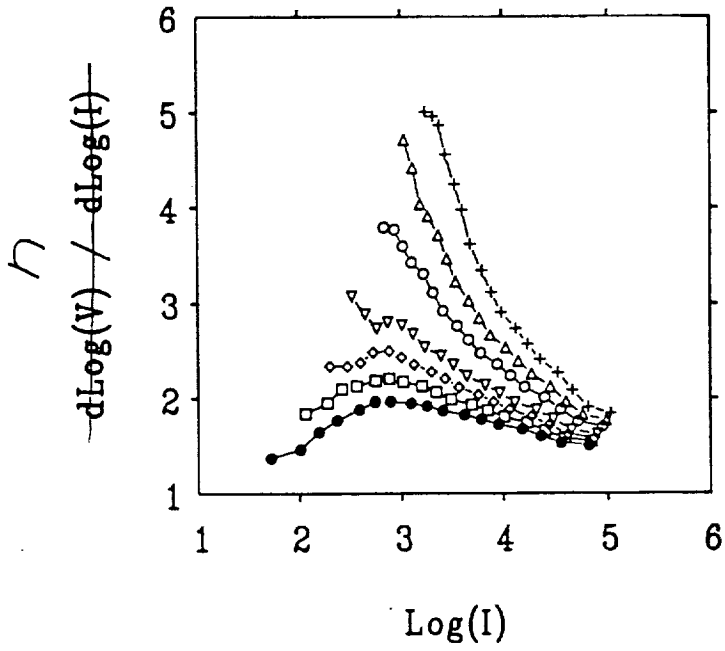

Fig. 3 Logarithmic derivative of the I-V data for a sequence of temperatures near T_c. From top to bottom: 54 K, 56 K, 58 K, 60 K, 61 K, 62 K, and 63 K.

a given temperature, the n value falls monotonically with increasing current. In addition, the I-V data shows evidence near T_c that the films are nearly in the independent filament limit, i.e. that the films are made up of independent chains of weak links. If one looks closely at the low voltage portion of the I-V characteristic for the two left most curves, a tail in the data is evident. The data designated by the open circles was obtained at T_c and the left most data about 1 K higher. To make the tail more prevalent we plot the n value against Log(I) in Fig. 3 for seven different temperatures spaced 1 K apart, with the lowest temperature being at the top of the graph. It is evident that the tail appears very abruptly within approximately 1 K of the T_c value determined in the resistivity measurement. In the experiments of Evetts et al.[11], where the magnetic field was varied and the temperature held constant, the same feature was observed to appear suddenly at a field of 2 mT for sintered Y-Ba-Cu-O wires immersed in LN_2. An obvious explanation for the tail is that the measured voltage contains an ohmic component and a nonlinear component. The ohmic component could be a result of tunnel junctions, which have been driven normal, in series with the nonlinear component from the remaining portion of the weak link connected filaments. The fact that an ohmic component of the voltage exists near T_c implies that the weak links are not multiply connected. If the junction array was multiply connected there would always be a superconducting path across the sample and the ohmic contribution from the normal

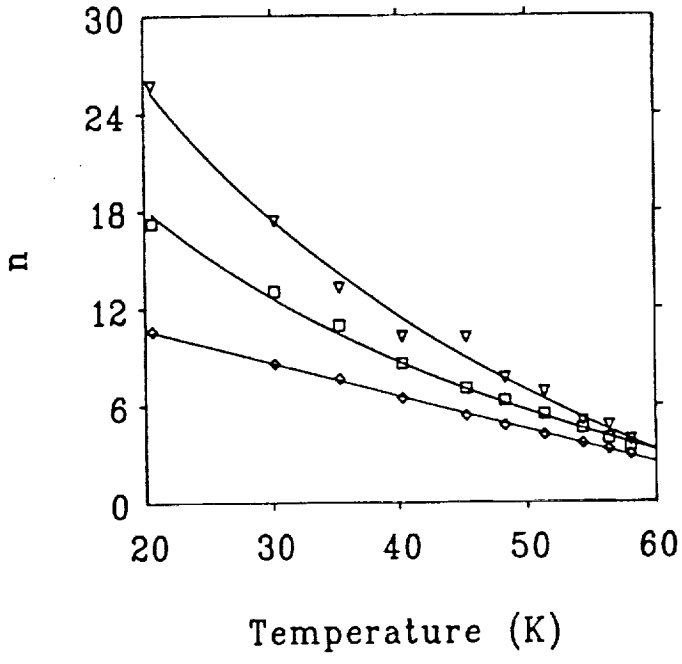

Fig. 4 Resistive transition n value against temperature obtained using different criteria. From top to bottom: 0.4 μV, 4 μV, and 40 μV.

junctions would not be visible.

An implication of the WLFA model on the measurement of the intergranular critical current is that the measured I_c is nearly equal to $\langle I_c \rangle$ at any given voltage criterion provided that the n value at the voltage criterion is large. However, when n becomes small one tends to underestimate $\langle I_c \rangle$ at any given voltage criterion. The latter point indicates that the I-V curves are being controlled by the weakest links, a result also deduced from magnetic field measurements[2]. In WLFA model, or more specifically, if the I-V characteristic results from switching of the weakest links which have a statistical distribution, we expect the temperature dependence of I_c, as determined using a constant field criterion, to be a convolution of the junction and statistical distribution temperature dependencies, casting doubt on interpretations of the temperature dependence based solely on the tunnelling model.

Continuing under the assumption that n is determined by $\langle I_c \rangle$ and σ, we plot in Fig. 4 the n value vs. temperature at three different voltage criteria spanning two orders of magnitude. The solid lines are guides to the eye. For large n values the dependence of n with temperature is of a nonlinear nature, while the small n values show a more or less linear temperature dependence. When n is large the I_c distribution is sharp and we expect that many weak links will be broken simultaneously resulting in a rapid reduction of n with increasing temperature. Small n values indicate a broad I_c distribution therefore few weak links switch co-operatively and n has a weaker temperature dependence.

Although the WLFA model provides no analytical expression for the I-V characteristic, and the temperature dependence of I_c obtained using a constant voltage criterion is open to question in light of a statistical interpretation of the I-V data, we have been very successful in obtaining the temperature dependance of I_c by appealing to the empirical relation $V = A(I-I_c)^m$, first applied to such films by England, et al.[9]. In this relation I_c and m are temperature dependent, and m was found to vary continuously from approximately $m = 3$ at low temperature to $m(T_c) = 2.2 \pm 0.1$, and finally to $m = 1$ at 90 K. This empirical relation has been applied with similar success on both Tl and Bi films[7,8] to describe the I-V data. We also find that the I-V characteristic of our films is reasonably described by this relation. In Fig. 5 we show the results of a least-squares fit of the data from Fig. 1 to the equation $V = A(I-I_c)^m$. The solid lines represent the least-squares fit at each temperature. In Fig. 6 we show the temperature dependence of the exponent, m, determined from the least-squares fit for the entire range of temperatures in which the I-V data were obtained. After performing least-squares fits on five

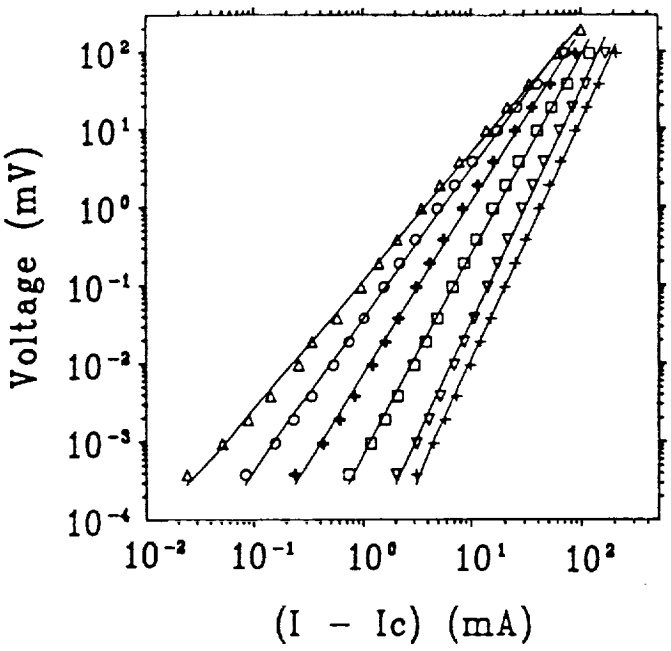

Fig. 5 Voltage against excess current obtained for a sequence of temperatures. From right to left: 20 K, 40 K, 51 K, 58 K, 62 K, and 64 K.

such films we find that the value of m in the low temperature limit, $m(20\ K) = 3.13 \pm 0.05$ is determined with far more confidence than $m(T_c) = 1.90 \pm 0.28$. It would seem that this is a natural consequence of the fact that $(dm/dT)_{20K} << (dm/dT)_{Tc}$. The I_c data of Fig. 5 are plotted in Fig. 2 and are denoted with a + symbol. This fitted data shows a simple power law behavior, with an exponent of 2.22, for all temperatures. The power law temperature dependence is seen at low temperatures in the upper four I_c data sets where the constant voltage criterion is expected to provide a more accurate value for I_c. The temperature dependence of I_c, deduced from the least-squares fitting procedure, on three separate films is shown in Fig. 7. The slope of the lines is 2.20 ± 0.05. The fit in Fig. 7 illustrates two points. The first point is that the temperature dependence is the same even for films whose J_c's differ by more than an order of magnitude, and second, that the power law fits the data from near T_c down to the lowest temperature measured (20 K). If one accepts that the I-V characteristic is controlled by a distribution of weak links, as described by the WLFA model, then the I_c obtained from fitting the I-V data to $V \propto (I-I_c)^m$ is characteristic of the weakest links in the distribution. It is not clear whether the $(1-T/T_c)^2$ dependence of I_c, deduced from $V \propto (I-I_c)^m$, is indicative of S-N-S tunnelling[17]. In other words, the temperature dependence of the I_c distribution may be admixed with the weak link

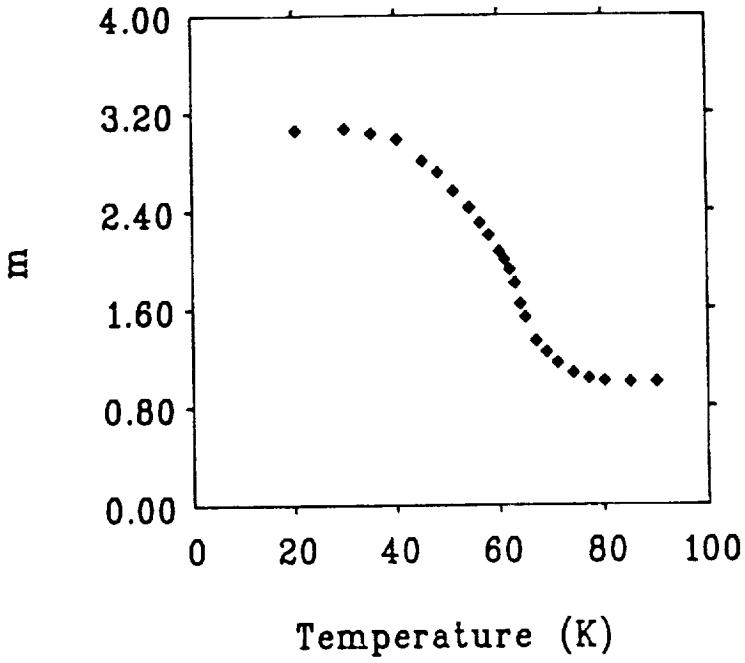

Fig. 6 Temperature dependence of the exponent, m, obtained from a least-squares fit of the I-V data to $V = A(I-I_c)^m$.

temperature dependence. In fact, what is puzzling about the $(1-T/T_c)^2$ dependence of I_c is the wide range of temperatures over which it fits the data, an observation which has been made in Tl- and Bi- based HTS films as well[7,8]. In any type of tunnelling model, whether it is S-N-S, S-I-N-S, or S-I-S, one expects to see a saturation at low temperatures because the energy gap and the decay length both become independent of temperature for $T \leq 0.5T_c$. Our measurements are made down to $T = 0.2T_c$ and still show no evidence of saturation in the I_c data. One other possibility is that there is a distribution of T_c's in the material, but again, it is not clear what type of a temperature dependence in I_c one is expected to observe from such an effect.

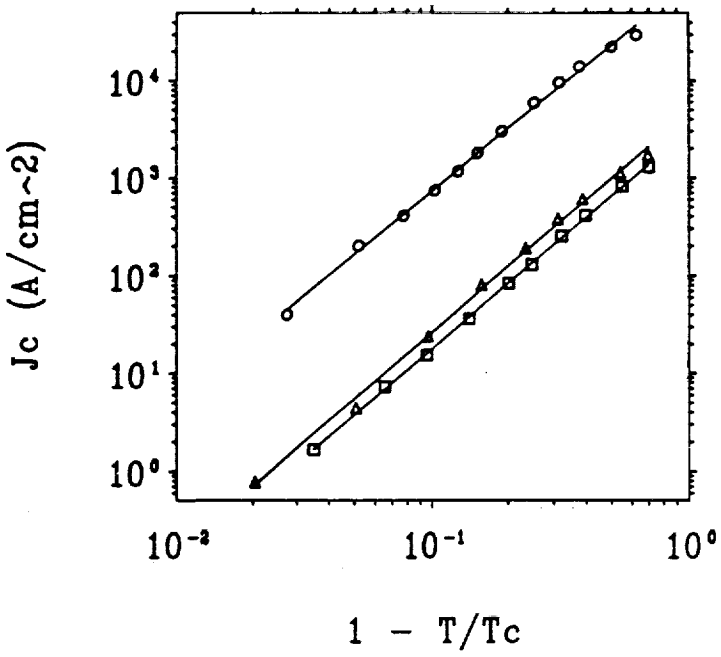

Fig. 7 J_c vs. $(1-T/T_c)$ for three films. In each case J_c was obtained from a least-squares fit of the I-V data to $V = A(I-I_c)^m$. The best fit straight lines through the data have a slope of 2.2.

CONCLUSIONS

We have shown that the I-V characteristics of the polycrystalline HTS films are qualitatively explained within the Weak Link Filament Array model (WLFA). In addition, our films show evidence of being in the filamentary limit of the WLFA model near T_c. The I-V data is well described by the empirical relation $V \propto (I-I_c)^m$ for the temperature range 20 K $\leq$ T $\leq$ 90 K. From this empirical I-V relation we find that $I_c \propto (1-T/T_c)^{2.2}$, and that this temperature dependence is characteristic of the weaker links in the I_c distribution.

ACKNOWLEDGEMENTS

The authors wish to thank Drs. G. J. Valco, Kul B. Bhasin, and Mr. N. J. Rohrer for providing the thin film samples used in these experiments.

REFERENCES

1. T. T. M. Palstra, B. Batlogg, L. F. Schneemeyer, and J. V. Wazczak, Thermally Activated Dissipation in Bi-Sr-Ca-Cu-O, Phys. Rev. Lett., 60:1662 (1988).

2. J. W. Ekin, T. M. Larson, A. M. Hermann, Z. Z. Sheng, K. Togano, and H. Kumakura, Double-Step Behavior of Critical Current vs. Magnetic Field in Y-, Bi-, and Tl- Based Bulk High-Tc Superconductors, (preprint submitted to Physica C).

3. T. T. M. Palstra, B. Batlogg, R. B. van Dover, L. F. Schneemeyer, and J. V. Wazczak, Critical Currents and Thermally Activated Flux Motion in High-Temperature Superconductors, Appl. Phys. Lett., 54:763 (1989).

4. J. W. Ekin, Offset Criterion for Determining Superconductor Critical Current, Appl. Phys. Lett., 55:905 (1989).

5. S. B. Ogale, D. Dijkkamp, and T. Venkatesan, Current Transport in High-T_c Polycrystalline Films of Y-Ba-Cu-O, Phys. Rev. B, 36:7210 (1987).

6. J. W. C. deVries, M. A. M. Gijs, G. M. Stollman, T. S. Baller, and G. N. A. Van Veen, Critical Current as a Function of Temperature in Thin Y-Ba-Cu-O Films, J. Appl. Phys., 64:426 (1988).

7. J. F. Kwak, E. L. Venturini, R. J. Baughman, B. Morosin, and D. S. Ginley, High Critical Currents in Polycrystalline Tl-Ca-Ba-Cu-O Films, Cryogenics, 29:291 (1989).

8. H. E. Horng, J. C. Jao, H. C. Chen, H. C. Yang, H. H. Sung, and F. C. Chen, Critical Current in Polycrystalline Bi-Ca-Sr-Cu-O Films, Phys. Rev. B, 39:9624 (1989).

9. P. England, T. Venkatesan, X. D. Wu, and A. Inam, Granular Superconductivity in R-Ba-Cu-O Thin Films, Phys. Rev. B, 38:7125 (1988).

10. C. Lebeau, J. Rosenblatt, A. Raboutou, and P. Peyral, Current-Voltage Hyperscaling in Arrays of Josephson Junctions, Europhys. Lett., 1:313 (1986).

11. J. E. Evetts, B. A. Glowacki, P. L. Sampson, M. G. Blamire, N. McN. Alford, and M. A. Harmer, Relation of the N-Value of the Resistive Transition to Microstructure and Inhomogeniety for Y-Ba-A_2-Cu_3-O_7 Wires, IEEE Trans. Magn., 25:2041 (1989).

12. C. J. G. Plummer and J. E. Evetts, Dependence of the Shape of the Resistive Transition on Composite Inhomogeneity in Multifilamentary Wires, IEEE Trans. Magn., 23:1179 (1987).

13. G. J. Valco, N. J. Rohrer, J. D. Warner, and K. B. Bhasin, Composition and Processing Effects in Sequentially Evaporated Y-Ba-Cu-O Thin films, A.I.P. Proceedings, 182:147 (1989).

14. S. S. Yom, T. S. Hahn, Y. H. Kim, H. Chu, and S. S. Choi, Exponential Temperature Dependence of the Critical Current in Y-Ba-Cu-O Films, Appl. Phys. Lett., 54:2370 (1989).

15. R. G. Jones, E. H. Rhoderick, and A. C. Rose-Innes, Non-Linearity in the Voltage-Current Characteristic of a Type-2 Superconductor, Phys. Lett. A, 24:318 (1967).

16. J. Baixeras and G. Fournet, Pertes par Deplacement de Vortex dans un Supraconducteur de Type II Non Ideal, J. Phys. Chem. Sol., 28:1541 (1967).

17. J. Clarke, Supercurrents in Lead-Copper-Lead Sandwiches, Proc. Roy. Soc. A, 308:447 (1969).

MICROWAVE CONDUCTIVITY OF SUPERCONDUCTING Bi-Sr-Ca-Cu-O THIN FILMS IN THE 26.5 TO 40.0 GHz FREQUENCY RANGE

F.A. MIRANDA
Case Western Reserve University, Cleveland, Ohio 44106, USA

K.B. BHASIN and V.O. HEINEN
Lewis Research Center, Cleveland, Ohio 44135, USA

R. KWOR and T.S. KALKUR
University of Colorado at Colorado Springs, Colorado Springs, Colorado 80833-7150, USA

Received 30 January 1990

The conductivity σ_N in the normal state and the real and imaginary parts of the conductivity in the superconducting state $\sigma^* = \sigma_1 - i\sigma_2$ of two Bi-Sr-Ca-Cu-O thin films (~ 5000 Å) are reported. The films were deposited on $LaAlO_3$ and MgO substrate by co-evaporation and have a transition temperature T_c of 80 K. The microwave conductivities were obtained from power transmission data, using a two-fluid model. Values for σ_N of 4.1×10^4 and 6.3×10^4 S/m at room temperature were obtained for the films on $LaAlO_3$ and MgO at 28.8 GHz, respectively. Below T_c, values of $\sigma_1 = 5.8 \times 10^4$ and $\sigma_2 = 1.4 \times 10^5$ S/m for the film on $LaAlO_3$ and $\sigma_1 = 7.3 \times 10^4$ and $\sigma_2 = 7.7 \times 10^4$ S/m for the film on MgO were obtained at 28.8 GHz. For the film on $LaAlO_3$, σ_2 decreased with increasing frequency, while for the one deposited on MgO, the behavior was completely opposite. The temperature dependence of the conductivity, both above and below T_c, was the same for both films. From σ_2, values for the magnetic penetration depth λ or 5.6 and 7.6 μm at 75 K were determined for the films on $LaAlO_3$ and MgO, respectively.

1. Introduction

The discovery of high temperature superconductors [1,2] has prompted efforts to develop their microwave applications. The low microwave and millimeter wave losses of these new superconducting oxides make them very attractive for the development of voltage dividers, resonators, phase shifters, and other high frequency analog devices. Microwave studies are of major importance in the view of the limitations of other traditional probes, such as specific heat and ultrasonic attenuation. These are strongly influenced by the phonon system which is heavily populated near the transition temperatures of these new superconductors [3]. In millimeter and microwave characterization, the parameter most often measured has been the surface resistance [3–6]. Less frequently, results have been reported for the complex conductivity [7–9]. A considerable amount of work in this area has been carried out in the Y-Ba-Cu-O superconducting oxide [3–6,9], and now similar measurements are underway in the recently discovered Bi-Sr-Ca-Cu-O [10] and Tl-Ba-Ca-Cu-O [11] superconductors. Although millimeter wave studies of Y-Ba-Cu-O thin films have been performed in the frequency range from 26.5 to 40.0 GHz [12], to the best of our knowledge no similar studies has been performed for Bi-Sr-Ca-Cu-O at these frequencies.

In this communication we are reporting our resulting of the characterization of Bi-Sr-Ca-Cu-O thin films at frequencies from 26.5 to 40.0 Ghz, in terms of the power transmitted through the films, assuming a two-fluid model. Values for the normal and complex conductivities, above and below T_c respectively, have been obtained along with values for the magnetic penetration depth as a function of temperature and frequency.

0921-4534/90/$03.50

2. Analysis

Since a complete understanding of the nature of superconductivity in the high-T_c superconductors is still rather limited, we have assumed that their superconducting state can be described in terms of a two-fluid model. The attributes of simplicity and success in yielding reasonably good estimates of the microwave properties of metallic superconductors for the case $\hbar\omega \ll E_{gap}$ [13] and also for Y–Ba–Cu–O at microwave frequencies [14,15] make this model an appropriate one for describing some of the phenomenological aspects of the behavior of the Bi–Sr–Ca–Cu–O superconductors. In this model the complex conductivity is $\sigma^* = \sigma_1 - i\sigma_2$, with

$$\sigma_1 = \sigma_c t^4, \quad \sigma_2 = \sigma_c (1 - t^4)/\omega\tau . \tag{1}$$

Here, σ_c is the normal conductivity at $T = T_c$, $\omega = 2\pi f$ is the angular frequency, t is the reduced temperature T/T_c, and τ is the mean carrier scattering time. Thus, to determine either σ_1 or σ_2 we need to know the transition temperature T_c and the value of σ_c. Furthermore, the value of τ must be known beforehand if σ_2 is to be obtained from eq. (1).

In order to determine the normal and complex conductivities of the films under study, we have used the method applied by Glover and Tinkham [16]. In this method, the transmission of a normally incident plane wave through a film of thickness d ($\ll$ wavelength or skin depth) deposited on a substrate of thickness l and index of refraction n is measured. Mathematically, the transmitted power can be expressed as

$$P = \frac{8n^2}{A + B\cos 2kl + C\sin 2kl}, \tag{2}$$

where

$$A = n^4 + 6n^2 + 1 + 2(3n^2 + 1)g + (n^2 + 1)(b^2 + g^2),$$

$$B = 2(n^2 - 1)g - (n^2 - 1)^2 + (n^2 - 1)(b^2 + g^2),$$

$$C = 2(n^2 - 1)nb,$$

$$k = n\omega/c,$$

and

$$y = g - ib = YZ_c = (G - iB)Z_c = (\sigma_1 - i\sigma_2)d\,Z_c$$

is the dimensionless complex admittance per square of the film in units of the characteristic admittance Z_c^{-1} of the waveguide (where $Z_c = Z_0/\sqrt{1 - (f_c/f)^2}$, $z_0 = 377\ \Omega$, mks; $Z_0 = 4\pi/c$, cgs; f_c = cutoff frequency of the TE mode waveguide, and f is the operational frequency).

In the normal state, eq. (2) becomes

$$P_N = \frac{8n^2}{\sigma_N^2 d^2 Z_c^2 Q + \sigma_N d Z_c R + J}, \tag{3}$$

where

σ_N = normal conductivity,

$$Q = (n^2 + 1) + (n^2 - 1)\cos 2kl,$$

$$R = 2(3n^2 + 1) + 2(n^2 - 1)\cos 2kl,$$

$$J = n^4 + 6n^2 + 1 - (n^2 - 1)\cos 2kl.$$

The normal state conductivity of the film can be expressed conveniently in terms of the power transmission as

$$\sigma_N = \frac{-RP_N \pm \sqrt{(RP_N)^2 - 4QP_N(JP_N - 8n^2)}}{2QP_N dZ_c}, \tag{4}$$

where only the expression with the + sign has physical relevance. It is convenient to use the ratio P_S/P_N in the analysis of the superconducting state, where P_S refers to the transmission in the superconducting state given by eq. (2). Thus,

$$\frac{P_S}{P_N} = \frac{(\sigma_N dZ_c)^2 Q + \sigma_N dZ_c R + J}{A + B\cos 2kl + C\sin 2kl}. \tag{5}$$

Solving eq. (5) for the imaginary part σ_2 of the conductivity and using the value of σ_N at $T = T_c$ we have

$$\frac{\sigma_2}{\sigma_c} = \left(\frac{-\beta}{2}\right)\frac{1}{\sigma_c dZ_c} + \left\{\frac{1}{(\sigma_c dZ_c)^2}\left[\left(\frac{\beta}{2}\right)^2 - \gamma\right] - \frac{\alpha\sigma_1}{\sigma_c^2 dZ_c} - \left(\frac{\sigma_1}{\sigma_c}\right)^2 + \left(\frac{P_c}{P_S}\right)\left[1 + \frac{\alpha}{\sigma_c dZ_c} + \frac{\gamma}{(\sigma_c dZ_c)^2}\right]\right\}^{1/2}, \tag{6}$$

where σ_c and P_c are the conductivity and the transmissivity at $T = T_c$, and

$$\alpha = (1/D)[6n^2 + 2 + 2(n^2 - 1)\cos 2kl],$$

$$\beta = (1/D)[-2n(n^2-1)\sin 2kl]\,,$$

$$\gamma = (1/D)[n^4+6n^2+1-(n^2+1)^2\cos 2kl]\,,$$

$$D = n^2+1+(n^2-1)\cos 2kl\,.$$

Thus, from the relation for σ_1 in eq. (1), and eq. (6), the real and imaginary parts of the conductivity can be determined.

The magnetic penetration depth λ can be obtained from London's equation

$$\lambda = (1/\mu_0\omega\sigma_2)^{1/2}\,, \tag{7}$$

where μ_0 is the permeability of free space. The magnetic penetration depth can then be written in terms of the superfluid density N_s as

$$\lambda = (m^*/\mu_0 N_s e^2)\,, \tag{8}$$

where m^* is the effective mass and e is the charge of the charge carriers. From the two-fluid model

$$\frac{N_s}{N} = 1-t^4\,, \tag{9}$$

where $N = N_n + N_s$ is the total number of carriers per unit volume, we have

$$\lambda = \left(\frac{m^*}{\mu_0 N e^2}\right)^{1/2}(1-t^4)^{-1/2} = \lambda_0(1-t^4)^{-1/2}\,. \tag{10}$$

From this expression the zero-temperature penetration depth λ_0 can be obtained. Note that since eq. (8) applies to homogeneous superconductors, the values of λ_0 obtained in this way are larger than those that would be obtained for homogeneous films.

Our measurements were made on $Bi_2Sr_2Ca_1Cu_2O_x$ superconducting films of approximately 5000 Å thickness deposited on MgO and $LaAlO_3$ substrates. The MgO and $LaAlO_3$ substrates were 0.113 and 0.025 cm thick, respectively. The films were deposited by co-evaporation in an oxygen atmosphere of 5×10^{-5} Torr. Then the film were post annealed at 725°C in a wet oxygen atmosphere for 30 to 60 min, followed by an anneal at 850°C for a period of 5 to 25 min. A more detailed explanation of the deposition technique is given in ref. [17]. The T_c for both films was approximately 80 K.

The power transmission measurements were made using a Hewlett–Packard model HP-8510 automatic network analyzer connected to a modified helium gas closed cycle refrigerator by Ka-band (26.5 to 40.0 GHz) waveguides. Inside the vacuum chamber of the refrigerator, the sample was clamped between two waveguide flanges which were in direct contact with the cold head of the refrigerator. The power transmitted through the sample was obtained by measuring the trasmission scattering parameter. The temperature gradient between the top and the bottom of the sample was estimated to be less than 1 K at 90 K. The system was properly calibrated with short, open, loads, and through calibration with short, open, loads, and through calibration standards before the beginning of each measurement cycle.

3. Results and discussion

The $Bi_2Sr_2Ca_1Cu_2O_x$ films deposited on $LaAlO_3$ and MgO substrates were inspected with a scanning electron microscope (SEM) and analyzed by X-ray diffraction. The surface morphology of the film deposited on MgO is smoother than for the one deposited on $LaAlO_3$, as can be seen from fig. 1. The voids seen in the SEM picture for the film deposited on the MgO were probably caused by hydrolyzing the CaF_2 and SrF_2 during the first step of the annealing. The hydrolyzation produces HF gas, which probably caused the voids. The same effect had been observed in sequentially evaporated $YBa_2Cu_3O_{7-\delta}$ superconducting films [18]. The films on both substrates are c-axis oriented. This can be observed from both the SEM pictures in fig. 1 and the X-ray diffraction data in fig. 2. One must conclude from the ratio of the $(00l)$ and $(00np)$ peaks in the X-ray diffraction pattern that the $Bi_2Sr_1Ca_1Cu_2O_x$ film on MgO is better c-axis aligned than the one on $LaAlO_3$.

Figures 3 and 4 show the transmitted power versus temperature plots, at three different frequencies, for the films considered in this study. The beginning of the superconducting transition is observed clearly in both films and for the three frequencies shown in the figures. Note that the starting point of this transition for both films remains approximately at the same temperature for the frequencies represented, suggesting that, at least for the frequencies and temperature intervals considered here, the frequency dependence of the starting point for the normal to the superconducting state transition is rather small. it is

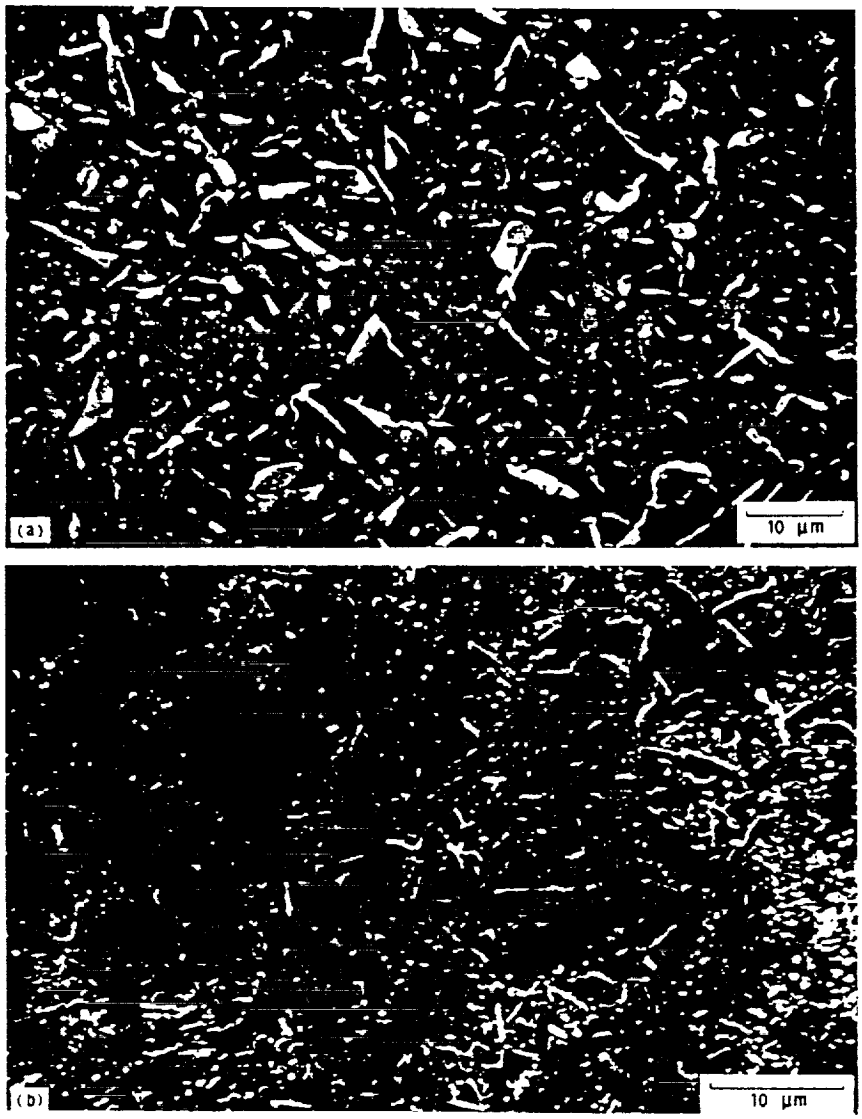

Fig. 1. Scanning electron micrograph for $Bi_2Sr_2Ca_1Cu_2O_x$ thin films (5000 Å) on $LaAlO_3$ (a) and MgO (b) substrates. The bar indicates 10 μm.

also observed that the temperature at which the normal to the superconducting state transition begins ($\sim$90 K) does not coincide with the transition temperature corresponding to zero DC resistance ($\sim$80 K). This behavior is in agreement with the rather broad resistive transition ($\Delta T_c \sim 10$ K) typical of this superconducting system, and it appears to indicate that within this region the sample is in a mixed state where all the superconducting clusters are not interconnected, as previously suggested by other researchers [19]. An interesting feature of the power transmission through the films is its frequency dependence. From fig. 3 it is observed that the power transmitted through the film on $LaAlO_3$ increases with increasing frequency, while the opposite behavior is observed for the film on MgO. Within the fre-

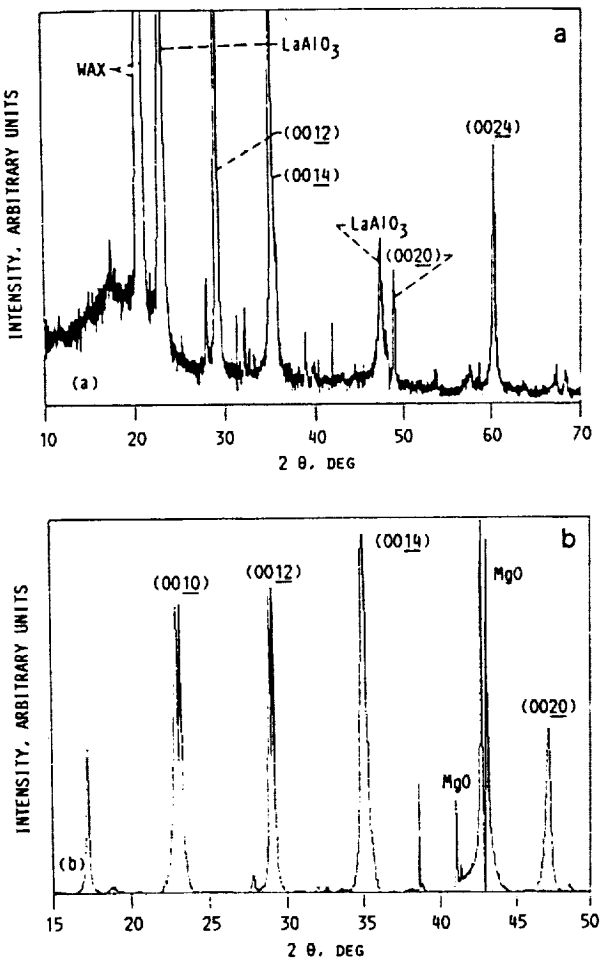

Fig. 2. X-ray diffraction pattern of 5000 Å superconducting BSCCO thin films on $LaAlO_3$ (a) and MgO (b) substrates. The films are the $Bi_2Sr_2Ca_1Cu_2O_x$ (2212) phase with the c-axis perpendicular to the $LaAlO_3$ and MgO substrates.

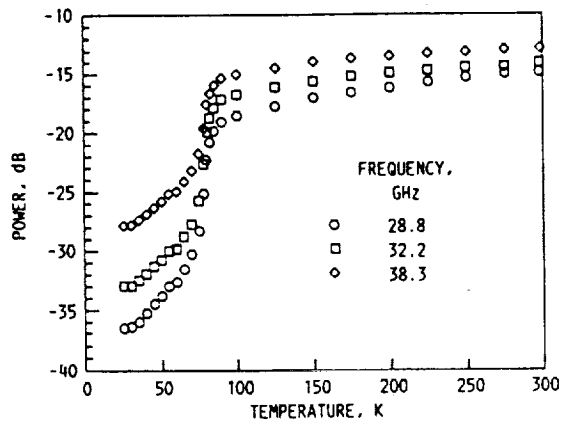

Fig. 3. Transmitted power vs. temperature for a co-evaporated $Bi_2Sr_2Ca_1Cu_2O_x$ thin film (5000 Å) on $LaAlO_3$.

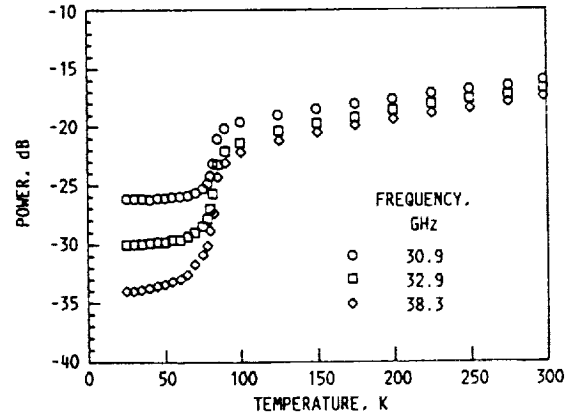

Fig. 4. Transmitted power vs. temperature for a co-evaporated $Bi_2Sr_2Ca_1Cu_2O_x$ thin film (5000 Å) on MgO.

quency range measured there is no frequency dependence in the power transmitted through bare $LaAlO_3$ and MgO substrates. This suggests that the observed frequency dependence is a film–substrate combination effect. No concrete explanation for this behavior is available yet, and further investigations are underway.

Figures 5 and 6 show the real and imaginary conductivities, σ_r and σ_2, respectively, for both films at 28.8 GHz. The values for the normal conductivities at room temperature for the films on MgO and $LaAlO_3$ are 6.3×10^4 and 4.1×10^4 S/m, respectively. Both values are lower than estimated values for the normal direct current conductivity at room temperature ($\sim 2.0\times10^5$ S/m) reported for very high quality $Bi_2Sr_2Ca_1Cu_2O_x$ superconducting films deposited on MgO by sequential electron beam evaporation [20]. No data within the normal to superconducting state transition region, clearly identified in fig. 5, were considered in our analysis. Although studies of this region had been done assuming different models, such as the presence of randomly diluted Josephson junctions [19], there is no simple physical model to account for the distribution of normal and superconducting carriers in this region, a fact that makes the determination of the normal

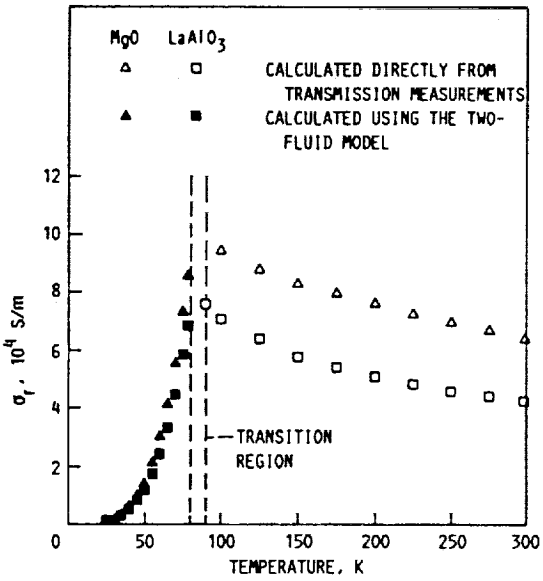

Fig. 5. Real part of the conductivity σ_r vs. temperature for co-evaporated $Bi_2Sr_2Ca_1Cu_2O_x$ thin films (5000 Å) on MgO and $LaAlO_3$ at 28.8 GHz. $\sigma_r = \sigma_N$ for $T > T_c$ and $\sigma_r = \sigma_1$ for $T < T_c$.

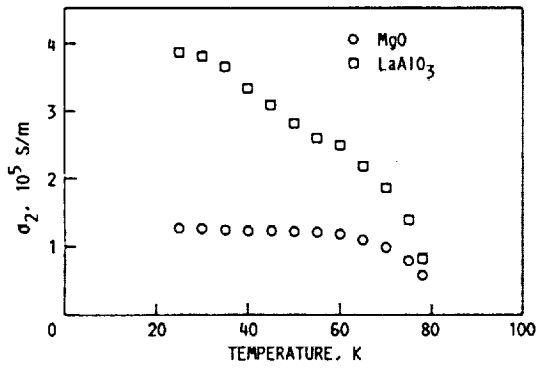

Fig. 6. Imaginary part of the conductivity σ_2 vs. temperature for co-evaporated $Bi_2Sr_2Ca_1Cu_2O_x$ thin films (5000 Å) on MgO and $LaAlO_3$ at 28.8 GHz.

conductivity down to T_c very cumbersome. Therefore, using the same approach applied in a previous work [12], we have considered the critical conductivity to be the conductivity at or just above the onset temperature. Since the two-fluid model assumes that all the regions of the sample become superconducting at once, the values of σ_1 obtained using $\sigma_c = \sigma_{onset}$ in eq. (1) will be smaller than those obtained from $\sigma_c = \sigma_{at\ T_c}$. How much these values differ will depend upon the width ΔT of the transition region and the overall quality of the superconducting properties of the film. For comparison purposes, an extrapolation of σ_r above T_{onset} to T_c was done. This resulted in a σ_c extrapolated 6.0 and 7.2 percent greater than σ_{onset} for the film on MgO and $LaAlO_3$, respectively. It is important to realize that this discrepancy will become smaller for films in which T_{onset} is very close to T_c. Using eq. (1), values of $\sigma_1 = 7.3 \times 10^4$ and $\sigma_1 = 5.9 \times 10^3$ S/m were obtained for the film on MgO at 75 and 40 K, respectively. For the film on $LaAlO_3$ we obtained $\sigma_1 = 5.8 \times 10^4$ and $\sigma_1 = 4.7 \times 10^3$ S/m at 75 and 40 K, respectively.

Figure 6 shows the imaginary part of the complex conductivity at 28.8 GHz for the two films under consideration. Observe that the values of σ_2 corresponding to the film on $LaAlO_3$ are greater than those of the film on MgO. This feature, together with the observation from fig. 5 that σ_1 for the film on MgO is greater than that for the film on $LaAlO_3$, appears to indicate that at this frequency the film on $LaAlO_3$ has better superconducting properties than the one on MgO. This raises an interesting observation that despite the film on $LaAlO_3$ being less c-axis oriented than the film on MgO, as concluded from the X-ray diffraction pattern, it still shows a higher degree of superconductivity. Therefore, the deposition of highly c-axis oriented $Bi_2Sr_2Ca_1Cu_2O_x$ on $LaAlO_3$ promises to yield films with excellent superconducting properties.

The imaginary part of the conductivity increases with decreasing temperature, a behavior expected from the two fluid model approximation. Values of 1.4×10^5 and 3.3×10^5 S/m are obtained for the film on $LaAlO_3$ at 75 and 40 K, respectively. For the film on MgO we obtained values of 7.7×10^4 and 1.2×10^5 S/m for the same temperatures mentioned above. Using eq. (7) we found the magnetic penetration depth λ for the film on $LaAlO_3$ to be 5.6 and 3.7 μm at 75 and 40 K, respectively. From the value of λ at 40 K we found $\lambda_0 = 3.6$ μm. For the film deposited on MgO we found $\lambda = 7.6$ μm at 75 K and $\lambda = 6.1$ μm at 40 K, and a value of λ_0 equal to 5.9 μm. The values of λ obtained for both films are considerably larger than the film's thickness, which implies a strong interaction between the microwave field parallel to the film surface and the substrate. The zero-temperature penetration depths are also large in compari-

son with the values obtained at the same frequencies and temperature for laser ablated $YBa_2Cu_3O_{7-\delta}$ superconducting thin films on $LaAlO_3$ and MgO [12].

Figures 7 to 10 show the real and imaginary conductivities versus temperature at 31.5 and 34.9 GHz. It can be seen that as the frequency increases so does the imaginary part of the conductivity of the film on MgO, while the imaginary part of the conductivity for the film on $LaAlO_3$ decreases with increasing frequency. No significant change as a function of frequency is observed for σ_1. Values for λ of 3.7 and 3.9 μm were obtained for the film on $LaAlO_3$ at 40 K and at 31.5 and 34.9 GHz, respectively. For the film deposited on MgO, λ was equal to 5.4 and 4.7 μm for the same temperature and frequencies.

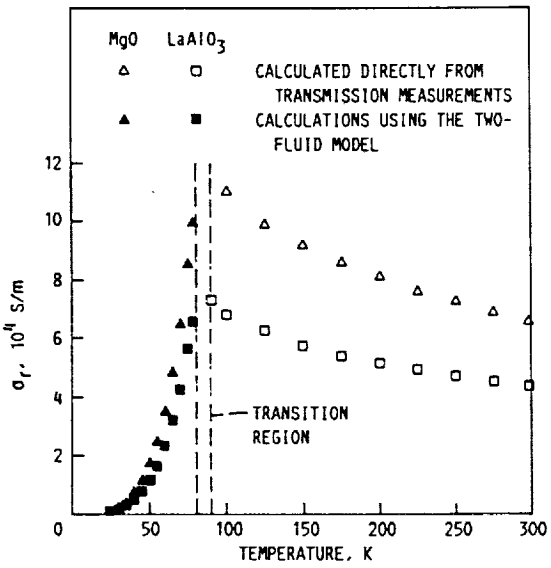

Fig. 7. Real part of the conductivity σ_r vs. temperature for co-evaporated $Bi_2Sr_2Ca_1Cu_2O_x$ thin films (5000 Å) on MgO and $LaAlO_3$ at 31.5 GHz. $\sigma_r=\sigma_N$ for $T>T_c$ and $\sigma_r=\sigma_1$ for $T<T_c$.

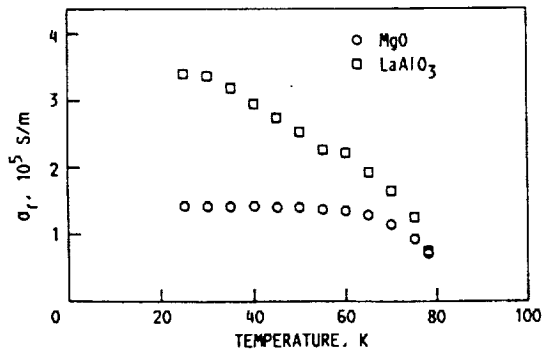

Fig. 8. Imaginary part of the conductivity σ_2 vs. temperature for co-evaporated $Bi_2Sr_2Ca_1Cu_2O_x$ thin films (5000 Å) on MgO and $LaAlO_3$ at 31.5 GHz.

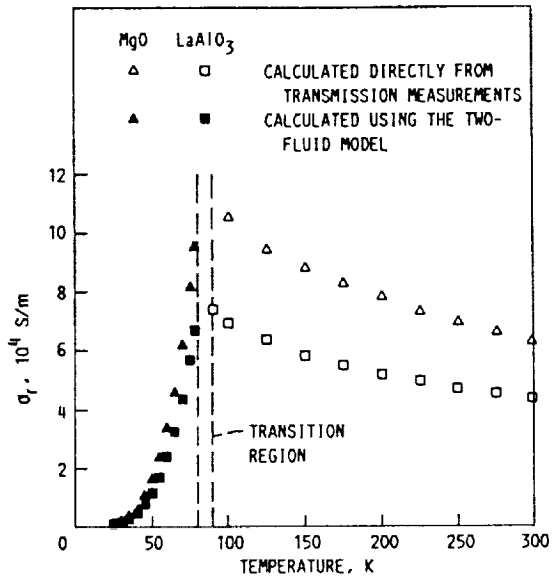

Fig. 9. Real part of the conductivity σ_r vs. temperature for co-evaporated $Bi_2Sr_2Ca_1Cu_2O_x$ thin films (5000 Å) on MgO and $LaAlO_3$ at 34.9 GHz. $\sigma_r=\sigma_N$ for $T>T_c$ and $\sigma_r=\sigma_1$ for $T<T_c$.

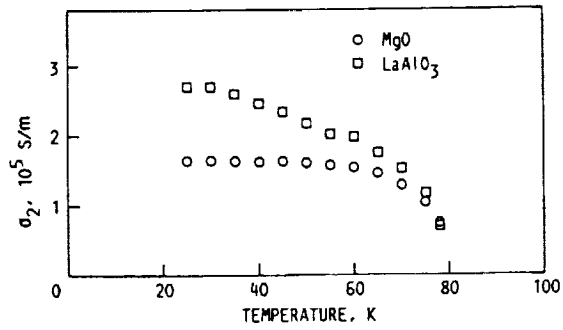

Fig. 10. Imaginary part of the conductivity σ_2 vs. temperature for co-evaporated $Bi_2Sr_2Ca_1Cu_2O_x$ thin films (5000 Å) on MgO and $LaAlO_3$ at 34.9 GHz.

4. Conclusions

Microwave conductivities of superconducting Bi-

Sr–Ca–Cu–O thin films at frequencies within 26.5 to 40.0 GHz and at temperatures from 25 to 300 K were determined. The conductivities, σ_N and $\sigma^* = \sigma_1 - i\sigma_2$, corresponding to the normal and the superconducting state, respectively, were obtained in terms of the transmitted power and a two-fluid model. The results obtained suggest that, at least from the standpoint of the complex conductivity and for the frequency range considered, the film deposited on $LaAlO_3$ shows better superconducting properties than the one deposited on MgO. Values for the magnetic penetration depth, determined using the obtained values of σ_2, were more than five times the film thicknesses, indicating a strong field substrate interaction in this frequency range. This aspect may be of importance in the proper selection of film-substrate combination for microwave devices operating in this frequency range.

References

[1] J.G. Bednorz and K.A. Muller, Z. Phys. B 64 (1986) 189.

[2] M.K. Wu, J.R. Ashburn, C.J. Torng, P.H. Hor, R.L. Meng, L. Gao, Z.J. Huang, Y.Q. Wang and C.W. Chu, Phys. Rev. Lett. 58 (1987) 908.

[3] S. Sridhar and W.L. Kennedy, Rev. Sci. Instrum. 59 (1988) 531.

[4] J.S. Martens, J.B. Beyer and D.S. Ginley, Appl. Phys. Lett. 52 (1988) 1822.

[5] J.P. Carini, A. Awasthi, W. Beyerman, G. Gruner, T. Hylton, K. Char, M.R. Beasley and N.A. Kapitulnik, Phys. Rev. B37 (1988) 9726.

[6] N. Klein, G. Muller, H. Piel, B. Roas, L. Schultz, V. Klein and M. Peiniger, Appl. Phys. Lett. 54 (1989) 757.

[7] L. Cohen, I.G. Gray, A. Porch and J.R. Waldram, J. Phys. F 17 (1987) L179.

[8] W. Ho, P.J. Hood, W.F. Hall, P. Kobrin, A.B. Harker and R.E. Dewames, Phys. Rev. B38 (1988) 7029.

[9] C.S. Nichols, N.S. Shiren, R.B. Leibowitz and T.G. Kazyaka, Phys. Rev. B38 (1988) 11970.

[10] H. Maeda, Y. Tanaka, M. Fukutomi and T. Asano, Jpn. J. Appl. Phys. Lett. 27 (1988) L209.

[11] Z.Z. Sheng and A.M. Hermann, Nature 332 (1988) 138.

[12] F.A. Miranda, W.L. Gordon, K.B. Bhasin, V.O. Heinen, J.D. Warner and G.J. Valco, NASA TM-102345 (1989) and to be published in: Superconductivity and Applications, (Plenum, 1990).

[13] J.I. Gittleman and B. Rosenblum, IEEE Proc. 52 (1964) 1138.

[14] W.J. Radclife, J.C. Gallop, C.D. Langham, M. Gee and M. Stewart, Physica C 153 (1988) 635.

[15] J.I. Gittleman and J.R. Matey, J. Appl. Phys. 65 (1989) 688.

[16] R.E. Glover III and M. Tinkham, Phys. Rev. 108 (1957) 243.

[17] T.S. Kalkur, R. Kwor, S. Jernigan and R. Smith,Coevaporated Bi–Sr–Ca–Cu Oxide Superconducting Films and Their Patterning, presented at the Conf. Sci. Technol. Thin Films Supercond., Colorado Springs, CO, 14–18 November, 1988.

[18] G.J. Valco, N.J. Rohrer, J.D. Warner and K.B. Bhasin, NASA TM-101388, and American Institute of Physics Conf. Proc., Vol. 182 (1989) p. 147.

[19] S.C. Gadkary, K.P. Muthe, S.K. Gupta, S.C. Sabharwal and M.K. Gupta, Physica C 160 (1989) 167.

[20] J. Steinbeck, B.Y. Tsaur, A.C. Anderson and A.J. Strauss, Appl. Phys. Lett. 54 (1989) 446.

NASA Technical Memorandum 103180

Sequentially Evaporated Thin Film $YBa_2Cu_3O_{7-x}$ Superconducting Microwave Ring Resonator

Norman J. Rohrer, Hing Y.To, and George J. Valco
Ohio State University
Columbus, Ohio

Kul B. Bhasin
Lewis Research Center
Cleveland, Ohio

Chris Chorey
Sverdrup Technology, Inc.
Lewis Research Center Group
Brook Park, Ohio

Joseph D. Warner
Lewis Research Center
Cleveland, Ohio

Prepared for the
Conference on the Science and Technology of Thin Film Superconductors
sponsored by the U.S. Department of Energy
Denver, Colorado, April 30—May 4, 1990

NASA

SEQUENTIALLY EVAPORATED THIN FILM $YBa_2Cu_3O_{7-x}$ SUPERCONDUCTING MICROWAVE RING RESONATOR

Norman J. Rohrer, Hing Y. To, and George J. Valco

Department of Electrical Engineering
Ohio State University, Columbus, Ohio 43210

Kul B. Bhasin

National Aeronautics and Space Administration
Lewis Research Center, Cleveland, Ohio 44135

Chris Chorey

Sverdrup Technology, Inc.
Lewis Research Center Group, Brook Park, Ohio 44142

Joseph D. Warner

National Aeronautics and Space Administration
Lewis Research Center, Cleveland, Ohio 44135

ABSTRACT

There is great interest in the application of thin film high temperature superconductors in high frequency electronic circuits. A ring resonator provides a good test vehicle for assessing the microwave losses in the superconductor and for comparing films made by different techniques. Ring resonators made of $YBa_2Cu_3O_{7-x}$ have been investigated on $LaAlO_3$ substrates. The superconducting thin films were deposited by sequential electron beam evaporation of Cu, Y, and BaF_2 with a post anneal. Patterning of the superconducting film was done using negative photolithography. A ring resonator was also fabricated from a thin gold film as a control. Both resonators had a gold ground plane on the backside of the substrate. The ring resonators' reflection coefficients were measured as a function of frequency from 33 to 37 GHz at temperatures ranging from 20 K to 68 K. The resonator exhibited two resonances which were at 34.5 and 35.7 GHz at 68 K. The resonant frequencies increased with decreasing temperature. The magnitude of the reflection coefficients is used in the calculation of the unloaded Q-values. The performance of the evaporated and gold resonator are compared with the performance of a laser ablated $YBa_2Cu_3O_{7-x}$ resonator. The causes of the double resonance are discussed.

INTRODUCTION

The advent of high temperature superconductors has drawn attention towards the possibilities of using thin films superconductors in microwave circuits. Several measurement techniques have been employed for characterization of the films including high Q cavities [1], stripline resonators [2] and

ring resonators [3]. The surface resistance of the the YBa2Cu3O7-x superconductor has been investigated on bulk samples, thin films and single crystals [4-6]. In this paper we employ a ring resonator to study the microwave properties of $YBa_2Cu_3O_{7-\delta}$ fabricated by multi-layer sequential evaporation with post-anneal.

DEPOSITION AND ANNEAL PROCEDURES

Electron beam evaporation was used for deposition of Cu, Y, and BaF_2 on $LaAlO_3$. The materials were deposited in that order which was repeated four times for a total of twelve layers. The thicknesses of the individual layers were 507 angstroms for Cu, 473 angstroms for Y, and 1704 angstroms for BaF_2. The details of the deposition process have been previously reported [7,8].

The multilayer stack was subjected to a post anneal to assist in the formation of the proper phase of $YBa_2Cu_3O_{7-x}$. The samples were inserted into a preheated furnace using a slow push. They were annealed at 900 °C for 45 minutes in oxygen bubbled through room temperature water. The temperature was then ramped down to 450 °C where it was held for six hours. Finally, the temperature was ramped down to room temperature. The ambient was dry oxygen during all stages except the high temperature anneal. This procedure resulted in a one micron thick superconducting thin film with an onset temperature of 93 K and a critical temperature of 85 K.

PATTERNING PROCEDURE

The ring resonator was patterned using negative photolithography. KTI 752 photoresist was spun on at a rate of 4,000 rpm for 60 seconds which resulted the photoresist being 1.7 μm thick. The sample was soft baked at 95 °C for 25 minutes and exposed through a dark field mask for five seconds with an illumination power density of 34.8 mW/cm^2. The photoresist was developed for 2 minutes and 45 seconds in 802 developer and rinsed in ethanol. A one percent molar bromine solution in ethanol was used for etching the thin film followed by a 30 second rinse. Finally, the photoresist was removed in SN-10 stripper.

Once the superconductor was patterned, a ground plane was deposited on the back of the substrate using electron beam evaporation. For adhesion, a 1400 angstrom titanium layer was deposited before the one micron gold ground plane.

RESONATOR ANALYSIS

The following dimensions correspond to the resonator shown in Figure 1. H is the substrate thickness.

H = 254 microns	W = 143.3 microns
S = 36 microns	R = $(r_1 + r_2)/2$ = 990 microns

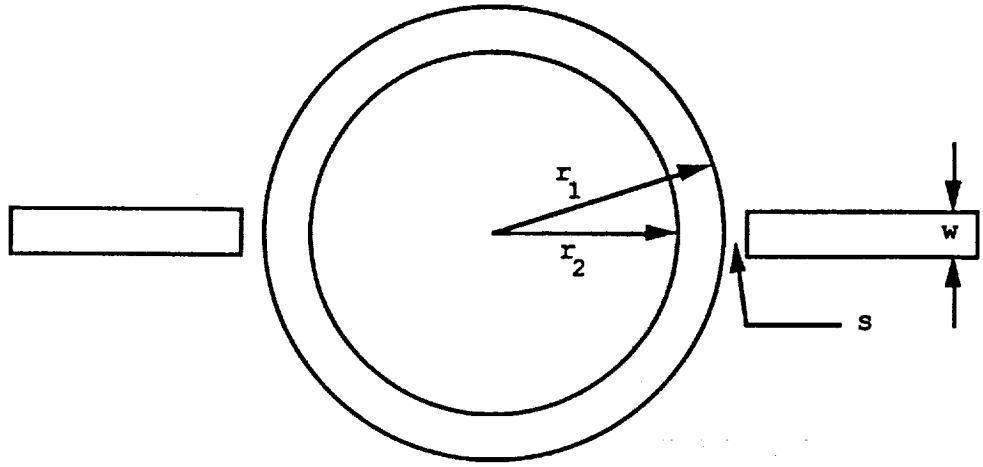

Figure 1: Ring resonator.

The resonator was designed for 50 ohm transmission lines with a resonant frequency of 30 GHz for the first harmonic. At the time of the design, the dielectric constant for $LaAlO_3$ was reported to be 15. Since then a more recent value reported for the dielectric constant is 21.9. This has resulted in a characteristic impedance for this geometry 42.9 ohms. The first harmonic was decreased below K-band. For this reason, we measured at the second harmonic which had a resonant frequency of 35.1 GHz at 25 K.

Microwave Testing

Once fabricated the ring resonator was experimentally tested using an HP 8510B network analyzer. The microwave test setup was configured using waveguides. Thus, a waveguide to microstrip transition was implemented using a cosine tapered ridge transition [9].

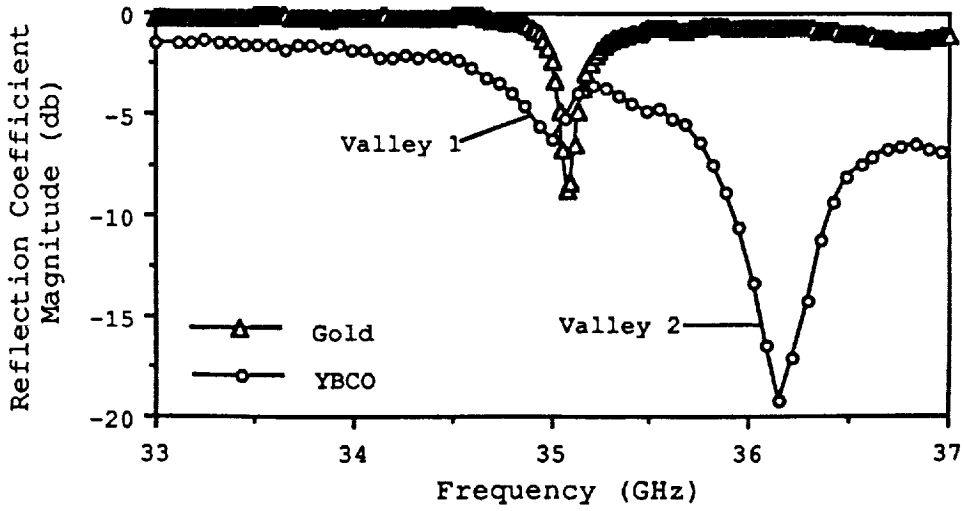

Figure 2: Magnitude of the reflection coefficient for ring resonator's fabricated from gold and $YBa_2Cu_3O_{7-x}$ at 30 K.

The reflection coefficient for the resonators was measured as a function of frequency at temperatures ranging from 20 K to 300 K using a CTI closed cycle cryogenic refrigerator. The superconducting resonator was measured from 20 K to its critical temperature. The resonant frequency superconducting resonator was 35.1 GHz at 25 K. Figure 2 shows the magnitude of the reflection coefficient for both the gold and the superconducting resonator at approximately 30 K.

The superconducting resonator exhibited two resonant valleys. Valley 1 matched the resonant frequency of the gold resonator while valley 2 occurred at 36.1 GHz. As will be discussed below, the occurrence of the second valley can be caused by one section of the ring resonator having a larger impedance than the rest of the ring.

Double Resonance Modeling

A transmission line model was implemented in Touchstone [10] to allow study of the double resonance. The resonator was simulated using transmission lines to match the physical layout and capacitors to model the gap. The capacitance values used were calculated from empirical equations derived in reference [11]. The impedance was increased in a region corresponding to three percent of the ring's circumference located closer to the transmission end. The location of this section for our model was 114° from the input. The impedance of this region was increased from a single line with 42.9 ohms to two parallel lines of 150 ohms each. This simulates a blister centered in the ring's transmission line. Figure 3 presents the results from this model.

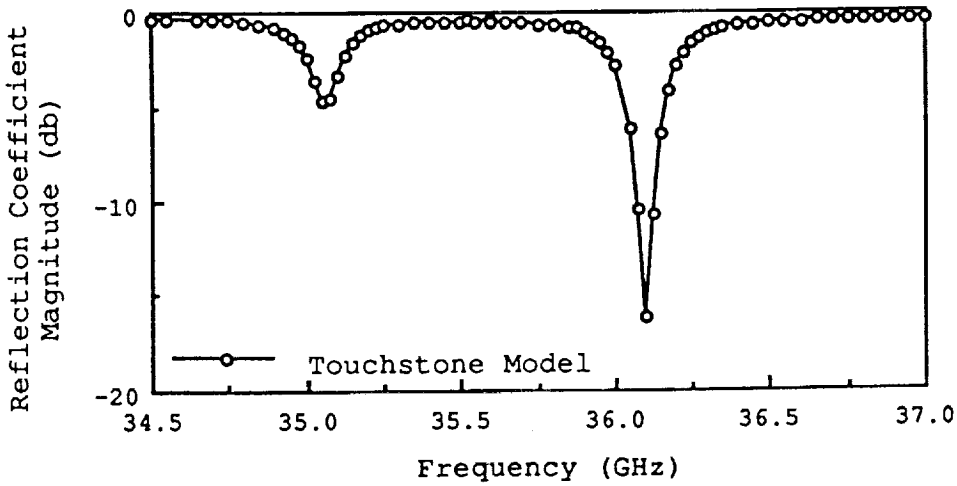

Figure 3: Modeled ring resonator with blister centered in the transmission line. Impedance of the lines around the blister were 150 ohms. Blister was located 1/3 the way around the ring.

The resonant frequencies of the model match directly with the resonant frequencies of the superconducting ring resonator. The width of valley 1 is quite similar, but the width of valley 2 is smaller for the modeled resonator. The reflection coefficient is much lower off resonance for the superconducting resonator. The the depth of the valley's peaks could be

altered by varying the position of the blister around the ring. The position used for the calculation shown in Figure 3 agrees with the location of a blistered region observed in the film of the resonator. The separation of the two valleys could be increased by increasing the impedance of the transmission lines around the blister. The response of the model remained the same for different number of transmission lines used within the high impedance region as long as the parallel combination of the characteristic impedances remained constant.

Resonant Frequency Shifts

The group velocity for a microstrip configuration with superconducting transmission lines varies as a function of temperature for temperatures less than the superconductor's critical temperature. This corresponds directly to a change in wavelength. Thus, the resonant frequency also varies as a function of temperature. The group velocity for a superconducting transmission line with a superconducting ground plane is given by [12]

$$v = \frac{c}{\sqrt{e_{eff(f)}}} \left[1 + \left(\lambda_1/h\right) \coth\left(t_1/\lambda_1\right) + \left(\lambda_2/h\right) \coth\left(t_2/\lambda_2\right)\right]^{-1/2}$$

where λ_1 and t_1 are the transmission line's penetration depth and thickness, respectively, and λ_2 and t_2 are the ground plane's penetration depth and thickness, respectively. If the ground plane is a normal metal, the group velocity is reduced to

$$v = \frac{c}{\sqrt{e_{eff(f)}}} \left[1 + \left(\lambda_1/h\right) \coth\left(t_1/\lambda_1\right)\right]^{-1/2}$$

Note that the first equation is general enough to accommodate microstrip circuitry with superconductors of different penetration depths for the transmission line and ground plane.

Figure 4 shows the calculated resonant frequency for a 0.7 micron thick film as a function of the temperature normalized to the critical temperature. This graph shows three plots. Two plots show the comparison of the resonant frequency with two different penetration depths for a sample with a gold ground plane and a superconducting resonator. The penetration depths were chosen to be on each side of the values experimentally determined by [13]. The third plot represented by the open squares shows the resonant frequency as a function of temperature for a sample with both the ground plane and the resonator being superconducting. Replacing both the transmission lines and the ground plane with a superconductor will decrease the losses in the circuit if the superconductor losses are lower than the gold losses. The resonant frequency for a sample with both a superconducting transmission line and a ground plane will exhibit a larger shift in the resonant frequency as the temperature nears the critical temperature for the superconducting film.

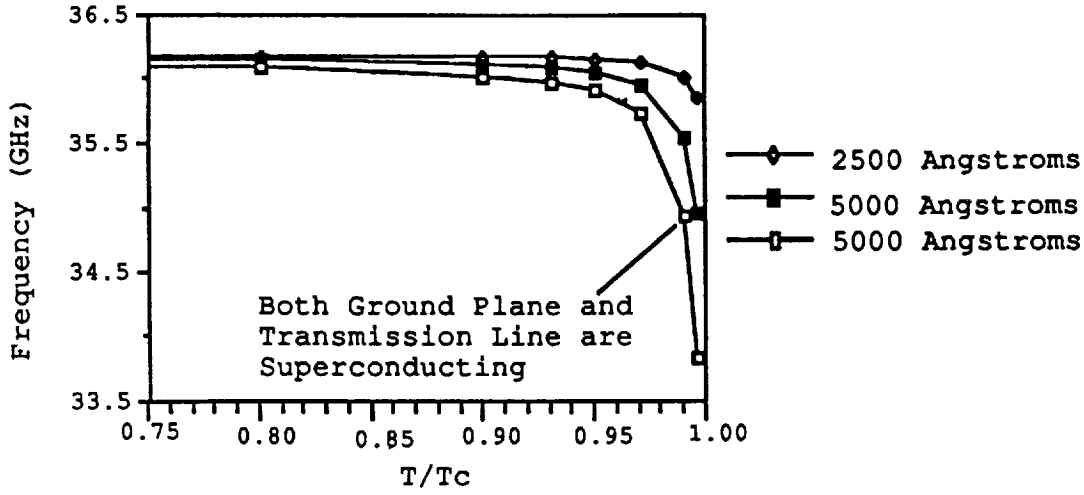

Figure 4: Resonant frequency versus normalized temperature for a 0.7 micron thick film. Different penetration depths are shown as well as an example of both ground plane and transmission lines being superconductors.

The shift in the resonant frequency for the sequentially evaporated superconducting ring resonator exhibited the same shape as the theoretical predictions. The measured resonant frequency as a function of temperature is given in Figure 5.

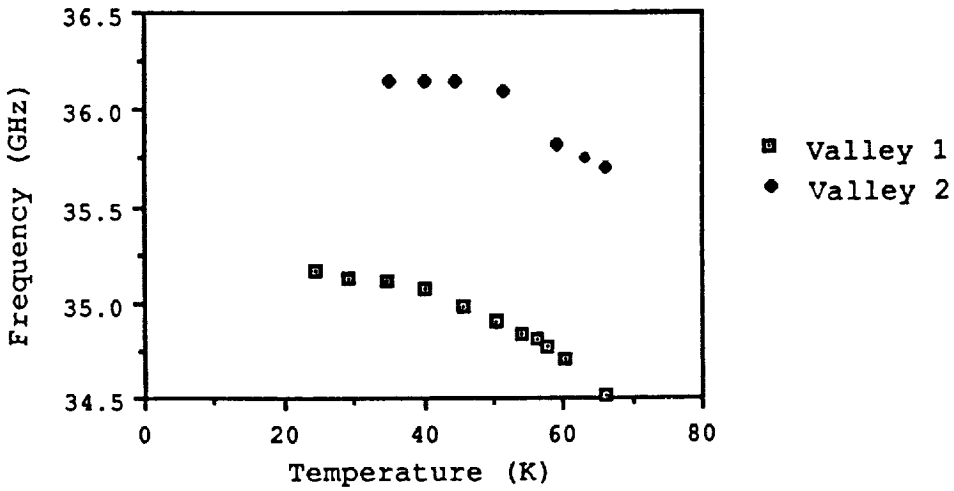

Figure 5: Resonant frequency versus temperature for the superconducting ring resonator. Both valleys are represented.

An attempt was performed to try to match the theoretical equations with the experimental data. The equations resulted in a penetration depth that was much larger than the thickness of the film. This is not reasonable since the film would no longer be superconducting for a large penetration depth. A possible explanation for the large penetration depth is due to the film being granular. This may allow more penetration at between grains.

Unloaded Q Calculation

The unloaded Q of the resonator can be extracted from the reflection coefficient. The model used for the derivation of the equation is a parallel RLC circuit with an ideal transformer in parallel and a series input resistance [14]. This model is for an unterminated resonator. It was used since the resonator was not loaded on the transmission side during our testing.

The derivation of the equations presented here are published in reference [14]. The loaded Q of a resonator is given by

$$Q_L = \frac{f_r}{f_1 - f_2}$$

where f_1 and f_2 are the half power points on each side of the resonant frequency f_r. The values for the half power levels are calculated by

$$p_{1/2} = \frac{1}{2}\left(\left[\frac{k' - 1}{k' + 1}\right]^2 + \left[\frac{\sigma - 1}{\sigma + 1}\right]^2\right)$$

where σ is the coupling loss and k' is the effective coupling coefficient. The coupling loss is calculated far off resonance where the reflection coefficient (Γ_i) is nearly constant.

$$\sigma = \frac{1 - \Gamma_i}{1 + \Gamma_i}$$

The effective coupling coefficient is the sum of the coupling coefficient and the coupling loss. The coupling coefficient can be easily calculated using the reflection coefficient (Γ_r) at the resonant frequency. The coupling coefficient can be calculated by

$$k = \frac{1 - \Gamma_r}{1 + \Gamma_r} \quad \text{or} \quad k = \frac{1 + \Gamma_r}{1 - \Gamma_r}$$

for the undercoupled and overcoupled cases, respectively. The unloaded Q can be calculated from the loaded Q by

$$Q_o = Q_L\left(\frac{1 + k'}{1 + \sigma}\right)$$

The unloaded Q as a function of temperature is shown in Figure 6. The unloaded Q for both valleys of the sequentially evaporated resonator are shown.

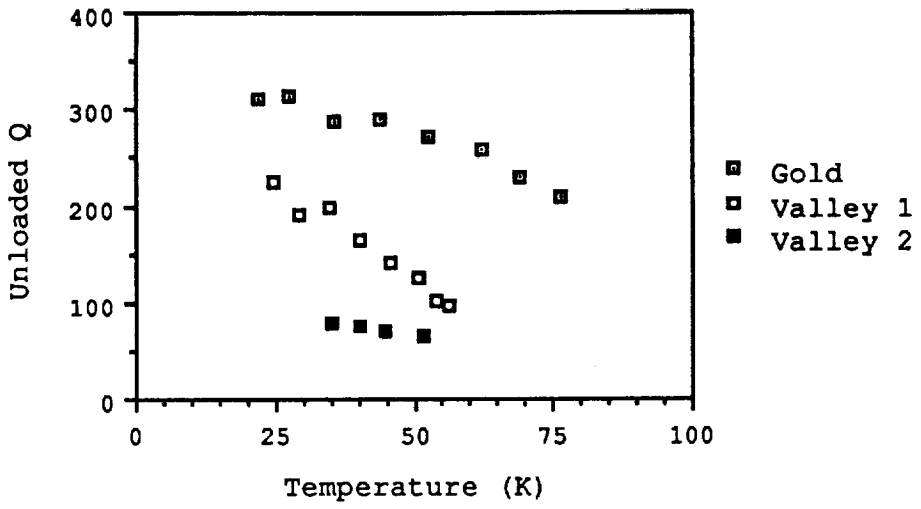

Figure 6: Unloaded Q versus temperature for the gold ring and the superconducting ring. Both valleys are shown for the superconducting ring.

The gold resonator had a larger unloaded Q than our sequentially evaporated film. At lower temperatures the difference between the unloaded Q values narrowed since the superconducting resonator's unloaded Q increased faster then the gold resonator's when compared to valley 1.

Surface Resistance

The surface resistance of the ring resonator can be extracted from the unloaded Q. The surface resistance is given by [15]

$$R_{SS} = R_{SAU} - \frac{4\pi Z_o}{B(C + D)} \frac{\pi}{\lambda} \left(\frac{1}{Q_{oAU}} - \frac{1}{Q_{oS}} \right)$$

where R_{SAU} is the surface resistance of gold, and Q_{oAU} and Q_{oS} are the unloaded Q values of the gold resonator and the superconducting resonator at the same temperature, respectively. The constants B, C, and D are related to the physical dimensions and are given in reference [15].

The surface resistance as a function of temperature for both the gold and the sequentially evaporated films are shown in Figure 7. For comparison a ring resonator was fabricated from a film deposited by laser ablation [16]. The surface resistance calculated for this film is also shown in Figure 7.

The graph shows that the sequentially evaporated film had the highest surface resistance at all temperatures. The gold film's surface resistance was about two-thirds the value of the sequentially evaporated film at 25 K. The laser ablated film had a surface resistance of approximately half that of gold at temperatures less than 50 K. As the temperature neared the critical temperature, the surface resistance of the laser ablated film started to increase rapidly to a value larger than that for gold at 70 K.

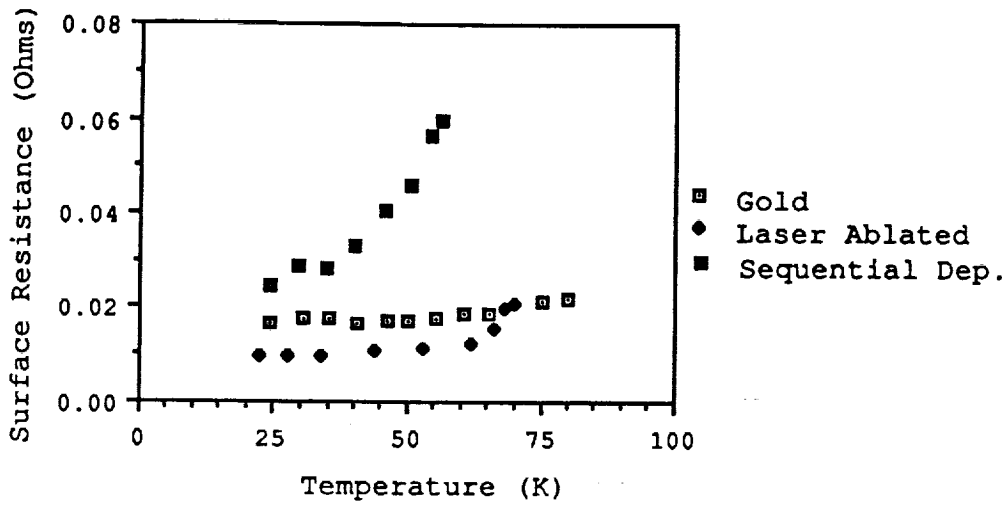

Figure 7: Surface resistance versus temperature for a gold resonator and two superconducting resonators. The superconducting resonators were deposited using different techniques. One was deposited by laser ablation and one by sequential evaporation.

CONCLUSION

A sequentially evaporated $YBa_2Cu_3O_{7-x}$ superconducting thin film was patterned into a ring resonator using negative photolithography. The ring resonators' reflection coefficients were measured using an HP 8510B network analyzer as a function of frequency from 33 to 37 GHz at temperatures ranging from 20 K to 68 K. The resonator exhibited two resonances which were at 34.5 and 35.7 GHz at 68 K. The resonant frequencies increased with decreasing temperature. The double resonance could be explained using a model that allowed for a small section of the ring resonator to have a larger impedance than the rest of the ring resonator. The location of the high impedance section in the model correlated well with the location of a blistered region of the film in the resonator. Once the reflection coefficient data was taken, the unloaded Q was extracted. The superconducting resonator was compared to a gold resonator. The gold resonator had a higher unloaded Q value at all temperatures. This translated into the gold having a lower surface resistance than the sequentially evaporated superconducting film. The surface resistance of the gold was about two-thirds the surface resistance of the sequentially evaporated superconducting film at 25 K. When compared to the laser ablated film, the laser ablated film's surface resistance was about one half that of gold for temperatures less than 50 K.

ACKNOWLEDGEMENTS

Design of the ring resonator was done by Robert Romanofsky and one of the authors (Kul Bhasin). This research was funded by the National Aeronautics and Space Administration, Lewis

Research Center under cooperative research agreement NCC 3-105 and under the graduate student research program NGT 50378.

REFERENCES

1. J. S. Marten, J. B. Beyer, and D. S. Ginley, Appl. Phys. Lett. **52** (21), 1822 (1988).
2. M. DiIorio, A. C. Anderson, and B. Y. Tsaur, Phys. Rev. B., **38** (10), 9726 1988.
3. J. H. Takemoto, F. K. Oshita, H. R. Fetterman, P. Korbin, E. Sovero, **MTT-37**, 1650 (1989).
4. M. K. Wu, J. R. Ashburn, C. J. Torng, P. H. Hor, R. L. Meng, L. Gao, Z. J. Huang, Y. O. Wang, and C. W. Chue, Phys. Rev. Lett., **58**,908 (1987).
5. T. M. P. Percival, J. S. Thorn, and R. Driver, Electron. Lett., **23**, 1225 (1987).
6. I. Sankawa, M. Sato, T. Konaka, M. Dobayashi, and K. Ishihara, Jap. Journ. Appl. Phys., **27** (9), L1637 (1988).
7. G. J. Valco, N. J. Rohrer, J. D. Warner and K. B. Bhasin, High T_c Superconducting Thin Films, Devices and Applications, G. Margaritiondo, R. Joynt and M. Onellion, AIP Conference Proceedings No. 182, pp. 147-154, American Institute of Physics, Atlanta, 1988.
8. G. J. Valco, N. J. Rohrer, J. D. Warner and K. B. Bhasin, Proceedings of the Workshop on High Temperature Superconductivity, pp. 197-203, GACIAC, Hunstville, 1989.
9. R. R. Romanofsky and K. A. Shalkhauser, NASA Technical Paper # 2875, 1989.
10. Commercially available software, EEsof, Westlake Village, CA 91632.
11. R. Garg and J. J. Bahl, Int. Journ. Elect., 45 (1978).
12. J. C. Swihart, Journ. Appl. Phys., **32** (3), 461 (1961).
13. S. M. Anlage, H. Sze, H. J. Snortland, S. Tahara, B. Langley, C. B. Eom, M. R. Beasley, R. Taber, Appl. Phys. Lett. **54** (26) 1989.
14. Robert R. Romanofsky, NASA Technical Paper #2899, 1989.
15. J. Takamoto, F. Oshita, H. Fetterman, IEEE Trans., **MTT-37**, 1650 (1989).
16. K. B. Bhasin, C. M. Chorey, J. D. Warner, R. R. Romanofsky, V. O. Heinen, K. S. Kong, H. Y. Lee, and T. Itoh, To be published in Symp. Digest of the 1990 IEEE Int. Microwave Symp., Dallas, TX.

NASA Technical Memorandum 103144

Photoresponse of $YBa_2Cu_3O_{7-\delta}$ Granular and Epitaxial Superconducting Thin Films

G.J. Valco
Ohio State University
Columbus, Ohio

P. Claspy
Case Western Researve University
Cleveland, Ohio

and

J.D. Warner, N. Varaljay, and K.B. Bhasin
Lewis Research Center
Cleveland, Ohio

Prepared for the
Technical Symposium on Optical Engineering and Photonics
in Aerospace Sensing
sponsored by the Society of Photo-Optical Instrumentation Engineers
Orlando, Florida, April 16–20, 1990

NASA

Photoresponse of $YBa_2Cu_3O_{7-\delta}$ Granular and Epitaxial Superconducting Thin Films

G.J. Valco
Department of Electrical Engineering
Ohio State University, Columbus, Ohio 43210

P. Claspy
Department of Electrical Engineering
Case Western Reserve University, Cleveland, Ohio 44106

J.D. Warner, N. Varaljay and K.B. Bhasin
National Aeronautics and Space Administration
Lewis Research Center, Cleveland, Ohio 44135

ABSTRACT

In this paper we report on the response of thin films of $YBa_2Cu_3O_{7-\delta}$ with either a very grainy or a smooth epitaxial morphology to visible radiation. $SrTiO_3$ substrates were employed for both types of films. The grainy films were formed by sequential multi-layer electron beam evaporation while the epitaxial films were formed by laser ablation. Both films were patterned into "H" shaped detectors via a negative photolithographic process employing a Br/ethanol etchant. The bridge region of the "H" was 50μm wide. The patterned films formed by laser ablation and sequential evaporation had critical temperatures of 74 K and 72 K respectively. The bridge was current biased and illuminated with chopped He-Ne laser radiation and the voltage developed in response to the illumination was measured. A signal was detected only above the critical temperature and the peak of the response coincided with the resistive transition for both types of films although the correspondence was less exact for the grainy film. The details of the responses and their analysis are presented.

1. INTRODUCTION

The discovery of high temperature superconductors has prompted a large amount of research into potential applications. These include their use in detectors for electromagnetic radiation over a wide range of frequencies, including optical frequencies[1-4]. Much of the reported work attributes the observed photoresponse to bolometric effects in which the film is heated by the incident radiation. Some authors have attributed some of their observations, particularly for grainy films with wide transitions, to non-bolometric phenomena but these interpretations have not been universally accepted.

We report here our observations on the photoresponse of two different $YBa_2Cu_3O_{7-\delta}$ films to visible radiation. One film was epitaxial and had a smooth morphology while the other film had a mixed orientation to the substrate and was quite grainy. Both of these films had comparable critical temperatures and transition widths after patterning into test structures.

2. EXPERIMENTAL PROCEDURES

The sequentially evaporated films were deposited by electron beam evaporation. Details on the formation of these films have been reported previously[5,6] but the main parts of the process will be reviewed here. The films were formed from Cu, Y and BaF_2 deposited in that order. Five layers of each were deposited for a total of

fifteen layers. $SrTiO_3$ substrates were used. Following deposition the films were annealed in a hot wall tube furnace to form the superconductor. The samples were slowly pushed into the preheated furnace over a five minute period. They were annealed at 900°C for 15 min. The temperature was lowered to 450°C at -2°C/min and held there for 6 hr. Finally the temperature was lowered to room temperature at approximately 2°C/min. The ambient was oxygen bubbled through room temperature water during the high temperature anneal and dry oxygen at all other times. The thickness of the sequentially evaporated film for these experiments was 0.5 μm. Films produced by this procedure typically have a critical temperature of 85 K, a granular morphology with a "basket weave" texture and mixed orientation.

The epitaxial film was formed by laser ablation from a $YBa_2Cu_3O_{7-\delta}$ target[7]. During deposition the substrate was heated to 630°C and the chamber pressure was 170 mtorr oxygen. The wavelength of the laser was 248 nm, the energy density was 1.5 J/cm^2/pulse and the pulse rate was 4 per second. The laser beam was incident on the target at 15° from the normal. After deposition the oxygen pressure was raised to 1 atm and the temperature was lowered to 450 °C at -2°C/min. It was held there for 2 hr and then slowly lowered to 250°C. The film had a thickness of approximately 0.2 μm and a smooth morphology.

For the photoresponse measurements the films were patterned into an "H" shaped detector. The photolithographic procedure employed KTI 752 negative photoresist. The films were etched in 1:100 bromine:ethanol (molar). The bridge region of the "H" was 50 μm wide.

Electrical contacts were made to each of the four legs of the "H." The metalization for the contacts consisted of 0.7 μm of Ag and 0.3 μm of Au. The Au top layer was used to facilitate wire bonding. The contacts were patterned through a chlorobenzene assisted lift-off procedure employing positive photoresist. Following deposition, the contacts were annealed at 500°C in oxygen[5].

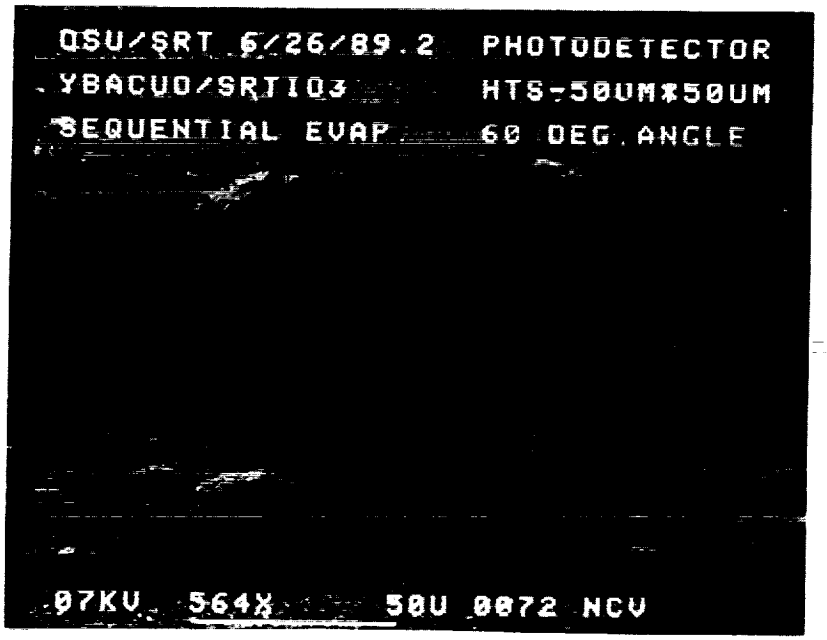

Figure 1. Scanning electron micrograph of a detector fabricated from a sequentially evaporated superconducting film.

Figure 1 shows a scanning electron micrograph of a detector made from the sequentially evaporated film. The darkest region is the superconductor. The four contacts are also visible on the legs of the "H". Also evident in this micrograph are many small blisters in the film. These blisters occasionally form on the sequentially evaporated films during the annealing procedure. They do not occur on all samples formed with nominally the same procedures but unfortunately did form on this sample. Electrical measurements showed continuity and measurements on this sample were carried out in spite of these defects. Figure 2 is a higher magnification micrograph of the bridge region of the same detector. The granular basket weave morphology is apparent. Notice that the basket weave structure is not apparent on the blister, where the film has come out of contact with the substrate.

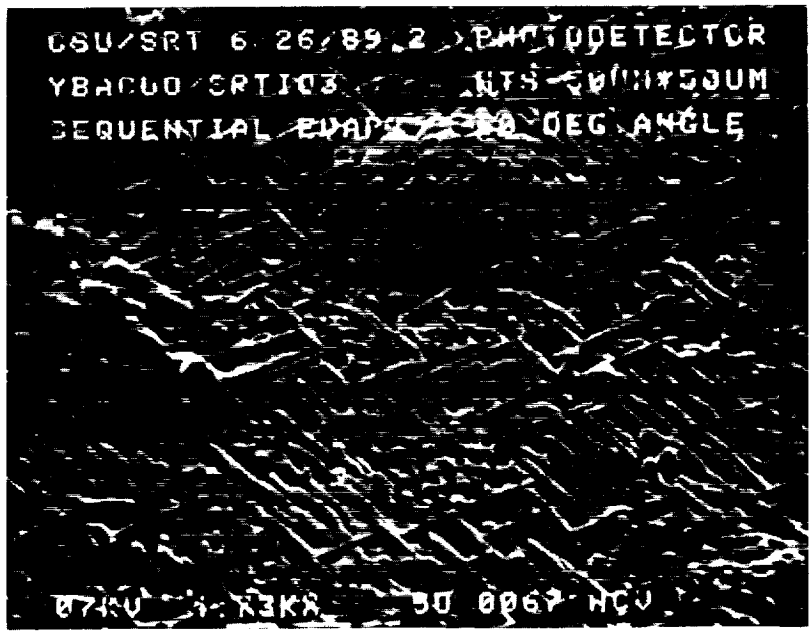

Figure 2. Higher magnification scanning electron micrograph of the bridge region of the sequentially evaporated detector.

The bridge region of a detector formed from the epitaxial laser ablated film is shown in Figure 3. The film is very smooth, although there are some small particles on the surface. (The large particles are dirt or dust.)

For measurement of the resistance-temperature characteristics and photoresponse of the samples, the substrates were mounted onto the sample holder of a closed cycle He cryostat. Gold wire bonds provided the electrical connections between the four contacts on the detectors and pins on the sample holder. Two of the contacts, one on each side of the bridge were used for current biasing while the other two were connected to either a voltmeter, for resistance measurements, or a lock-in amplifier, for photoresponse measurements.

For the photoresponse measurements the sample was illuminated with chopped He-Ne laser radiation. The light was focused onto the bridge region of the detectors through a window in the housing of the cryostat. To position the beam on the bridge for initial measurements, the temperature was adjusted to approximately the midpoint of the resistive transition. The detector was then illuminated and the position and focus of the beam was adjusted to maximize the detected signal. Additional comments on this will be made later in the paper. The diameter of the focused beam was small

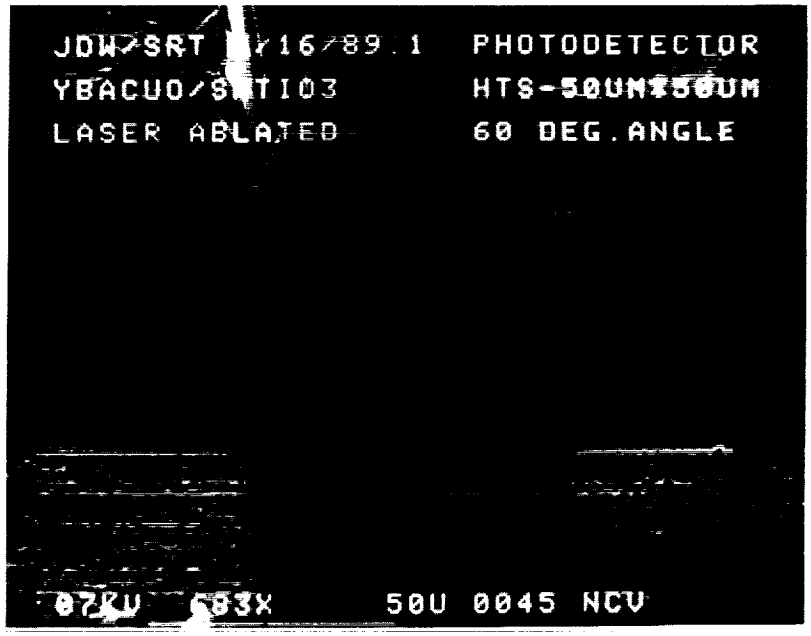

Figure 3. Scanning electron micrograph made from a laser ablated superconducting film.

enough to avoid illumination of the contacts so that spurious signals due to thermocouple effects were prevented. Such signals were observed on occasion for mispositioned beams, but not during actual measurements.

After positioning the beam, the photoresponse was measured as the temperature of the sample was varied. The measurements reported in this paper were made with the illumination chopped at 400 Hz and the sample biased at 100 μA. A few measurements of the photoresponse as a function of chopping frequency up to 4 KHz were made with the temperature fixed. The signal was found to decrease by approximately 40% as the frequency increased over this range. Measurements were also made at several lower bias currents. The response was found to scale with current and those results will not be further reported here.

3. RESULTS

The resistance (R) in ohms, dR/dT in ohms/K and measured signal in μV for the detector made from the epitaxial film are shown as a function of temperature from 70 to 90 K in Figure 4. The curve for dR/dT has been multiplied by a factor of five so that it could be plotted on the same scale as the others. The temperature of the sample was held at 79.4 K during optimization of the beam position. During the measurement it was varied down to approximately 12 K. The only observed response was in the range plotted in the figure. (Neglecting the small and nearly constant response at higher temperatures.) The peak of the photoresponse coincides well with the peak in dR/dT and the two curves agree well. The slight displacement of the two peaks is within the uncertainty in thermometry as the resistance-temperature characteristic and the photoresponse were not measured simultaneously. The agreement indicates a bolometric photoresponse.

Figure 5 is a graph of the resistance, dR/dT and the initial measurement of the

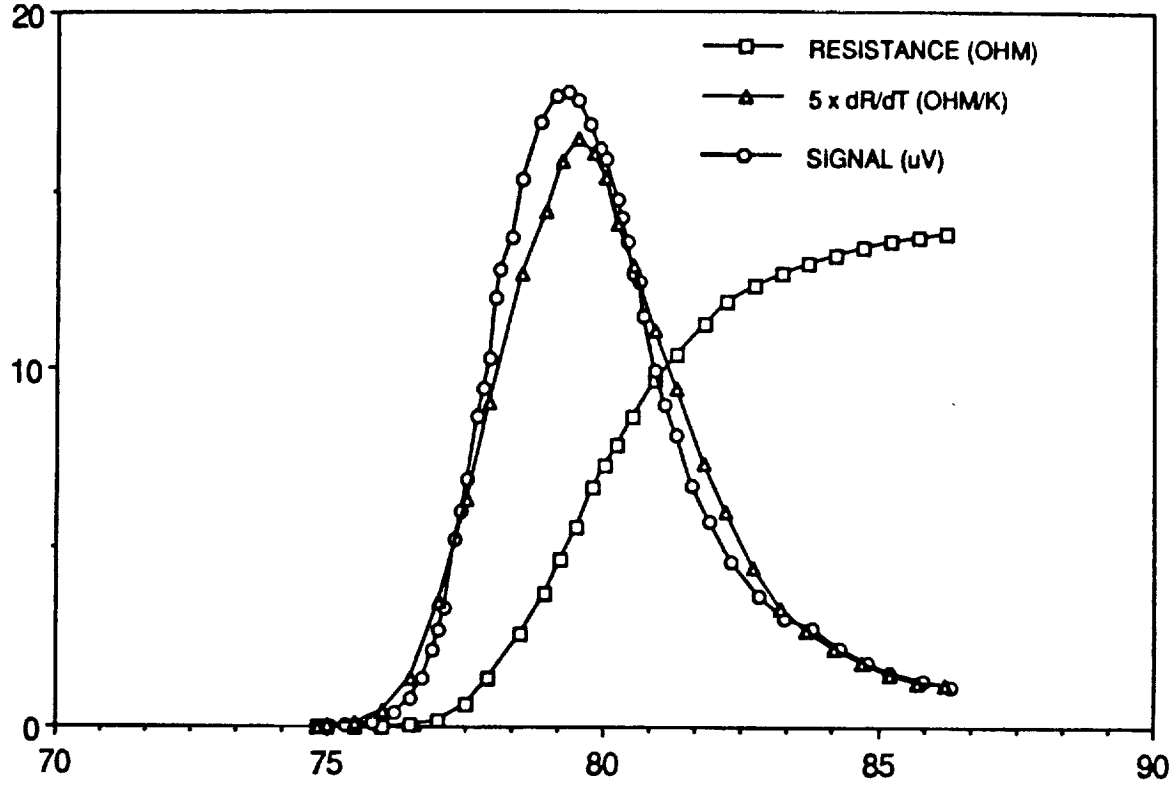

Figure 4. Resistance (squares), 5 x dR/dT (triangles) and photoresponse (circles) of the laser ablated superconducting film. 400 Hz chopping frequency, He-Ne laser illumination, 100 μA bias.

photoresponse signal for a detector made from the sequentially evaporated film. The curve for dR/dT has been multiplied by a factor of 10. The temperature of this sample was held at 78.5 K during optimization of the beam position. As with the epitaxial sample, the temperature was varied down to approximately 12 K and no photoresponse other than that shown in this figure was observed. The agreement between the photoresponse and dR/dT is poor. The maximum of the signal is displaced from the maximum of dR/dT by approximately 3 K to a higher temperature. Notice however that there is a shoulder on the peak of the signal at approximately the temperature of the peak in dR/dT and that there appears to be a shoulder on the peak of dR/dT at the peak in the signal.

In speculating on the possibility of experimental problems that might explain this result, a rough calculation showed that thermal expansion of parts in the cryostat could shift the sample on the order of 10 μm relative to the focused laser beam. The sample was remeasured and, to correct for motion due to expansion, the beam was repositioned every one to two degrees of temperature change.

The remeasured response is plotted in Figure 6. The resistance-temperature characteristic was also remeasured using finer temperature increments. Note that while R and dR/dT are plotted on the same scale in this figure as in Figure 5, the signal is divided by a factor of 2. The measured signal voltage was nearly a factor

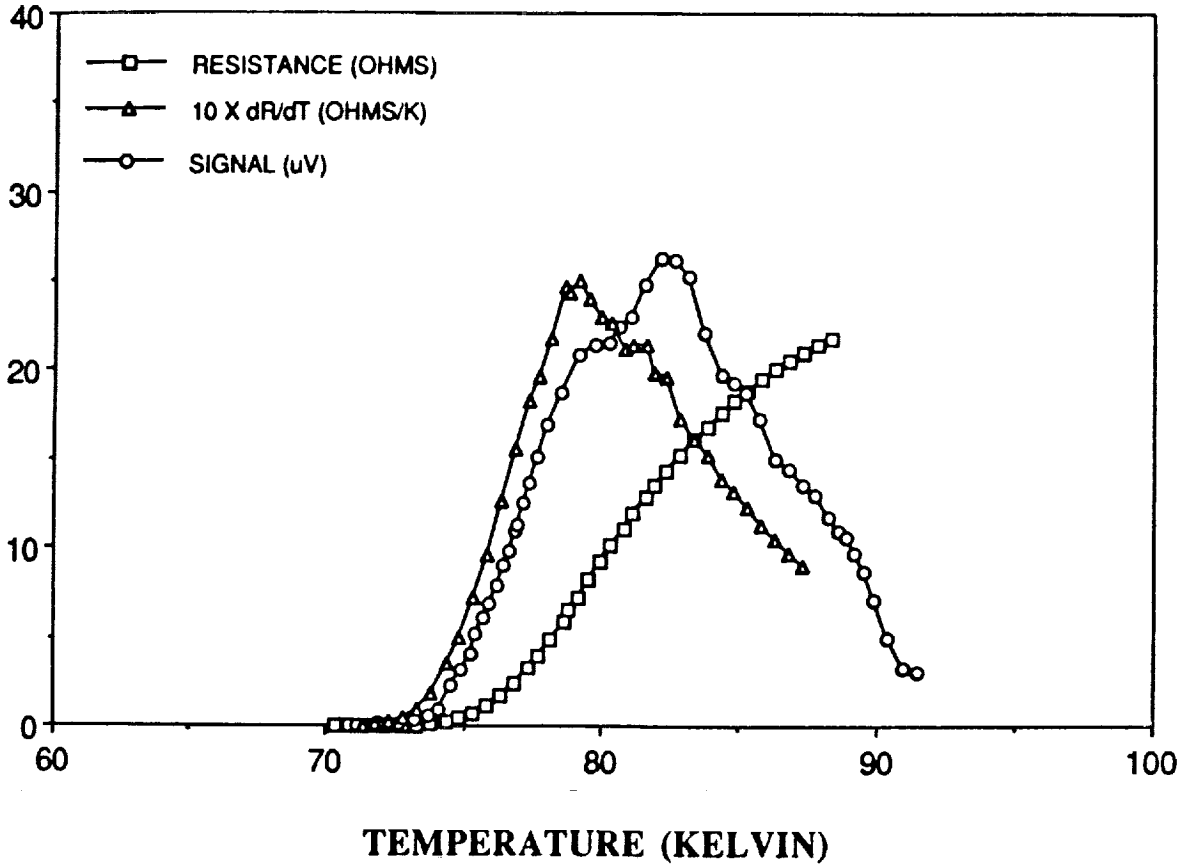

Figure 5. Resistance (squares), 10 x dR/dT (triangles) and initial measurement of the photoresponse (circles) of the sequentially evaporated superconducting film. 400 Hz chopping frequency, He-Ne laser illumination, 100 μA bias.

of three larger when the position of the beam was optimized as the measurement progressed. The agreement between the peak positions was still approximately the same. In addition a shoulder still appeared to exist on the signal peak at about the temperature of the peak in dR/dT and on the dR/dT curve at about the peak in the signal.

4. DISCUSSION

The observed photoresponse of the granular sequentially evaporated film can be explained with two assumptions: 1) That the film is spatially nonuniform with different critical temperatures in different regions, and 2) That the laser beam was not uniformly illuminating the entire bridge area. With these assumptions, as the signal is optimized at a given temperature, the laser beam can be positioned at a location on the film that has a locally high dR/dT, even if it doesn't make a dominant contribution to the total resistance of the film. This can be particularly true if the size of the laser spot is comparable in size to the non-uniformities.

Several simple one dimensional simulations were made to explore this possibility. Three of these will be presented here. In the first two a one dimensional detector was assumed to consist of a series combination of two regions, one with a

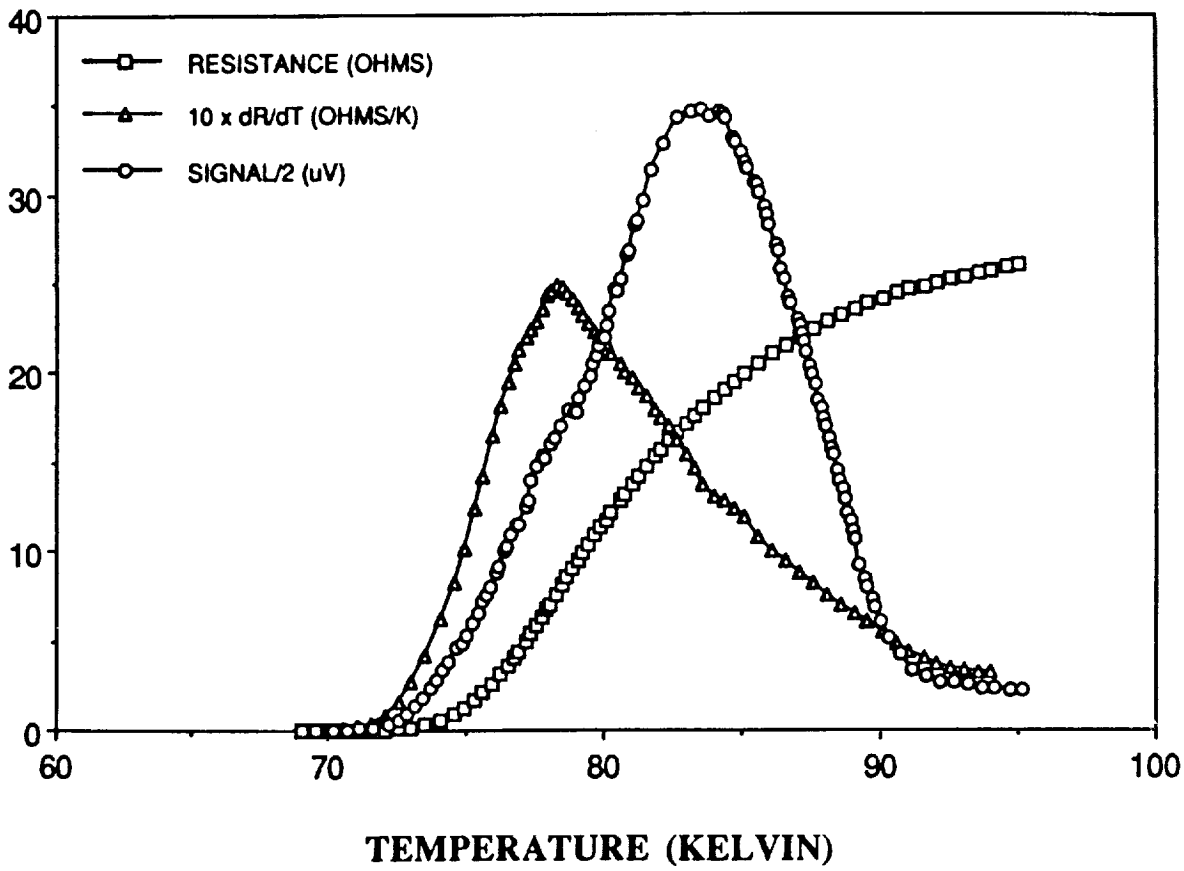

Figure 6. Resistance (squares), 10 x dR/dT (triangles) and remeasured photoresponse/2 (circles) of the sequentially evaporated superconducting film. 400 Hz chopping frequency, He-Ne laser illumination, 100 μA bias.

transition centered about 83 K and another with a transition centered about 79 K. The higher temperature transition was assumed to be broader. The illumination was assumed to result in a temperature increase that had a Gaussian distribution along the detector. The resistance, dR/dT and the signal for two beam positions are plotted in Figures 7 and 8. In Figure 7 the position of the beam was optimized at 77 K resulting in a strong response due to the low T_c region of the detector while for Figure 8 it was optimized at 87 K resulting in a strong response due to the high T_c portion of the detector.

A slightly more sophisticated simulation was also made. The one dimensional detector was assumed to consist of a narrow region of high T_c with broader regions of lower T_c on either side. The simulation was then run with the beam position re-optimized at 1 K intervals. The result in Figure 9 shows many of the features observed in the measurement on the sequentially evaporated film. The peak in the photoresponse is at a higher temperature than the peak in dR/dT and each peak has a shoulder that corresponds with the other, although the shoulders are much stronger here. The cusp in the signal between the peaks results from the sharp boundary between the regions. The parameters of the model could be adjusted to give a better reproduction of the measured data but this simulation demonstrates that a bolometric response in a nonuniform film can explain the observed signal.

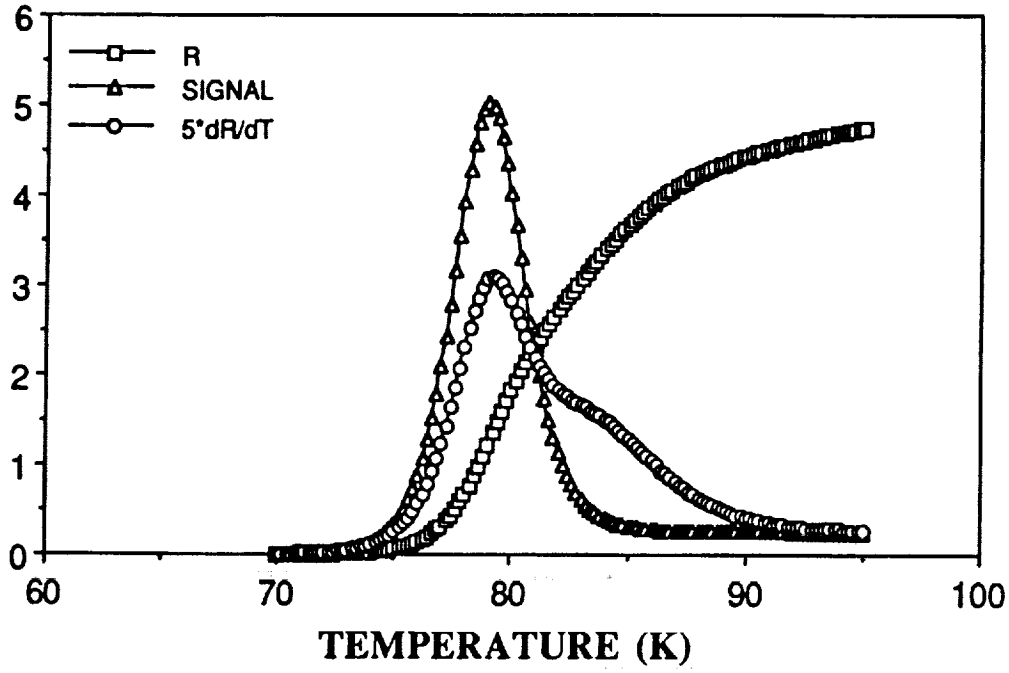

Figure 7. Simulated resistance, 5 x dR/dT and signal of a nonuniform detector. Beam position optimized at 77 K.

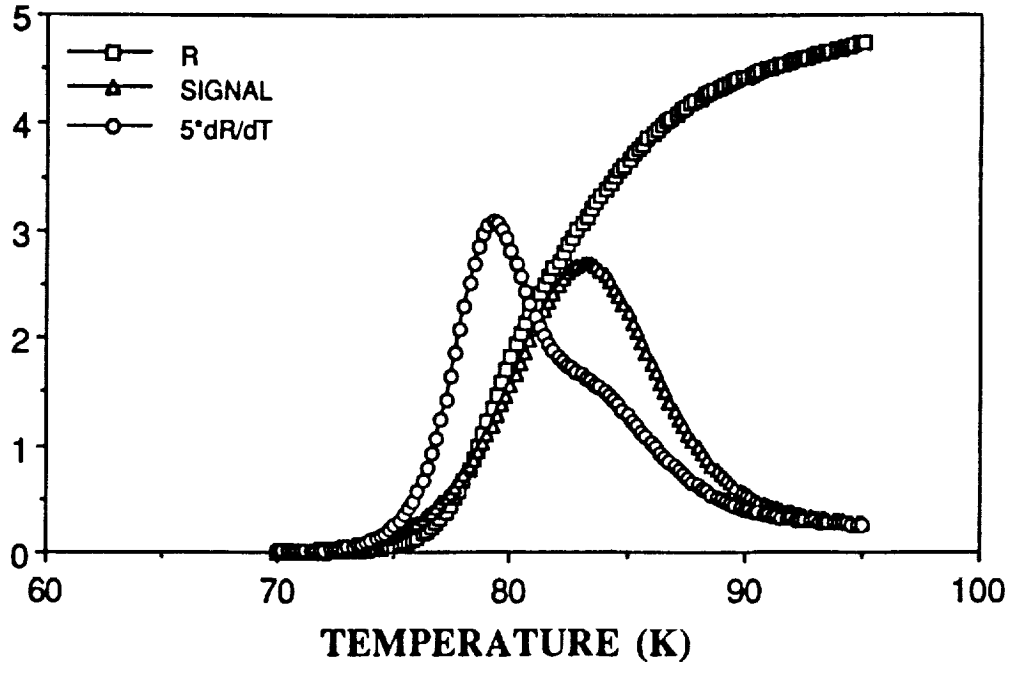

Figure 8. Simulated resistance, 5 x dR/dT and signal of a nonuniform detector. Beam position optimized at 87 K.

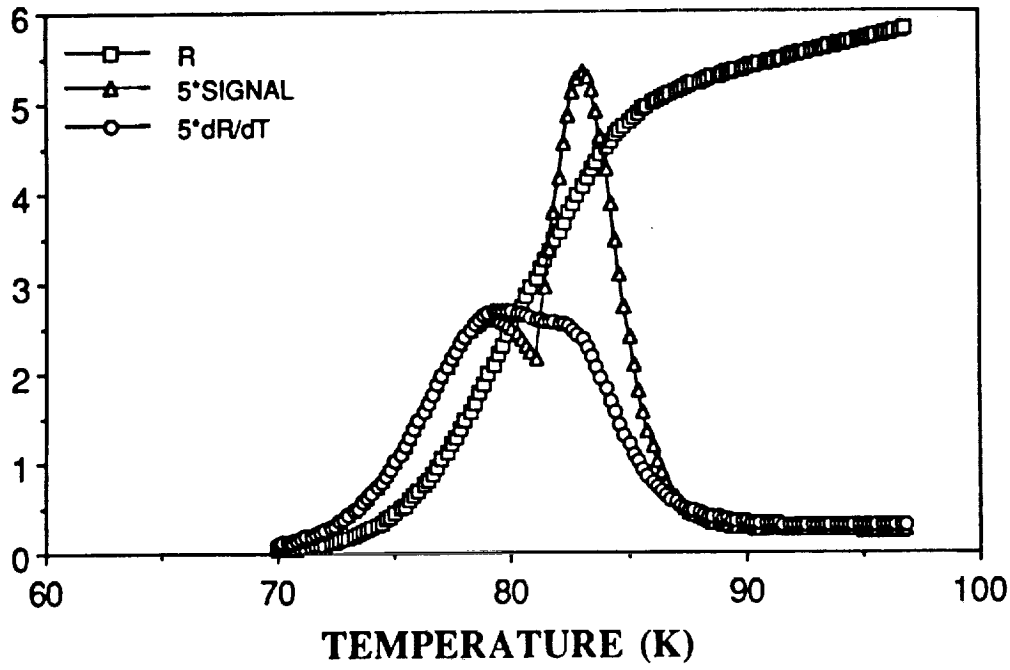

Figure 9. Simulated resistance, 5 x dR/dT and 5 x signal of a nonuniform detector. Beam position re-optimized at 1 K intervals.

5. CONCLUSIONS

The photoresponses of a laser ablated epitaxial film and a granular sequentially evaporated film of $YBa_2Cu_3O_{7-\delta}$ have been measured. For both films the only observed signal occurred for temperatures near the transition temperature. For the epitaxial film there was good correspondence between the measured signal and the temperature derivative of the resistance indicating that the photoresponse was bolometric in nature. The photoresponse of the granular films did not coincide as well with dR/dT, however simulations based on the assumption that the film is nonuniform lead to the conclusion that nonuniformities, coupled with a bolometric effect, are sufficient to explain the observations.

6. ACKNOWLEDGEMENTS

This research was supported by the National Aeronautics and Space Administration, Lewis Research Center under cooperative research agreement NCC 3-105.

REFERENCES

1. M. G. Forrester, M. Gottlieb, J. R. Gavaler and A. I. Braginski, "Optical response of epitaxial films of $YBa_2Cu_3O_{7-\delta}$," Appl. Phys. Lett., 53 (14), pp. 1332-1334, 1988.

2. M. Leung, P. R. Broussard, J. H. Claassen, M. Osofsky, S. A. Wolf and U. Strom, "Optical detection in thin granular films of Y-Ba-Cu-O at temperatures between 4.2 and 100 K," Appl. Phys. Lett., 51(24), pp. 2046-2047, 1987.

3. M. G. Forrester, J. Talvacchio and A. I. Braginski, "Electrical response of high-T_c superconducting films to laser radiation," Proceedings of the Workshop on High Temperature Superconductivity," pp. 241-248, GACIAC, Huntsville, 1989.

4. P. L. Richards, J. Clarke, R. Leoni, Ph. Lerch, S. Verghese, M. R. Beasley, T. H. Geballe, R. H. Hammond, P. Rosenthal and S. R. Spielman, "Feasibility of the high T_c superconducting bolometer," Appl. Phys. Lett., 54(3), pp. 283-285, 1989.

5. G. J. Valco, N. J. Rohrer, J. D. Warner and K. B. Bhasin, "Sequentially evaporated thin Y-Ba-Cu-O superconductor films: composition and processing effects," High T_c Superconducting Thin Films, Devices and Applications, G. Margaritondo, R. Joynt and M. Onellion, AIP Conference Proceedings No. 182, pp. 147-154, American Institute of Physics, Atlanta, 1988.

6. G. J. Valco, N. J. Rohrer, J. D. Warner and K. B. Bhasin, "Sequentially evaporated thin Y-Ba-Cu-O Superconducting Films on Microwave Substrates," Proceedings of the Workshop on High Temperature Superconductivity," pp. 197-203, GACIAC, Huntsville, 1989.

7. J. D. Warner, J. D. Meola and K. A. Jenkins, "Study of Deposition of $YBa_2Cu_3O_{7-x}$ on cubic zirconia," preprint.

NASA Technical Memorandum 103235

High Temperature Superconducting Thin Film Microwave Circuits: Fabrication, Characterization, and Applications

K.B. Bhasin, J.D. Warner, R.R. Romanofsky, and V.O. Heinen
National Aeronautics and Space Administration
Lewis Research Center
Cleveland, Ohio

and

C.M. Chorey
Sverdrup Technology, Inc.
Lewis Research Center Group
Brook Park, Ohio

Prepared for the
Technical Symposium on Optical Engineering and Photonics
in Aerospace Sensing
sponsored by the Society of Photo-Optical Instrumentation Engineers
Orlando, Florida, April 16–20, 1990

NASA

HIGH TEMPERATURE SUPERCONDUCTING THIN FILM MICROWAVE CIRCUITS: FABRICATION, CHARACTERIZATION, AND APPLICATIONS

K.B. Bhasin, J.D. Warner, R.R. Romanofsky, and V.O. Heinen
National Aeronautics and Space Administration
Lewis Research Center
Cleveland, Ohio 44135

and

C.M. Chorey
Sverdrup Technology, Inc.
Lewis Research Center Group
Brook Park, Ohio 44142

SUMMARY

Epitaxial $YBa_2Cu_3O_7$ films have been grown on several microwave substrates. Surface resistance and penetration depth measurements have been performed to determine the quality of these films. In this paper, the properties of these films on key microwave substrates are described. The fabrication and characterization of a microwave ring resonator circuit to determine transmission line losses is presented. Lower losses than those observed in gold resonator circuits were observed at temperatures lower than critical transition temperature.

Based on these results, potential applications of microwave superconducting circuits such as filters, resonators, oscillators, phase shifters, and antenna elements in space communication systems are identified.

E-5515

INTRODUCTION

The discovery of superconductivity in ceramic oxides such as Y-Ba-Cu-O, Bi-Sr-Ca-Cu-O and Tl-Ca-Ba-Cu-O with transition temperatures T_c around 100 K has inspired many researchers around the world to manipulate and to alter these ceramic oxides to form beneficial products for various applications. One important application where high T_c superconductors have begun to show promise is in the area of microwave communication and radar systems. The use of high T_c superconductors in a microwave system requires development of thin films on microwave substrates which then can be patterned into desired microwave circuits such as filters, phase shifters, ring resonators, and delay lines. The superconducting thin films for microwave circuits need to be deposited on low dielectric constant and low loss substrates, have smooth morphology, high critical temperature T_c, high critical current density J_c and low surface resistance R_s. Furthermore, films on the substrates must be evaluated as microstrip or ring resonator circuit to determine the quality factor "Q", and various losses prior to developing microwave circuit applications.

In this paper, we describe the characteristics of high quality Y-Ba-Cu-O thin films on microwave substrates and evaluation of their microwave properties. We discuss the fabrication, characterization, and performance of ring resonator circuits. In conclusion, we present some examples of applications of superconducting microwave circuits.

FABRICATION OF THIN FILMS ON MICROWAVE SUBSTRATES

To obtain high quality $YBa_2Cu_3O_7$ films on suitable substrates the substrate lattice constants must be matched to those of the films and there must not be a detrimental chemical reaction between the substrates and the film. In addition, the film composition must be as close to the correct composition as possible. To date, to obtain the highest quality films several physical and chemical deposition techniques have been used. Many of these require post-annealing at high temperatures. This high temperature anneal causes chemical interactions at the film-substrate interface, making the substrate/film interface unsuitable for microwave applications (ref. 1). See table I for the properties of sequential evaporated films on microwave substrates. To circumvent this problem, an in situ annealing procedure which allows lower growth temperatures have been used to grow epitaxial films using a laser ablation technique (ref. 2).

The details of the geometry of the laser ablation are shown in figure 1(a). The substrates were mounted onto a stainless steel plate with a diameter of 63 mm. The plate was heated from the backside using a resistive heater. The sample chamber was evacuated to 3×10^{-7} torr, or lower, using a liquid nitrogen cold trapped diffusion pump before the sample was warmed up to 700 °C. During deposition the chamber pressure was 170 mtorr; the laser wavelength was 248 nm; the energy density was 1.5 (J/cm^2)/pulse; the pulse rate was two pulses per second; and the distance between the target and the sample was 8 cm. The laser beam was rastered up and down 1 cm over the target using an external lens on a translator. After deposition the oxygen pressure was raised to 1 atm, and the temperature was lowered to 450 °C at a rate of 2 °C/min. The temperature was held at 450 °C and held for 2 hr, then cooled to room temperature.

The best film had a T_c of 89.8 K immediately after deposition as determined by a standard four point resistance measurement. Its resistance versus temperature behavior is shown in figure 1(b). From x-ray diffraction data the film was determined to be c-axis aligned. Critical current density J_c versus temperature is shown in figure 1(c). As can be seen, the value of J_c was greater than 10^6 A/cm^2 at 77 K. The surface morphology of the HTS on $LaAlO_3$ is shown in figure 1(d). The surface is very smooth with some small structure of about 0.25 μ in size. This size of structure has been confirmed by Scanning Tunneling Microscopy. We do not observe large numbers of HTS particulates due to the laser ablation process. In table I, we list the performance of $YBa_2Cu_3O_7$ thin films on various microwave substrates along with properties of these substrates.

SURFACE RESISTANCE

Surface resistance characterization of superconducting film offers valuable information on the film quality for microwave circuit applications. Currently, surface resistance values are obtained by cavity (refs. 3 and 4) and stripline measurements (ref. 5). Correlation between material properties (i.e., dc conductivity above T_c, penetration depth, and T_c) and surface resistance are still not well understood for new high T_c superconducting films. Theoretically, surface resistance of metal conductor is given by

$$R_N = \left(\frac{\omega\mu}{2\sigma}\right)^{1/2} = \frac{1}{\sigma_N \delta_N} \quad (1)$$

where

$$\delta = \left(\frac{2}{\mu\sigma\omega}\right)^{1/2} \text{ is the skin depth.}$$

σ_N is the normal conductivity, μ_o is the magnetic permeability, and ω is the angular frequency. For superconducting films, conductivity is a complex quantity $\sigma = \sigma_1 + j\sigma_2$. For $\sigma_2 >> \sigma_1$ one can obtain the surface resistance of superconducting film

$$R_s = \frac{0.5\sigma_1\omega\mu}{\sigma_2^{3/2}} \quad (2)$$

where σ_2 is related to the penetration depth λ by

$$\sigma_2 = \frac{1}{\omega\mu\lambda^2} \quad (3)$$

From equations (1) and (2)

$$\frac{R_s}{R_N} = \frac{2\sigma_1}{\sigma_N}\left(\frac{\lambda}{\delta_c}\right)^3 \quad (4)$$

Clearly, from this expression to obtain surface resistance for superconducting film lower than for a normal metal, the lowest values of σ_1 and λ are desired. Miranda et al. (ref. 6) have measured microwave transmission in a waveguide for superconducting films as shown in figure 2. From the transmission data, using the two fluid models, σ_1 and λ have been obtained. A summary of results for Y-Ba-Cu-O films on various substrates is shown in table II. The penetration depth value was small for laser ablated film on lanthanum aluminate substrates. Using these values in equation (4), a surface resistance for films on $LaAlO_3$ is calculated. In figure 3, which is adopted from reference 7, we show how the quadratic variation f^2 of the surface resistance varies with frequency for laser ablated Y-Ba-Cu-O films on microwave substrates. The surface resistance is several orders of magnitude lower than that of copper. Clearly surface resistance, penetration depth, and microwave conductivity measurements provide valuable information on the quality of these films for microwave circuits.

BASIC MICROWAVE CIRCUIT - RING RESONATOR

Measurements of surface resistance by the cavity technique fail to model microstrip losses completely because it neglects substrate losses and fails to adequately probe the film-substrate interface. Microstrip resonators patterned from thin films on microwave substrates allow direct measurement of microstrip losses. We have fabricated microstrip ring resonators operating at 35 GHz

from laser ablated YBCO thin films deposited on lanthanum aluminate substrate (ref. 11). Also, several groups have studied resonator circuits at lower frequencies (refs. 5 and 8 to 10). The resonator circuits we fabricated were patterned by standard photolithography using negative photoresist and a 'wet' chemical etchant. This etchant was either a 3-percent solution of bromine in ethanol or dilute phosphoric acid in water. A metal ground plane was deposited by first evaporating 100 Å of Ti for adhesion followed by 1 μ of gold. In addition to the resonator, each chip also had a test bar for directly determining T_c of the patterned film. Identical resonators were fabricated entirely from gold (both strip and ground plane) using evaporation and lift-off to define the strip.

The resonators were measured using a Hewlett-Packard 8510 Automatic Network Analyzer, operating in WR-28 waveguide. The microstrip circuit mounted in a tapered ridge waveguide to microstrip test fixture is shown in figure 4. The design of a cosine tapered ridge used inside the waveguide to couple the incoming signal to microwave circuit is shown in figure 5. The plot of the reflected power from the resonator (which is a measure of the loaded 'Q') is shown in figure 6 for several frequencies. Two features are apparent; (1) the coupling changes with temperature (the coupling coefficient increases with decreasing temperature) and (2) the resonant frequency shifts with temperature. The change in the resonant frequency versus temperature for a superconducting resonator is plotted in figure 7. This change is a consequence of the dependence of the internal impedance of the strip on the changing normal superconducting electron densities. The internal inductance of a superconducting strip over a ground plane is given by (ref. 8):

$$L_{int} = \mu_o \lambda \coth\left(\frac{t}{\lambda}\right)$$

Assuming the Gorter-Casimir temperature dependence of λ:

$$\lambda(T) = \frac{\lambda_o}{\left[1 - \left(\frac{T}{T_c}\right)^4\right]^{1/2}}$$

the form of the resonant frequency variation based on the changing line inductance matches the experimental observations (fig. 7).

The best resonators measured to date have shown unloaded 'Q's ranging from 2500 to 1000 at 20 and 77 K, respectively. This corresponds to a surface resistance value of, at most, 15 mΩ at 77 K at 35 GHz, a value two to three times better than copper at the same temperature and frequency.

POTENTIAL APPLICATIONS

High T_c superconducting thin films have shown lower surface resistance than copper. Low conductor losses for high T_c superconducting ring resonator circuit have been demonstrated. These characteristics are desirable in passive microwave circuits used in communication and radar systems since they reduce loss and size, increase bandwidth, and provide low noise. Complete system

analysis of the impact of the advantages of high T_c superconducting microwave circuits is yet not available. From a block diagram of satellite transponder (fig. 8), we have considered the following examples of potential applications of HTS microwave circuits in satellite communications applications. One can easily project the application of superconducting passive circuits as low loss, high 'Q' filters (ref. 11), high 'Q' resonators, delay lines, power splitter combiners, and resonator stabilized oscillators. Based on results obtained to date on the performance of superconducting microstrip resonator circuits with high 'Q' values.

In addition to these applications, extremely low loss phase shifters using superconducting switches are also feasible. In figure 9, we show a phase shifter which utilizes superconducting-normal-superconducting switches in place of FET/diode switches. The switches are fabricated from high temperature thin films of YBCO. The switches operate in the bolometric mode with the film held near its transition temperature. Radiation from a light source raises the temperature and consequently causes the film to become resistive. If the switches in the reference path are illuminated, they will become resistive. The switches on the opposite side of the device are superconducting. Since each switch is positioned one quarter of a wavelength from the junction, the signal will be reflected from the delay path in phase. A similar phenomenon occurs at the output port. To achieve the desired phase shift, the opposite set of switches is illuminated. Figure 9 shows the predicted behavior for a 180° phase shifter, with exceptional narrow insertion loss envelope and excellent return loss.

In figure 10, we show an example of hybrid semiconductor/superconductor device. It is possible that by combining the excellent low noise properties of GaAs devices with the low loss and low noise properties of superconducting transmission lines one can achieve ultra low noise receivers for satellite communications applications. If these promising concepts of high T_c superconducting devices are actually brought to fruition, then one can conceive their use in low loss, low noise superconducting phased array antenna in space communications systems as shown in figure 11. HTS transmission lines can provide low loss feed network which is a major problem in antenna networks.

SUMMARY OF RESULTS

We have demonstrated that rare-Earth oxide thin superconducting films can be deposited on various microwave substrates with critical temperature T_c above 77 K, critical current densities J_c above 10^6 Å/cm^2, and low surface resistance. Films can be easily etched into microwave transmission line circuits. The basic microwave circuit ring resonator fabricated on a $YBa_2Cu_3O_7$ superconducting film on $LaAlO_3$ substrate showed higher 'Q' than gold circuits at 77 K. Such circuits can provide propagation characteristics of microwave signals at the film-substrate interface. Several key HTS circuits such as filters, oscillators, phase shifters, and phased array antennas' feeds are feasible in the near future. For technology to improve further, reproducible, large area films have to be grown on low dielectric constant, low loss microwave substrates. Tradeoffs between superconducting microwave circuits with cryogenic systems and normal metal microwave circuits will have to be quantitatively established to determine their suitability for advanced communication and sensor systems.

REFERENCES

1. Valco, G.J., et al.: Sequentially Evaporated Thin Y-Ba-Cu-O Superconducting Films on Microwave Substrates. NASA TM-102068, 1989.

2. Warner, J.D., et al.: Growth and Patterning of Laser Ablated Superconducting YBCO Films on $LaAlO_3$ Substrates. NASA TM-102436, 1989.

3. Klein, N., et al.: Millimeter Wave Surface Resistance of Epitaxially Grown $YBa_2Cu_3O_7$ Thin Films. Appl. Phys. Lett. vol. 54, no. 8, Feb. 20, 1989, pp. 757-759.

4. Miranda, F.A., et al.: Millimeter Wave Surface Resistance of Laser Ablated Y-Ba-Cu-O Superconducting Films. Accepted for publication in Appl. Phys. Lett., Sept. 1990.

5. Fathy, A., et al.: Microwave Properties and Modeling of High T_c Superconducting Thin Film Meander Line. IEEE MTT-S Internatinal Symposium (Dallas, TX, May 1990) Digest, 1990, pp. 859-862.

6. Miranda, F.A., et al.: Microwave Conductivity of Superconducting Bi-Sr-Ca-Cu-O Thin Films in the 26.5 to 40.0 GHz Frequency Range. Pysica C., vol. 188, 1990, pp. 91-98.

7. Inam, A., et al.: Microwave Properties of Highly Oriented $YBa_2Cu_3O_7$ Thin Films. Appl. Phys. Lett., vol. 56, no. 12, Mar. 19, 1990, pp. 1178-1180.

8. Valenzuela, A.A., and Russer, P.: High-Q Coplanar Transmission Line Resonators of YBCO on MgO. Appl. Phys. Lett., vol. 55, no. 10, Sept. 4, 1989, pp. 1029-1031.

9. McAroy, B.R., et al.: Superconducting Stripline Resonator Performance. IEEE Trans. Magn., vol. 25, no. 10, Oct 1989, pp. 1104-1106.

10. Takemoto, J.H., et al.: Microstrip Ring Resonator Technique for Measuring Microwave Attenuation in High T_c Superconducting Thin Films. IEEE Trans. Microwave Theory Tech., vol. MTT-37, no. 10, Oct. 1989, pp. 1650-1652.

11. Bhasin, K.B., et al.: Performance and Modeling of Superconducting Ring Resonators at Millimeter-wave Frequencies. IEEE MTT-S International Microwave Symposium (Dallas, Tx, May 1990) Digest, 1990, pp. 269-272. (Also NASA TM-102526, 1990).

12. Fiedziuszko, S.J., Holme, S., and Heidmann, P.: Novel Filter Implementations Using HTS Materials. To be published.

TABLE I. - KEY PROPERTIES OF MICROWAVE SUBSTRATE MATERIALS

Material	T_c achieved		Dielectric constant	Loss tangent	Lattice size, Å
	Sequential evaporation, K	Laser ablation, K			
Magnesium oxide (MgO)	70	88	9.65	4×10^{-4}	4.178 (100)
Lanthanum aluminate ($LaAlO_3$)	82	90	22	5.8×10^{-4}	3.792 (110)
Lanthanum gallate ($LaGaO_3$)	--	88	27	2×10^{-3}	3.892 (110)
Sapphire (Al_2O_3)	71	60	9.4 11.6	1×10^{-6}	5.111 ($0\overline{1}\overline{1}$)
Yttria stabilized zirconia (ZrO)	70	89	27	6×10^{-4}	3.8795 (100)
Silicon (Si)	—	--	12	10×10^{-4}	5.43 (100)
Gallium arsenide (GaAs)	—	--	13	6×10^{-4}	5.653 (100)

TABLE II. - MICROWAVE CONDUCTIVITIES (σ_n, $\sigma^* = \sigma_1 - 1\sigma_2$) AND ZERO TEMPERATURE PENETRATION DEPTH (λ_0) at 33.3 GHz FOR LASER ABLATED $YBa_2Cu_3O_{7-\delta}$ SUPERCONDUCTING THIN FILMS

Parameter	YBCO on $LaAlO_3$			YBCO on MgO	YBCO on ZrO_2
	828 Å	1769 Å	5000 Å	3500 Å	1200 Å
σ_n (300 K)	3.0×10^5 S/m	2.2×10^5 S/m	1.5×10^5 S/m	1.4×10^5 S/m	2.8×10^5 S/m
σ_1 (77 K)	2.8×10^5 S/m	2.5×10^5 S/m	1.8×10^5 S/m	1.2×10^5 S/m	2.4×10^5 S/m
σ_2 (77 K)	5.4×10^6 S/m	1.1×10^7 S/m	4.6×10^5 S/m	3.0×10^6 S/m	8.4×10^6 S/m
λ_0	0.43 μm	0.36 μm	0.39 μm	0.53 μm	0.59 μm

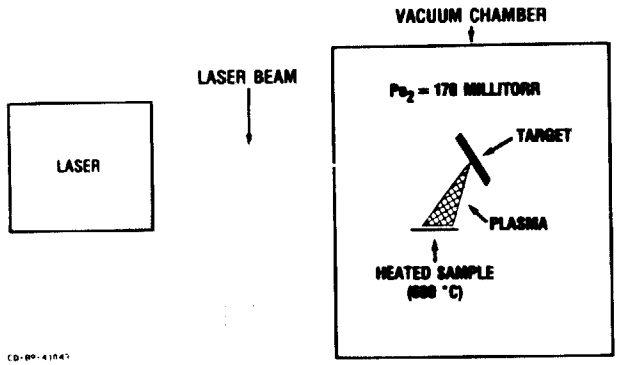

(a) LASER ABLATION TECHNIQUE.

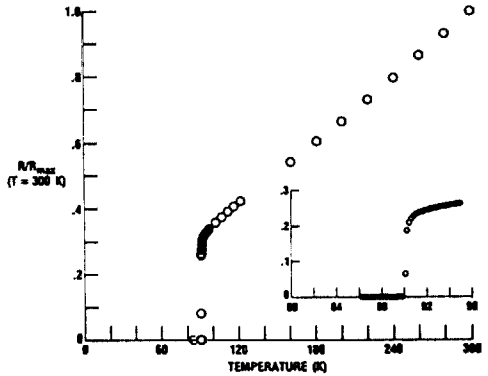

(b) RESISTANCE VERSUS TEMPERATURE OF $YBa_2Cu_3O_7$.

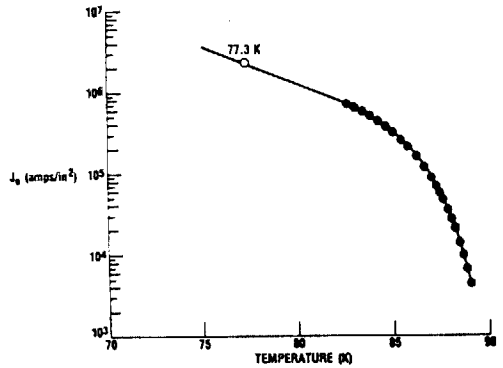

(c) CRITICAL CURRENT DENSITY OF $YBa_2Cu_3O_7$ ON $SrTiO_3$.

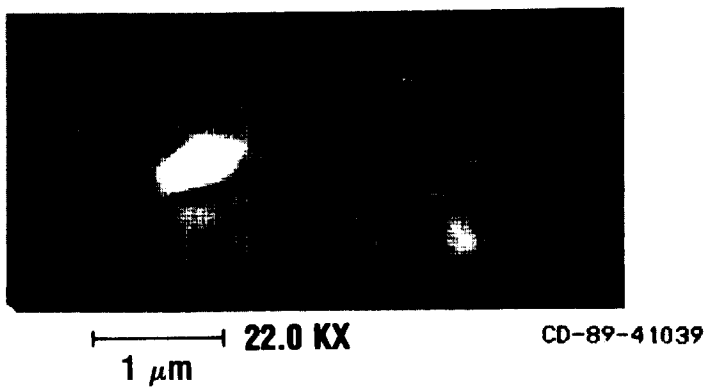

(d) SEM MICROGRAPHS OF $YBa_2Cu_3O_7$ FILM ON $LaAlO_3$.

FIGURE 1.

C-3

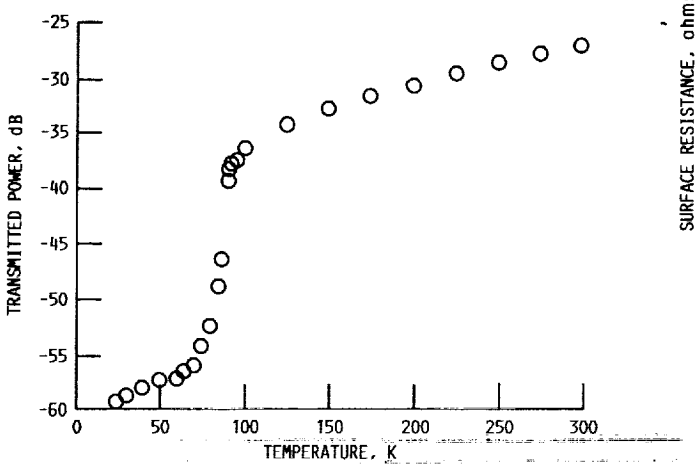

FIGURE 2. - TRANSMITTED POWER IN dB THROUGH A Y-Ba-Cu-O FILM ON $LaAlO_3$ SUBSTRATE AT 37 GHz.

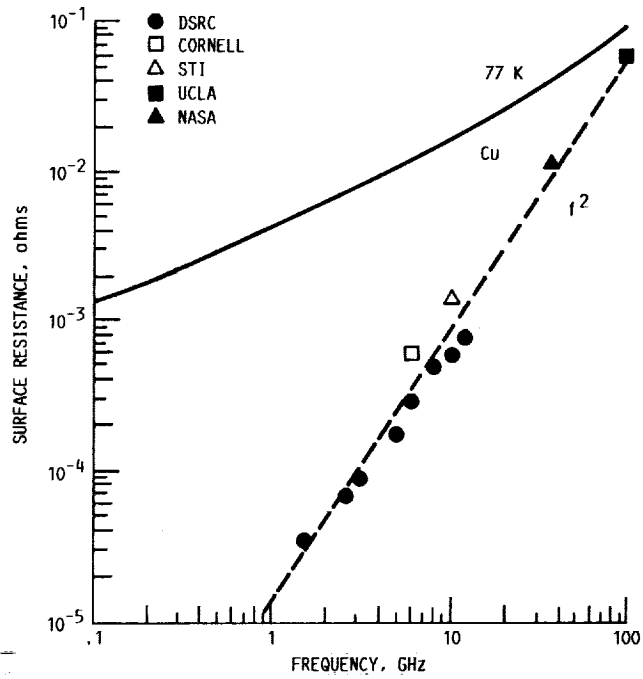

FIGURE 3. - SURFACE RESISTANCE OF LASER ABLATED Y-Ba-Cu-O FILMS ON $LaAlO_3$ SUBSTRATE VERSUS FREQUENCY. ADOPTED FROM APPLIED PHYSICAL LETTERS VOLUME 56, P.P. 1178-1180. NASA DATA OBTAINED BY MICROWAVE CONDUCTIVITY MEASUREMENTS.

ORIGINAL PAGE
BLACK AND WHITE PHOTOGRAPH

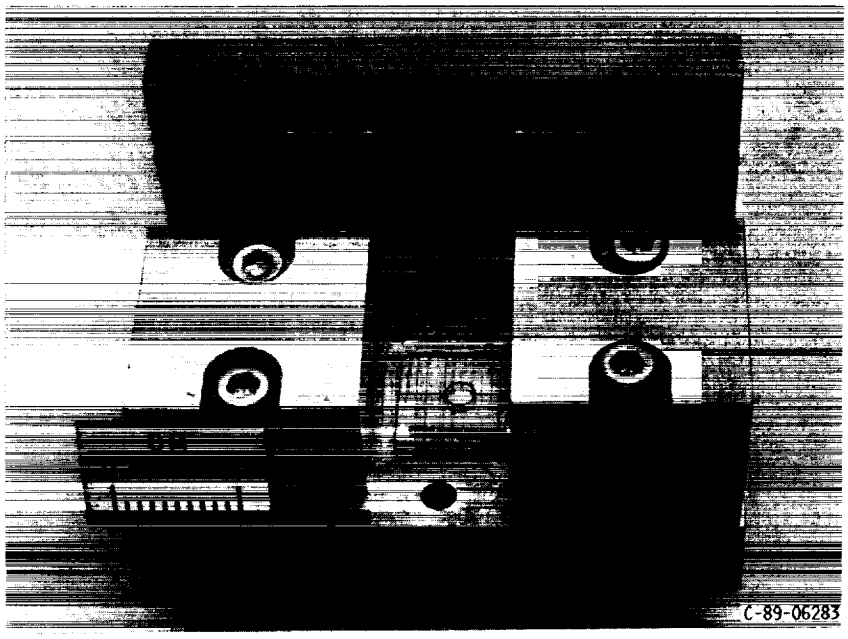

FIGURE 4. - WAVEGUIDE TEST FIXTURE USED FOR THE MEASUREMENT OF "Q" VALUES OF SUPERCONDUCTING RING RESONATORS.

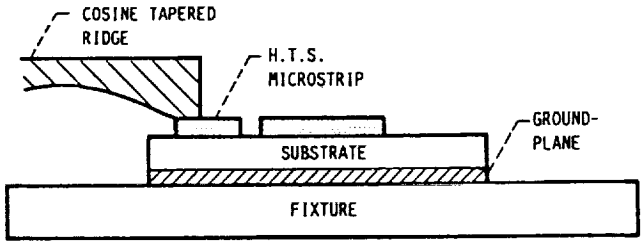

FIGURE 5. Design of the cosine taper ridge inside the waveguide used for waveguide to microstrip. transition

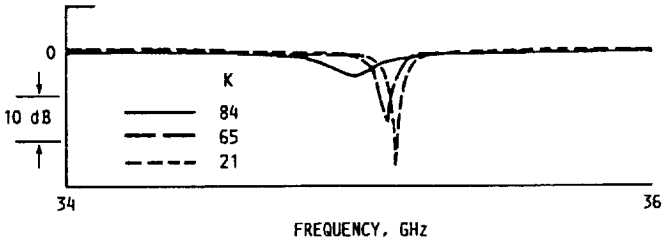

FIGURE 6. Resonances of Y-Ba-Cu-O ring resonator at three temperatures. Note the frequency shift with temperature.

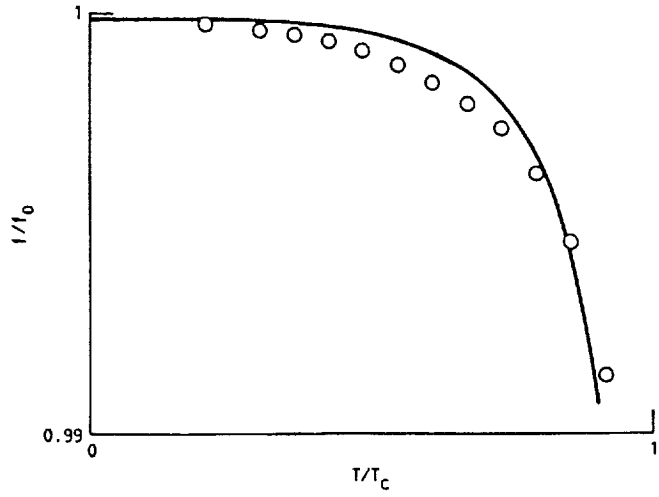

FIGURE 7. Ratio of the observed resonant frequency (f) to the zero temperature frequency (f_o) versus the T/T_c. O represent experimental values. Solid lines represents calculations based on Gorter-Casimir model.

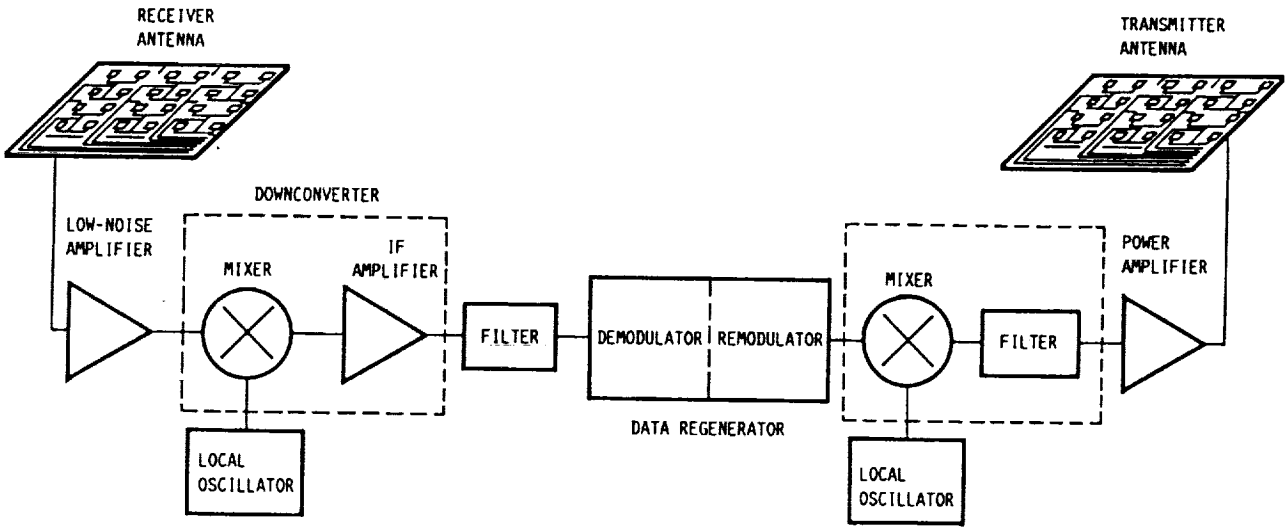

FIGURE 8. Block Diagram of a satellite transponder.

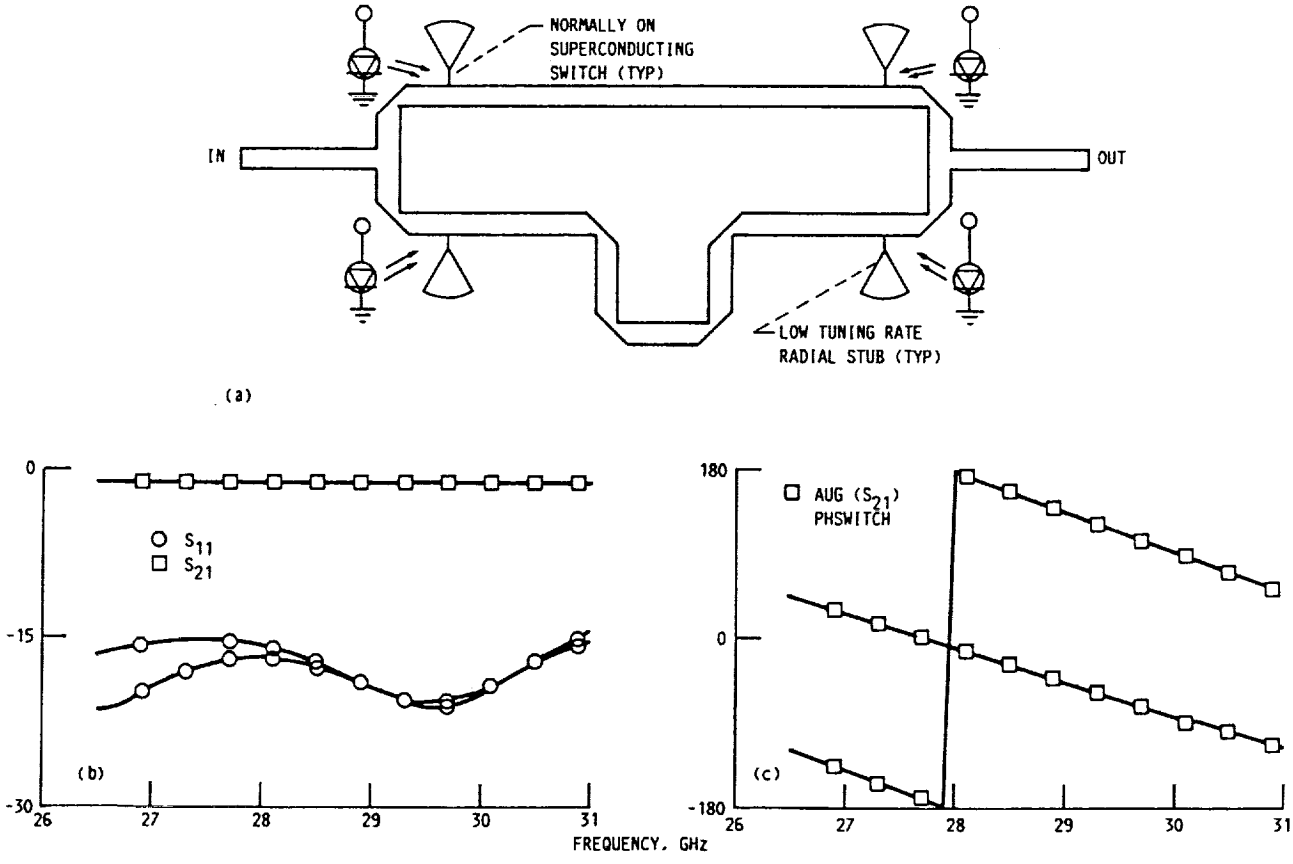

FIGURE 9. (a) Optically controlled High-T_c superconducting switch-line phase shifter. (b) Insertion loss and return loss for both reference and delay states. (c) Insertion phase for reference and delay states.

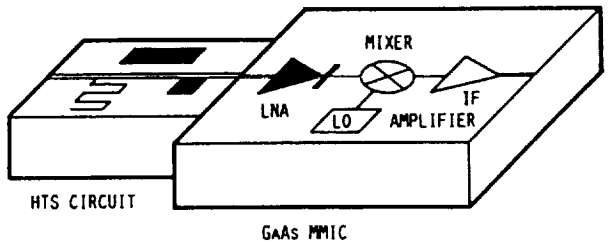

FIGURE 10. Superconducting GaAs MMIC Hybrid Receiver

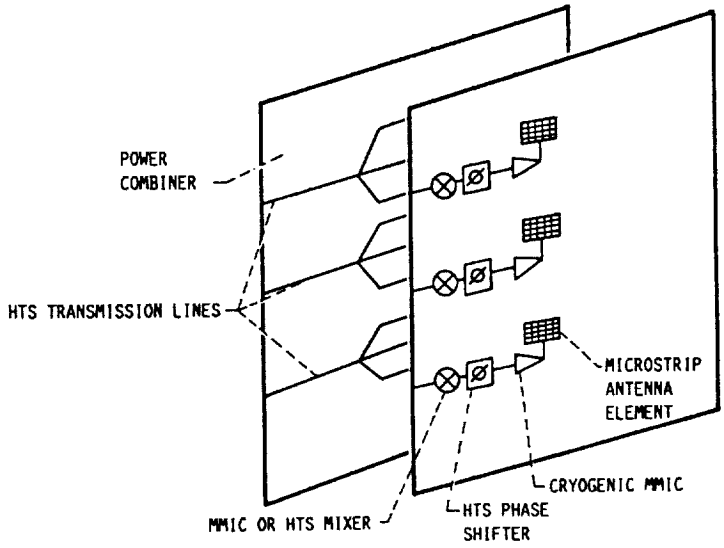

FIGURE 11. Conceptual diagram of a MMIC-Superconducting hybrid phase array antenna.

IV. SEMICONDUCTOR MATERIAL CHARACTERIZATION